NASA CONTRACTOR REPORT

NASA CR-13

C. 1

THEORETICAL FLOW FIELD CALCULATIONS FOR PROJECT RAM

by H. Webb, Jr., H. Dresser, K. Korkan, and R. Raparelli

Prepared by
NORTH AMERICAN ROCKWELL CORPORATION
Downey, Calif.
for Langley Research Center

0060602

NASA CR-1308

THEORETICAL FLOW FIELD CALCULATIONS FOR PROJECT RAM

By H. Webb, Jr., H. Dresser, K. Korkan, and R. Raparelli

FOREWORD

The work described in this report was completed for the Langley Research Center, National Aeronautics and Space Administration, under the terms and specifications of their contract NAS 1-8172 issued June 4, 1968 at Hampton, Virginia.

The work was performed in the Special Projects group headed by Dr. G. A. Etemad, within the Flight Technology Section, Dr. C. R. Faulders, Manager, of the North American Rockwell Corporation's Space Division.

Mr. W. L. Grantham was the NASA Technical Monitor responsible for this study.

ABSTRACT

Theoretical flow fields for seven flight conditions for the RAM-C blunted cone configuration are presented. Both viscous and inviscid flow regions are considered in an analysis leading to predictions of nonequilibrium chemical effects within the entire flow field. Special emphasis is placed on the presence of free electron concentrations which are responsible for the phenomena of radio attenuation. The flight investigation of these effects is the purpose of the RAM Project. Nonequilibrium flow is predicted by using a one-dimensional analysis along streamlines both in the boundary layer region and in the inviscid flow region. For two of the flight conditions, calculations were performed to evaluate the influence of a larger nose radius on the flow field. This change in geometry occurs when the beryllium nosecap is ejected. Very small plottable differences were found on outer streamlines for the lower speed flight condition when comparisons were made on similarly located normals.

CONTENTS

THEORETICAL FLOW FIELD CALCULATIONS

FOR PROJECT RAM

By H. Webb, Jr., H. Dresser, K. Korkan, and R. Raparelli

SUMMARY

The results of a theoretical prediction of equilibrium and chemical non-equilibrium flow fields for seven flight conditions and two nose radii of the RAM-C vehicle are presented. The RAM-C configuration is a hemispherically blunted, 9° semi-apex angle cone at zero angle of attack. The surface was assumed to be nonablating and at a constant wall temperature of 700°K. A set of computer programs was used to perform the analysis starting with a prediction of the wall pressure distribution. Following an analysis of the equilibrium laminar boundary layer and the definition of an effective body shape, the equilibrium inviscid flow was computed by a solution of the blunt body problem and a prediction of the supersonic flow field by the method of characteristics. Boundary layer displacement thickness effects were accounted for in this calculation. The assumption was made that the streamline pattern, pressure distribution, and shock shape were unaltered by chemical nonequilibrium effects and that the nonequilibrium composition could be computed by a simple one-dimensional analysis along streamlines by matching suitably chosen parameters. These streamlines were defined in the boundary layer using the principle of mass flow conservation, while the matching parameters were defined by a properties merger between inviscid and boundary layer values. Vorticity interaction effects were thus accounted for by defining a smooth variation of properties across the shock layer. Final results presented in this report show the variation across the shock layer, on normals to the body, of species composition, pressure, temperature, and flow velocity. Both equilibrium and non-equilibrium data are presented.

INTRODUCTION

The NASA Langley Research Center has for several years been conducting a series of flight experiments referred to as Project RAM (Radio Attenuation Measurements). The purpose of these tests is to study the interactions which take place between electromagnetic signals and the ionized flow field over entry vehicles, and to develop methods of alleviating or eliminating the so-called "blackout" or attenuation of radio signals. Several flight tests already have been conducted in this series, and the current effort involves the RAM-C vehicle which is designed to enter the earth's atmosphere at a speed of approximately 25,000 ft/sec. Of great importance to the overall project is the state-of-the-art that exists regarding a knowledge of the processes of formation of the ionized flow field. This knowledge is tested by comparison of predicted and measured plasma properties. North American Rockwell's Space Division has previously participated in conducting theoretical predictions of RAM flow fields, References 1, 2 and 3, and is now participating with the

NASA/Langley Research Center in a similar task for the RAM-C program. Both equilibrium and nonequilibrium predictions are presented as an aid to the understanding of flight measurements and to show the importance of nonequilibrium chemical effects. Essentially, the same technical approach was proposed for the current study as was used on the two previously completed contracts. The flight conditions to be considered cover a large range of both altitude and velocity. This analysis assumes that nonequilibrium chemical effects do not alter the shock shape, streamline pattern, or pressure distribution, and that nonequilibrium effects on flow properties and composition may be computed throughout the viscous and inviscid flow by a simple one-dimensional "streamtube analysis" which neglects diffusion effects.

SYMBOLS

a	speed of sound
A	streamtube area
C_p	specific heat at constant pressure
D	nose diameter
g	gravitational constant
h	static enthalpy
H	total enthalpy
j	dimensional flow indicator $\begin{cases} 0 - \text{two-dimensional} \\ 1 - \text{axisymmetric} \end{cases}$
J	mechanical equivalent of heat
K_b	backward chemical rate constant
K_{EQ}	chemical equilibrium constant
K_f	forward chemical rate constant
$\dot{m}$	mass flow
M	Mach number
n	intrinsic normal coordinate; chemical specie mole-to-mass ratio; distance outward along body normal
$N1$	total number of chemical species
$N2$	total number of chemical reactions

p	pressure
r	radial body coordinate
R	universal gas constant
R_c	radius of curvature
R_s	shock radius
Re	Reynolds number
s	streamline intrinsic coordinate, distance along body surface from stagnation point
S	entropy
t	time
T	temperature
u	total velocity
w	chemical specie molecular weight
X	chemical mole fraction, axial coordinate
$\bar{X}$	axial distance downstream from stagnation point
Z	compressibility factor, altitude
α	forward stoichiometric coefficient
β	backward stoichiometric coefficient
γ	specific heat-ratio
γ_e	effective specific heat ratio
δ	boundary layer thickness
δ^*	boundary layer displacement thickness
Δn	streamtube width
Δu	velocity defect $u_{in} - u_v$
θ	flow angle; body surface slope
μ	Mach angle
ρ	density

Subscripts

∞	free-stream conditions
e	edge of boundary layer
o	stagnation conditions
i	subscript denoting species
in	inviscid
k	subscript denoting reactions
v	viscous
x	measured in x-direction
max	maximum value
w	wall or body conditions
1	outboard streamline designation
2	inboard streamline designation

DISCUSSION OF METHODS

General

The basic technical approach, used previously in References 1, 2 and 3, is to compute detailed equilibrium chemistry flow fields over the RAM-C shape, followed by a one-dimensional computation of the nonequilibrium chemistry along particular streamlines selected from the equilibrium solutions. It is assumed that the shock shape, standoff distance, pressure distributions and streamline locations in the flow field are unaffected by the nonequilibrium chemistry effects.

The analysis is divided into a series of individual calculations which are performed in a sequence shown graphically in Figure 1. All calculations are performed by means of IBM computer programs, with the exception of the frozen chemistry shock property calculations, and the selection of boundary layer streamlines and matching properties which are required for the non-equilibrium analysis. The first step, leading to the definition of an effective body shape for the inviscid flow prediction, is to estimate the body pressure distribution. A laminar boundary layer growth calculation is then performed from which the displacement thickness distribution is obtained. By adding the displacement thickness to the bare body, an effective body shape is found and an improved pressure distribution prediction is made. If this pressure distribution is significantly different from the initial estimate, the procedure is repeated until acceptable convergence is obtained. Using the effective body shape, the subsonic-transonic flow field is computed and a left-running characteristic (start line) is located in the transonic region. The supersonic inviscid flow is then computed by the method of characteristics using properties on this start line for initial conditions. At this point the computed pressure distribution on the body is compared to that used in the boundary layer calculations. If reasonable agreement is not found, the boundary layer analysis and inviscid flow calculations are repeated until acceptable convergence is obtained.

Using mass flow conservation, boundary layer streamlines are defined and the properties of temperature and velocity are merged between the viscous and inviscid solutions. Equilibrium species composition is then determined by use of a minimization of free-energy calculation. The results of this equilibrium calculation are presented herein for the four most forward normals shown in Figure 2.

The nonequilibrium analysis is performed along a set of about 10 streamlines for each flow field. These streamlines are located in both the boundary layer and inviscid regions, and include the special case of the stagnation streamline. Different versions of the one-dimensional nonequilibrium computer program are used for each class of streamline. Pressure is used as a matching parameter for the inviscid streamlines while velocity is selected as the matching parameter on the stagnation streamline. Three parameters, pressure, streamtube area for unit mass flow, and velocity, are matched on streamlines in the boundary layer. The matching parameters of velocity and streamtube area in the boundary layer are found by merging the boundary layer properties

5

of velocity and density-velocity product into the nonequilibrium inviscid values at the outer edge. A smooth variation of all properties and species concentrations across the shock layer is thus obtained. The details of these steps will be described in the following discussion.

The RAM-C vehicle is a spherically-blunted, nine-degree, semi-apex angle cone at zero angle of attack. The vehicle geometry, coordinate system, and normal locations are presented in Figure 2. Flight conditions and free stream properties, selected from the 1962 ARDC Standard Atmosphere, Reference 4, are presented in Table 1. This selection was made following a review of the data presented in Reference 5 for the altitudes of interest for the Fall months at 30°N latitude which is representative of Bermuda Is. near the planned impact point. The data shows that the 1962 Standard Atmosphere is a good representation, to within 5-10%, of the expected mean conditions. In view of the expected daily fluctuations, this is considered to be sufficiently accurate.

Estimated Body Pressure Distributions

It was found on the previous RAM-B3 flow field prediction study, Reference 2, that the pressure distribution over the spherically blunted nose was accurately predicted by a combination of modified Newtonian theory and a Prandtl-Meyer expansion matched at the point of equal pressure gradient. This method was adopted for the present investigation. The pressure distribution downstream of the nose was obtained by correlating the RAM-B3 results using the parameters suggested by Cheng's hypersonic blunt body analysis, Reference 6. This correlation is shown in Figure 3 and was used in this study with a local value of Θ (body surface slope) determined by the effective body.

Boundary Layer Analysis

The objectives of the boundary layer analysis are two-fold. First, the displacement thickness distribution over the body is required to proceed with the inviscid analysis. Secondly, the property distributions across the boundary layer are required to define boundary layer streamlines and matching properties for the nonequilibrium analysis.

The combined integral-similarity boundary layer program, Reference 7, used for previous RAM studies, was also utilized in this study. This program has been found to produce results for the RAM configuration that are in good agreement with results obtained with a more exact finite-difference program. In essence, the method assumes locally similar profiles with the absolute thickness being determined by satisfying the momentum integral equation. The program starts at the stagnation point and uses an estimated body pressure distribution and entropy distribution at the outer edge of the boundary layer. It determines S, δ^*, Θ, and the state and thermodynamic profiles in the boundary layer.

It was originally planned to permit the edge entropy to vary with distance along the body with the local entropy being determined by the streamline entering the outer edge of the boundary layer at each location. A more

thorough assessment of this procedure has shown that the simpler approach of using a constant edge entropy, evaluated at the stagnation point of an inviscid analysis, permits a more reliable property merger to be performed. A small effect of variable edge entropy on boundary layer thickness is neglected by this approach. The continuum boundary layer analysis is based on classical theory in which the boundary layer is assumed thin in comparison with the body radii of curvature in both the transverse and longitudinal directions. The theory also assumes zero property gradients (vorticity) in the normal direction at the outer edge. There currently exists an absence of exact techniques and computer programs to handle these factors in addition to the strong rarefaction effects present in the current study for the highest altitude cases. The vorticity can be best accounted for by a merger procedure accounting for the vorticity interactions discussed in Reference 8. Thus, using the velocity profile as an example, the situation is seen below.
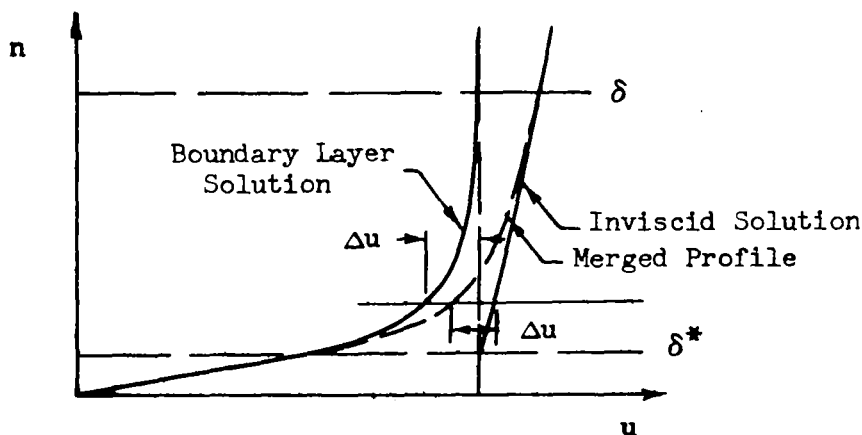
By using the same velocity defect $\Delta u = u_{in} - u_v$ for the boundary layer analysis and the merged profile at the same height, n, the velocity distributions merge together at the height δ^*, which is usually a small fraction of the total boundary layer height δ. If the entropy, and hence local flow velocity, were evaluated at the outer edge of the boundary layer and the merger was performed using this procedure, then the merger would result in obviously unacceptable negative values of velocity near the wall. It was judged that the best procedure would be to merge using the same defect velocity at heights having the same mass flows. Since results showed that mass flow is nearly linear with n beyond $n/\delta = .3$ to .4, the procedure was approximated by merging at the same height rather than at the same mass flow. The error introduced in the high altitude cases from this source is less than that incurred by using classical boundary layer theory rather than solving the Navier-Stokes equations for the entire shock layer. For those cases where the boundary layer is truly thin compared to the shock layer thickness, the amount of merging of the properties is so small as to make the error negligible.

The initial boundary layer calculation for each case used the bare body

with no allowance for displacement thickness. The displacement thickness from this boundary layer calculation was then used to define an effective body shape for which a revised pressure distribution was predicted from the correlated RAM-B3 results. The displacement thickness was found to alter the effective body surface slopes, and hence the body pressure distribution, appreciably only for Cases 5, 6, and 7. Consequently, for these cases the boundary layer computation was redone. The effective body surface slopes resulting from the second calculation were sufficiently close to those of the previous calculation to be acceptably accurate. The boundary layer displacement thickness distributions for Cases 1-7 are shown in Figure 4.

For Cases 8 and 9, it has been assumed that the boundary layer thicknesses, nondimensionalized by the nose radius, are the same as for Cases 2 and 3, respectively. The absolute boundary layer thicknesses for Cases 2 and 3 are very small, indicating no measurable change in effective body surface slope compared to the bare body. The well-known laminar boundary layer scaling rule

$$\delta \sim \frac{x}{\sqrt{Re_x}} \qquad (1)$$

shows that with essentially identical local flow properties at the outer edge of the boundary layer, the nondimensionalized boundary layer thickness at the same X/D will be 2.7% less for Cases 8 and 9 than for Cases 2 and 3, respectively. With the same edge and wall properties, the property changes within the boundary layer for Cases 8 and 9 will be between 0-2.7% and can be assumed negligible in comparison with the possibly large effect of a scale change on nonequilibrium chemical rate effects.

In contrast to previous RAM studies the actual displacement thickness variation over the body was used for the effective body shape in the method-of-characteristics solution. For the subsonic-transonic solution the effective body was approximated by a spherical shape which included allowance for a mean displacement thickness.

Blunt Body Flow Field

The method used in computing the transonic flow field is based on the concept of mass flow conservation (Reference 9). This method is related to other direct methods in that the free-stream conditions and body shape are known; and the flow field, shock wave shape, and streamline locations are obtained as a solution. The three equations of conservation are solved as a function of the streamtube cross section. As a result, the streamlines are a direct outgrowth of the solution. A high level of accuracy is required in the input data, as in most other methods of solving the transonic flow field, to avoid instabilities in the numerical solution. Recent IBM system changes have made it necessary to modify the computer program used for the previous RAM studies, Reference 9, to maintain satisfactory accuracy. The major change is that all calculations are now performed in double precision accuracy in a program written for the IBM 360. The method requires, in addition to the

flight conditions and the body shape, a preliminary estimate of the body pressure and shock shape. Although this method normally requires iteration on input data so as to satisfy the Rankine-Hugoniot shock relationships, the initial choices of body pressure distribution and shock shape obtained from the data correlations of Reference 10 were deemed sufficiently accurate that iterative calculations were not needed. Sample output data for Case 1 are presented in Figures 5-9. Figure 5 shows the CRT (cathode ray tube) plot of the streamline pattern. Figure 6 shows an enlarged plot of data near the start line (left-running characteristic) where the method-of-characteristics solution was initiated. The automatic output of property variations on the start line is illustrated by the data plotted in Figures 7, 8, and 9.

The solution near the stagnation point cannot be determined accurately by this flow field method, since the calculated pressure gradient depends on the streamline curvature and becomes unusable near the stagnation point where the flow radius of curvature becomes infinitely small. The method used to obtain the stagnation line flow properties is discussed in the section on Matching Parameters.

Theoretical Development. - The equations of conservation, when applied to the flow field under analysis, are used in the following forms:

Continuity Equation:

The usual form of the equation of continuity

$$\nabla \cdot (\rho \vec{u}) = 0 \tag{2}$$

is expressed along a streamtube for the axisymmetrical case as,

$$\pi \rho_\infty \, u_\infty (r_1^2 - r_2^2) = \frac{(\rho_{I,J} \, u_{I,J} + \rho_{I,J+1} \, u_{I,J+1})}{2} \, \pi \, (r_3 + r_4) \quad \Delta n \tag{3}$$

Momentum Equation:

The equation of momentum

$$\frac{d\vec{u}}{dt} = - \frac{1}{\rho} \, \vec{grad} \quad p \tag{4}$$

when applied normals to the streamline becomes

$$\frac{dp}{dn} = \rho_{I,J} \, \frac{u^2_{I,J}}{R_{c_{I,J}}} \tag{5}$$

9

Shock

n

J+1

I,J+1   S   Streamline
        J

Δn θ Body

I,J

ρ_∞, u_∞

r_1

r_2 r_3 r_4

Reference Axis

x
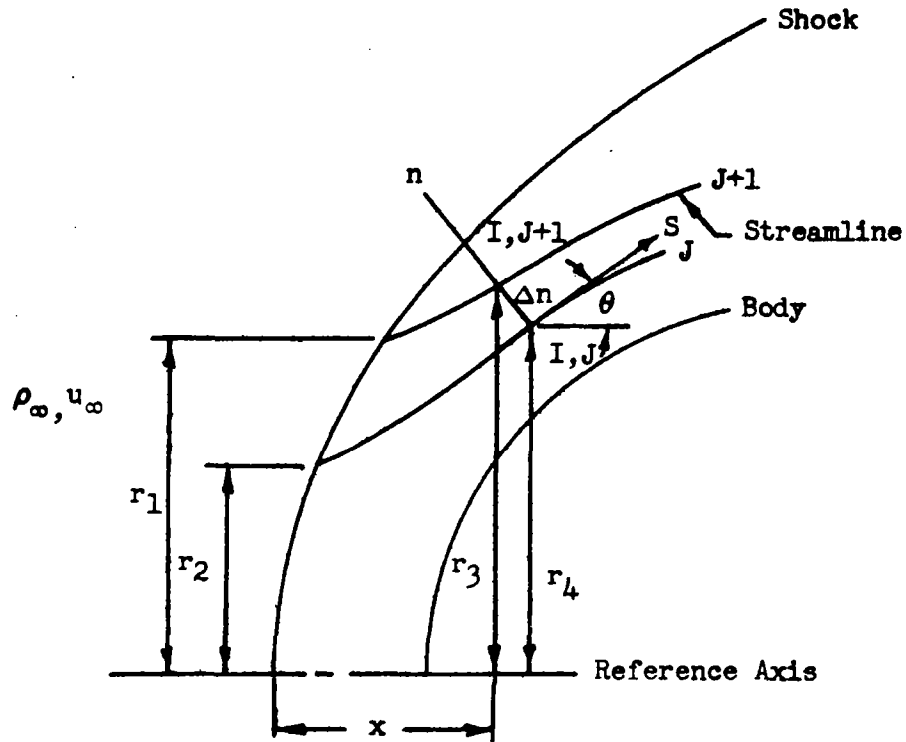
Energy Equation:

Along a streamline, the energy equation can be written as

$$\frac{dS}{dt} = 0 \qquad (6)$$

and, as a consequence,

$$h + \frac{u^2}{2} = H_o \qquad (7)$$

It can be seen that the three conservation equations now have assumed a very simple form under these conditions. The Hugoniot relationships are used across the shock to obtain the entropy for each newly computed streamline. The general procedure for the calculation proceeds step by step, starting from the body where geometric and fluid properties (i.e., pressure and entropy) are known or estimated to a high degree of accuracy. The details of the process are as follows:

a. At all points on the body where pressure and entropy are known the hypothesis of thermodynamic equilibrium permits the remaining fluid properties to be defined using available equilibrium thermodynamic property data for air and the energy equation. The term $\Delta p/\Delta n$ stemming from the momentum equation (5) can then be computed along the body knowing the body radius of curvature at each I grid point.

10

b. The continuity equation is used to compute the normal distance Δn to each point on the next outboard streamline. The geometry of this streamline is defined from $r_3 = r_4 + \Delta n \cos \theta_w$. In the first approximation of Δn it is assumed that $\rho_{I,J+1}$ and $u_{I,J+1}$ on the new streamline are the same as those on the body at the I point. From Equation (3) the Δn can then be calculated; and its introduction in the momentum equation gives $p_{I,J+1}$. Pressure and entropy define a new state; and, with the assumption of thermodynamic equilibrium, the other parameters required -- $\rho_{I,J+1}$ and $u_{I,J+1}$ for instance -- are obtained easily. Next, mean values of the fluid properties for the streamtube, based on averaging the properties on the inboard and outboard streamlines, are used to refine the first approximation of Δn. Final properties are then determined on the outboard streamline.

c. The determination of subsequent streamlines follows the procedures outlined above where properties on the inboard streamline result from the integration across the previous streamtube.

d. Once the streamline pattern is established a new shock shape is defined from the intersections of the computed streamlines with their homologues in front of the shock.

e. The Hugoniot relationships are used to compute the pressure across the newly obtained shock wave and it is compared to the pressure on the streamline at the same ordinate. If satisfactory agreement is obtained, iterations on the shock shape and body pressure distribution are not required.

Supersonic Inviscid Flow Field

The equilibrium supersonic inviscid flow field computations were accomplished by means of an IBM 360 computer program utilizing the well-known method of characteristics. This method entails solving a system of first-order, hyperbolic partial differential flow equations using the simplifications made possible by recognition and use of characteristic equations. Once the characteristic equations are available, finite difference techniques can be applied; and the flow field problem is easily adapted to solution by means of high-speed computers.

The basic theoretical development for the method of characteristics is found in most texts on gasdynamics, such as Reference 8. After transforming the three basic flow conservation relationships (mass, momentum, and energy) from an intrinsic coordinate form into ordinary differential equations along characteristic lines, the following equation is obtained:

$$dp \pm \frac{\rho u^2}{\sqrt{M^2 - 1}} d\theta + \frac{i \rho u^2 \sin \theta}{\sqrt{M^2 - 1}} \frac{ds}{r} = 0 \qquad (8)$$

11

The positive sign applies to a left-running characteristic line and the negative sign to a right-running characteristic line. Since the characteristics are Mach lines, their directions with respect to the streamline are given by the Mach angle. In Equation (8), the symbol "j" is used to adapt the expression to either two-dimensional (j = 0) or axisymmetric (j = 1) flow. In addition to the characteristic relationships along Mach lines, there is another characteristic relationship defined along the streamline itself. This is the streamline energy relationship. Assuming the flow to be inviscid and adiabatic, this energy relationship implies a constant entropy along streamlines. These flow conditions also make available the relationship between the flow velocity and thermodynamic state of the gas given by

$$H_o = h + \frac{u^2}{2} \tag{7}$$

The characteristics computer program, described in Reference 11, is designed to solve the supersonic flow field over convex, two-dimensional or axisymmetric body shapes in a real gas, chemical equilibrium air media. Since the speed of sound is needed to compute Mach number, it is convenient to introduce the effective specific heat-ratio data into the program. These data are entered in tabulated form as functions of temperature and pressure.

Starting line properties, as stated earlier, are obtained from a direct method transonic solution. Typical distributions of properties along the starting line are shown in Figures 7-9. The body shape downstream of the sonic point is altered to include boundary layer displacement thickness. This alteration to the basic body shape defines the body coordinates supplied as input to the characteristic program. The streamline pattern determined by the transonic solution is continued downstream by the characteristics program. In addition to supplying the streamline pattern, the characteristic program determines the shock shape and the flow properties throughout the flow field. The method-of-characteristics solution produces complete flow field details downstream of the starting line, both on a characteristic network and along streamlines. As a typical example, the characteristic network for Case 1, obtained from this program, is shown in Figure 10. Only left-running characteristics are shown, and it should be noted that the cutoff at $r \approx 1.67$ does not mean that flow field calculations stop here, but merely that the next computed point on that characteristic lies aft of the cutoff (x = 5).

Final Boundary Layer Analysis

The use of correlated RAM-B3 conical surface pressure distributions has resulted in agreement of final pressure distributions to within approximately 10% of the boundary layer program input data, as may be seen in the typical results shown on Figure 11. It was observed that in iterating on the effect of displacement thickness on boundary layer growth for the high altitude cases, the percentage change in displacement thickness is about one-fourth the percentage change in pressure, while other properties in the boundary layer varied less than pressure. On this basis, pressure deviations of about 10% were deemed acceptable. The accuracy of the final property merger, to be discussed subsequently, does not call for a more accurate boundary layer growth calculation than has been performed with the above procedures.

Equilibrium Composition

To complete the equilibrium flow analysis, the chemical composition was determined at a large number of points along normals 1, 4, 6, and 7 for all cases after a merger was performed on velocity and temperature along these normals. The defect principle explained in the Boundary Layer Analysis section was used in performing the merger. The inviscid pressure distributions are smoothly varying functions and were used without change. The need for a merger of the equilibrium boundary layer and equilibrium inviscid values of u and T is brought about by the vorticity existing in the inviscid flow and the resulting difference in properties and their derivatives at the edge of the boundary layer. After defining smooth variations of p and T across the shock layer, determination of equilibrium chemical composition was possible. The computation was performed with the aid of a Rocketdyne Division free-energy minimization program. This program uses the method of steepest descent to minimize the mixture free-energy to thus determine the mole-fractions of all the high temperature air species considered in this study.

Streamline Definition

It was assumed, as in previous RAM studies, that the shock location and shape, streamline paths, and pressure distribution are independent of chemical nonequilibrium effects. This assumption is widely used in the analysis of nonequilibrium flows and has been substantiated in many publications, such as Reference 12. It is obvious that the accuracy of these assumptions must be degraded as the nonequilibrium state closely approaches frozen flow. To first order for example, the constant density shock standoff distance for a sphere varies inversely with the density ratio across the normal shock. This ratio varies by a factor of about three between equilibrium and frozen flow for Case 7. Thus the accuracy of the basic assumption of nonequilibrium independence is poorest near the stagnation region for the highest altitude case. Conversely, the increase in shock standoff distance at high altitude is somewhat self-compensating since the increased residence time permits reactions to proceed further. An additional problem at these high altitudes is the very thick viscous layer which may invalidate a boundary layer type approach. What is required but not presently available, is a fully-coupled viscous nonequilibrium flow field program. The work of McKenzie, Reference 13, offers a rapid and simple means of scaling an equilibrium flow field for nonequilibrium effects if the change in shock standoff distance is known. Future efforts on this problem may result in the development of some practical solutions of an approximate nature.

The problem at this point then is reduced to the location of streamlines in the equilibrium flow field. By using the concept of an effective body it has been possible to develop a good prediction of the inviscid flow field which is farther from the wall than the boundary layer thickness δ, ($u/u_e \approx .99$). At normal distances less than δ, the inviscid streamlines must be displaced toward the wall to represent a real viscous flow over the bare body. The inviscid wall streamline on the effective body surface will be thus moved to the bare body surface in this adjustment. Other streamlines

within the height δ will be moved proportionately less depending on their proximity to the outer edge of the boundary layer. Certain selected stream-lines within the boundary layer were located accurately at all numbered normals (1-12) for subsequent analysis of nonequilibrium chemical effects within the boundary layer. The streamlines were located by mass flow conservation requirements as follows. The boundary layer program gives, as part of its output, the parameter

$$M = \int_0^n \rho\, u\, dn \tag{9}$$

For axisymmetric flow the mass flow is given by

$$\dot{m} = 2\pi \int_0^n \rho\, u\, r\, dn \tag{10}$$

The value of r in this integral was treated as a constant since for Cases 1-3 the entire boundary layer is very thin. For Cases 4-7 the boundary layer is thick enough that a merger of the mass flow variation between the boundary layer and inviscid flow must be performed to develop a unique set of stream-lines.

For Cases 1-3 the boundary layer is so thin that several new boundary layer streamlines must be located. However, for these same cases, all invis-cid streamlines defined by the method-of-characteristics computer program lie outside of the boundary layer and need no adjustment in their geometry. With r considered constant, the following plots were prepared for these cases with the term

$$\int_0^n \rho\, u\, dn$$

obtained directly from the printouts of the boundary layer program.

14

Typical Normals

n

$$\dot{m} = 2\pi r_w \int_0^{} \rho u \, dn$$

Computed from
Boundary Layer
Program

N4

N5

N6

S 85

S 80

S 75

δ^*

δ

n
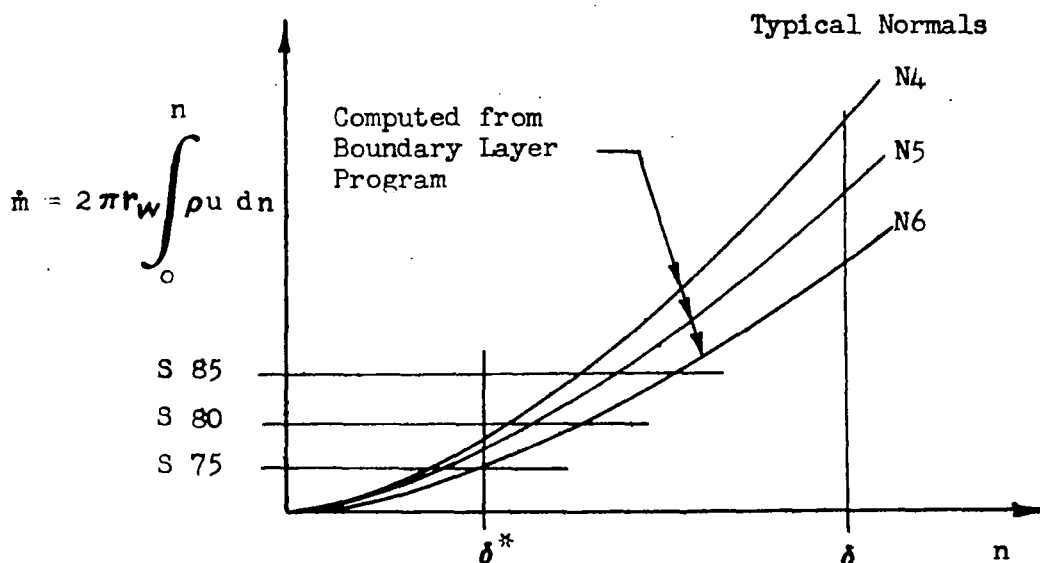
The new streamlines are defined by constant values of mass flow, and the normal distances to these streamlines at all numbered normals are used to define their geometry.

For Cases 4-7 the boundary layer mass flow, defined in the above manner, was merged into the variation of mass flow in the inviscid solution. This was easily done even for Cases 5, 6, and 7 where the boundary layer thickness was predicted to be as great or greater than the shock layer thickness, since it was always observed that the product ρu essentially reached the boundary layer edge value at a height $n/\delta \approx .4$ to .5. The following sketch shows the form of a typical merger plot.

Typical Normal

$\dot{m}$

Inviscid Mass Flow

Merged Mass
Flow Profile

Boundary Layer
Mass Flow

S 85

S 80

S 75

δ^*

δ

n

15
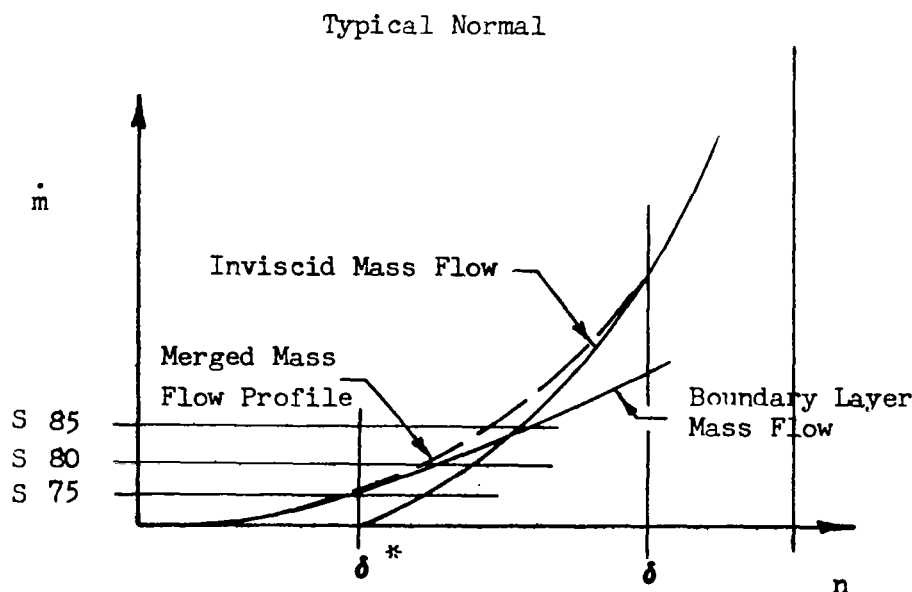
Matching Parameters

In the analysis of inviscid nonequilibrium flow fields it is necessary to use a flow field property obtained from an equilibrium flow field solution. This property is commonly referred to as a "matching parameter" and is selected on the basis of its relative invariance with the introduction of nonequilibrium effects. References 14 and 15 substantiate the use of pressure as a matching parameter for most inviscid, nonequilibrium one-dimensional streamtube studies. However, velocity was found to be a more suitable parameter on the stagnation streamline because of its more accurately known variation across the shock layer. In performing the analysis of the viscous flow field, streamtube area and velocity in addition to the pressure were matched to their equilibrium flow field counterparts, leaving only the chemistry to be integrated in the analysis. Throughout the nonequilibrium analysis, streamline geometry and shock location were assumed to remain identical to the equilibrium flow field results.

The inviscid, equilibrium pressure matching parameter distribution was obtained with the streamline-curvature method patterned after Gravalos (Reference 9) in the transonic region of flow and with the method of characteristics in the region of supersonic flow. Since the Gravalos method is not applicable in the stagnation region, engineering estimates of the property variations based on the results presented in Reference 10 were used to arrive at matching parameter distributions in this region and along the stagnation streamline. Data presented in Reference 10 indicates that the velocity distribution along the stagnation streamline can be accurately approximated by a linear distribution with negligible error in the computed pressure distribution. Frozen oblique shock calculations were used to obtain initial conditions on streamlines downstream of the shock and the frozen pressure value was merged into the equilibrium pressure matching distribution over a short region behind the shock. The frozen shock properties were based on immediate equilibration of the translational, rotational, vibrational, and electronic energy modes behind the shock and a frozen chemical composition equal to that in the free-stream.

In the inviscid flow region only one matching parameter distribution is required in the nonequilibrium analysis. It is appropriate to discuss at this point the matching parameters used in the nonequilibrium boundary layer analysis. Pressures are again obtained directly from the inviscid flow field results. The one-dimensional energy and momentum equations used in the pressure-matching version (inviscid version) of the nonequilibrium reacting gas computer program are valid only in inviscid flow, since viscous stresses and heat conduction invalidate such an approach in the boundary layer. This requires replacing the energy and momentum equations by known distributions of two additional matching parameters (velocity and streamtube area). The boundary layer nonequilibrium analysis thus is reduced to the calculation of chemical reactions along streamlines, while satisfying continuity and the equation of state.

The velocity and streamtube area matching parameter distributions were obtained from streamline crossplots of merged inviscid nonequilibrium data,

16

when available, and equilibrium boundary layer data as specified along normals. One further requirement in the merging of properties along normals was the use of frozen properties at the shock. In Cases 5, 6, and 7 where no inviscid nonequilibrium results were obtained because of the extreme boundary layer thickness, equilibrium boundary layer properties were merged directly into the frozen shock properties using the lower altitude cases as a guide to the profiles. The merging of data along normals where nonequilibrium inviscid results were available was performed primarily by means of the defect principle previously discussed in the Boundary Layer section of this report. Where the defect principle was not completely applicable, judicious fairing using engineering judgement was employed to merge the data. The merger was employed for u and ρu, the latter quantity defining streamtube area according to the unit mass flow relationship

$$A \equiv \frac{1}{\rho u} \qquad (11)$$

This merger procedure is consistent with the equilibrium boundary layer analysis in regions of near equilibrium flow, and provides a reasonable boundary layer distribution in nonequilibrium or frozen flow regions. A schematic of a typical merger plot is shown below.

Typical Normal

17
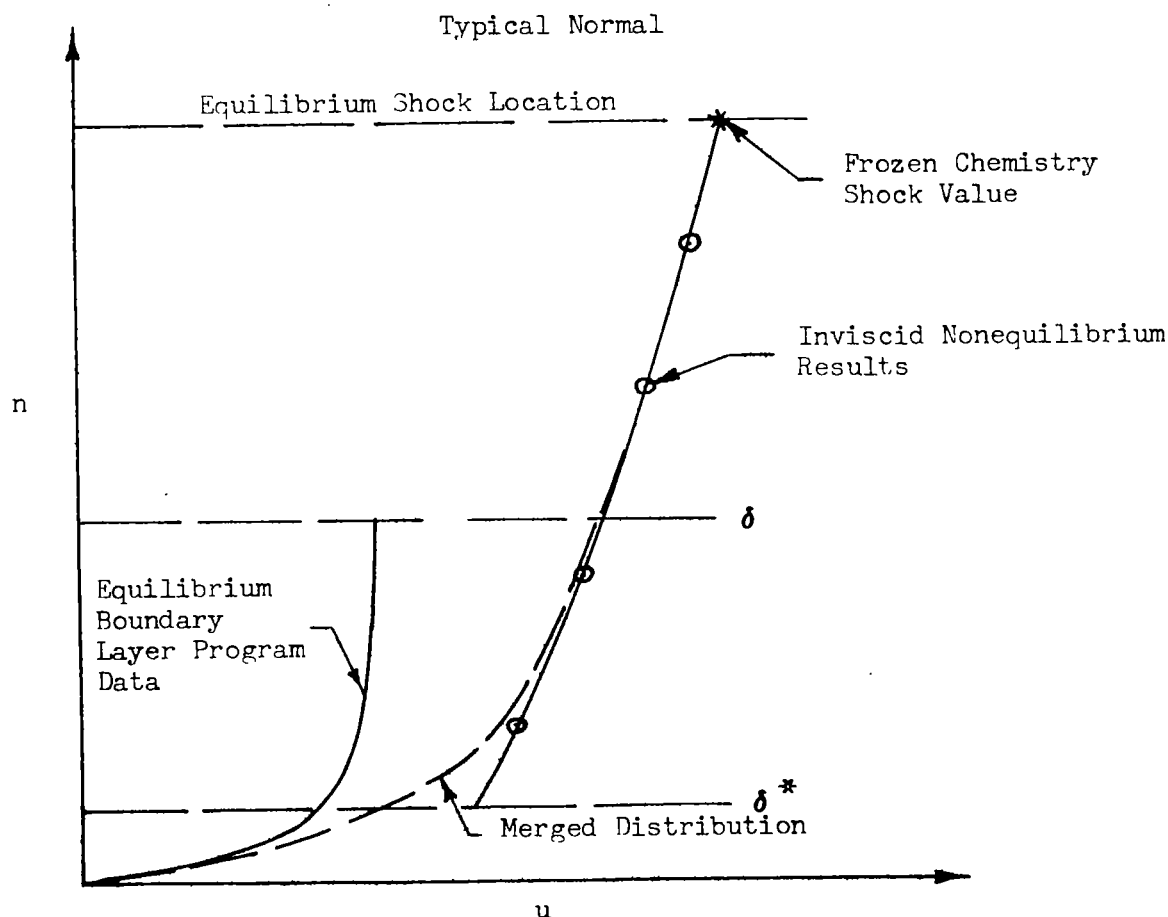
Typical matching parameter distributions for pressure, velocity, and streamtube area are shown in Figures 12, 13, and 14, respectively, for the boundary layer Streamlines 74, 75, 80, 85, and a segment of Streamline 2 for Case 3. The remaining portion of Streamline 2, not shown in the figures, lies in the inviscid flow region.

Nonequilibrium Chemistry Analysis

The analysis of flow fields with nonequilibrium chemistry involves coupling the chemical rate equations for the formation and destruction of chemical species with the fluid dynamic equations describing the flowing media. The media in this analysis is air, and the fluid dynamic relations are the conservation equations for one-dimensional flow. The coupling is achieved through modifications to the energy and state equations, causing them to reflect the contributive effects of each specie considered in the chemical model. The details of this method are described in the following paragraphs.

Basic Equations. - Nonequilibrium flows may be described by a set of fluid flow relationships, i.e., the one-dimensional flow equations for mass, momentum, and energy conservation; thermodynamic relationships in the form of the state equation and definition of enthalpy; and a set of chemical rate expressions. Basing the analysis on inviscid, one-dimensional flow along streamlines, the conservation equations assume the following form:

$$\frac{d\rho}{\rho} + \frac{du}{u} + \frac{dA}{A} = 0 \tag{12}$$

$$\frac{dp}{ds} = - \rho u \frac{du}{ds} \tag{13}$$

$$h + \frac{u^2}{2} = H_o \tag{7}$$

The thermodynamic equations, represented by the equation of state and the definition for enthalpy, must include the contributive effects of each chemical specie. The equations illustrate this point.

$$p = \rho R T \sum_{i=1}^{N1} n_i \tag{14}$$

$$h = \sum_{i=1}^{N1} n_i w_i h_i \tag{15}$$

18

Finally, the chemical rate for the i'th specie is obtained from the following expression:

$$\frac{dn_i}{ds} = \frac{1}{\rho u} \sum_{k=1}^{N2} (\beta_{i,k} - \alpha_{i,k}) \left[K_{f_k} \prod_{j=1}^{N1} (\rho n_j)^{\alpha_{j,k}} \right.$$

$$\left. - K_{b_k} \sum_{j=1}^{N1} (\rho n_j)^{\beta_{j,k}} \right] \qquad (16)$$

The subscript j applies to the particular species participating in the k particular reactions. This equation is derived from basic kinetic theory (References 16 and 17) and summarizes the effective influence of a particular specie in the chemical reactions comprising the chemical model. The forward and reverse reaction rate constants, K_{f_k} and K_{b_k}, in the chemical analysis are related to one another through the chemical equilibrium constant by the following relationship:

$$K_{EQ_k} = \frac{K_{f_k}}{K_{b_k}} \qquad (17)$$

These are the basic equations to be solved in a nonequilibrium flow analysis, and it is a simple matter to combine them into a form that will follow a prescribed streamline path. The coupling equations for the change in temperature with distance using pressure and velocity as matching parameters are presented below:

Pressure Match:

$$\frac{dT}{ds} = \frac{\dfrac{1}{\rho} \dfrac{dp}{ds} - \sum\limits_{i=1}^{N1} w_i h_i \dfrac{dn_i}{ds}}{\sum\limits_{i=1}^{N1} c_{p_i} n_i} \qquad (18a)$$

Velocity Match:

$$\frac{dT}{ds} = \frac{-\left(u \dfrac{du}{ds} + \sum\limits_{i=1}^{N1} w_i h_i \dfrac{dn_i}{ds} \right)}{\sum\limits_{i=1}^{N1} c_{p_i} ni} \qquad (18b)$$

19

The detailed derivations of these coupling equations are presented in Reference 18. In addition to the coupling equation above, chemical rate equations and the momentum equation must be solved for each integrated interval along the streamline path.

The first step in the nonequilibrium solution using the pressure match version as an example, is the evaluation of the chemical rate for each specie. This depends only on known conditions at the beginning of the integration interval. These rates, along with the local slope of the matching parameter curve (i.e. dp/ ds), are sufficient to evaluate the coupling equation for dT/ds. The quantity du/ds is obtained from the momentum equation and the argument dp/ds. These three differential equations, after evaluation, are integrated over an interval of streamline path to give temperature, velocity, and the chemical composition at some new downstream point. The value of pressure at this new point is determined from the matching parameter curve. Density and streamtube area are obtained from the equation of state and the mass conservation equation, respectively. This completes the calculation of a new downstream point, and the procedure is repeated for each of the subsequent downstream points.

A special version of the calculation procedure is used to study nonequilibrium chemistry effects in the boundary layer. This version simultaneously matches pressure, velocity, and streamtube area along streamlines. In using all three of these properties as matching parameters, it is no longer necessary to integrate the coupled flow equation and the momentum equation, but only the chemical rate equations. The procedure followed in the boundary layer version consists of evaluating the chemical rate equations at a known point and then integrating to find the chemistry at the new downstream point. The pressure, velocity, and streamtube area at the new point are obtained from tabulated values of the matching parameter distribution. Density at the new point is determined from the mass conservation equation and used in the state equation to determine temperature. The cycle is then repeated for each new integration interval.

<u>Nonequilibrium Reacting Gas Program</u>. – The IBM 7090/7094 nonequilibrium computer program is described in detail in Reference 18. It requires a complete knowledge of all of the fluid and chemical properties at a starting point. This point generally is chosen immediately downstream of the shock, assuming no dissociation of the free-stream air but complete relaxation of the translational, rotational, vibrational, and electronic modes of excitation. Coordinates of the streamline path and a description of the matching parameter along this path must be specified as program input information, in addition to starting point properties. The differential equations are integrated with a fourth-order Runge-Kutta scheme modified for a Gill-type correction (Reference 19).

The program has a built-in provision for altering integration step size. Step size must be small in regions where the flow is near equilibrium, since there is a tendency for the integration of the chemical rate equations to become unstable. This is due to the extreme sensitivity of the rates to slight changes in the local chemical composition. Conversely, if the program is operating in a region of the flow field where the rates are insensitive to

changes in chemical composition (as in the case of frozen chemistry flow), integration step size is increased to minimize program running time.

The results of this computer program compare very well with theoretical results obtained by Vincenti (References 20 and 21) for nozzle flow in a spark-heated facility.

BASIC DATA

Thermodynamic and Transport Properties

Referring to Figure 1 to identify the computer programs and hand calculations, the following computer programs utilize analytic equations of state for equilibrium air presented in Reference 22, and the effective specific heat ratios presented in Reference 23.

> Oblique Shock Property Program
> Modified Newtonian-Prandtl/Meyer Program
> Laminar Boundary Layer Program
> Subsonic-Transonic Flow Program
> Method-of-Characteristics Program

The Grabau procedure has been programmed as a subroutine. It evaluates three thermodynamic functions, $H\rho'/p'$, S/R, and Z for equilibrium air using p and ρ as arguments. p' and ρ' are nondimensionalized quantities in terms of reference conditions at 1 atmosphere of pressure and $273°K$ temperature. The subroutine is designed to cover the thermodynamic regime bounded by the temperature range of $200°K$ to $15,000°K$, and the density range of 10^{-6} to 10^2 relative atmospheres. The program was designed to duplicate, with an average error of 1 percent or less, the data of Reference 24. The specific heat ratio data of Hansen is also programmed as a subroutine in a table lookup with inputs of pressure and temperature. It is called for in calculations involving speed of sound and/or Mach number.

The thermodynamic properties of enthalpy and specific heat at constant pressure are determined from statistical mechanics and results of experimental spectroscopy, and are entered into all versions of the nonequilibrium program in tabulated form as a function of temperature. These properties are obtained from the high temperature air properties program described in Reference 25. The basic assumptions and method for solving the partition functions are discussed thoroughly in References 1 and 25. These data were also used in the hand calculation of properties behind the shock with a frozen chemistry. The free-energy minimization program uses thermodynamic data computed by essentially the same approach as in Reference 25. Details of the program and procedures are given in References 26 and 27. As noted in Reference 3, comparative results of equilibrium electron densities predicted by the free-energy program with data from Reference 28 showed excellent agreement.

The calculations performed by the laminar boundary layer program are the only calculations which involve transport properties. The analysis assumes

that both Lewis number and Prandtl number are unity. It also assumes a coefficient of viscosity which is linearly proportional to temperature and matched to the Sutherland value at the wall (assumed to be 700°K throughout this study).

Chemical Kinetics

The chemical model used in the nonequilibrium reacting gas computer program (Reference 18) is depicted in Table 2 and consists of eleven reactions involving the following twelve chemical species:

$$N_2, \quad N, \quad O_2, \quad O, \quad NO, \quad NO^+, \quad e^-, \quad N_2^+, \quad O_2^+, \quad N^+, \quad O^+, \quad \text{and} \quad A$$

In the computer program, the nitrogen dissociation reaction is listed as two separate reactions; since two forms of the rate constant expression are needed, depending on the third body participating in the reaction. Catalytic efficiencies are presented in Table 2 for Reactions 1 through 3. The specie argon (A) is used as a reference point for assigning values of catalytic efficiency to each of the species in the chemical model. For example, in Reaction 1 of Table 2, the species A, N, N^+, NO, and NO^+ all possess catalytic efficiencies of two, etc. Reactions 1 through 3 actually represent a series of reactions, since the symbol M can represent any of the catalytic species listed in the table exclusive of electrons. The catalytic efficiencies allow this series of reactions to be grouped into a single reaction, since they differ only in the sense that the rate constants are simple multiples of one another. The basic reaction rate data used in the program are obtained from References 29 and 30.

Equilibrium constants for the reactions listed in Table 2 are obtained from the difference in the free energies of products and reactants. The theoretical considerations for determining equilibrium constants over the desired temperature range are presented in Reference 1. Data for the equilibrium constants employed in the nonequilibrium program also are determined from the air properties program (Reference 25) and are entered into the nonequilibrium program as tabulated data. It is difficult to obtain closely spaced data for temperatures below 9000°R and still employ a linear interpolation on temperature to determine intermediate values. This problem is solved by using analytic expressions for the equilibrium constants below 9000°R. These relationships are presented in Table 3.

It is necessary to use the equilibrium constant to determine the opposing rate constant, since Table 2 only presents either the forward or reverse rate constants. The opposing rate constant is obtained from the equilibrium relationship presented in Equation (19).

Simplified Chemical Model for Cases 1,2. - To save unnecessary computation time, the basic chemical model was modified for Cases 1 and 2. An examination of the data in Reference 31 for the expected temperatures and densities on the stagnation streamlines indicated that no plottable ion mole-fractions would be present at equilibrium except for the NO^+ ion. Thus, Reactions 8-11 were deleted for these two cases.

RESULTS

The final plots are presented in Figures 15 through 113. These plots were prepared from CRT data presentations especially programmed for this effort. To use this special plotting routine it was also necessary to modify all computer programs to produce, in addition to normal tabulated printouts, punched cards with appropriate information on geometry and flow properties. These punched cards were used to prepare the merger plots using a simple plotting routine. The punched card outputs from the nonequilibrium programs were input into the final plotting routine to produce the figures presented herein. Equilibrium compositions and properties were also transferred to the required punched card format and used to prepare the final equilibrium plots. Data points are shown with a legend. All equilibrium data are presented together, sequenced by case number and subsequenced by normal number. Equilibrium data are given only on Normals 1, 4, 6, and 7. Nonequilibrium data plots follow the equilibrium presentation and are identically sequenced, except that data are given for Normals 1, 4, 6, 7, 9, 11, and 12.

The final results are displayed in two plots for each normal location for each case. The first plot shows the variation of electron density, temperature, pressure, velocity, and streamline locations as a function of distance outward along the normal from the body surface. The second plot shows the variation of chemical species concentration along normals. The variations of electron density, pressure, temperature, velocity and chemical species concentration have been drawn as straight lines between computed points. Streamline locations are indicated by short lines at the top of the first plot for each normal. The number of data points selected for the equilibrium flow calculations was based on obtaining smooth property variations along the normals and was not restricted to any set number as in the case of nonequilibrium flow. The nonequilibrium data are available only at streamline-normal intersections. Since approximately 10 streamlines were run for each case, the final variations are not as smooth as in the equilibrium case. Also, the integrated effect of many merger operations on the time histories along streamlines results in more apparent noise on the nonequilibrium normal plots.

The neutral species are plotted as mole fraction (X_i) versus normal distance, and the ions are plotted as the log of the mole fraction versus normal distance since they are present in very small but important concentrations. In the data plots, all ion concentrations greater than 10^{-6} mole fraction are considered to be of significance. This value was selected as a reasonable minimum value for data presentation.

The shock layer thickness is clearly indicated on each normal plot by the limit of the normal scale. The data curves originate at the body and continue through the viscous and inviscid regions of the shock layer terminating at the shock. For all cases, it is assumed that the wall is at a temperature of 700°K and that the local wall flow velocity is zero, consistent with the assumptions of classical boundary layer theory. Under these conditions, the wall is always at a condition of chemical equilibrium (i.e., no dissociation or ionization is present) and the chemical composition corresponds to

undissociated equilibrium air at the local pressure and temperature. In non-equilibrium flow at the shock, the air is initially undissociated and at a temperature corresponding to that of a mixture of gases of the same composition as free stream. The enthalpy and density levels at the shock are compatible with an iterative solution of the real gas shock equations, including vibrational and electronic excitation but frozen chemistry. The conditions at the wall and shock were used to establish the end points of the data plots. Between the body and shock, the local properties are dependent on the fluid dynamic conditions, and for nonequilibrium flow the time history of the chemical reactions which occur along each streamline.

The following general result is seen by examination of the data. Case 1 is nearly frozen with a low ionization level even in equilibrium flow. Case 2 is probably the nearest to an equilibrium case due to the high velocity at a rather low altitude (high density). Although Case 3 reaches a higher velocity than Case 2, the higher altitude results in greater deviation from equilibrium chemistry. Cases 5, 6, and 7, all at approximately the same flight velocity, exhibit progressively more deviation from equilibrium, and a corresponding approach to a frozen chemistry throughout the flow field as the flight altitude increases.

It is necessary to discuss next in more detail some particular problems and features of the calculations.

Case 1 Results. - The equilibrium chemistry results were obtained in the usual manner. It was found that on the four outermost inviscid streamlines, no plottable electron concentrations were computed by the nonequilibrium program. Also, no plottable ion or atom concentrations were computed. The stagnation streamline was computed next and, despite the nearly frozen chemistry and simplified chemical model used for this case, it proved to require long computation time. This difficulty is easily traced to the shuffle reaction

$$NO + O + 1.4 \text{ ev} \rightleftharpoons O_2 + N$$
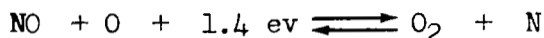
Because of the large mole-fraction of O_2, the net formation rate of N becomes very sensitive to its own concentration. This "stiffness," referred to in Reference 21, is a well-known problem with nonequilibrium flow programs using an explicit integration procedure. Since this particular reaction is vital as a link in the process of electron production, no further simplification of the chemical model was possible. A computer run was thus made that took approximately 30 minutes of machine time, and computed flow properties over about 75% of the distance from the shock to the body. The last computed electron concentration was still only 0.499×10^6 particles/cc. An analysis of the computer results was made by data correlation and hand calculation of production and destruction rates of the important species N, O, and e^-. The chief reactions responsible for production of these species were identified and the following conclusions were reached.

1. N concentration varied linearly with particle flow time.
2. O concentration varied linearly with particle flow time.
3. e^- concentration varied as the square of particle flow time.

Conclusion 1 is explained by a near-equilibrium concentration of N between the two fast shuffle reactions (#4 and #5 in Table 2). The linear variation of O atoms is merely the result of O production from forward Reaction #1. Conclusion 3 follows directly from the linear time dependence of O and N concentrations in the forward rate of Reaction #7. Based on this variation the e^- concentration was predicted for locations nearer the wall. Despite the large increase in particle flow time as the wall is approached, the electron density is only predicted to reach 1.17×10^7 particles/cc at the outer edge of the boundary layer. At this point the falling temperature, to which the forward ionization rate is most sensitive, essentially stops production of electrons. Between this point and the wall, two compensating effects modify the electron concentration.

1. Flow compression at constant pressure due to the wall influence on temperature.

2. Recombination of $NO^+ + e^- \longrightarrow N + O + 2.8$ ev.

The recombination rate is so low that it is negligible until the distance from the wall is too small to plot. The plot thus shows only the effect of compression with the final destruction of free electrons occurring too close to the wall to be apparent. The neglected diffusion effects would, of course, drastically alter any such distribution with a decrease in the predicted electron concentration near the wall.

Similar hand calculations were made along a boundary layer streamline very close to the wall. The sensitivity of O production to temperature, combined with the drop in flow temperature along the streamline path as the gas is carried away from the stagnation region, was shown to result in insufficient electrons to exceed a concentration of 10^6 particles/cc on Normal 4 or beyond. Accordingly, on Normals 4, 6, 7, 9, 11, and 12 for Case 1 the equilibrium data have been used in the nonequilibrium plots since no plottable atom, ion, or electron concentrations occur and therefore the two sets of data are identical. No data symbols are shown to avoid confusion with streamline data points resulting from the nonequilibrium computer program streamtube analysis results.

Case 2 Results. – Nonequilibrium chemistry calculations along the stagnation streamline show a rapid approach to equilibrium composition. The relaxation distance behind the shock is about 0.005 ft. Since the flow aft of this point along the stagnation streamline will remain in equilibrium because of the low flow velocity, the nonequilibrium solution was merged into the equilibrium data. Note that the O^+ mole-fraction did reach a peak value of 1.4×10^{-6} which is just barely plottable and substantiates the acceptability of the use of the simplified chemical model for all other streamlines in this case.

Cases 3 and 4 Results. – Cases 3 and 4 represent the most easily analyzed nonequilibrium flow situations in that the boundary layer has begun to thicken appreciably but not to the extent that it covers the entire shock layer. There is a sufficient portion of the inviscid flow field remaining to clearly define

inviscid nonequilibrium property trends through the shock layer. The stream-
line pattern used in the inviscid nonequilibrium analysis can be readily ob-
tained from an equilibrium flow analysis and the approach of using a classical
boundary layer analysis is still considered quite acceptable. It is also
quite easy to use the defect method of merging the boundary layer results to
the inviscid nonequilibrium results. It should be noted in the figures depic-
ting the specie variations along normals that the curves representing the ion
concentrations have not been extended beyond the innermost streamline for the
purpose of clarity. Actually, these curves end at equilibrium conditions at
the wall pressure and temperature.

Cases 5, 6, and 7 Results. - It is seen in all plotted results that the
electron concentration decreases very rapidly at the wall, except in the case
of the stagnation normals for Cases 6 and 7 an increase is found with no de-
tectable decrease. It is known, however, that the wall conditions must be in
equilibrium, and that for the assumed cold wall the electron concentration is
well below 10^6 particles/cc. The explanation lies in the extremely low free-
stream density for these cases. The chemical reactions are so slow that only
on streamlines which pass near the stagnation point region does particle flow
time permit significant reactions to occur. The stagnation streamline behav-
ior was studied in some detail for these cases. Due to the thick boundary
layer predicted for these conditions, the matching temperature distribution
falls continuously toward the wall with the result that at some point between
the shock and the wall electron production will essentially stop. The strong
dependence of the exponential term involving temperature in the important re-
actions of the electron-producing chains essentially eliminates the production
terms. However, the point at which electron production stops is very close
to the wall. These extremely low reaction rates have kept the mole-fractions
of the species NO^+ and e^- at low absolute levels so that the backward rates
of Reaction 7 are very small. Thus even as the forward rate drops exponen-
tially, the near absence of a backward rate permits the e^- mole-fractions to
continue increasing. As close as it was possible to integrate to the wall for
Cases 6 and 7, no reduction could be computed in electron concentration in
particles/cc. In Case 5 (the chemistry is closer to being frozen for Cases
6 and 7) the integration accurately proceeded to $X = 0.9997$. The wall is lo-
cated exactly at $X = 1$. The electron concentration at the end of accurate
integration is about 25% below its peak value but is not dropping as fast as
expected due to the increasing density and decreasing temperature as the wall
is approached. The factor which prevents further accurate integration is a
freezing at low temperatures of the species N^+ and an equal mole-fraction of
free electrons (due to charge balance) due to the decrease in the forward rate
of Reaction #11. This prevents the correct limiting decrease of electron con-
centration at a low temperature and density. Additional charge exchange re-
actions would be needed to handle this problem, but the nonequilibrium com-
puter program presently will not accept a more complex model. Although these
conclusions apply to the stagnation streamlines, similar results on other
normals are evident and the identification of the drop -off in electron den-
sity at the wall is similarly difficult. The decrease in electron concentra-
tion on the innermost streamline at all downstream normals results from the
decreased production of electrons at the lower temperature quickly reached on
this streamline in the region of the stagnation point. In summary, it is seen
that the value of the peak electron density is well defined and that it is

certain that, in the absence of diffusion effects, the electron density gradient at the wall is extremely high.

Cases 8 and 9 Results. – Three nonequilibrium streamlines each were run for both Cases 8 and 9 to determine if a plottable difference in results could be seen for similarly located points, compared to Cases 2 and 3, respectively. These streamlines covered the shock layer from the boundary layer to the shock. Differences of less than 5% in all properties were computed for Case 9. For this case then it was considered justified to assume that nonequilibrium properties were the same for Cases 3 and 9 for points located identically by coordinates nondimensionalized to nose radius. The geometry involved in this comparison is represented on Figure 2, which also tabulates the X-locations of the base of normals for the two comparable cases.

For Case 8, however, plottable differences in properties were observed for streamlines near the shock downstream of the blunt nose. This results from the fact that Cases 2 and 8 are in near-equilibrium flow. For these streamlines that enter the shock downstream of the blunt nose region, the flow velocity is high behind the weak oblique shock. Thus, after crossing the shock on a specified outer streamline, the large property gradient which is characteristic of near-equilibrium flow produces a significantly different set of properties over a path length change of 5.4% required to reach the next numbered normal location. If the gradient is large enough a plottable difference results. For Cases 3 and 9, which are not as close to equilibrium as Cases 2 and 8, the property gradients are not large enough to result in an appreciable difference in properties over a 5.4% change in path length. The reason that plottable differences are not calculable on inner streamlines for Case 8 is that these streamlines originate at a point on the strong shock and have such a short relaxation distance to near equilibrium properties that any appreciable difference would occur in a very small region immediately behind the shock. This difference is not detectable on normal plots because of the comparatively large distance between numbered streamlines. Over most of their path length these inner streamlines exhibit small property gradients where a 5.4% change in distance has a negligible effect. The limiting case is fully equilibrium flow, e.g., note that the equilibrium data shown for Cases 2 and 8 and for Cases 3 and 9 are identical except for the 5.4% increase in normal distance. Again, this is a result of the identity of flow properties on non-dimensionally located normals. If Cases 2 and 8 were changed to a very low altitude (e.g., sea level), then the comparison would very likely show less change than was seen here because the flow would be even closer to equilibrium and the thickness of the high gradient region near the shock would approach the fully equilibrium limit of zero and hence not be detected. In summary, no differences would be seen if the flow is in either an equilibrium or frozen limiting condition and therefore a maximum difference occurs due to scale change somewhere in between.

CONCLUDING REMARKS

Flow fields in chemical nonequilibrium have been evaluated for a set of seven flight conditions for the RAM-C shape, and have been plotted by a CRT technique utilizing punch card computer program outputs. The flight conditions

covered nonequilibrium and near-equilibrium chemistry in the range between a chemistry nearly frozen due to a very high altitude (Case 7) and a chemistry nearly frozen due to a low temperature (Case 1). Boundary layer displacement thickness interaction effects were accounted for by an iterative computation while vorticity effects were taken into account by a merger of viscous and inviscid properties. The following conclusions were reached following examination of results:

1. Significant electron concentrations for Case 1 ($> 10^6$ particles/cc) were only predicted to occur near the stagnation point.

2. Case 2 exhibits nearly equilibrium electron concentrations throughout the flow field.

3. Case 3 shows marked difference in composition from equilibrium values, the effects being most evident in the neutral chemistry over the conical surface. Electron density normal profiles still appear similar to the equilibrium distributions.

4. Case 4 shows large deviations from the equilibrium chemistry throughout the flow field. Peak electron concentrations occur somewhat away from the wall because electron recombinations in the cooler regions of the flow near the cold wall still are significant. Electron density tends to decrease rapidly toward the shock along body normals, due to limited production of electrons on outer streamlines.

5. Cases 5, 6, and 7 show progressively an approach toward frozen chemistry with electron production limited essentially to a correspondingly diminishing region near the stagnation point. Peak electron concentrations occur very near the wall on all normals.

6. The effect of a 5.4% increase in nose radius for Cases 8 and 9 is essentially negligible. The results are almost the same along normals located in terms of nose radius as for Cases 2 and 3, respectively.

REFERENCES

1. Webb, H. G., Jr.: Final Report, Flow Field Prediction Analysis for Project RAM - Phase II. North American Rockwell Space Division Report SID64-548, February 1964.

2. Ball, W. H.: Flow Field Prediction and Analysis Study for Project RAM-B3. North American Rockwell Space Division Final Report SID65-1113, 20 August 1965.

3. Ball, W. H.: Supplementary Report - Flow Field Prediction and Analysis Study for Project RAM-B3. North American Rockwell Space Division Final Report SID66-213, 27 April 1966.

4. U. S. Standard Atmosphere, 1962, United States Government Printing Office, Washington 25, D.C., December 1962.

5. U. S. Standard Atmosphere Supplements, 1966 (ESSA, NASA, USAF), United Stated Government Printing Office, Washington 25, D.C.

6. Cheng, H. K.: Similitude of Hypersonic Real-Gas Flows Over Slender Bodies with Blunted Noses. J. Aero. Sci., Vol. 26, No. 9, pp 575-585, September 1959.

7. Waiter, S. A.: Analytical Study of Laminar Boundary Layer Growth at Hypersonic Velocities. North American Rockwell Space Division Report SID64-1929, November 1964.

8. Hayes, W. D.; and Probstein, R. F.: Hypersonic Flow Theory. New York: Academis Press, 1959.

9. Waiter, S. A.; and Anderson, R. B.: Determination of the Transonic Flow Field Around a Blunt Body. North American Rockwell Space Division Report SID64-634, February 1964.

10. Lomax, H.; and Inouye, M.: Numerical Analysis of Flow Properties About Blunt Bodies Moving at Supersonic Speeds in an Equilibrium Gas. NASA TR R-204, July 1964.

11. Dresser, H. S.: Method of Characteristics Program for Real Gas Equilibrium Flow. North American Rockwell Space Division Report SID64-633, March 1964.

12. Wood, A. D.; Springfield, J. F.; and Pallone, A. J.: Chemical and Vibrational Relaxation of an Inviscid Hypersonic Flow. AIAA Journal, Vol. 2, No. 10, pp 1697-1705, October 1964.

13. McKenzie, R. L.: A Correspondence of Blunt-Body Nonequilibrium Shock Layers. AIAA Journal, Vol. 6, No. 5, pp 944-946, May 1968.

14. Vaglio-Laurin, R.; and Bloom, M. H.: Chemical Effects in External Hypersonic Flows. ARS Paper 1976-61. Presented at International Hypersonic Conference, August 1961.

15. Eschenroeder, A. Q.; Boyer, D. W.; and Hall, G. J.: Exact Solutions for Nonequilibrium Expansions of Air With Coupled Chemical Reactions. Cornell Aeronautical Laboratory Report AF-1413-A-1, May 1961.

16. Penner, S. S.: Chemistry Problems in Jet Propulsion, Vol. I. New York: Pergamon Press, 1957.

17. Stein, A. M.: High-Temperature Thermodynamics and Chemical Equilibria for a Hypersonic Flow Air Model. North American Rockwell Space Division Report SID TNA63-1, December, 1963.

18. Dresser, H. A.; and Stein, A. J.: One-Dimensional, Reacting Gas Flow Program. North American Rockwell Space Division Report SID64-632, February 1964.

19. Ralston, A.; and Wilf, H. S.: Mathematical Methods for Digital Computers. New York: John Wiley and Sons, 1960.

20. Vincenti, W. G.: Calculations of the One-Dimensional Nonequilibrium Flow of Air Through a Hypersonic Nozzle - Interim Report. AEDC-TN-61-65, May 1961.

21. Emanual, G.; and Vincenti, W. G.: Method for Calculation of the One-Dimensional Nonequilibrium Flow of a General Gas Mixture Through a Hypersonic Nozzle. AEDC-TDR-62-131, June 1962.

22. Grabau, M.: A Method of Forming Continuous Empirical Equations for the Thermodynamic Properties of Air from Ambient Temperatures to 15,000 K, With Applications. AEDC-TN-59-102, August 1959.

23. Hansen, C. F.: Approximations for the Thermodynamic and Transport Properties of High-Temperature Air. NASA TR-50, 1959.

24. Hilsenrath, J.; Klein, M.; and Wooley, H. W.: Tables of Thermodynamic Properties of Air Including Dissociation and Ionization from 1500 K to 15,000 K. AEDC-TR-59-20, December 1959.

25. Stein, A. M.; and Anderson, R. B.: Computer Program, Thermodynamic and Thermal Functions of Individual Species Including Elementary Ablation Products, for Hypersonic Flow Air Model. North American Rockwell Space Division Report SID64-635, December 1963.

26. Wilkins, Roger L.: Note on the Linearization Method for Computing Chemical Equilibrium in Complex Systems in Kinetics, Equilibrium and Performance of High Temperature Systems. Edited by Bahn and Zukoski, Butterworths, Inc., 1960.

27. Wilkins, Roger L.: Theoretical Evaluation of Chemical Propellants. Prentice-Hall, Inc., 1963.

28. Logan, J. F., Jr.; and Treanor, C. E.: Thermodynamic Properties of Air from 3000 K to 10,000 K at Intervals of 100 K. Cornell Aeronautical Laboratory Report BE-1007-A-3, January 1957.

29. Wray, K.; Teare, J. D.; Kivel, B.; and Hammerling, P.: Relaxation Processes and Reaction Rates Behind Shock Fronts in Air and Component Gases. Avco-Everett Research Laboratory, Research Report 83, 1959.

30. Wray, K.: Chemical Kinetics of High-Temperature Air. Avco-Everett Research Laboratory, Report 104, 1961.

31. Hilsenrath, J.; and Klein, Max: Tables of Thermodynamic Properties of Air in Chemical Equilibrium Including Second Virial Corrections from 1500°K to 15,000°K. Arnold Engineering Development Center Report AEDC-TR-65-58, March 1965.

Table 1.– RAM–C Flight Conditions

Case Number	Velocity (ft/sec)	Altitude (ft)	Ambient Pressure (lb/ft^2)	Ambient Temperature (°R)	Ambient Density (slugs/ft^3)	Nose Radius (ft)	Wall Temperature (°K)
1	8,020	60,000	1.5100×10^2	389.97	2.256×10^{-4}	0.500	700
2	16,780	80,300	5.768×10^1	397.86	8.447×10^{-5}	"	"
3	24,750	149,800	$2,862 \times 10^0$	478.77	3.484×10^{-6}	"	"
4	25,130	250,300	4.181×10^{-2}	351.19	6.938×10^{-8}	"	"
5	25,090	269,800	1.434×10^{-2}	325.17	2.570×10^{-8}	"	"
6	25,090	299,900	2.658×10^{-3}	332.74	4.653×10^{-9}	"	"
7	25,030	325,500	7.114×10^{-4}	373.99	1.106×10^{-9}	"	"
8	SAME AS CASE 2 —————————————————————————————————————→					0.527	"
9	SAME AS CASE 3 —————————————————————————————————————→					"	"

Table 2.- Chemical Reactions and Rate Constants

No.	Reaction	Catalyst, M	Rate Constant Expression
1	$O_2 + M + 5.1\ ev \rightleftharpoons O + O + M$ $(D_K = 211,644)$	A, N, N^+, NO, NO^+ N_2, N_2^+ O_2, O_2^+ O, O^+	$K_{f_1} = 2.98 \times 10^9\ T^{1/2}\ (JD_K/RT)^{3/2}\ EXP(-JD_K/RT)$ $K_{f_1} = 2\ K_{f_{1(A)}}$ $K_{f_1} = 9\ K_{f_{1(A)}}$ $K_{f_1} = 25\ K_{f_{1(A)}}$
2a	$N_2 + M + 9.8\ ev \rightleftharpoons N + N + M$ $(D_K = 406,690)$	$A, O, O^+, O_2, O_2^+, NO, NO^+$ N_2, N_2^+	$K_{f_{2a}} = 2.207 \times 10^{10}\ T^{1/2} (JD_K/RT)\ EXP(-JD_K/RT)$ $K_{f_{2a}} = 2.47\ K_{f_{2a(A)}}$
2b	$N_2 + M + 9.8\ ev \rightleftharpoons N + N + M$ $(D_K = 406,690)$	N, N^+	$K_{f_{2b}} = 3.82 \times 10^{10}\ T^{1/2}\ (JD_K/RT)^2\ EXP(-JD_K/RT)$
3	$NO + M + 6.5\ ev \rightleftharpoons N + O + M$ $(D_K = 269,744)$	$A, O_2, O_2^+, N_2, N_2^+$ NO, NO^+, O, O^+, N, N^+	$K_{f_3} = 8.35 \times 10^8\ T^{1/2}\ (JD_K/RT)^2\ EXP(-JD_K/RT)$ $K_{f_3} = 20\ K_{f_{3(A)}}$
4	$N_2 + O + 3.3\ ev \rightleftharpoons NO + N$		$K_{f_4} = 1.120 \times 10^{12}\ EXP\ (-J \times 1.359 \times 10^5/RT)$
5	$NO + O + 1.4\ ev \rightleftharpoons O_2 + N$		$K_{f_5} = 2.842 \times 10^7\ T\ EXP\ (-J \times 7.038 \times 10^4/RT)$
6	$N_2 + O_2\ 1.9\ ev \rightleftharpoons NO + NO$		$K_{f_6} = 6.32 \times 10^{23}\ T^{-5/2}\ EXP\ (-J \times 2.31 \times 10^5/RT)$
7	$N + O \pm 2.8\ ev \rightleftharpoons NO^+ + e^-$		$K_{f_7} = 7.63 \times 10^7\ T^{1/2}\ EXP\ (-J \times 1.139 \times 10^5/RT)$
8	$N + N + 5.8\ ev \rightleftharpoons N_2^+ + e^-$		$K_{b_8} = 3.72 \times 10^{20}\ T^{-3/2}$
9	$O + O + 6.9\ ev \rightleftharpoons O_2^+ + e^-$		$K_{b_9} = 7.45 \times 10^{19}\ T^{-3/2}$
10	$O_2^+ + O + 1.6\ ev \rightleftharpoons O_2 + O^+$		$K_{b_{10}} = 9.349 \times 10^9\ T^{1/2}$
11	$N_2 + N^+ + 1.0\ ev \rightleftharpoons N + N_2^+$		$K_{b_{11}} = 9.349 \times 10^9\ T^{1/2}$

1. All units are in the English system. The units of D_K are BTU/LbMole and the units of K_f and K_b are Ft^3/LbMole-Sec.
2. The forward and backward rate constant expressions were taken from References 19 and 20
3. The 'A' in parentheses refers to Argon.

33

Table 3.— Analytic Expressions for Equilibrium Constants $K_p(j)$ vs. Temperature

Reaction Number	$K_p(j)$	E_O^O Heat of Reaction at $O^{\circ}K$	
		Calories Per Mole	Electron Volts
1	$9.16 \times 10^6 \exp\left[-\Delta E_o^O/RT\right]$	117,580.5	5.1
2	$1.72 \times 10^2\, T^{5/4} \exp\left[-\Delta E_o^O/RT\right]$	225,939	9.8
3	$1.28 \times 10^2\, T^{1.1} \exp\left[-\Delta E_o^O/RT\right]$	149,857.5	6.5
4	$5.42 \exp\left[-\Delta E_o^O/RT\right]$	76,081.5	3.3
5	$8.2 \times 10^{-2}\, T^{0.124} \exp\left[-\Delta E_o^O/RT\right]$	32,274.2	1.4
6	$1.71 \times 10^1 \exp\left[-\Delta E_o^O/RT\right]$	43,800.7	1.9
7	$4.20 \times 10^{-11}\, T^{7/4} \exp\left[-\Delta E_o^O/RT\right]$	64,554	2.8
8	$3.00 \times 10^{-10}\, T^{5/3} \exp\left[-\Delta E_o^O/RT\right]$	133,719	5.8
9	$2.56 \times 10^{-12}\, T^{2.1} \exp\left[-\Delta E_o^O/RT\right]$	159,079.5	6.9
10	$1.12 \times 10^{-1}\, T^{0.177} \exp\left[-\Delta E_o^O/RT\right]$	36,888	1.6
11	$8.09 \times 10^{-4}\, T^{0.863} \exp\left[-\Delta E_o^O/RT\right]$	23,053	1

$R = 1.9872$ Calories $\deg^{-1}$ $mole^{-1}$
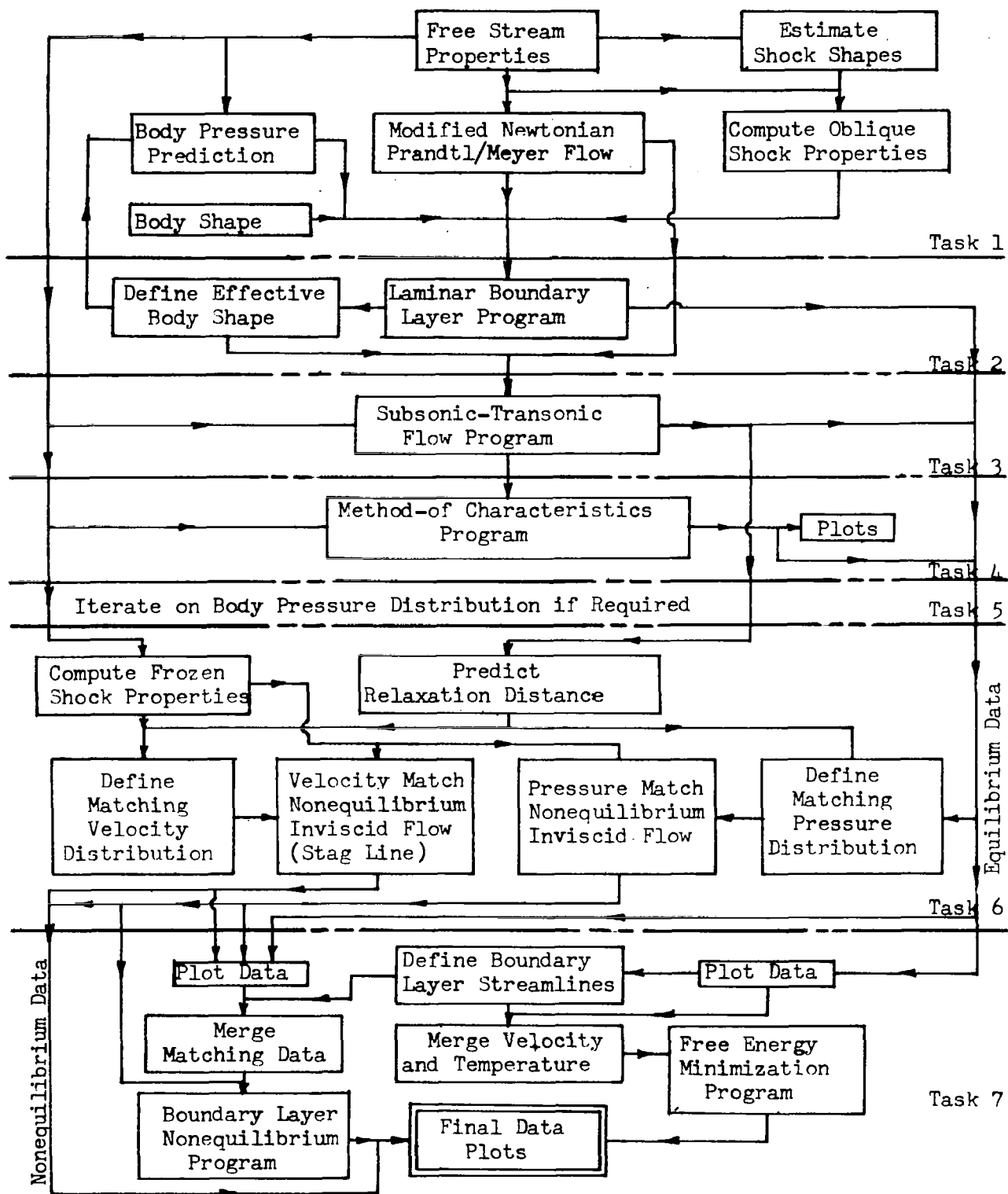
Figure 1.- Flow Field Analysis Logic Diagram
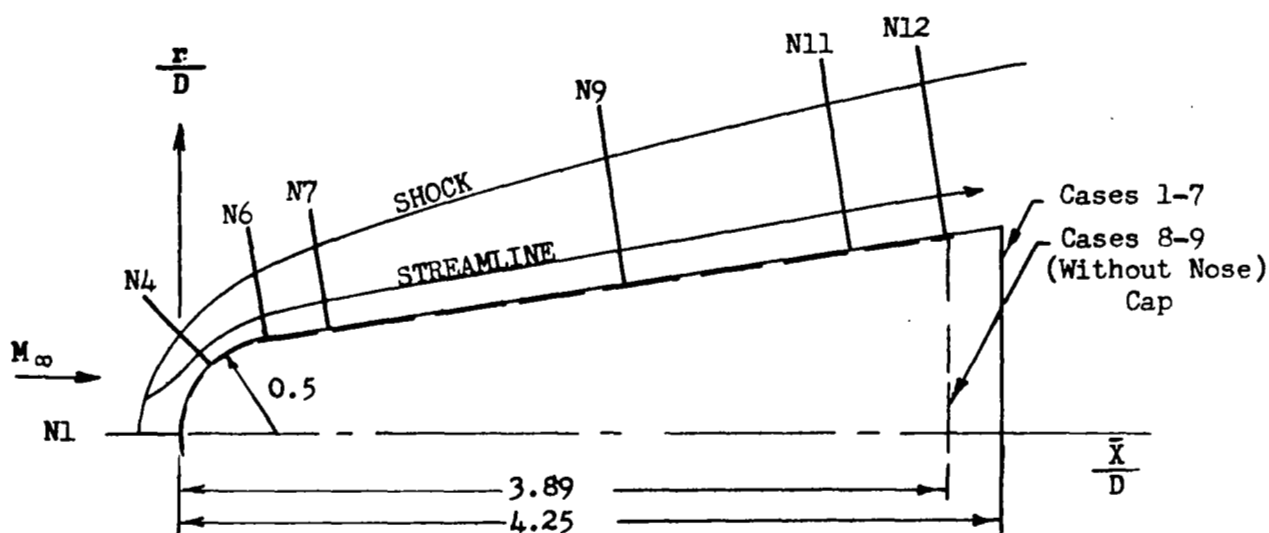
$$\bar{\bar{X}} = 0$$
$$X = 1 \ (\text{Cases 1-7})$$
$$X = 1.0541 \ (\text{Cases 8-9})$$

Normal Number	Dimensionless Axial Coordinate of Base of Normal from Stagnation Point, $\frac{\bar{X}}{D}$	Axial Coordinate, $\bar{X}$, (ft)	
		Cases 1-7 $D = 1$	Cases 8-9 $D = 1.0541$
1	0	0	0
4	0.1475	0.1475	0.1555
6	0.4100	0.4100	0.4322
7	0.7600	0.7600	0.8011
9	2.3000	2.3000	2.4244
11	3.4800	3.4800	3.6683
12	3.9800	3.9800	4.1953

Figure 2.- Geometry and Coordinates, RAM-C Vehicle
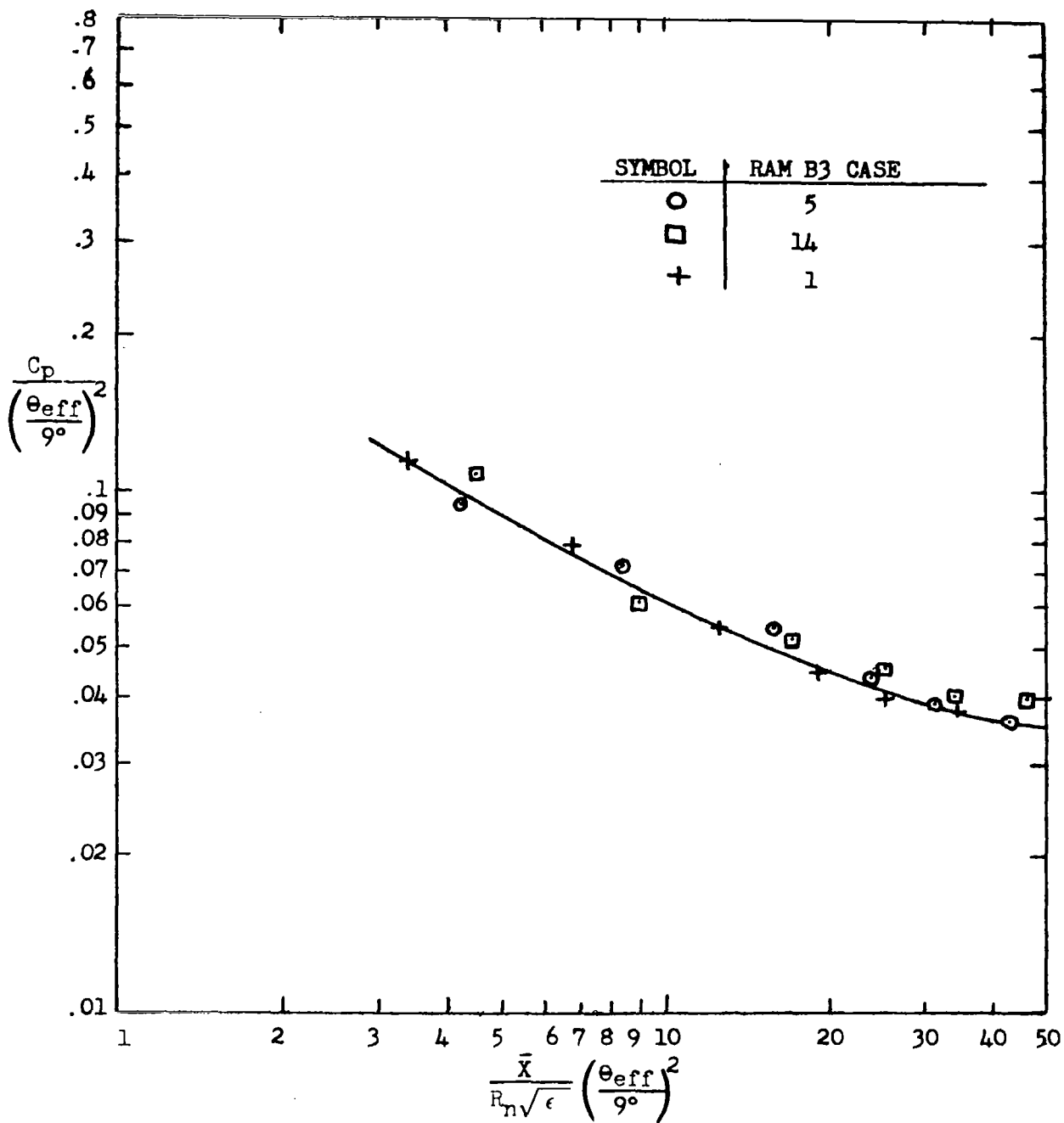
Figure 3.- Pressures on Hemispherically Blunted 9° Half-Angle Cones
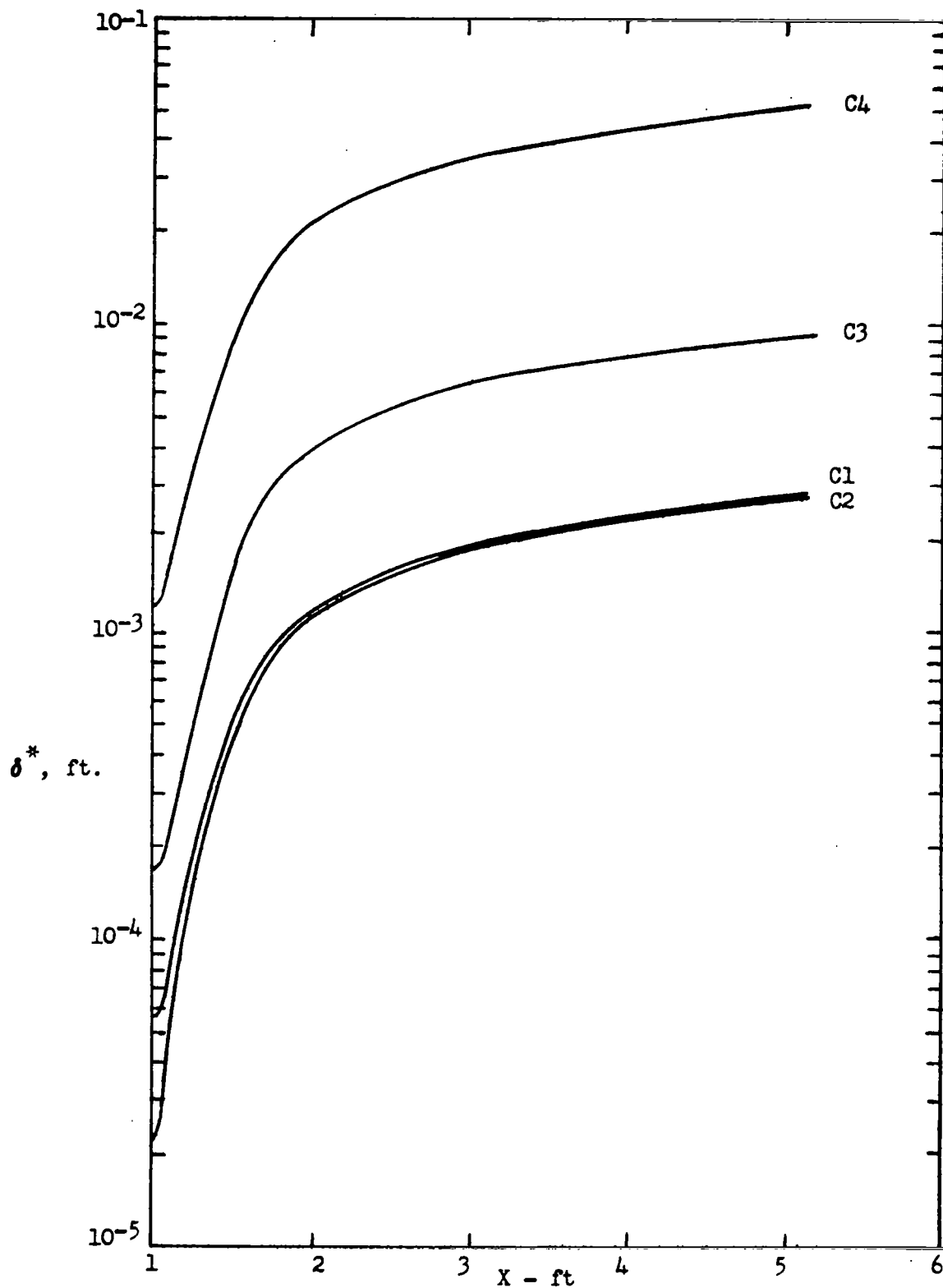
a. Cases 1-4

Figure 4.- Boundary Layer Displacement Thickness Variations
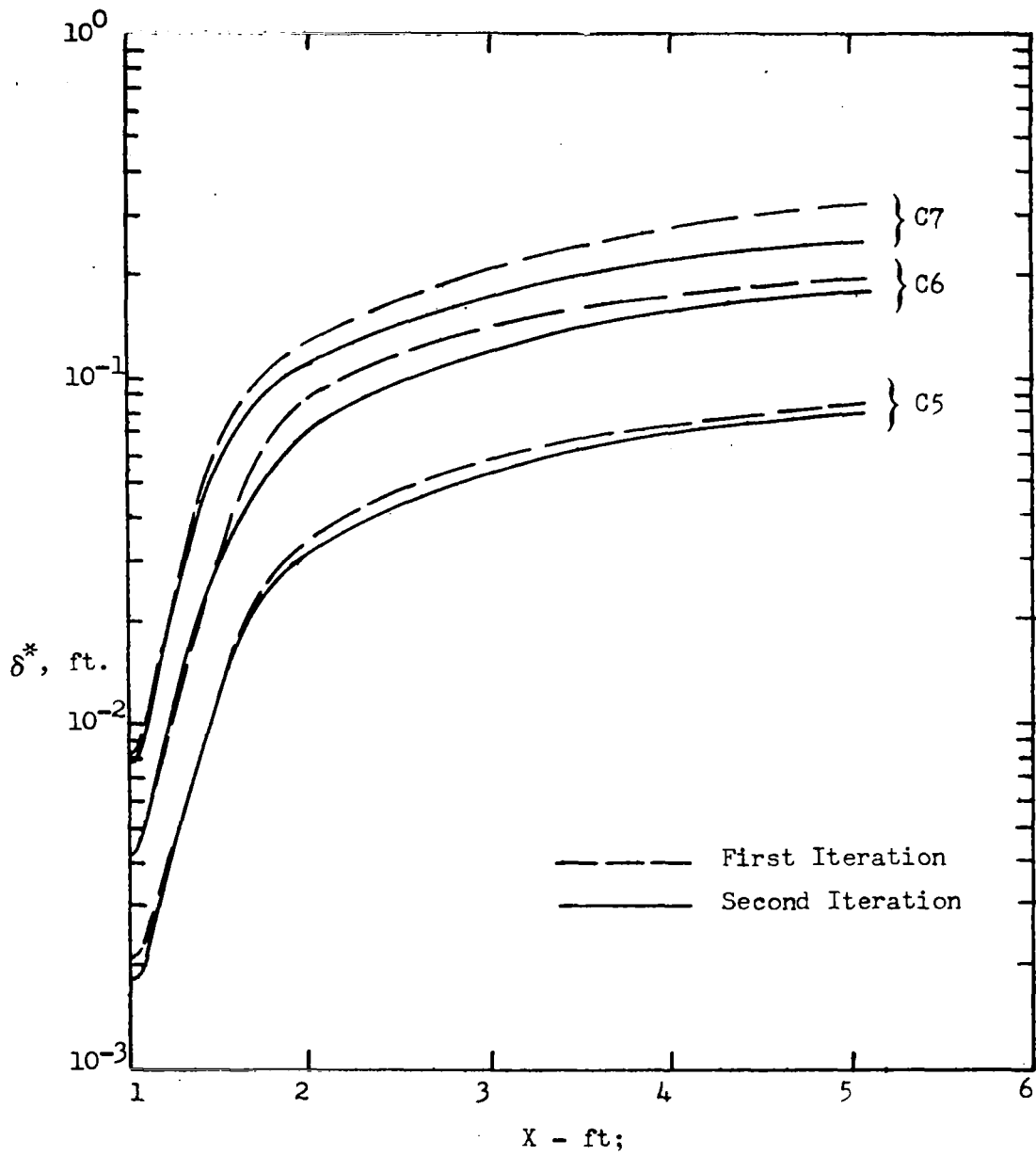
b. Cases 5-7

Figure 4.- Concluded

39

TRANSONIC FLOW FIELD STREAM LINES
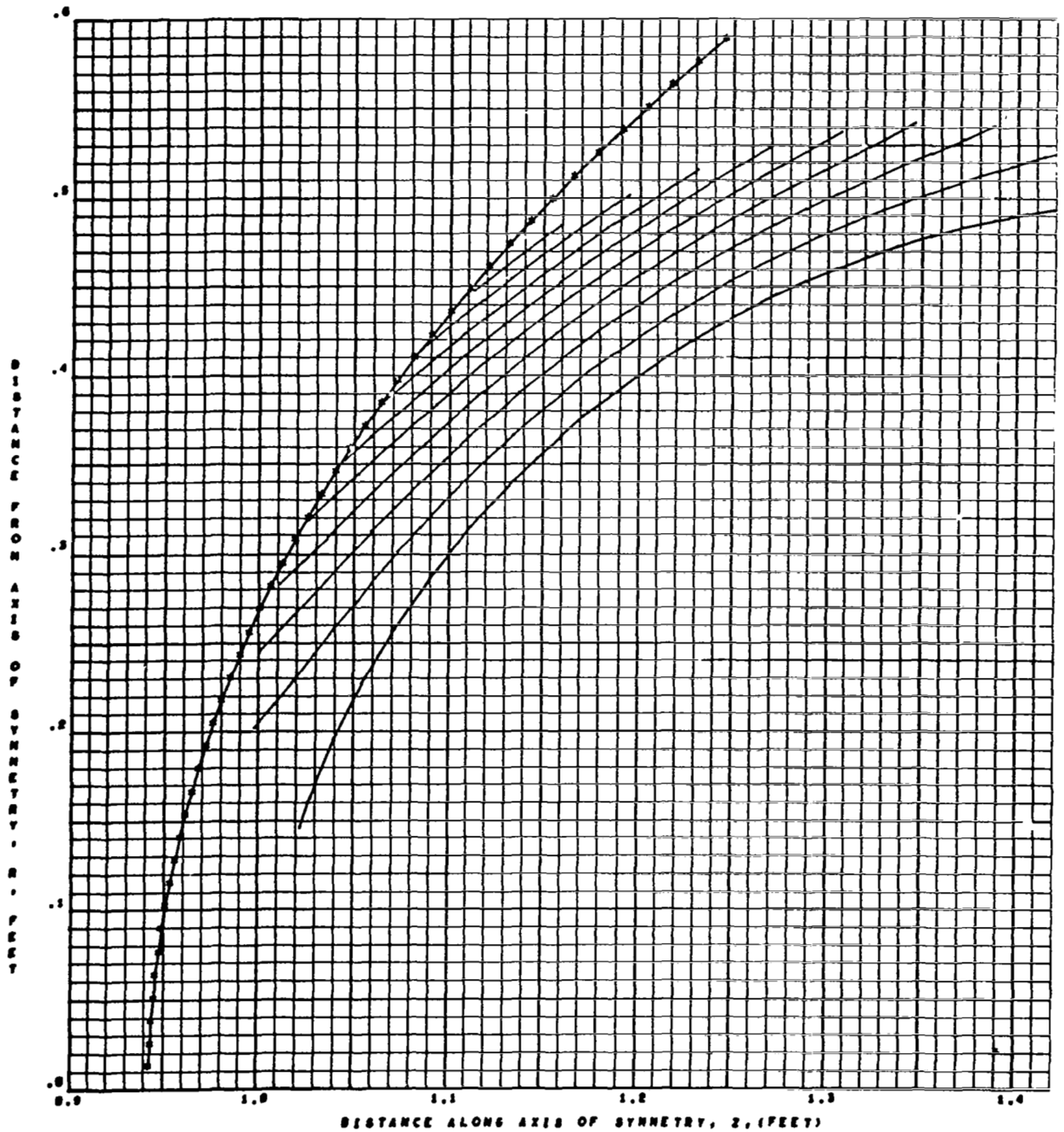
Figure 5.- Case 1, Blunt Body Flow - Streamline Pattern
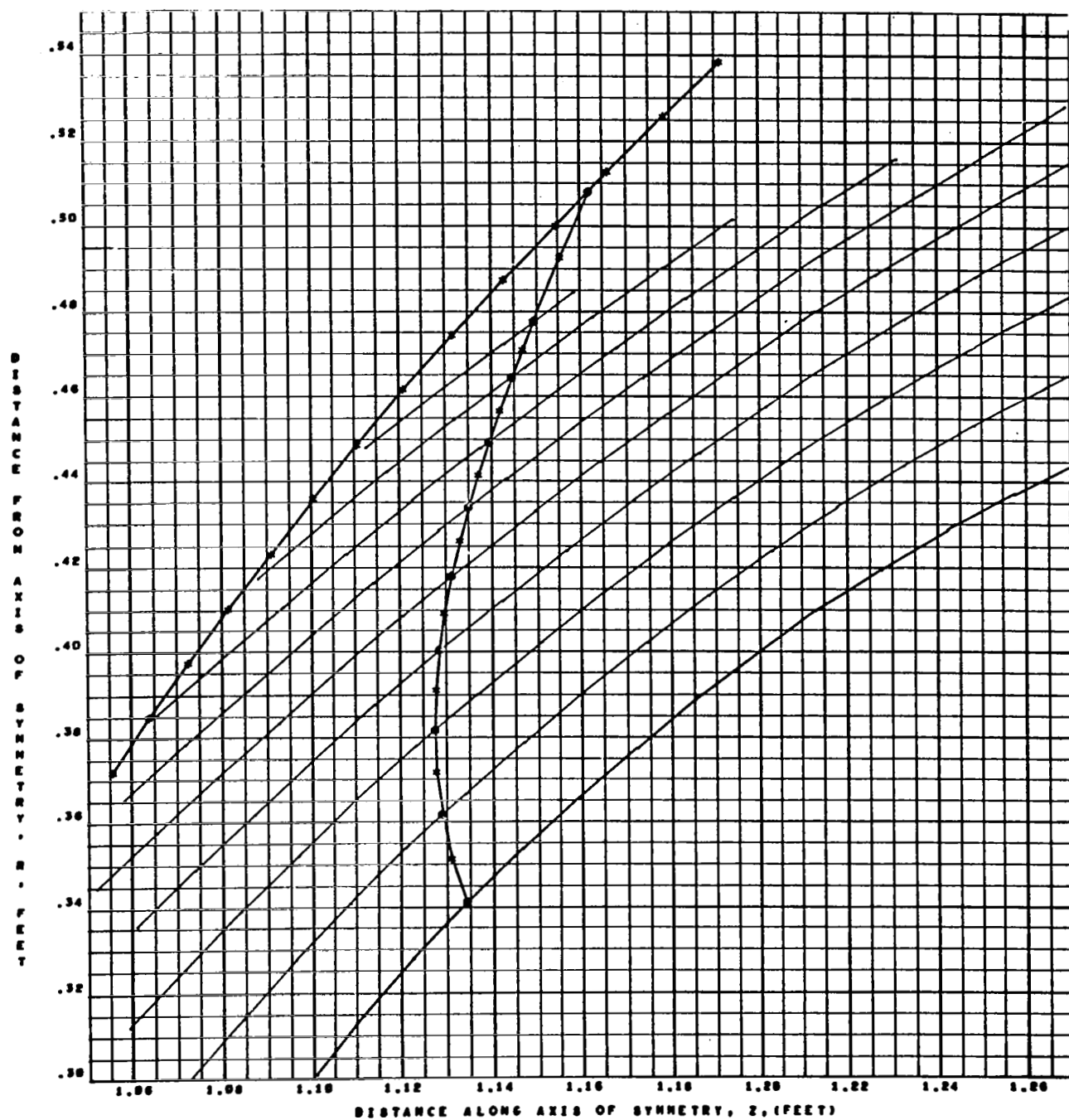
Figure 6.– Case 1, Blunt Body Flow – Start Line Geometry

41
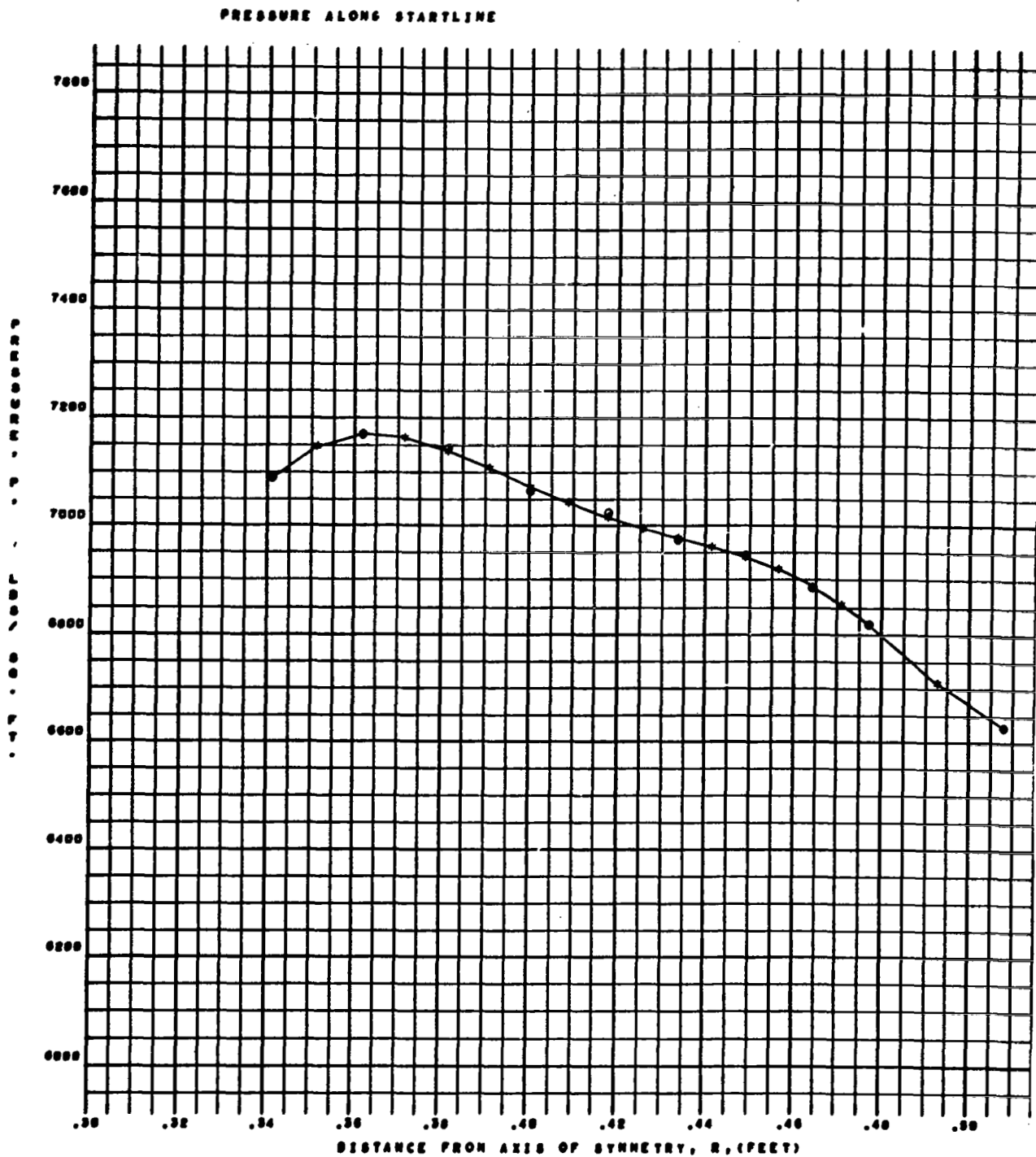
Figure 7.- Case 1, Blunt Body Flow - Start Line Pressure

42
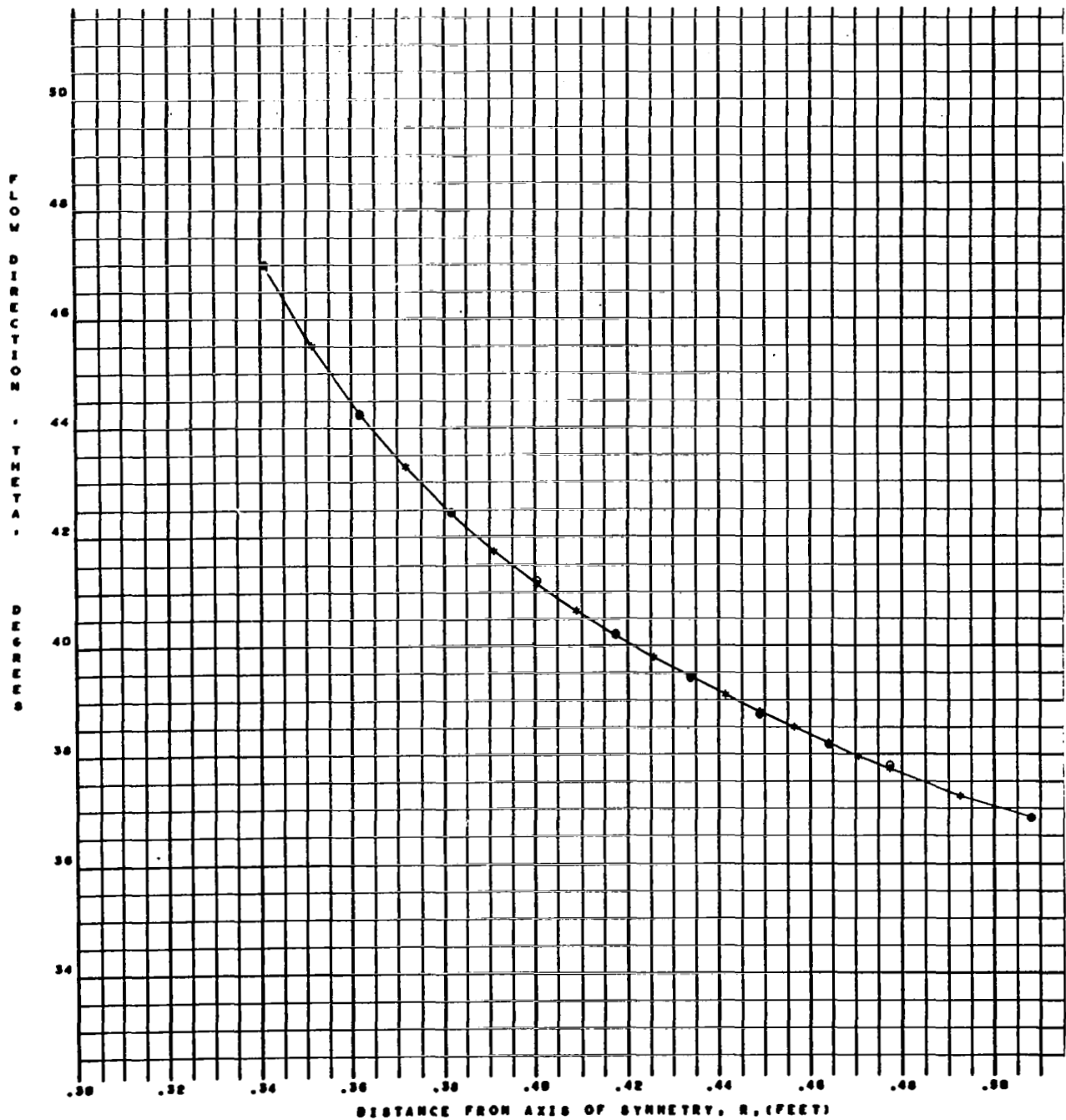
Figure 8.— Case 1, Blunt Body Flow — Start Line Flow Direction

43
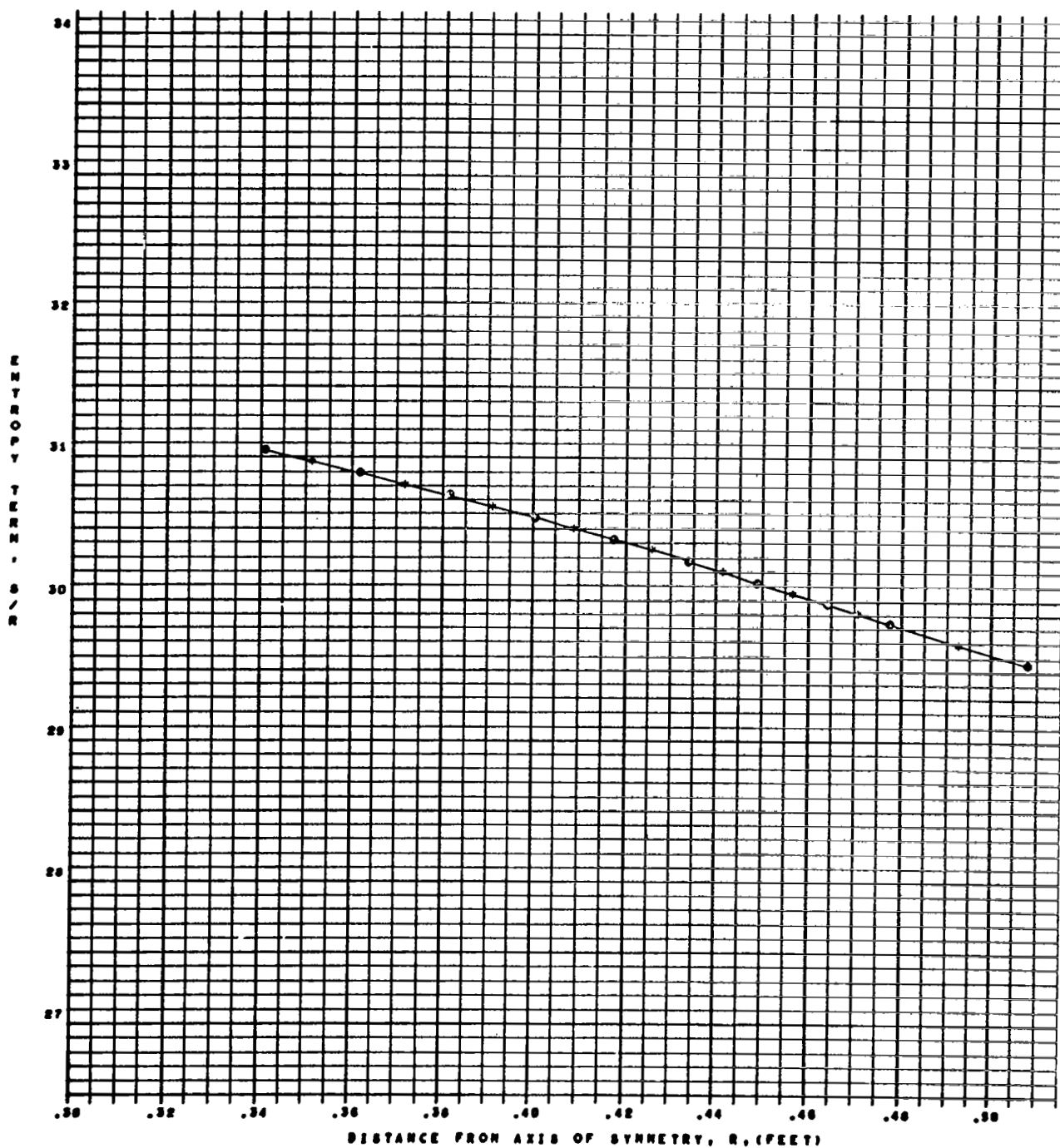
Figure 9.- Case 1, Blunt Body Flow - Start Line Entropy
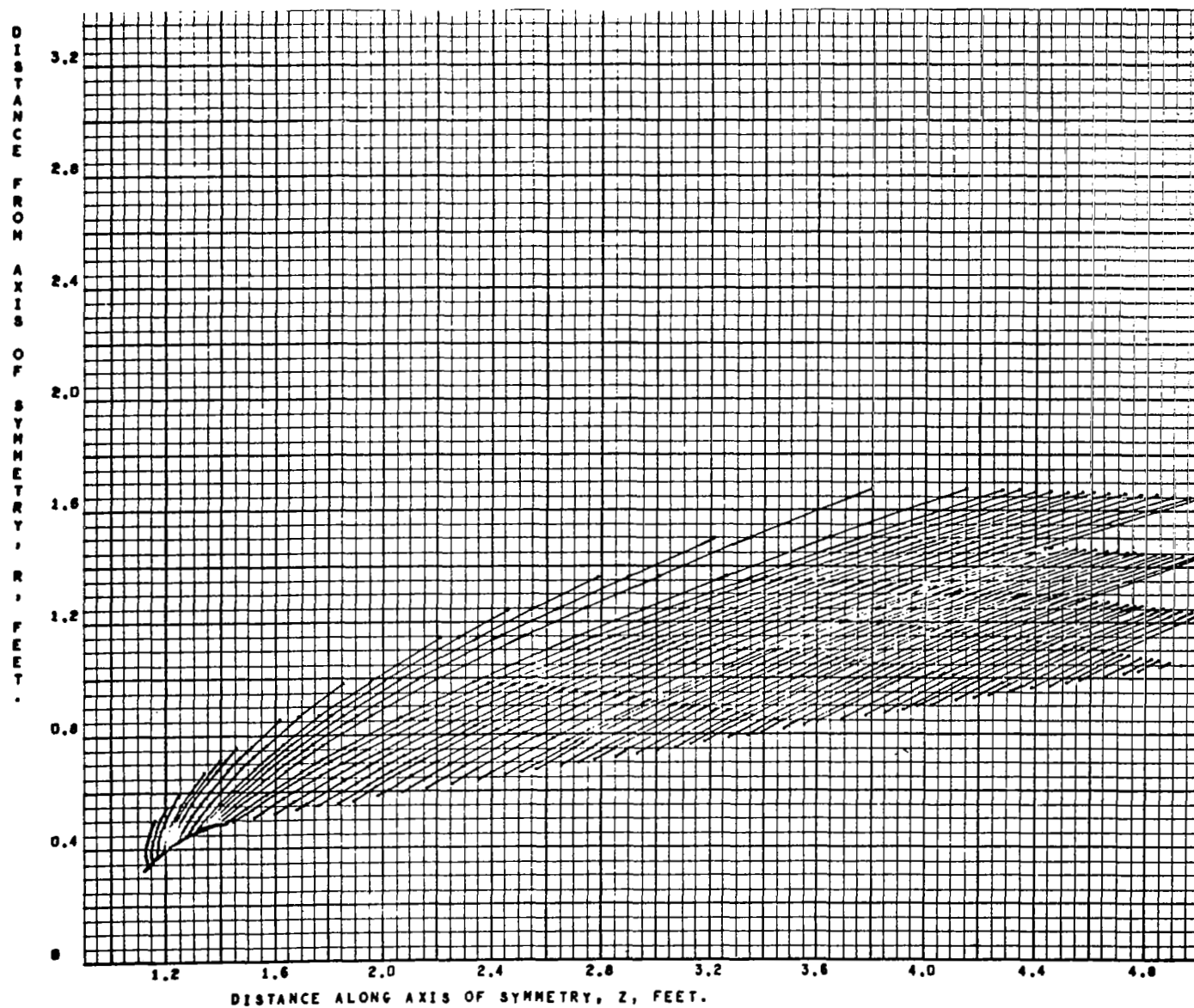
Figure 10.- Case 1, Left-Running Characteristic Network
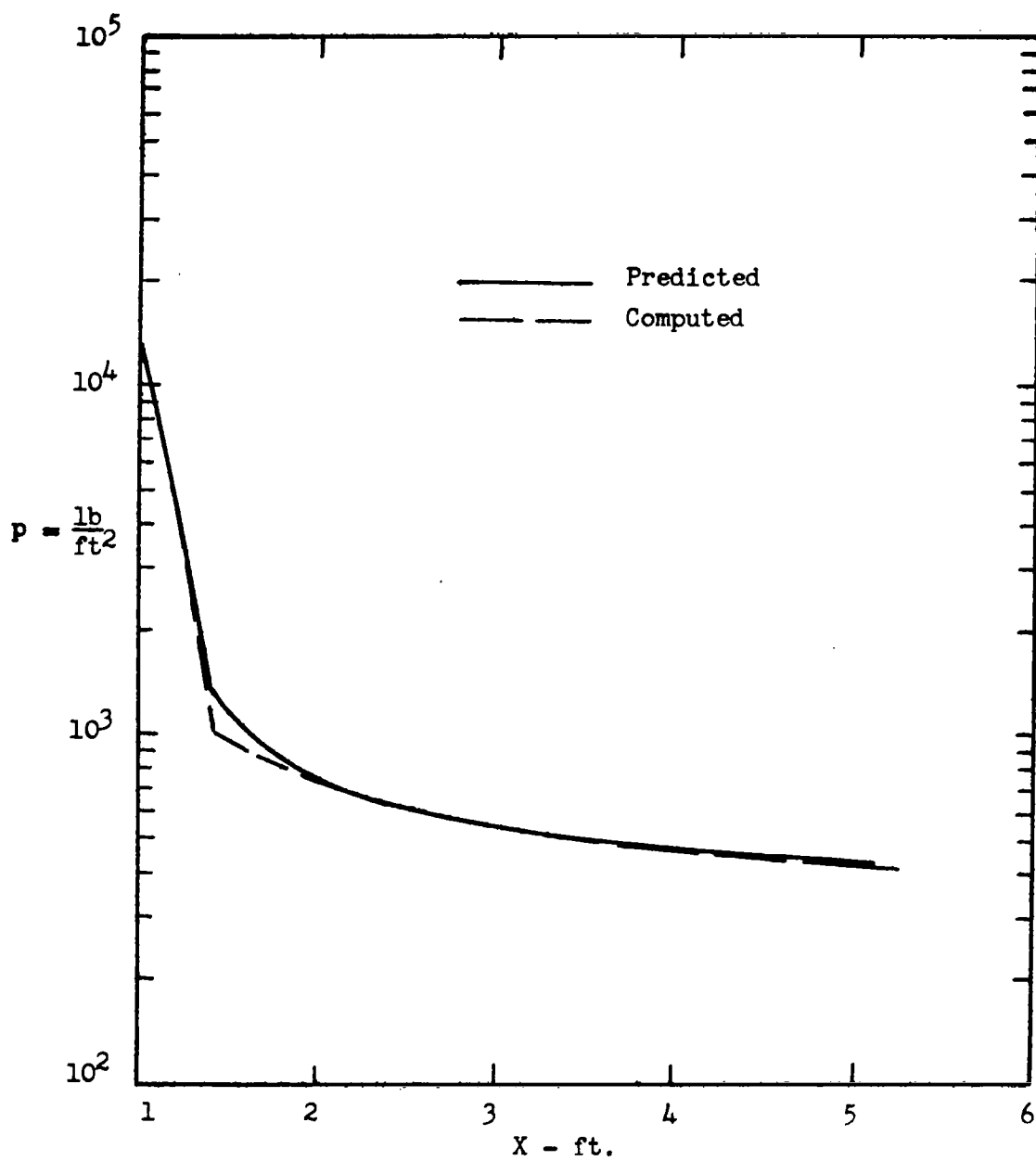
Figure 11.- Case 1, Comparison of Predicted and Computed
Inviscid Pressure Distributions on Body
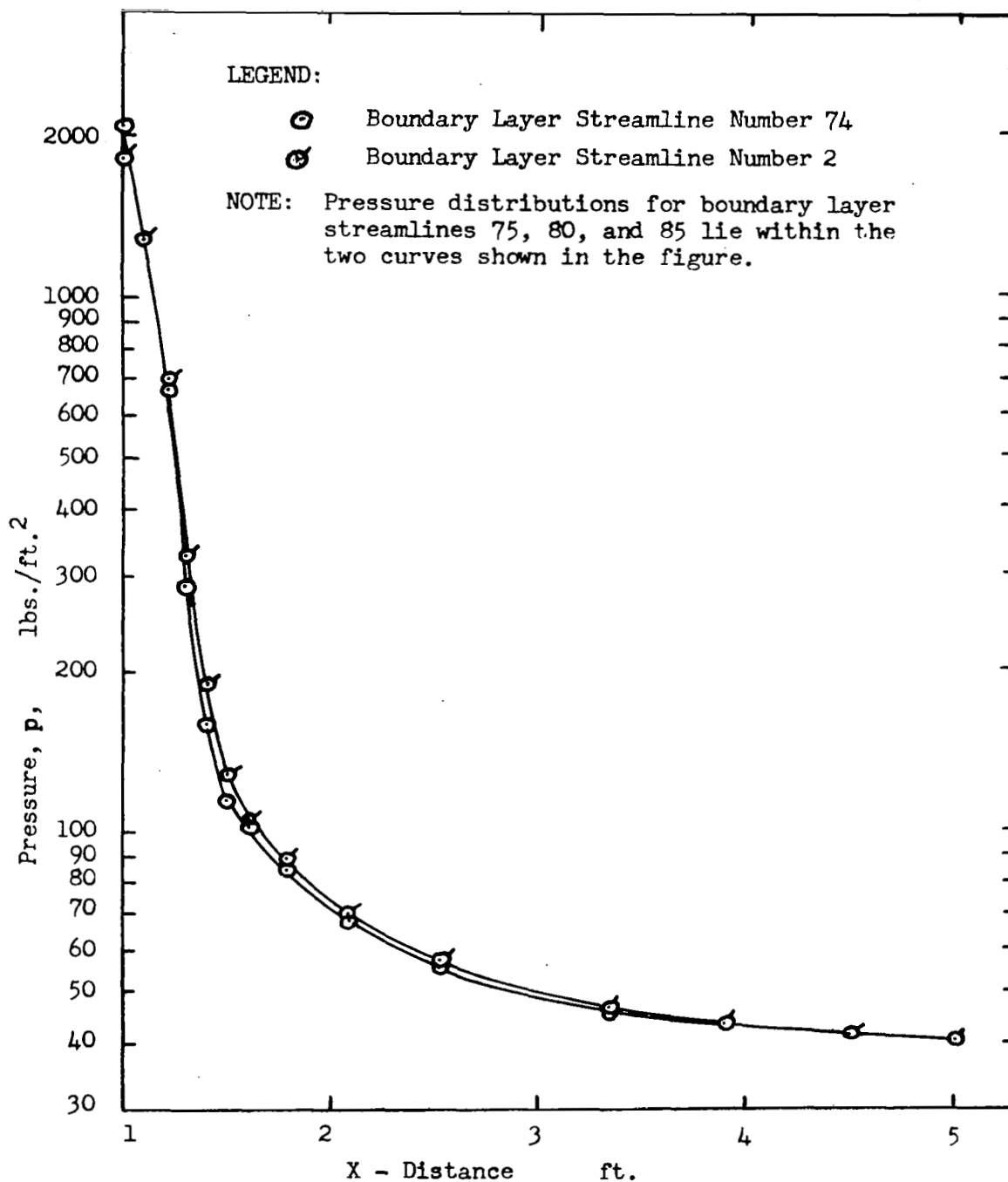
Figure 12.– Pressure Matching Parameter Distribution
For Case 3 Boundary Layer Streamlines
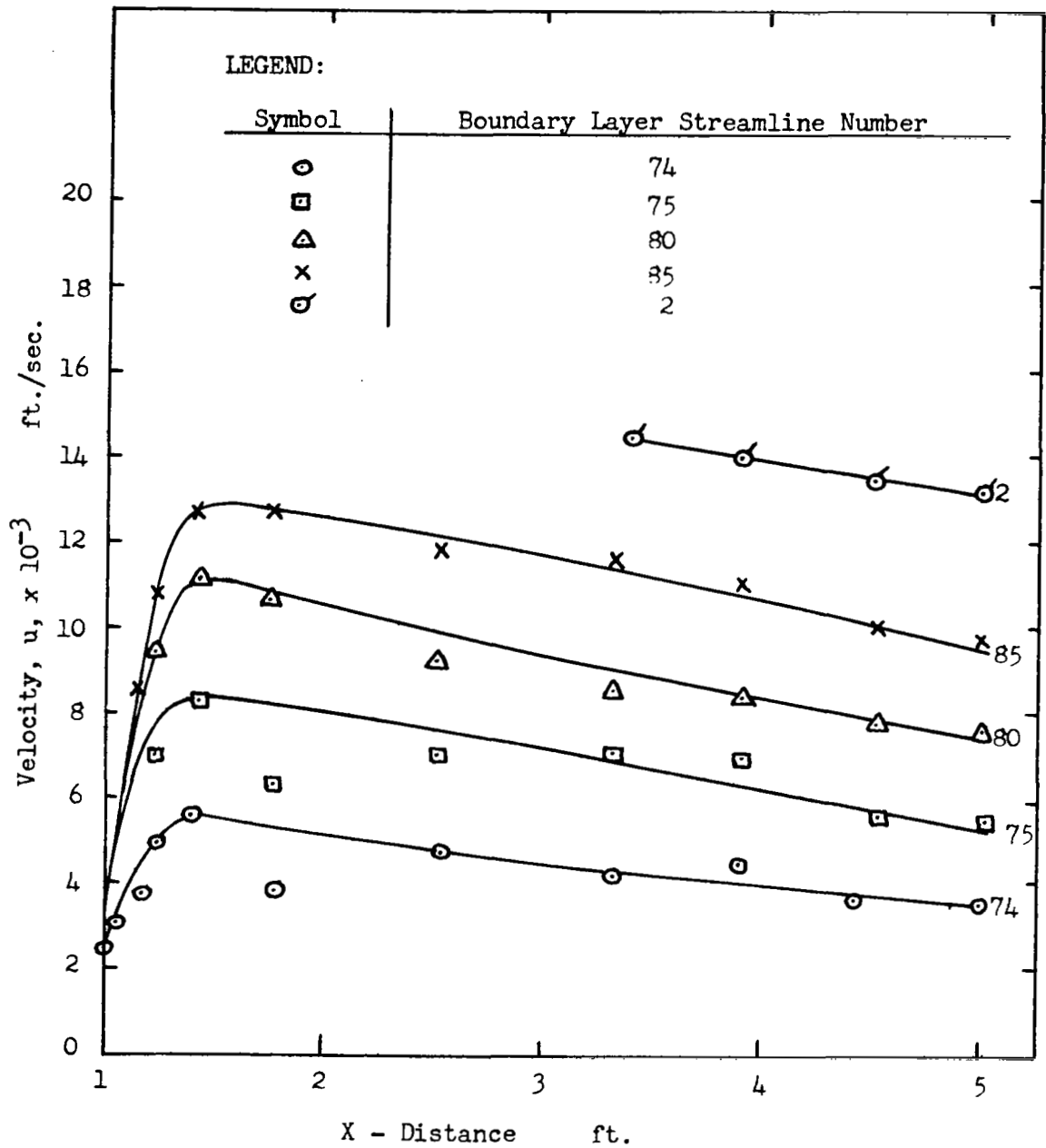
Figure 13.- Velocity Matching Parameter Distribution
For Case 3 Boundary Layer Streamlines
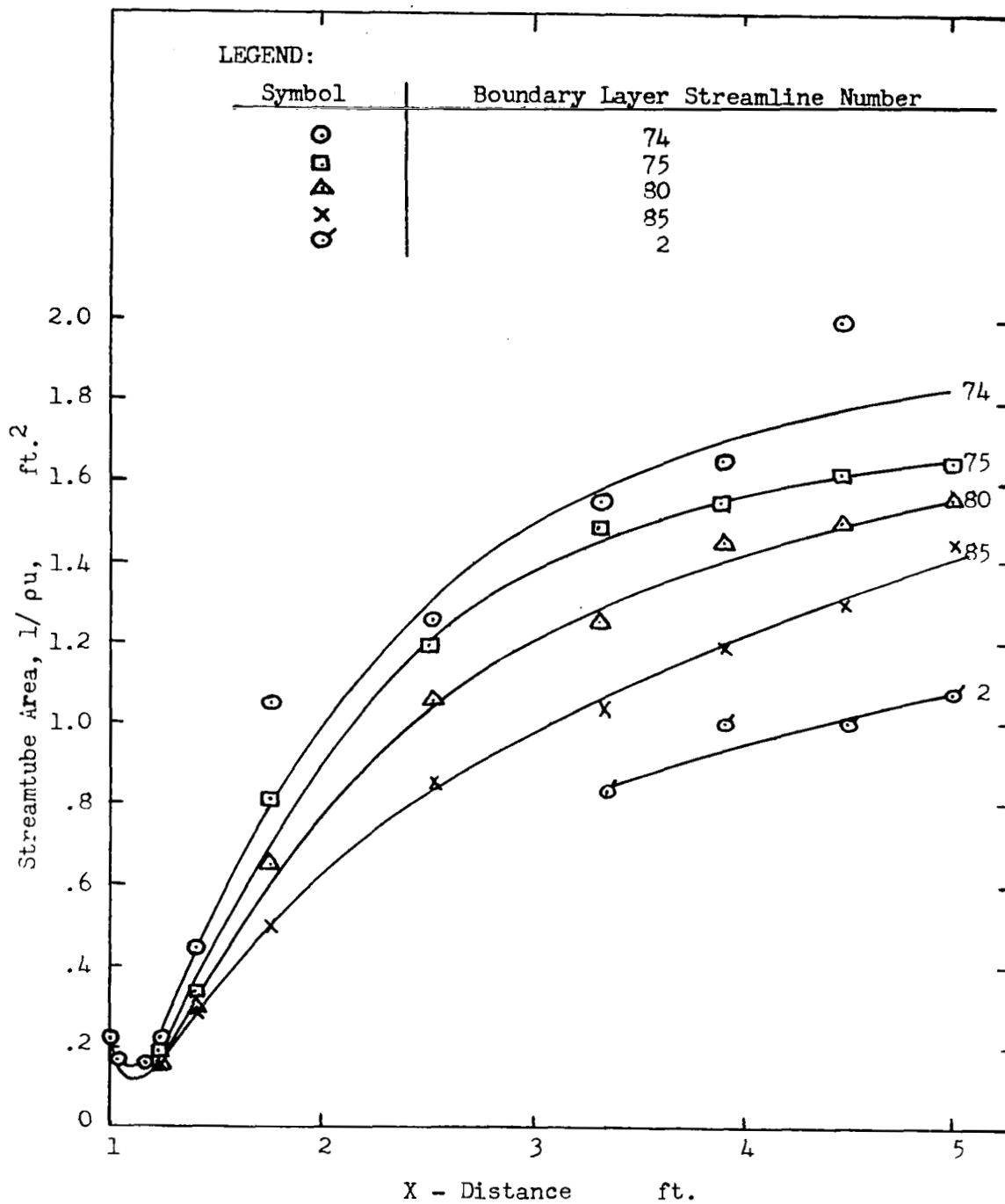
Figure 14.- Streamtube Area Matching Parameter Distribution
For Case 3 Boundary Layer Streamlines

49
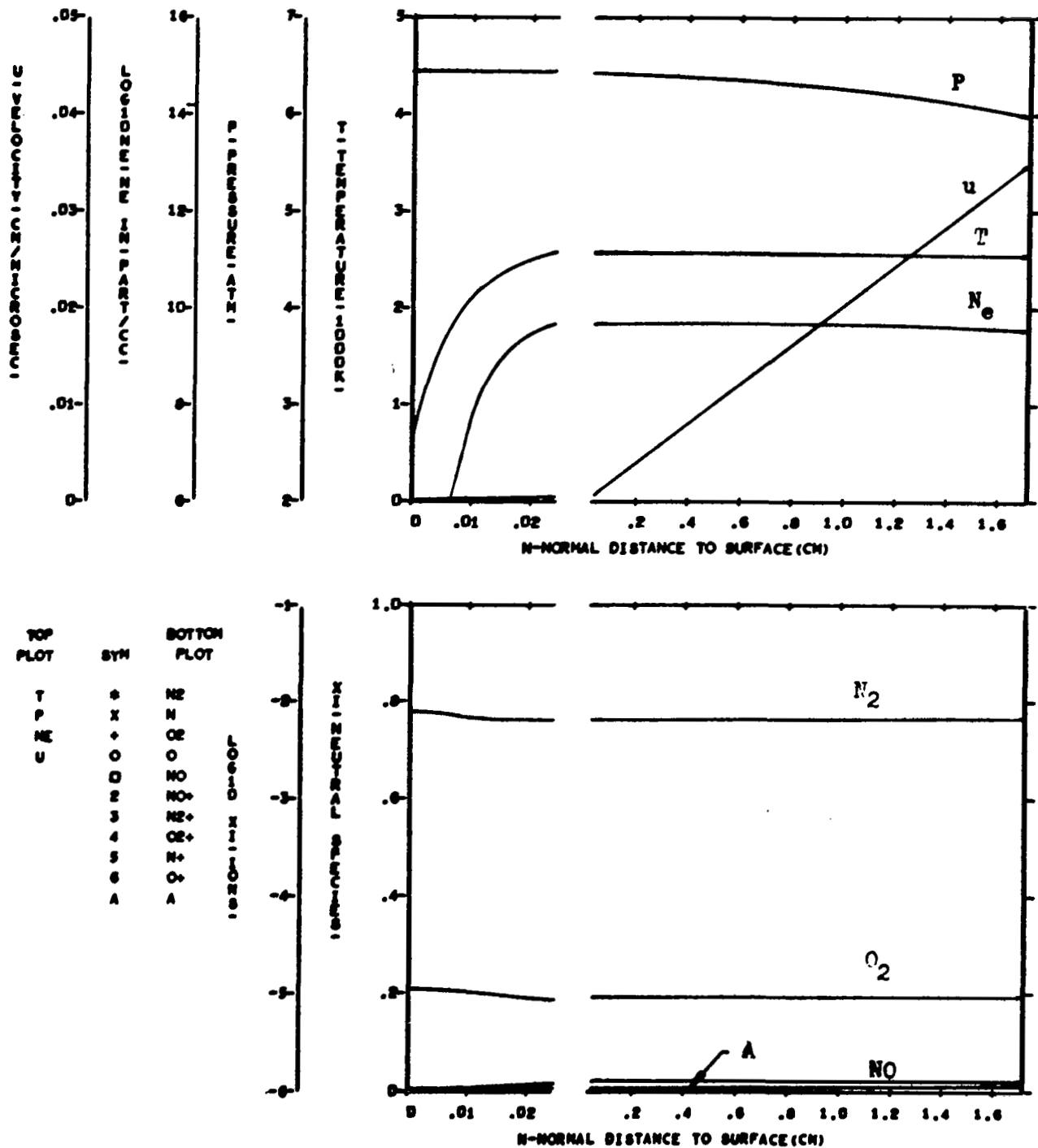
FIGURE 25 EQUILIBRIUM FLOW FIELD PROPERTIES - CASE 1, NORMAL 1
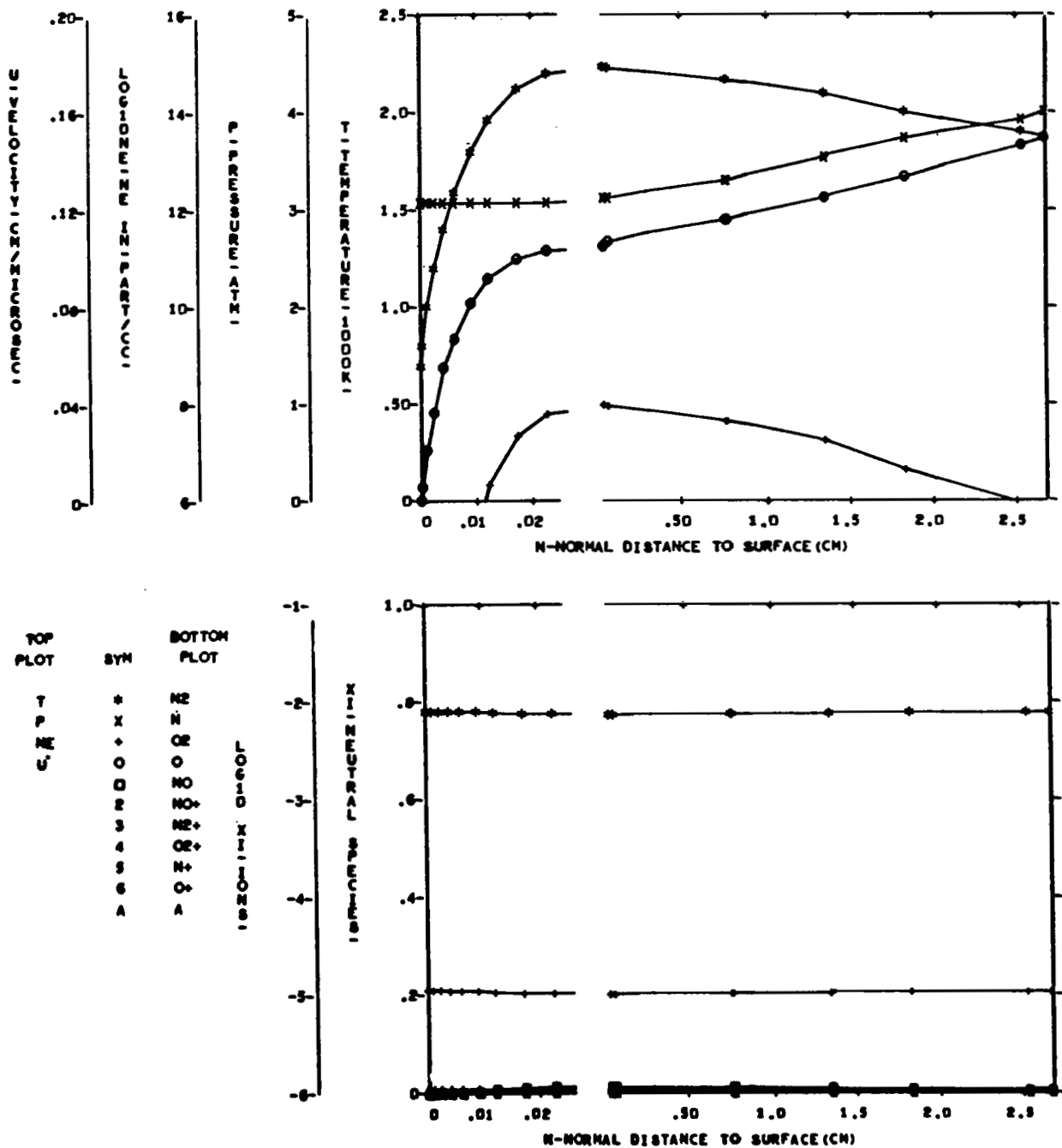
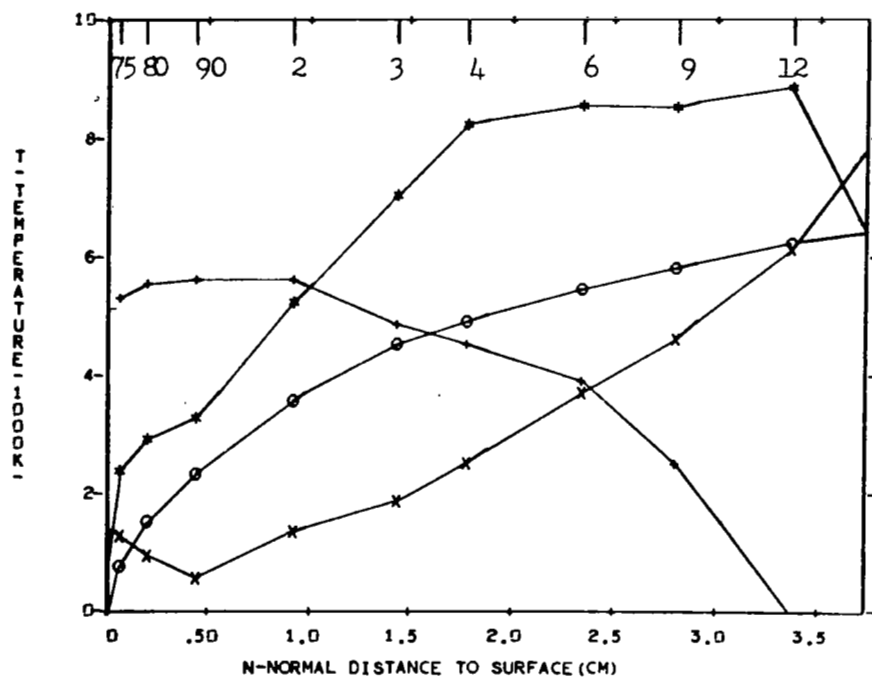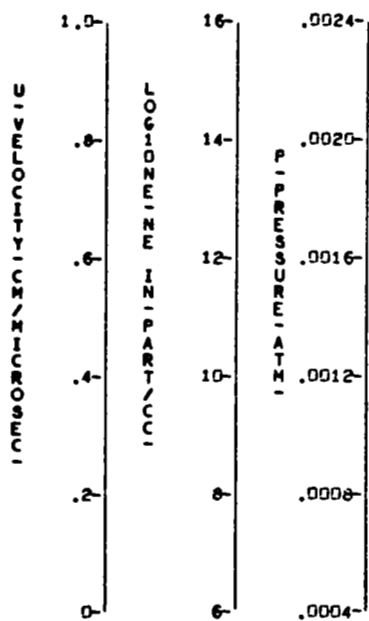FIGURE 16 EQUILIBRIUM FLOW FIELD PROPERTIES - CASE 1, NORMAL 4

51
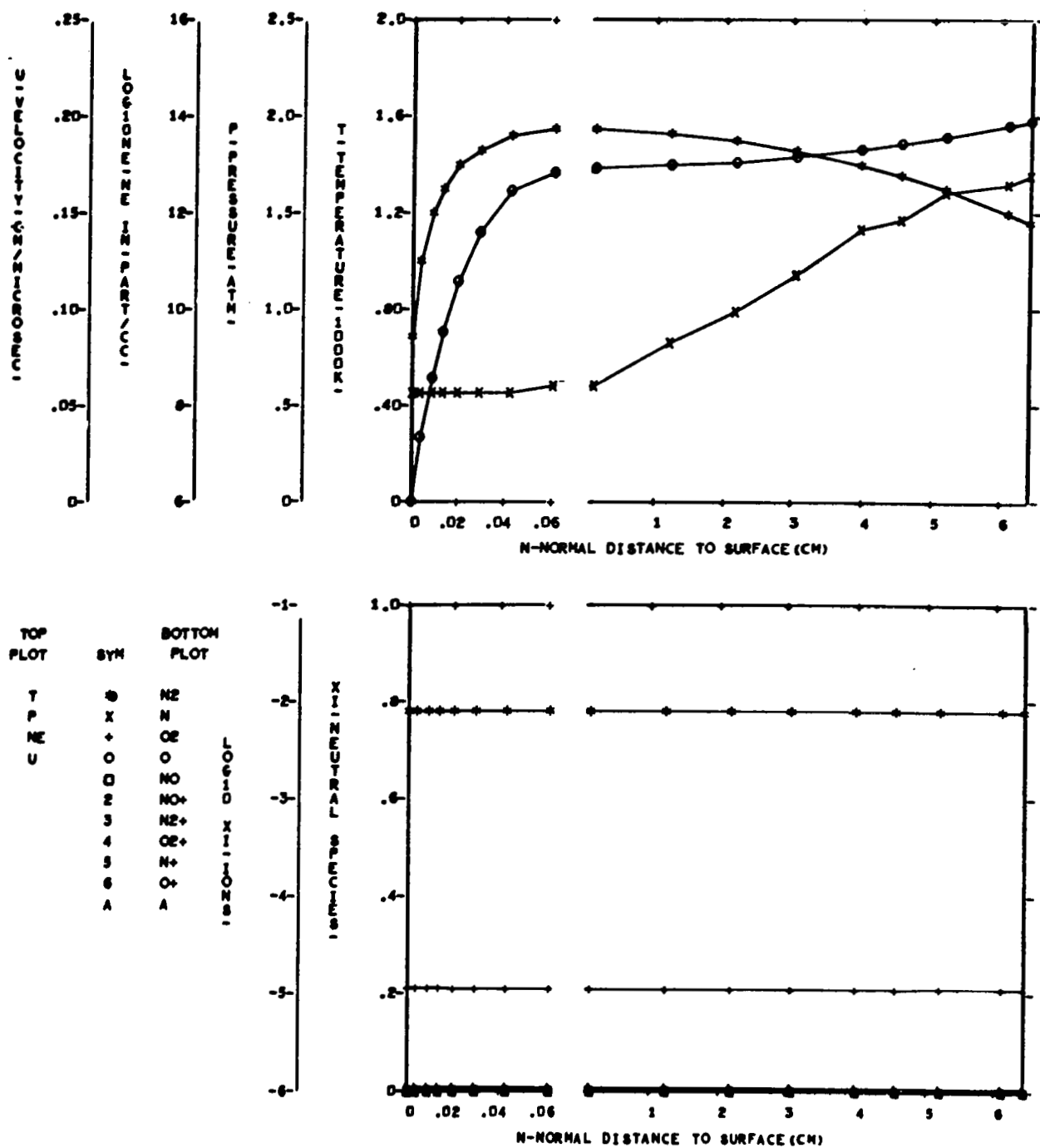
FIGURE 17 EQUILIBRIUM FLOW FIELD PROPERTIES - CASE 1, NORMAL 6
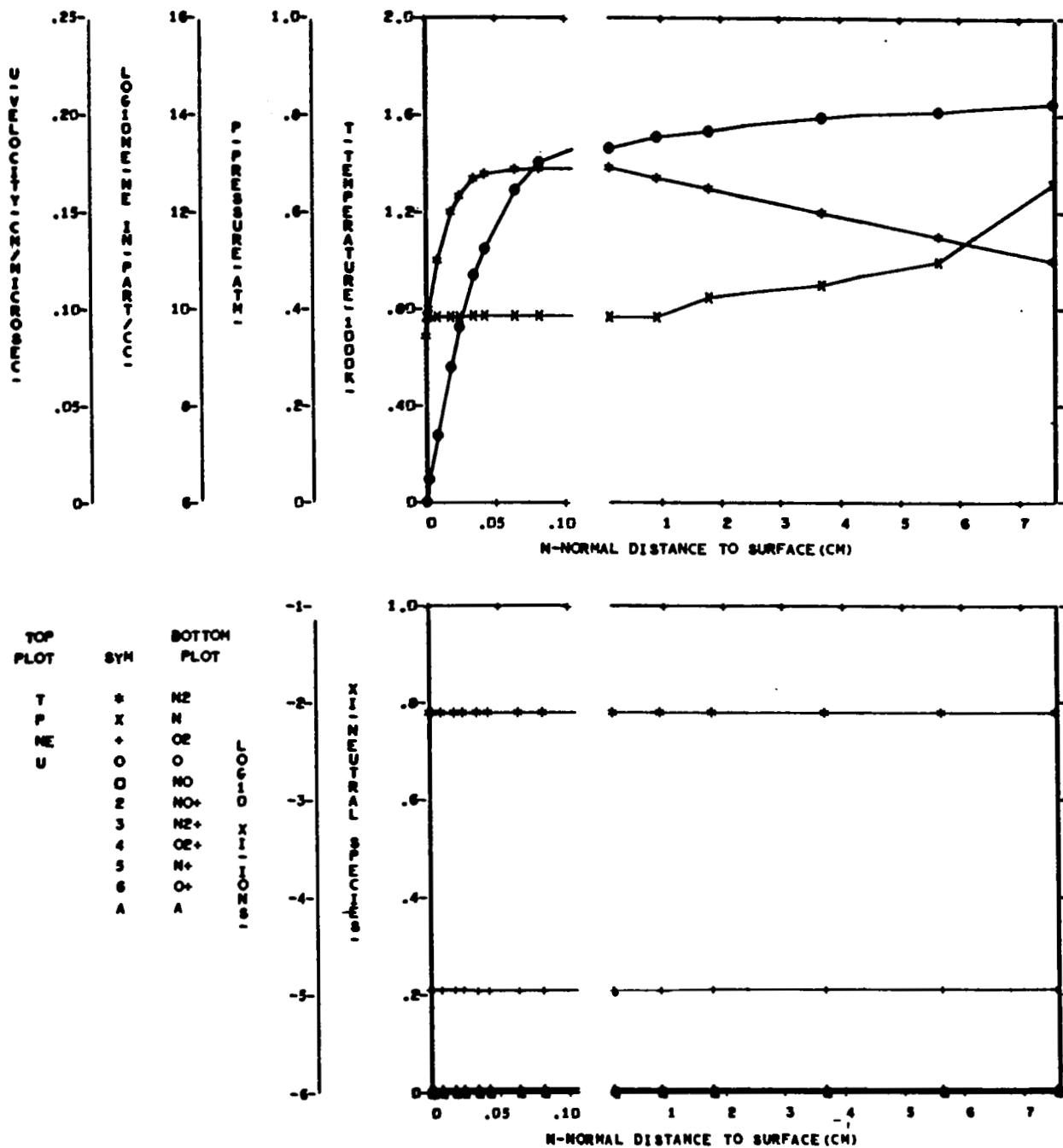
FIGURE 18 EQUILIBRIUM FLOW FIELD PROPERTIES - CASE 1, NORMAL 7
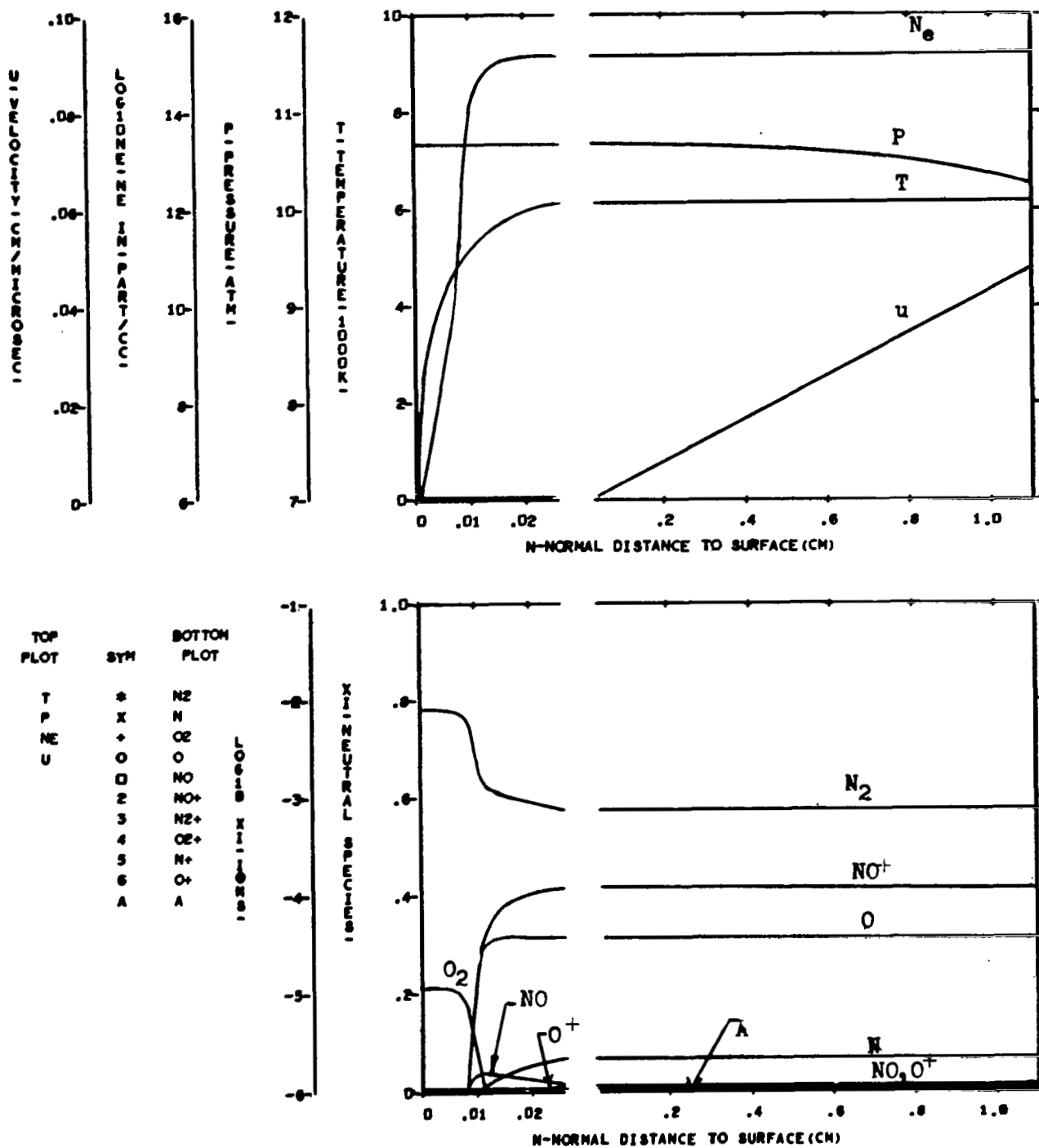
FIGURE 19 EQUILIBRIUM FLOW FIELD PROPERTIES - CASE 2, NORMAL 1

54
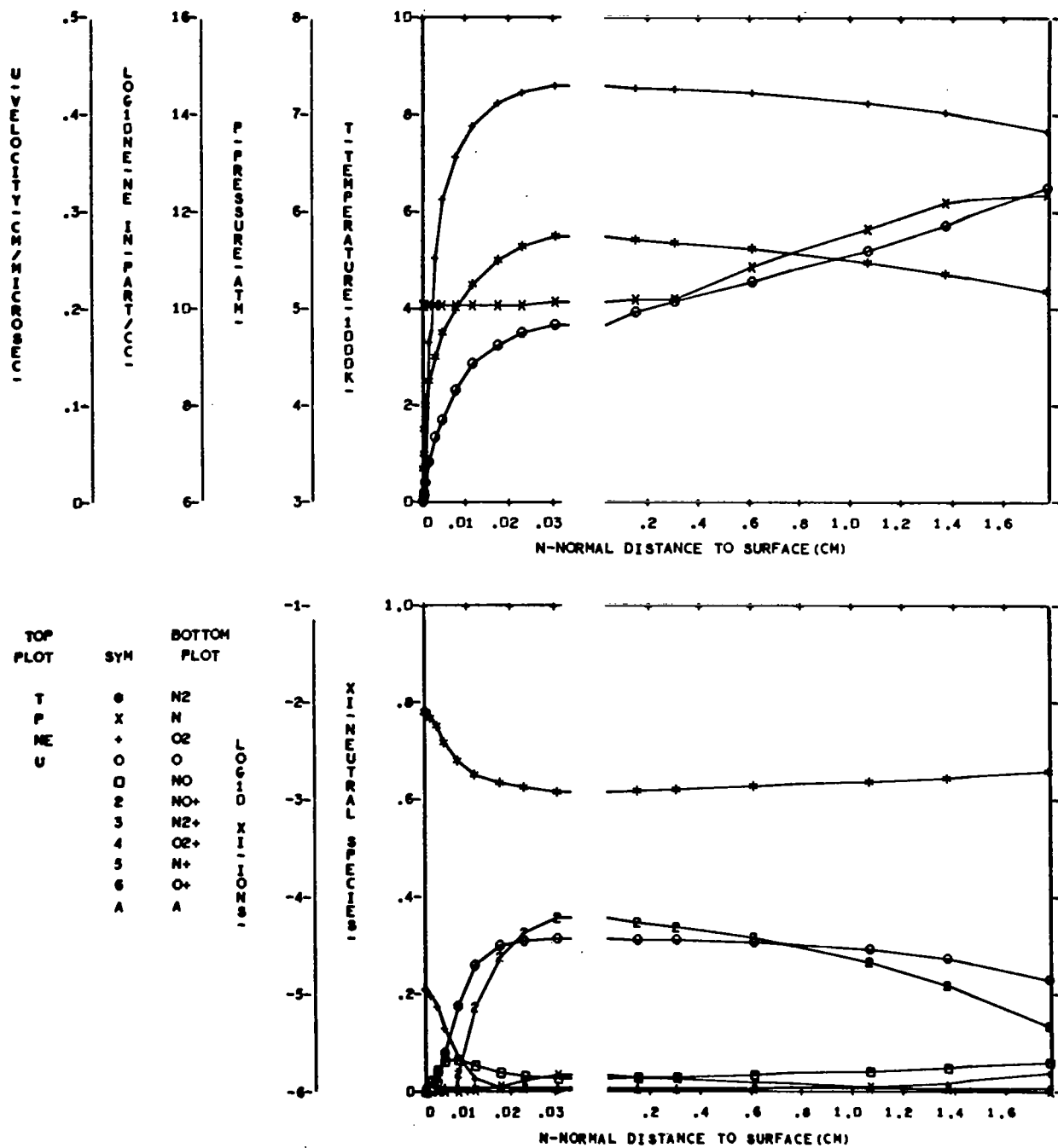
FIGURE 20 EQUILIBRIUM FLOW FIELD PROPERTIES – CASE 2, NORMAL 4
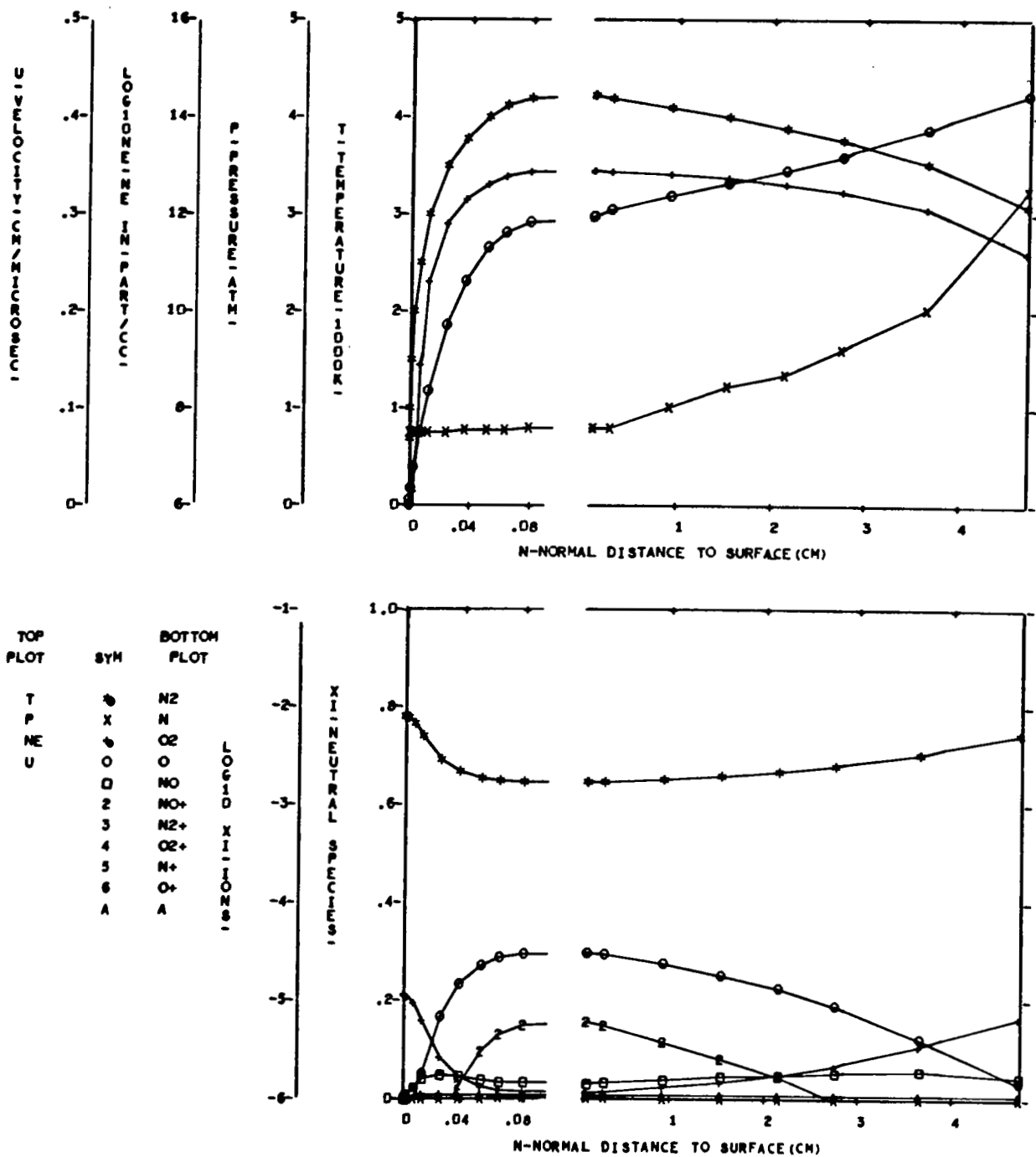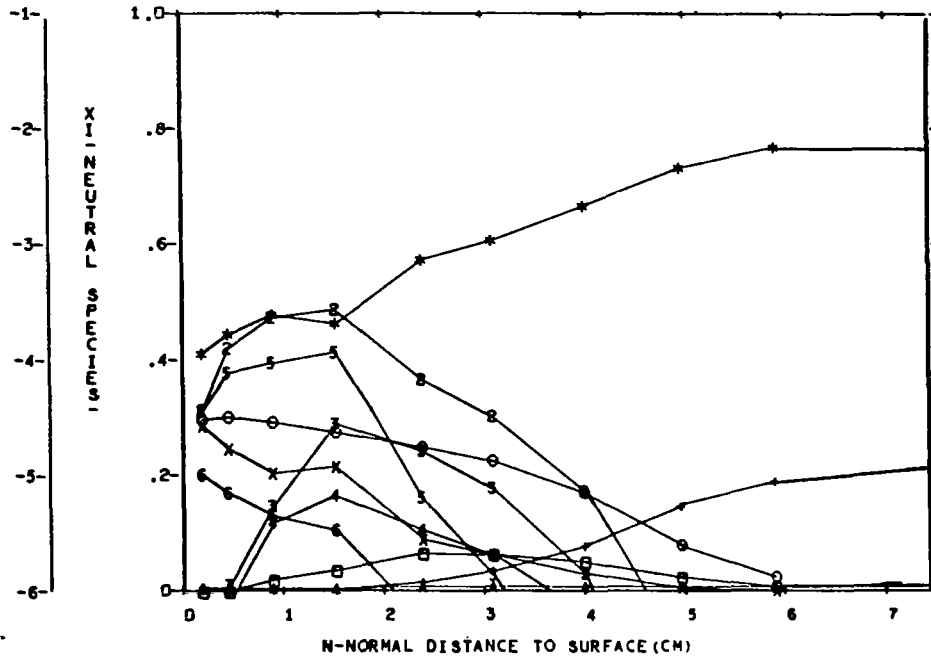
FIGURE 21 EQUILIBRIUM FLOW FIELD PROPERTIES - CASE 2, NORMAL 6
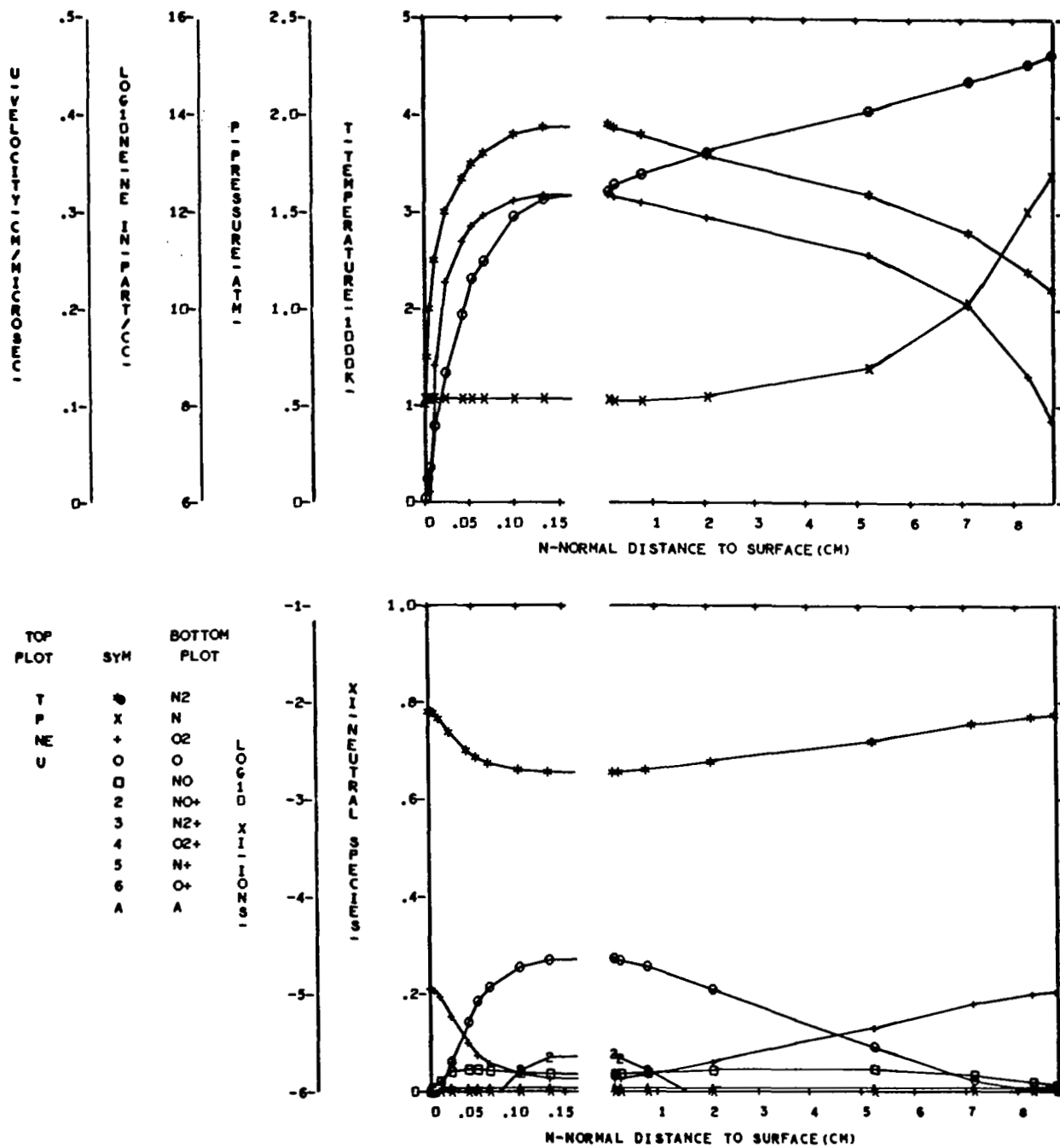
FIGURE 22 EQUILIBRIUM FLOW FIELD PROPERTIES - CASE 2, NORMAL 7
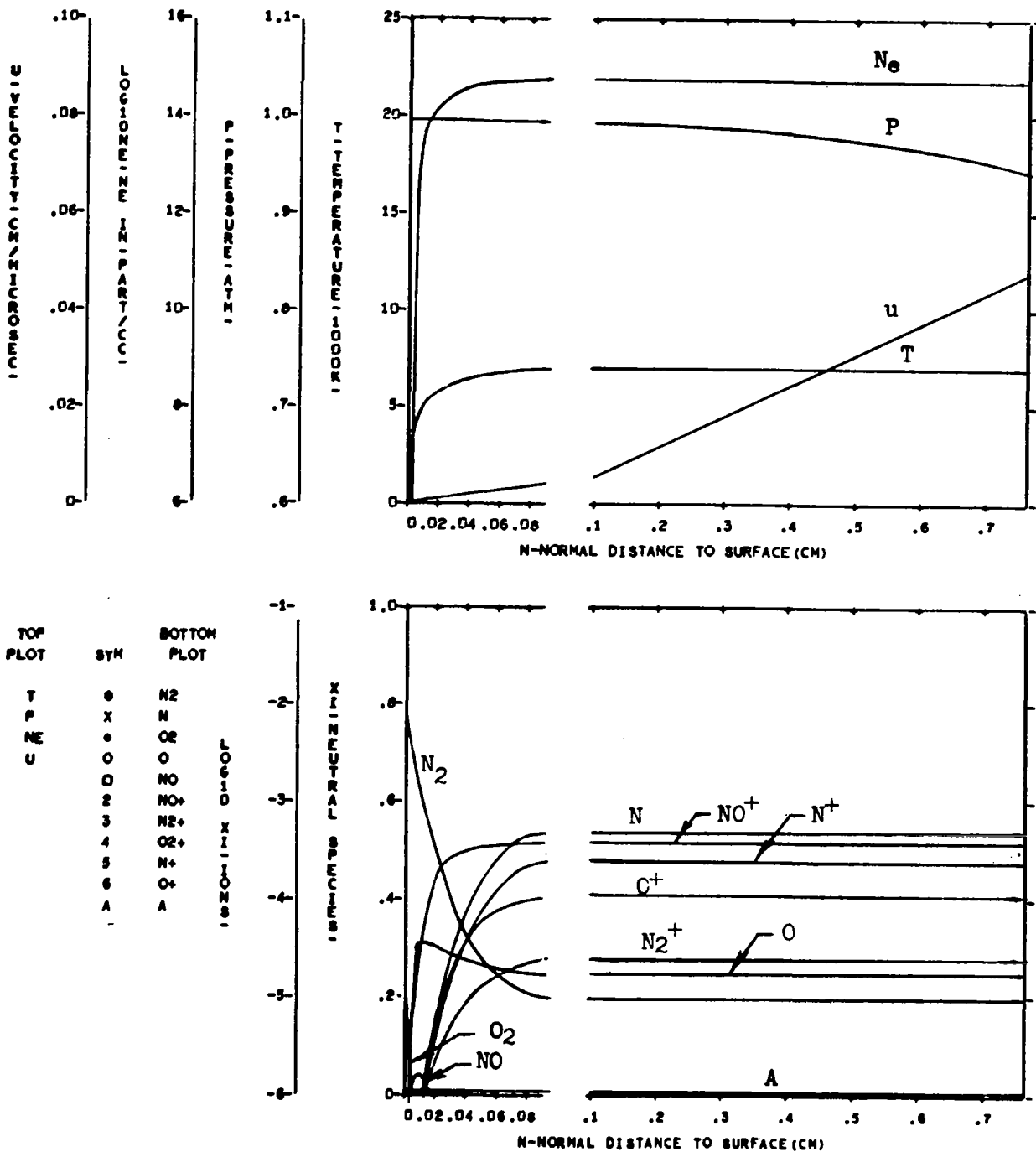
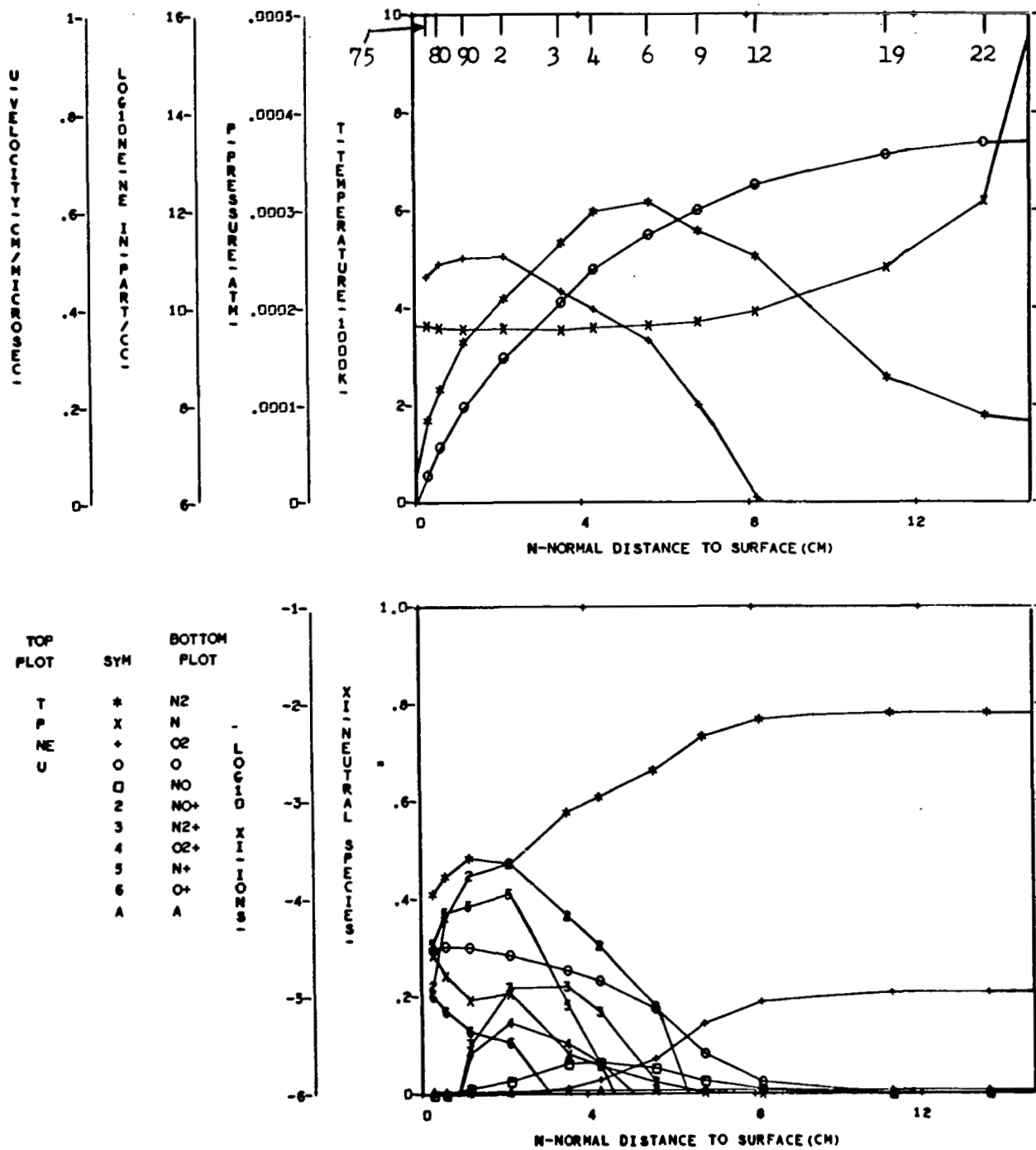FIGURE 23   EQUILIBRIUM FLOW FIELD PROPERTIES - CASE 3, NORMAL 1
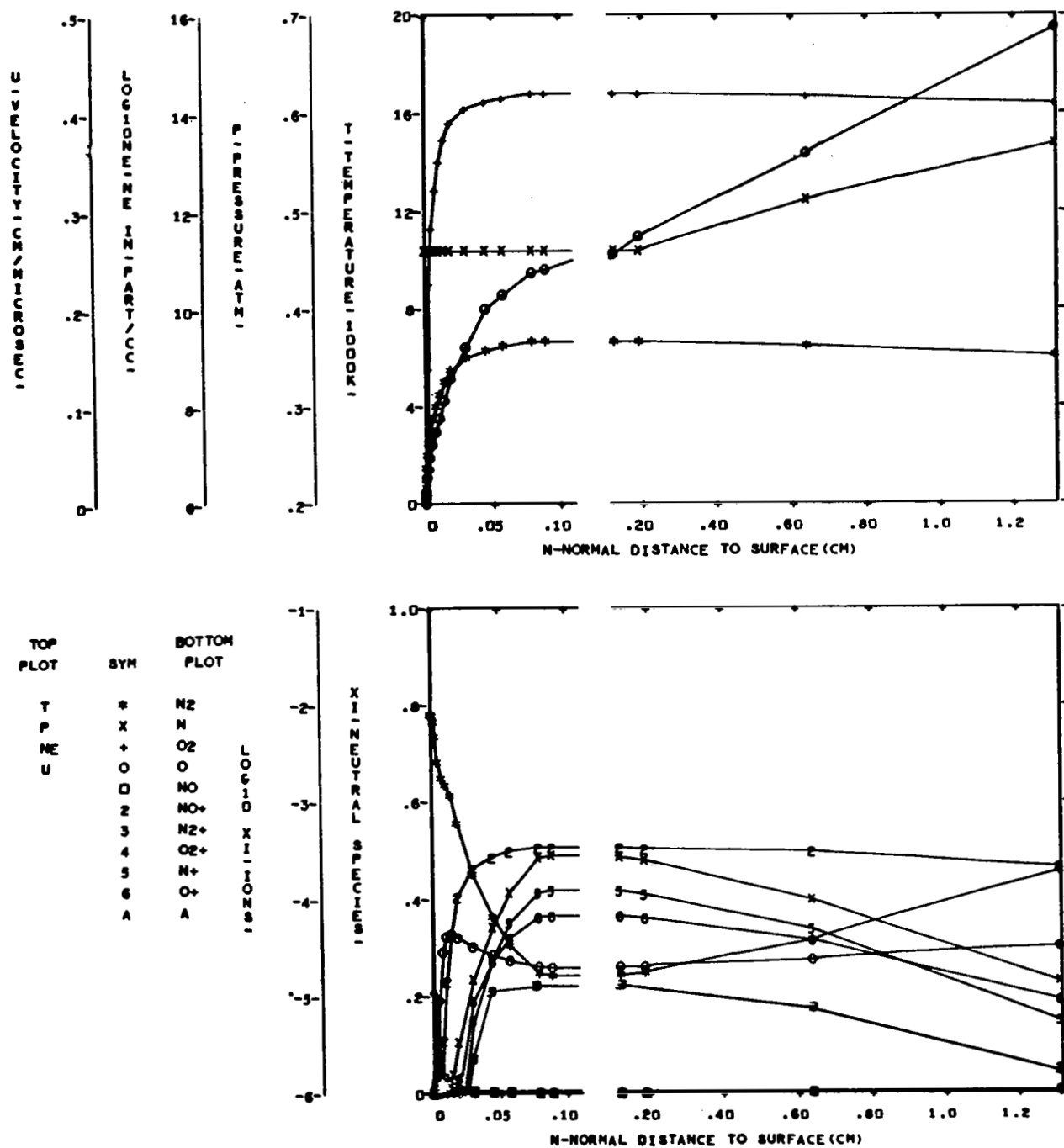
FIGURE 24 EQUILIBRIUM FLOW FIELD PROPERTIES - CASE 3, NORMAL 4

FIGURE 25 EQUILIBRIUM FLOW FIELD PROPERTIES - CASE 3, NORMAL 6
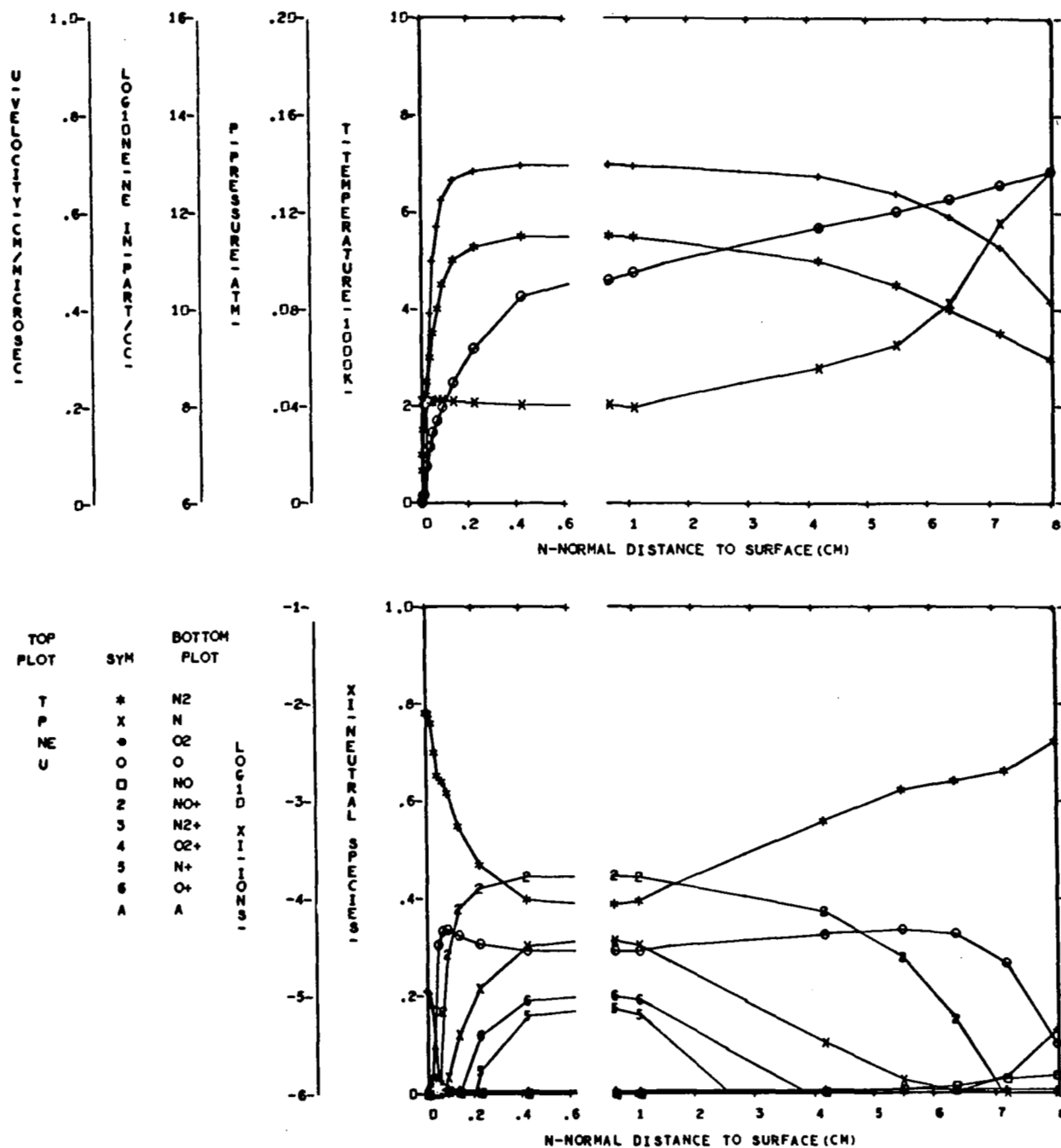
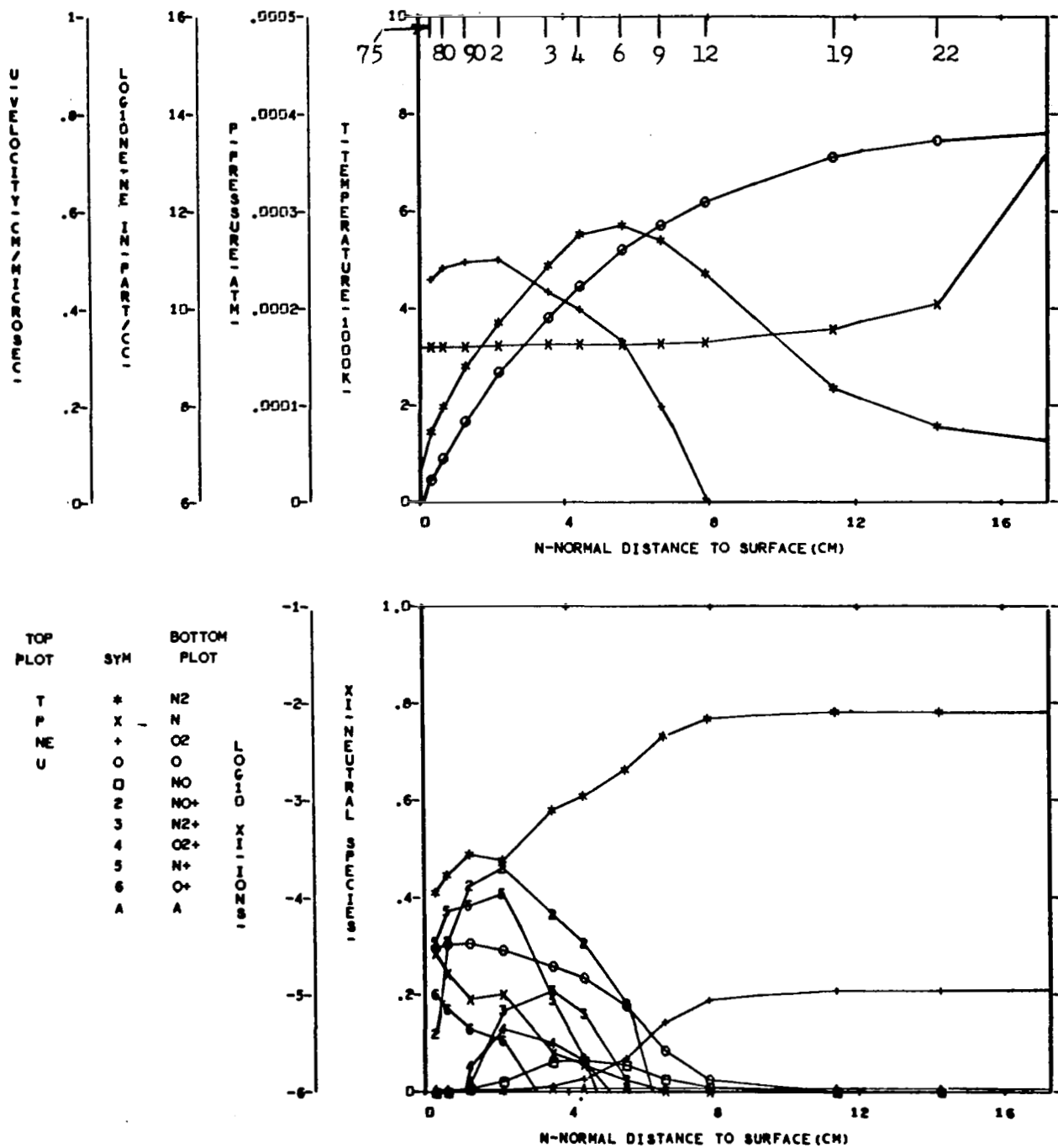FIGURE 26 EQUILIBRIUM FLOW FIELD PROPERTIES - CASE 3, NORMAL 7

61
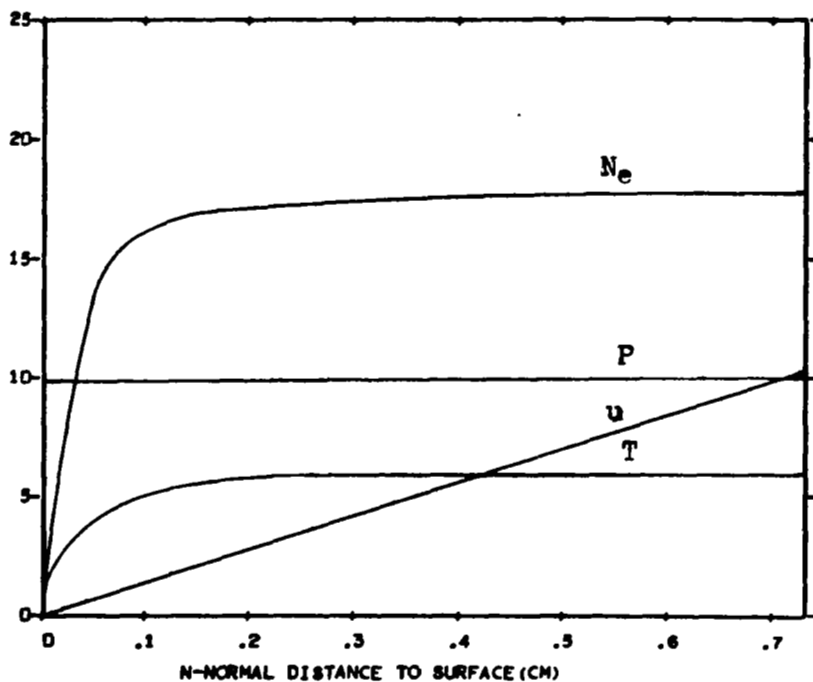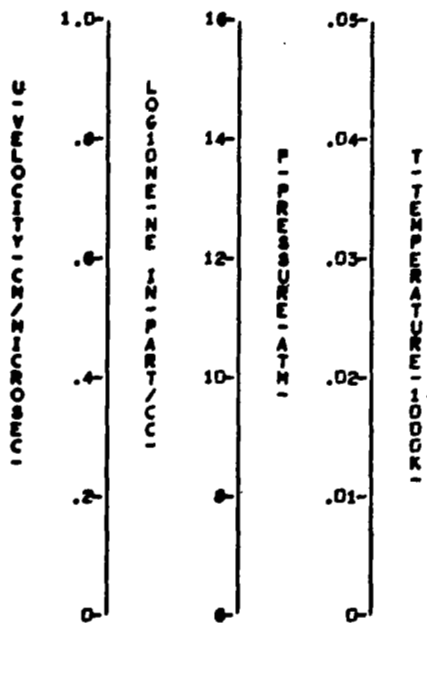
FIGURE 27 EQUILIBRIUM FLOW FIELD PROPERTIES - CASE 4, NORMAL 1
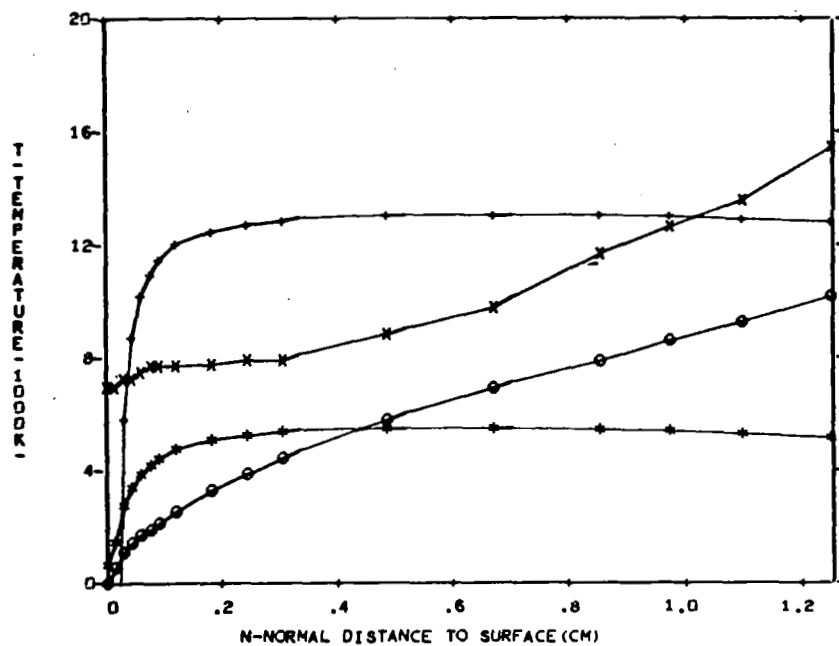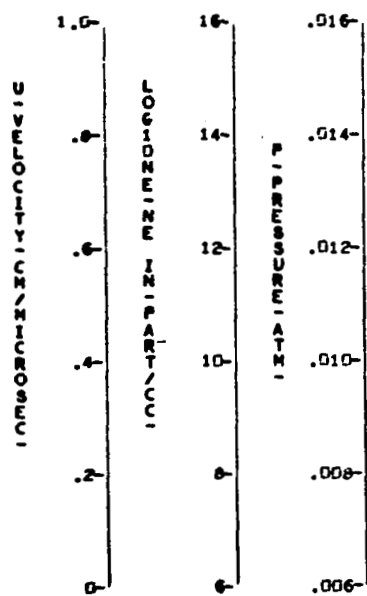
FIGURE 28 EQUILIBRIUM FLOW FIELD PROPERTIES - CASE 4, NORMAL 4

63
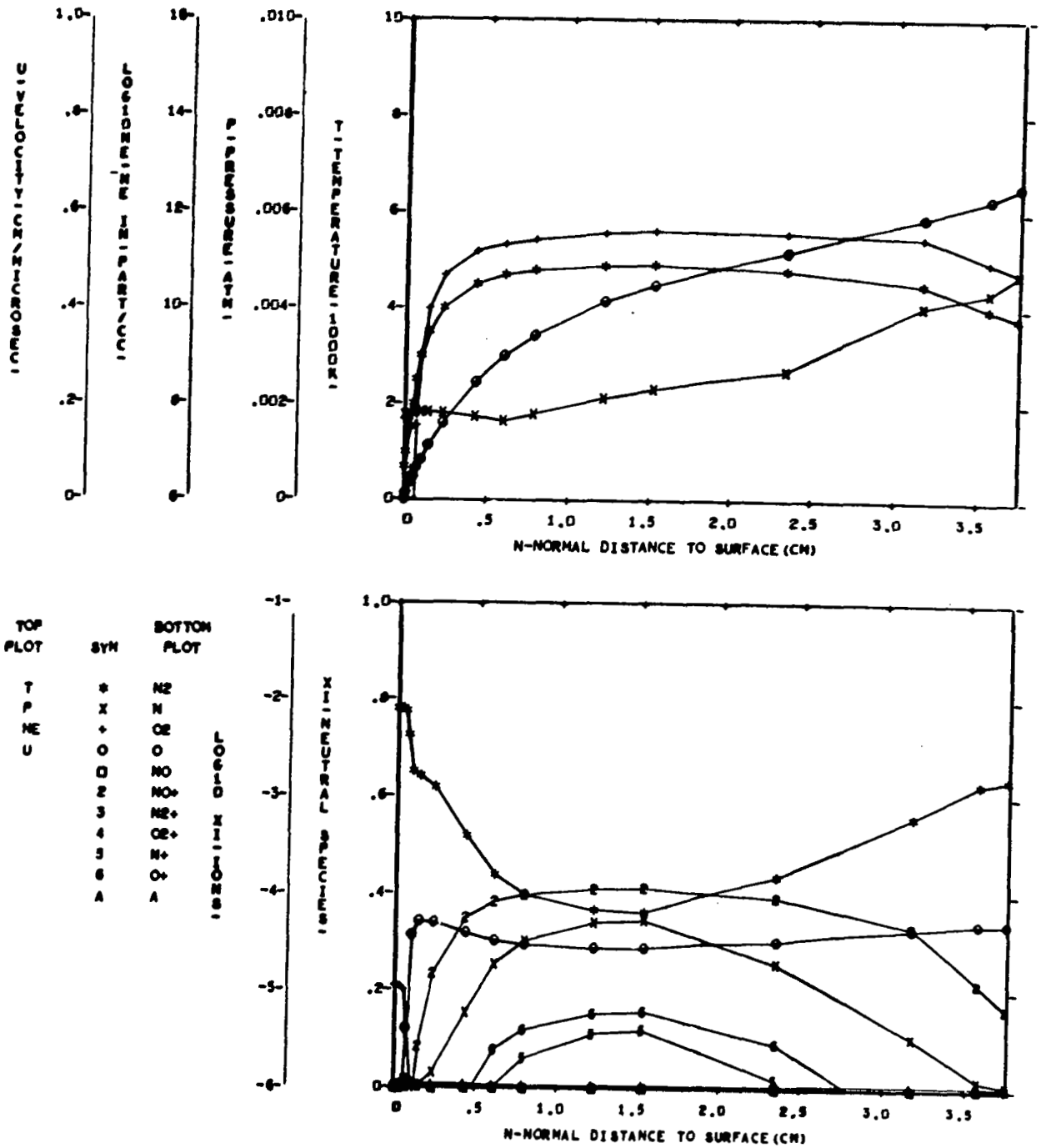
FIGURE 29 EQUILIBRIUM FLOW FIELD PROPERTIES - CASE 4, NORMAL 6
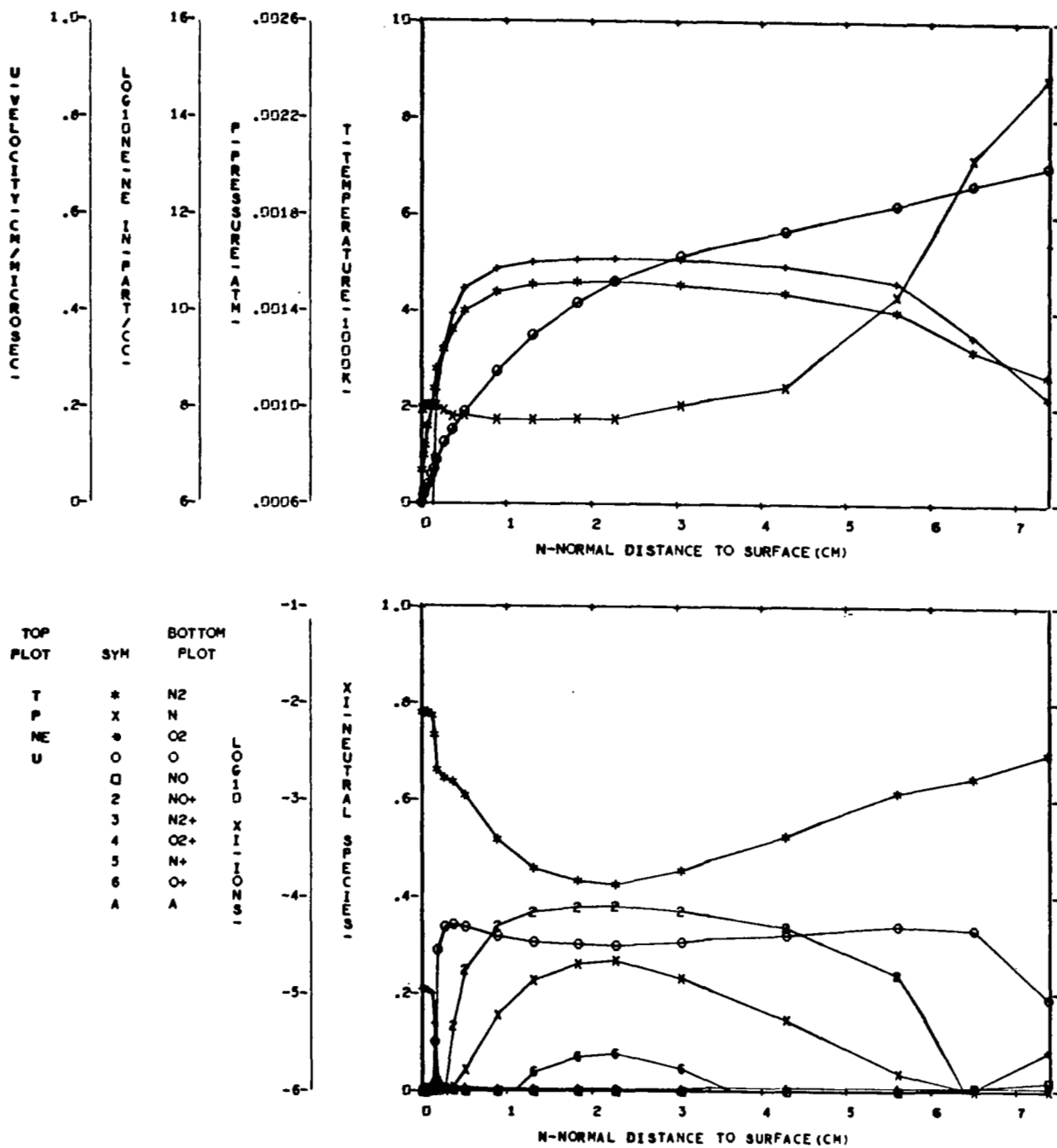
FIGURE 30   EQUILIBRIUM FLOW FIELD PROPERTIES - CASE 4, NORMAL 7
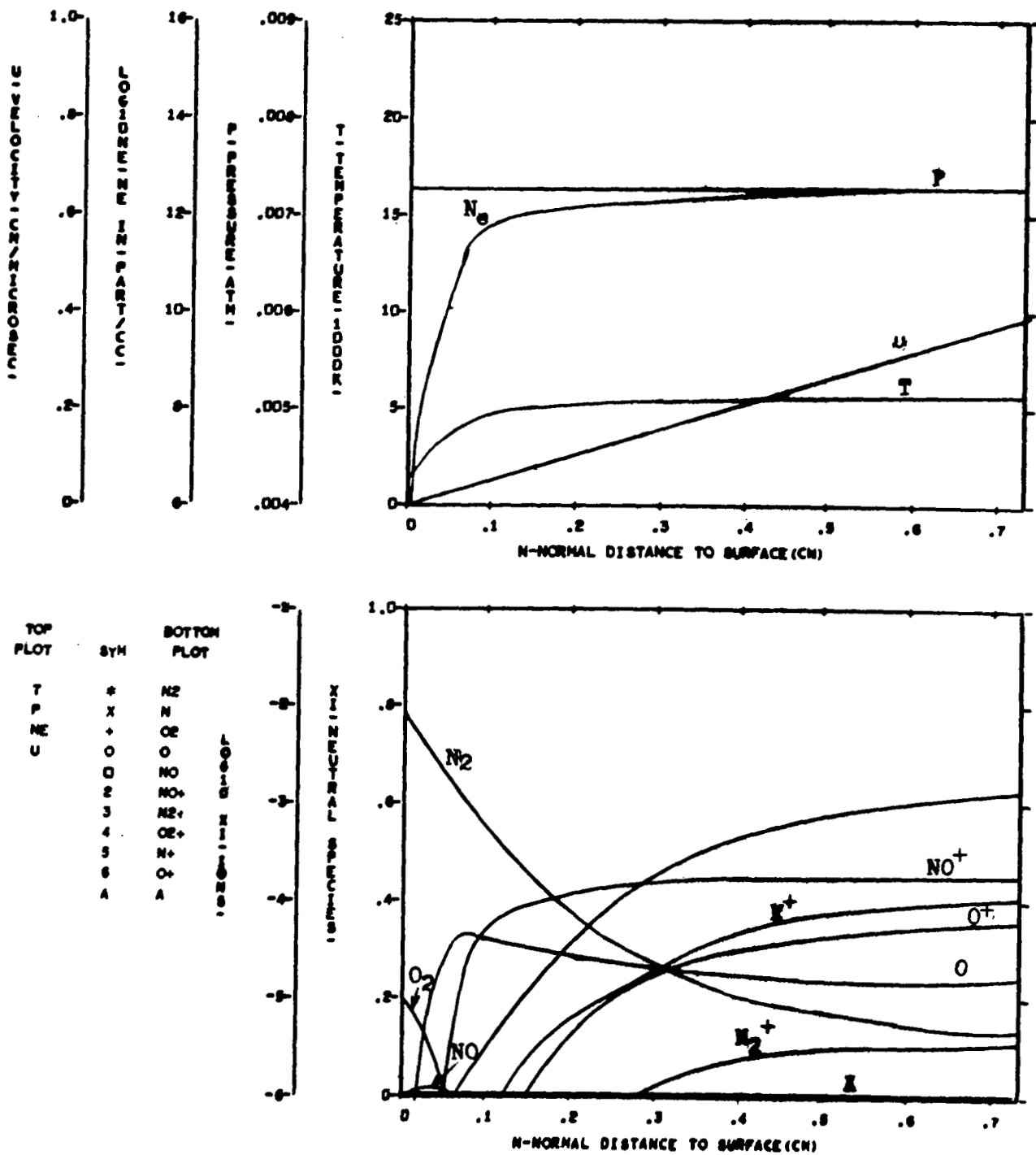
FIGURE 31 EQUILIBRIUM FLOW FIELD PROPERTIES - CASE 5, NORMAL 1
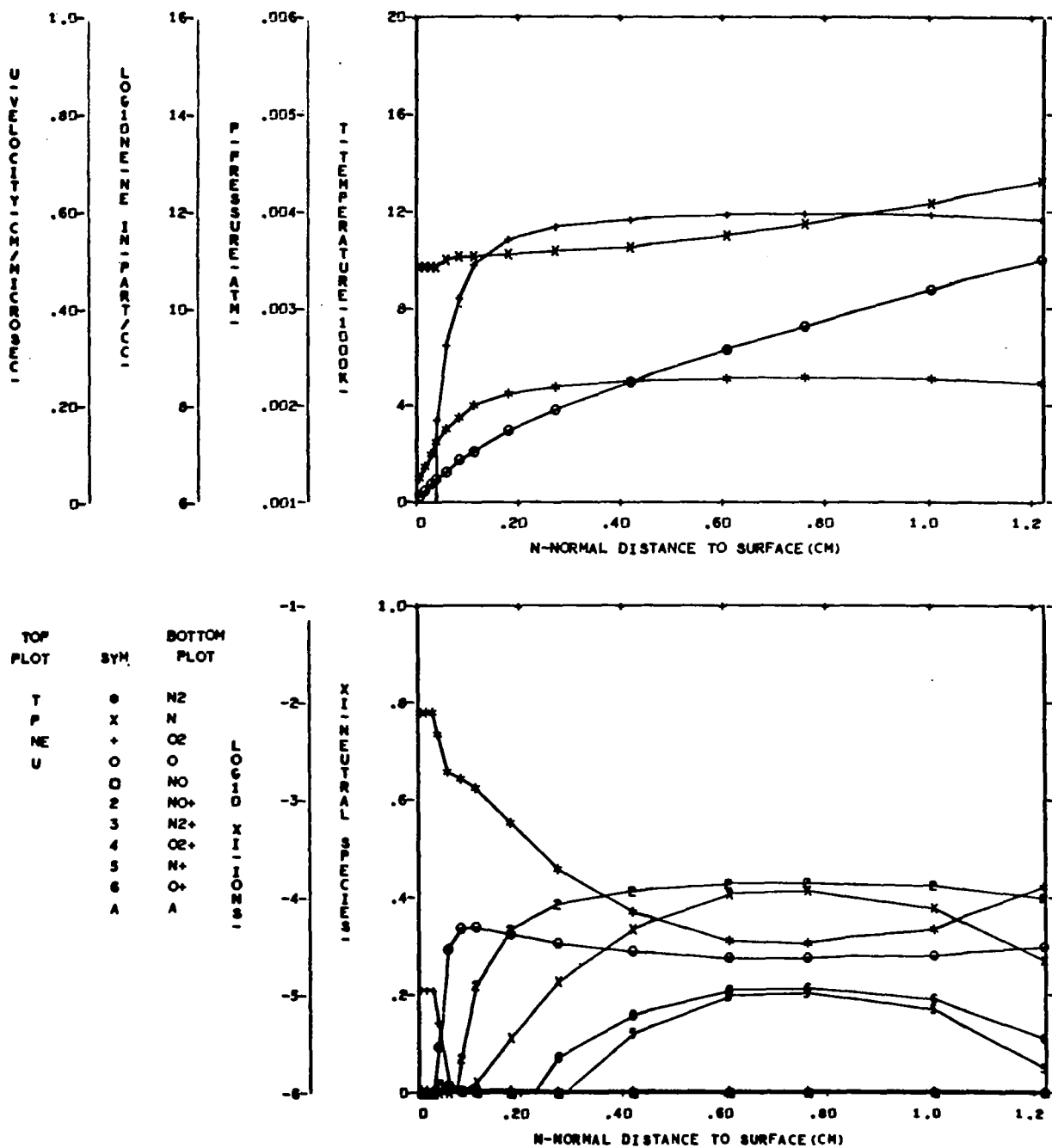
FIGURE 32 EQUILIBRIUM FLOW FIELD PROPERTIES - CASE 5, NORMAL 4
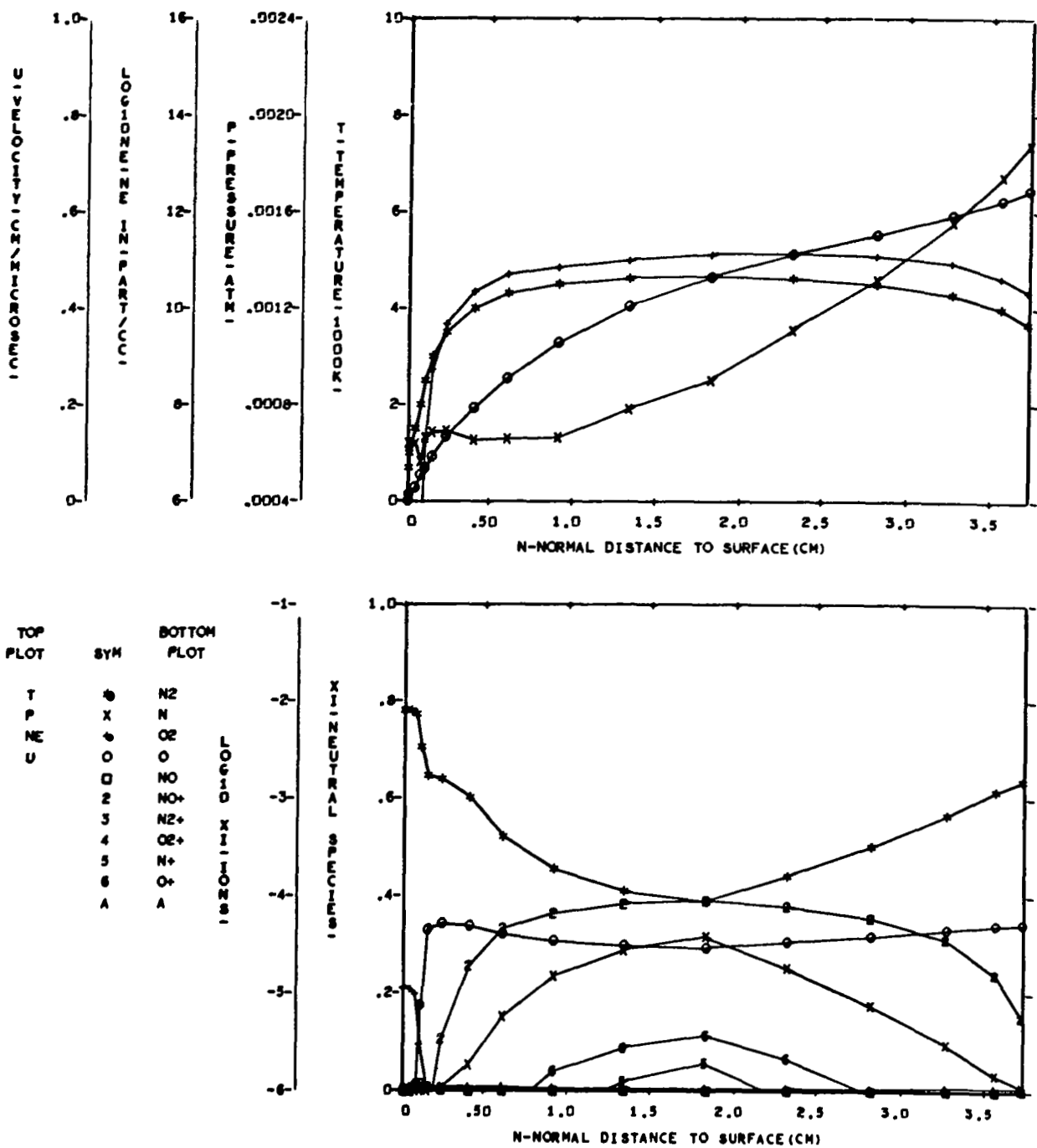
FIGURE 33 EQUILIBRIUM FLOW FIELD PROPERTIES - CASE 5, NORMAL 6

68
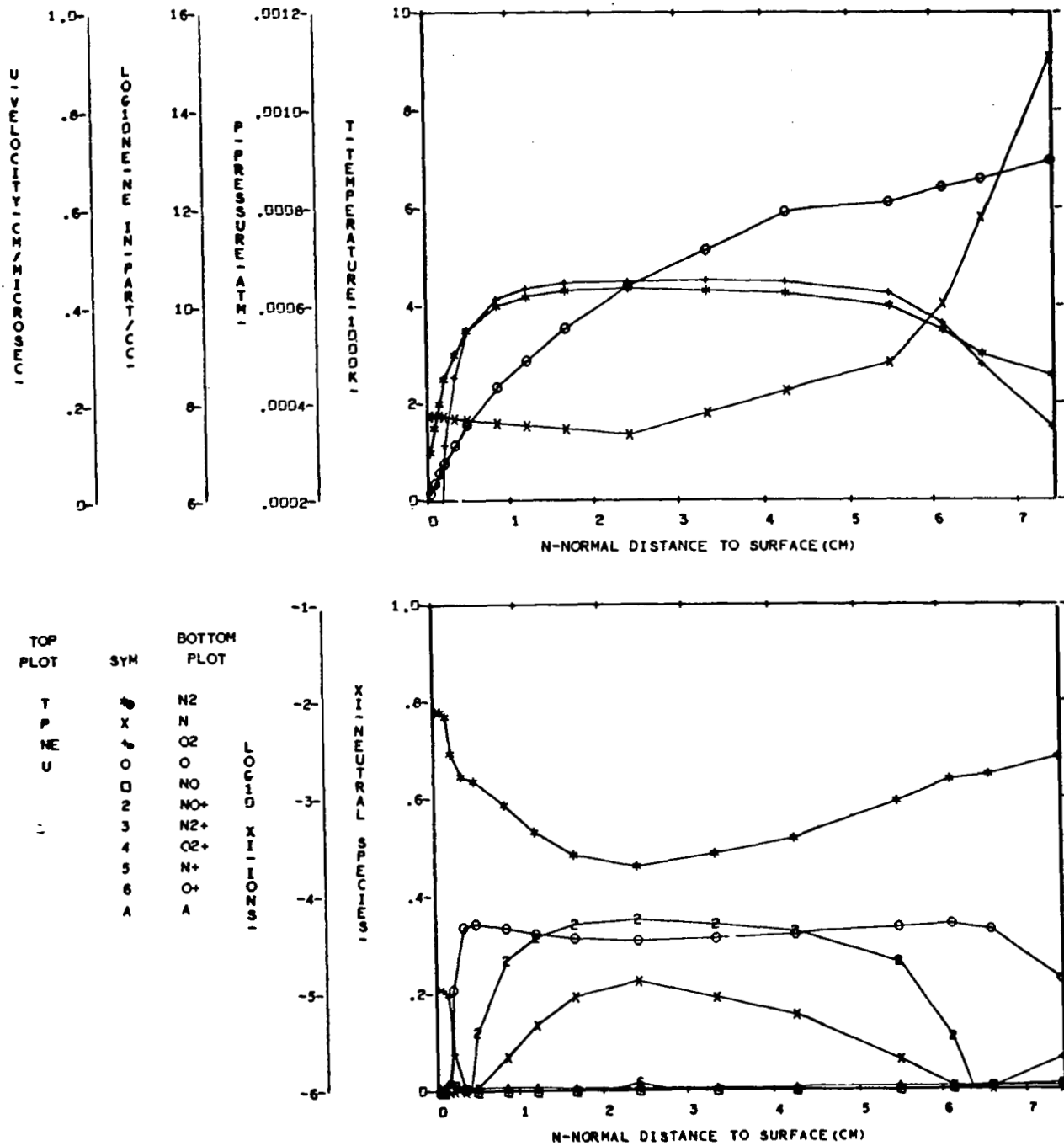
FIGURE 34   EQUILIBRIUM FLOW FIELD PROPERTIES - CASE 5, NORMAL 7
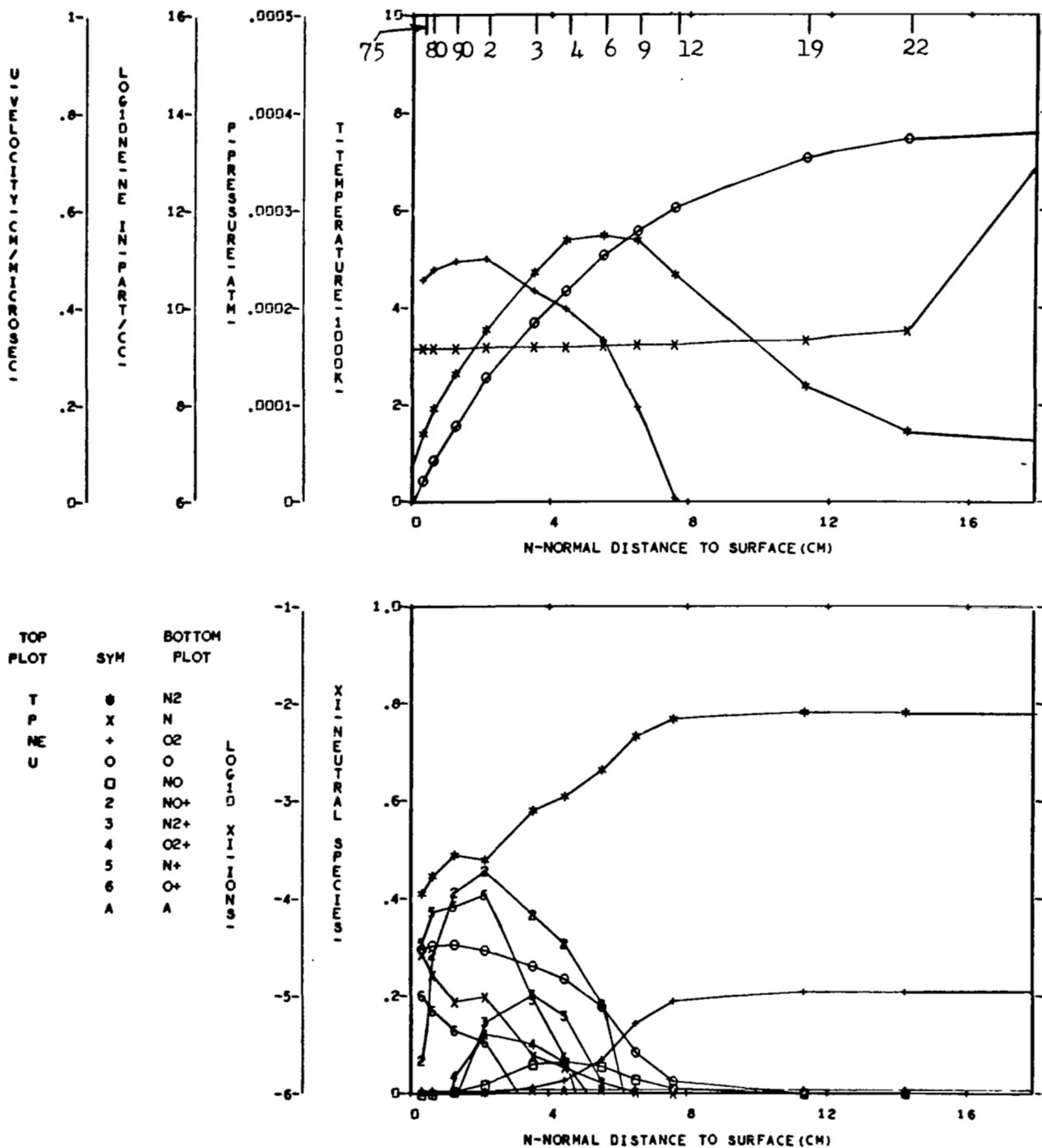
69
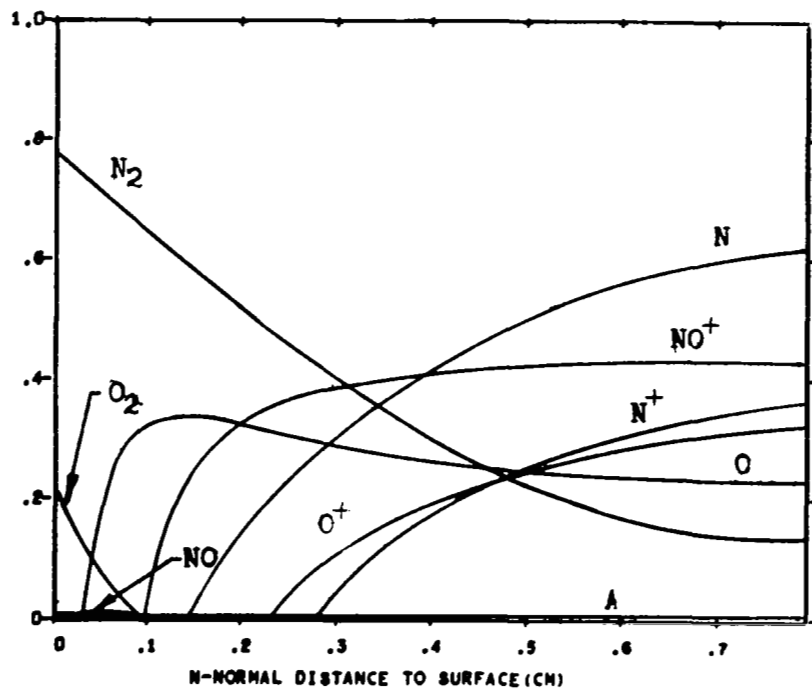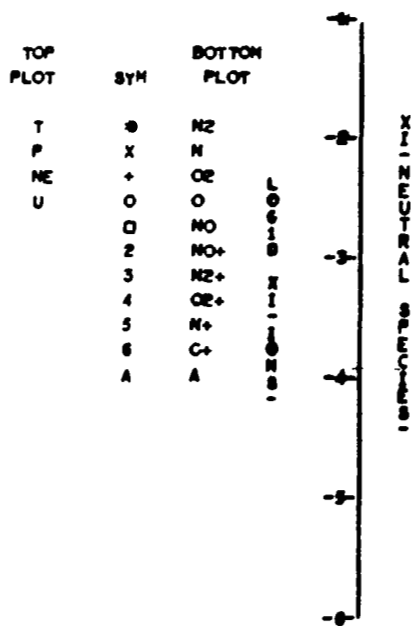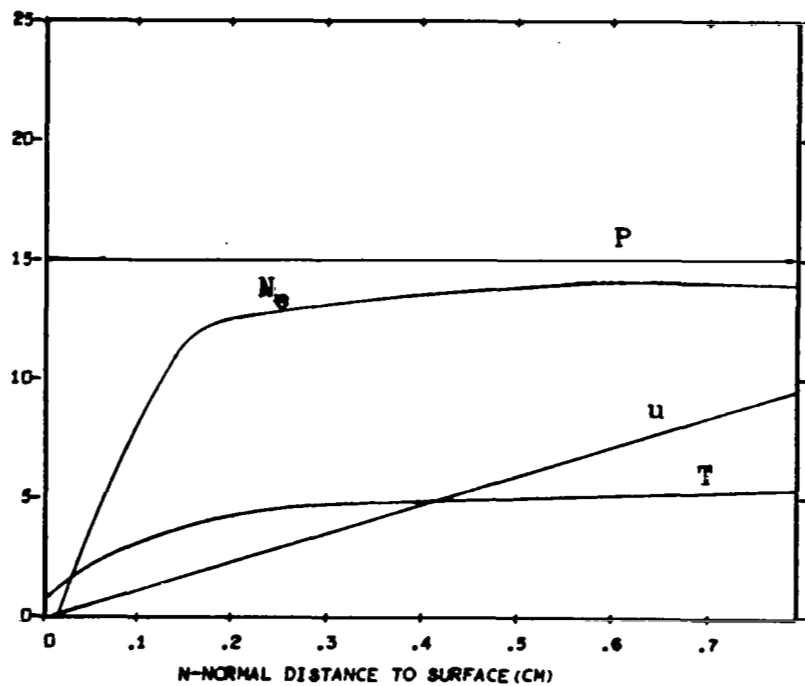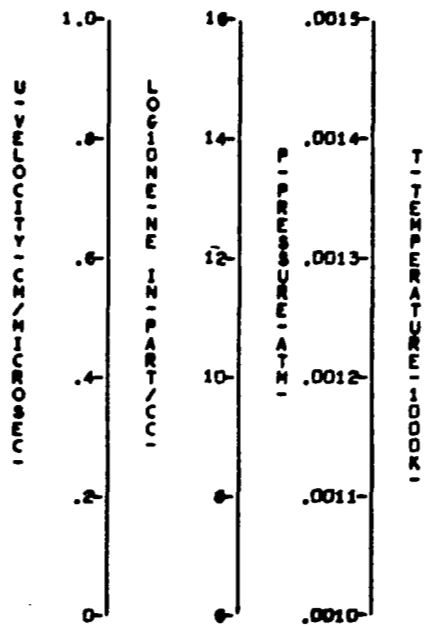
FIGURE 35 EQUILIBRIUM FLOW FIELD PROPERTIES - CASE 6, NORMAL 1
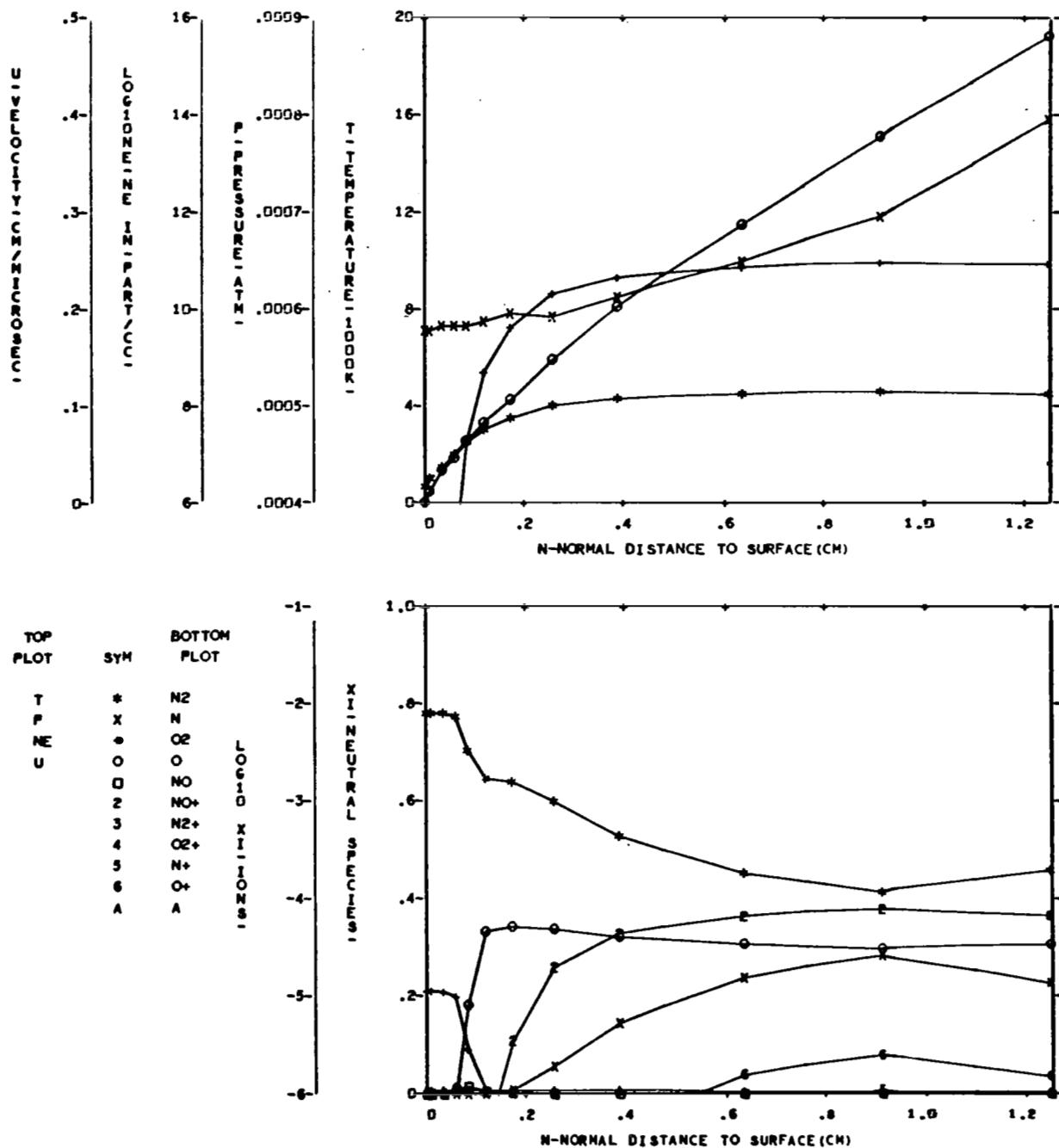
FIGURE 36 EQUILIBRIUM FLOW FIELD PROPERTIES - CASE 6, NORMAL 4

71
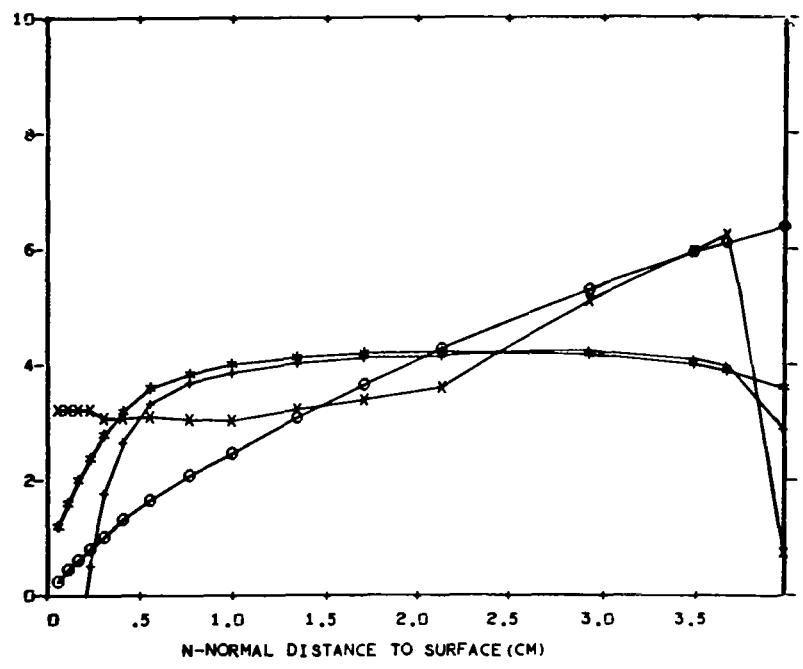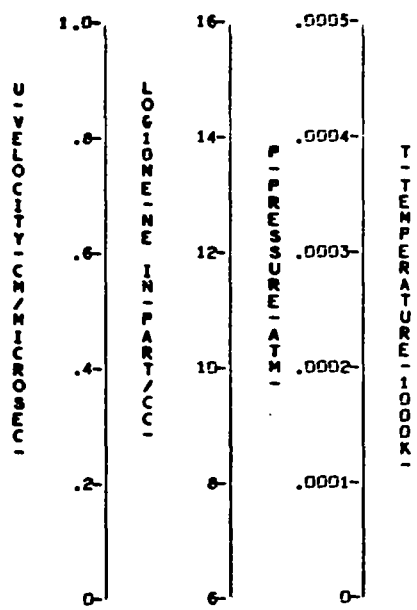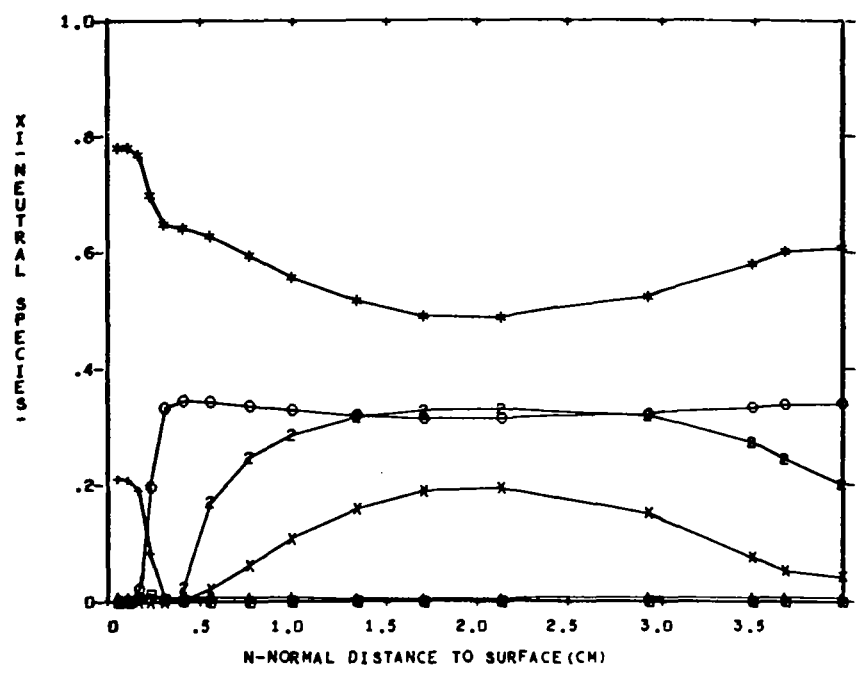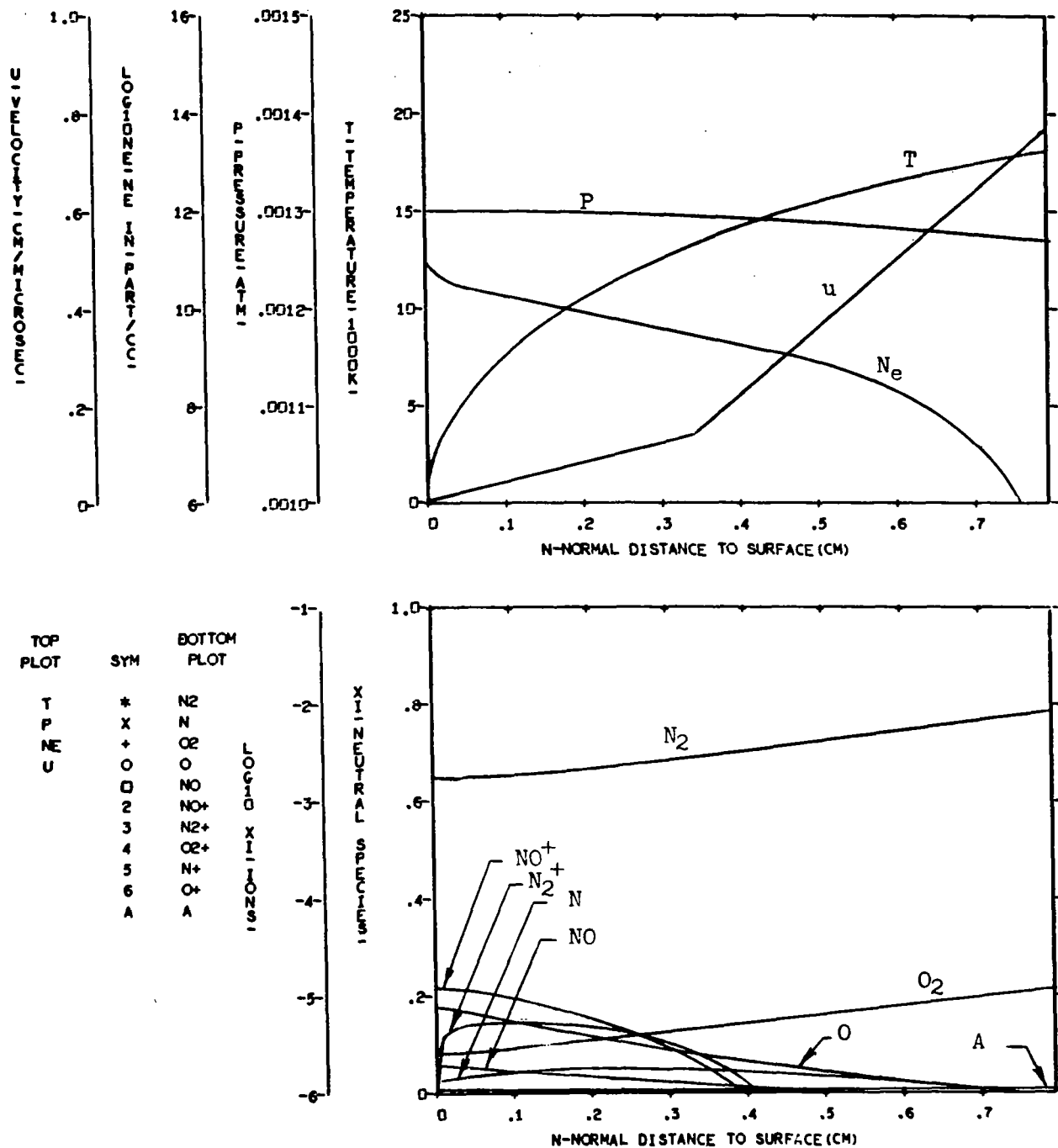
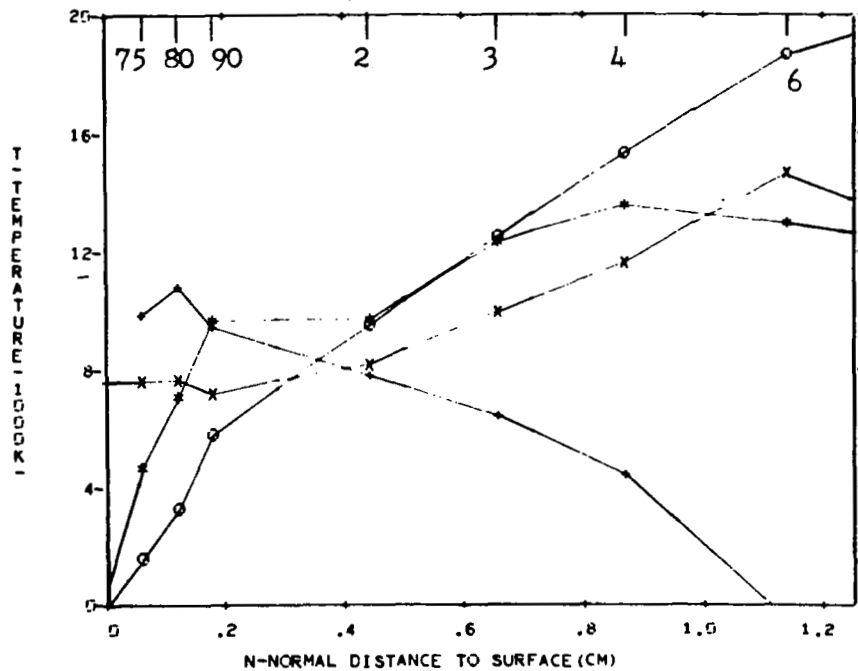FIGURE 37 EQUILIBRIUM FLOW FIELD PROPERTIES - CASE 6, NORMAL 6
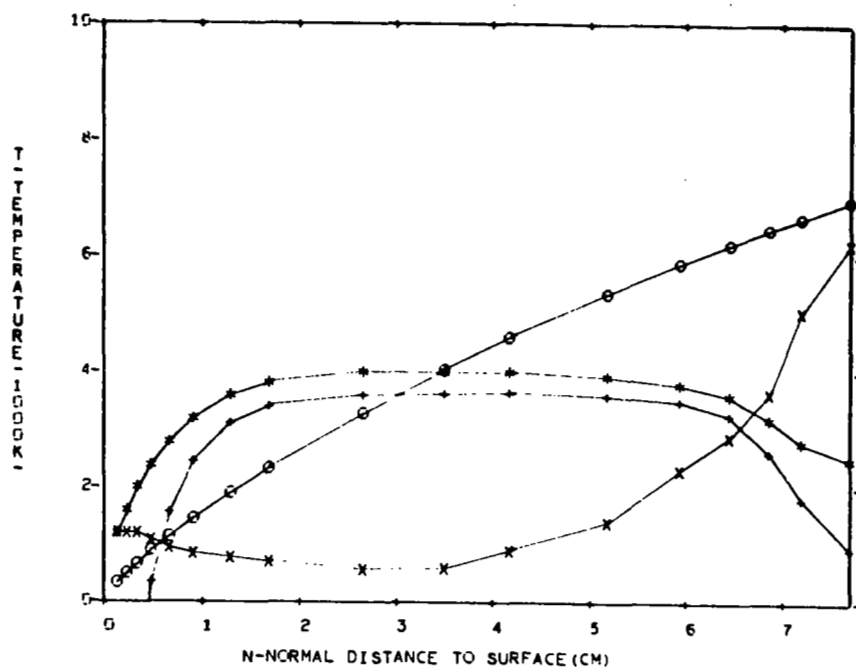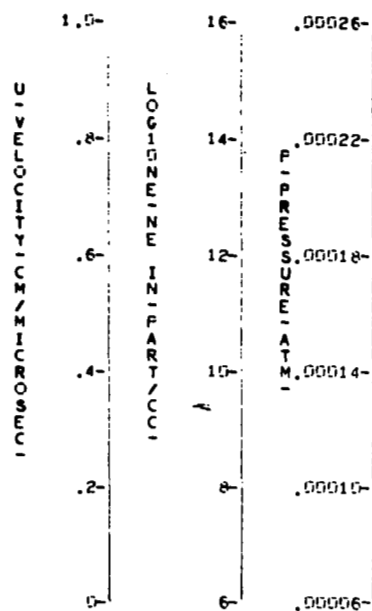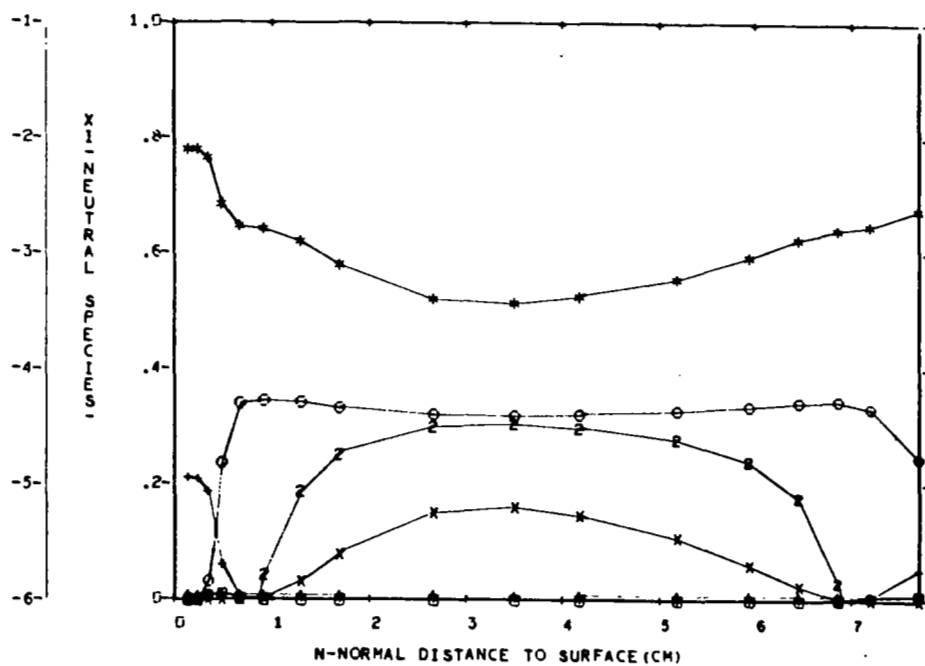
FIGURE 38 EQUILIBRIUM FLOW FIELD PROPERTIES - CASE 6, NORMAL 7

73
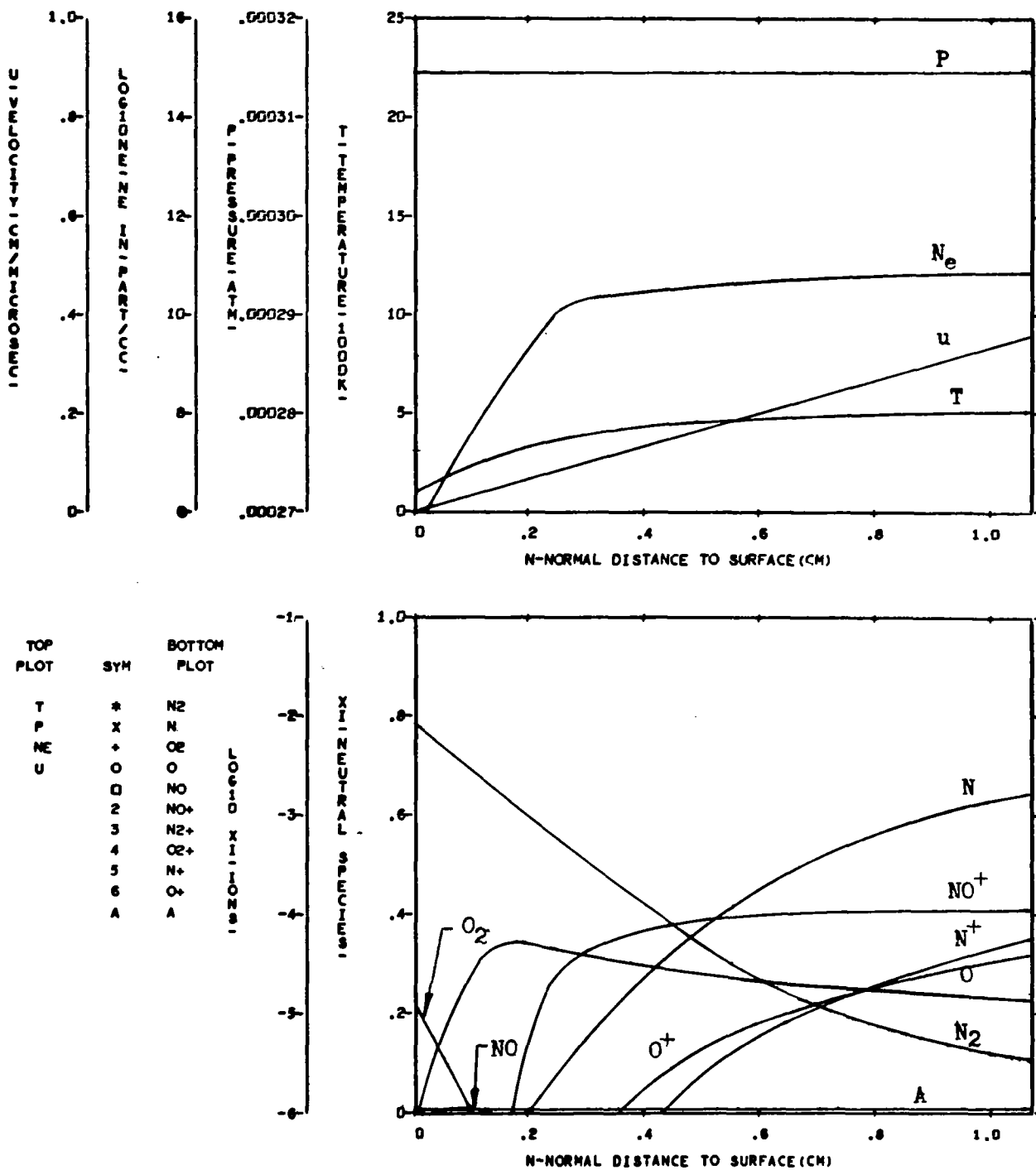
FIGURE 39   EQUILIBRIUM FLOW FIELD PROPERTIES - CASE 7, NORMAL 1

74
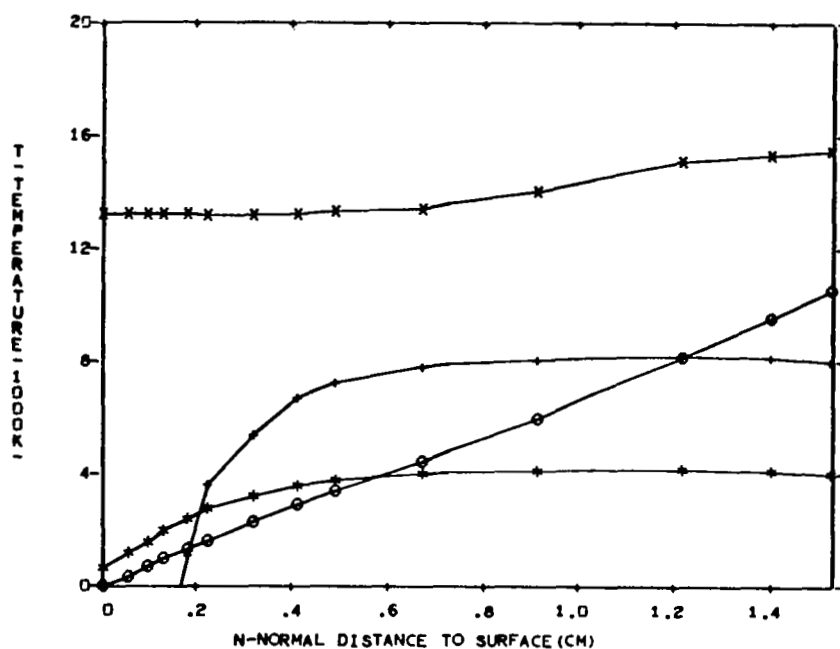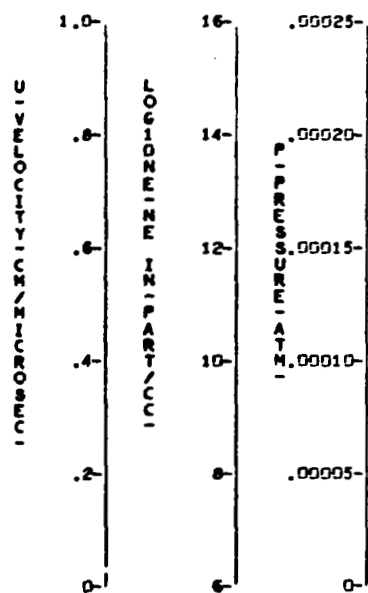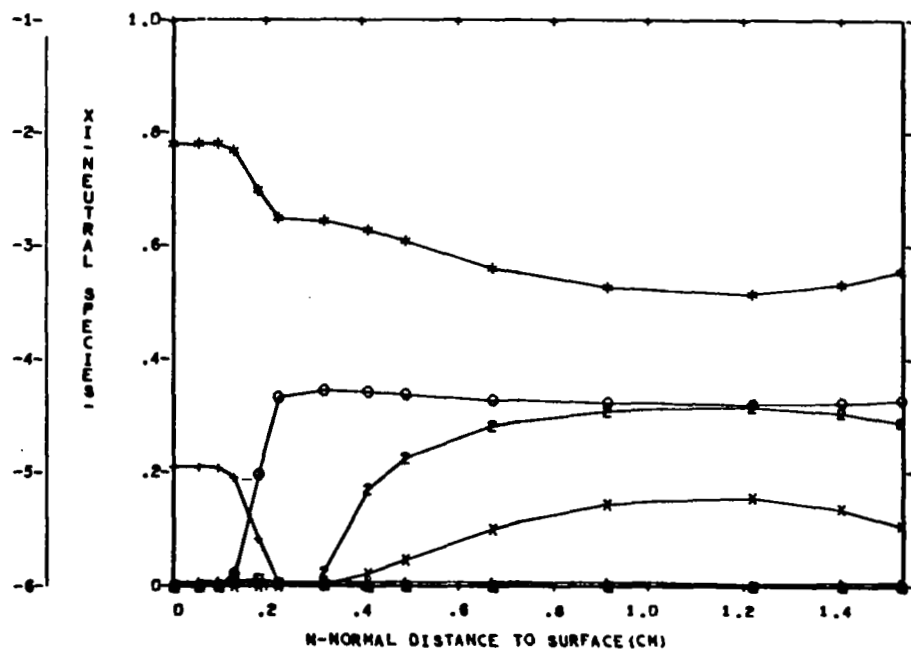
FIGURE 40 EQUILIBRIUM FLOW FIELD PROPERTIES - CASE 7, NORMAL 4
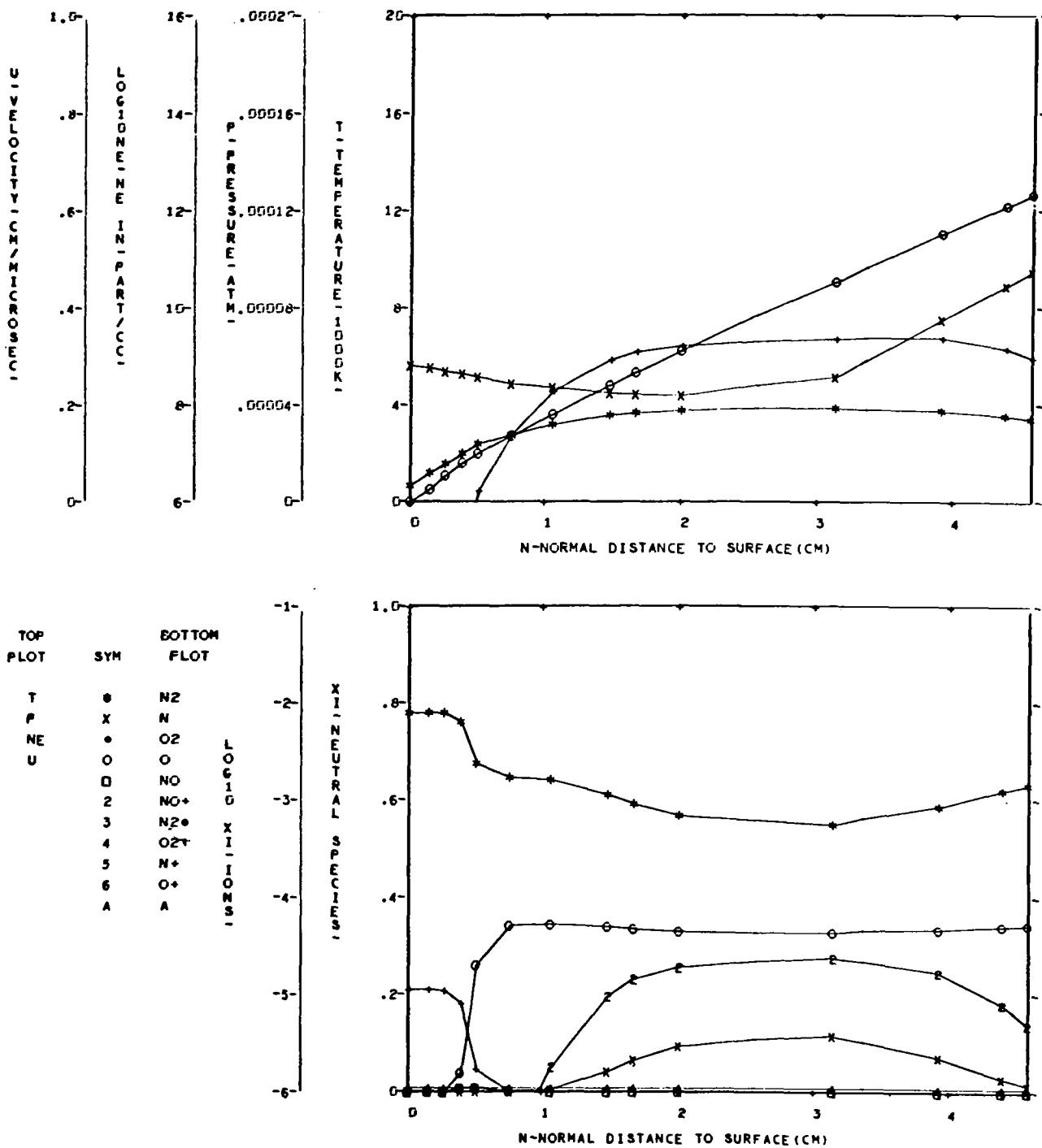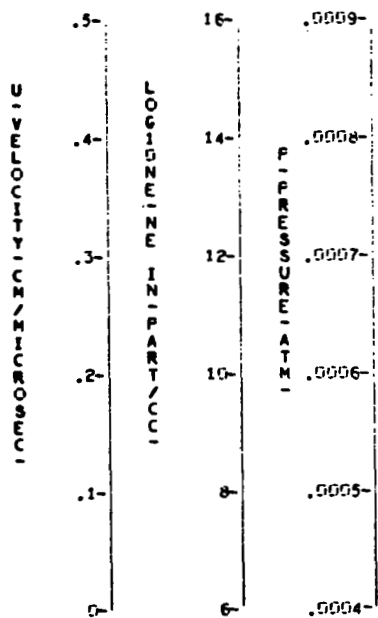
FIGURE 41 EQUILIBRIUM FLOW FIELD PROPERTIES - CASE 7, NORMAL 6
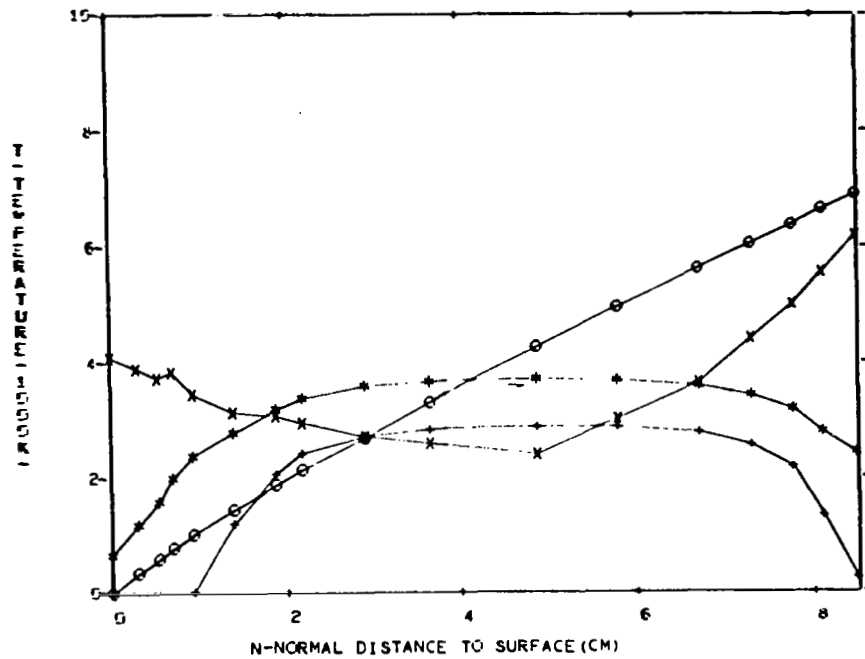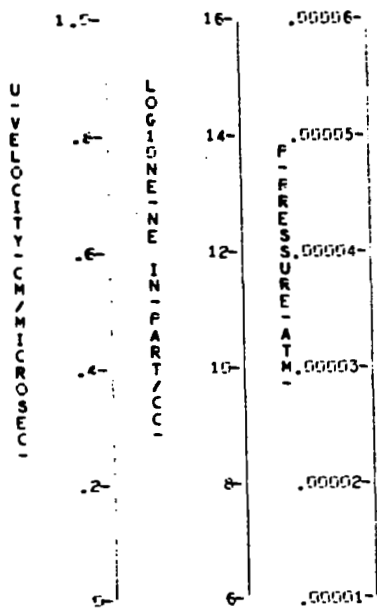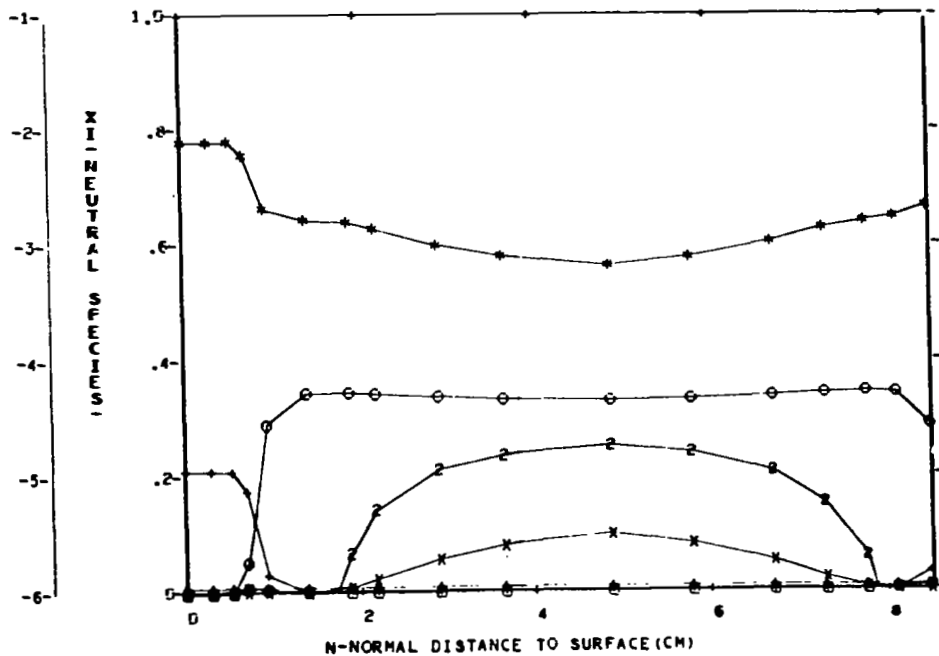
FIGURE 42 EQUILIBRIUM FLOW FIELD PROPERTIES - CASE 7, NORMAL 7

77
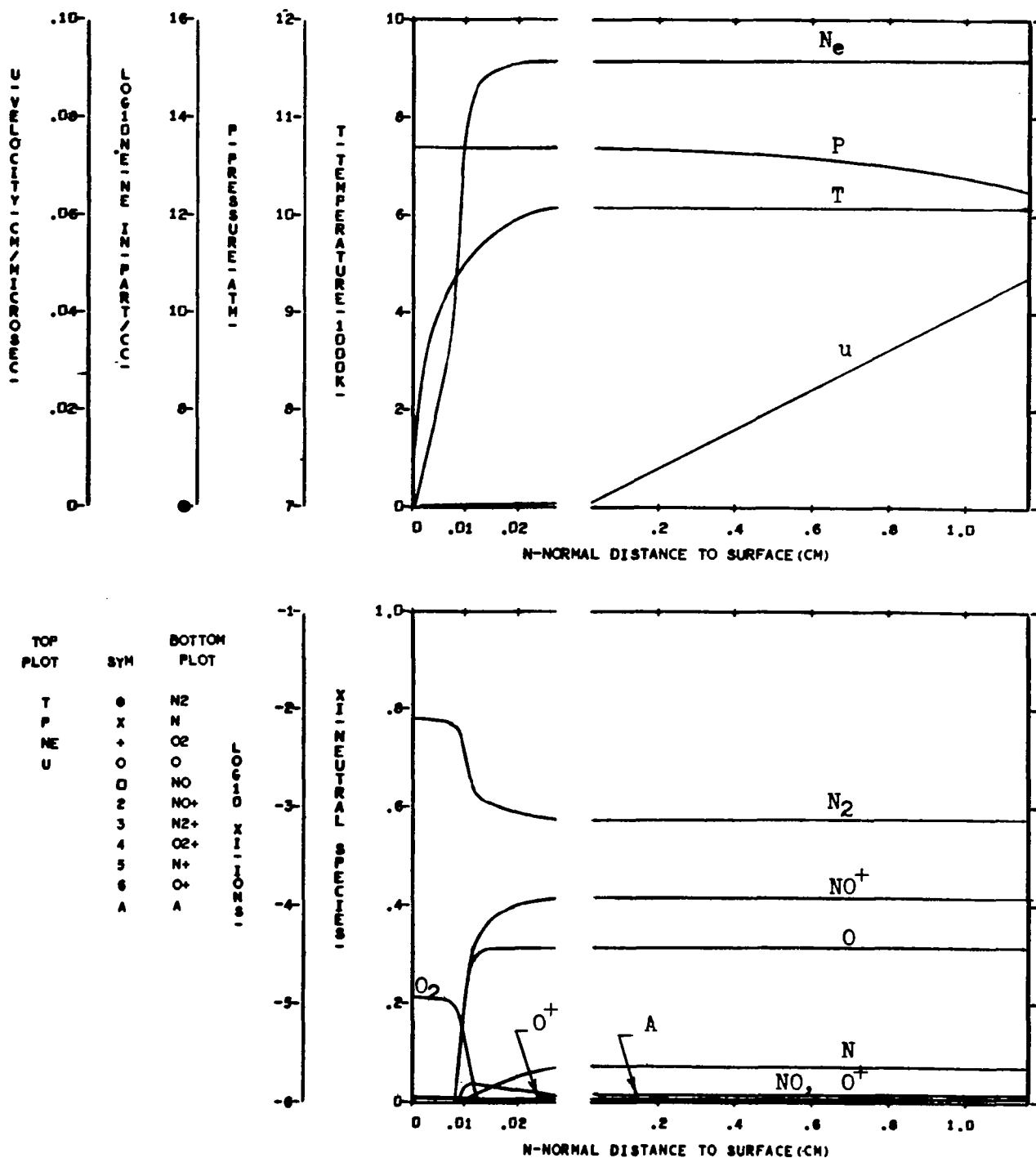
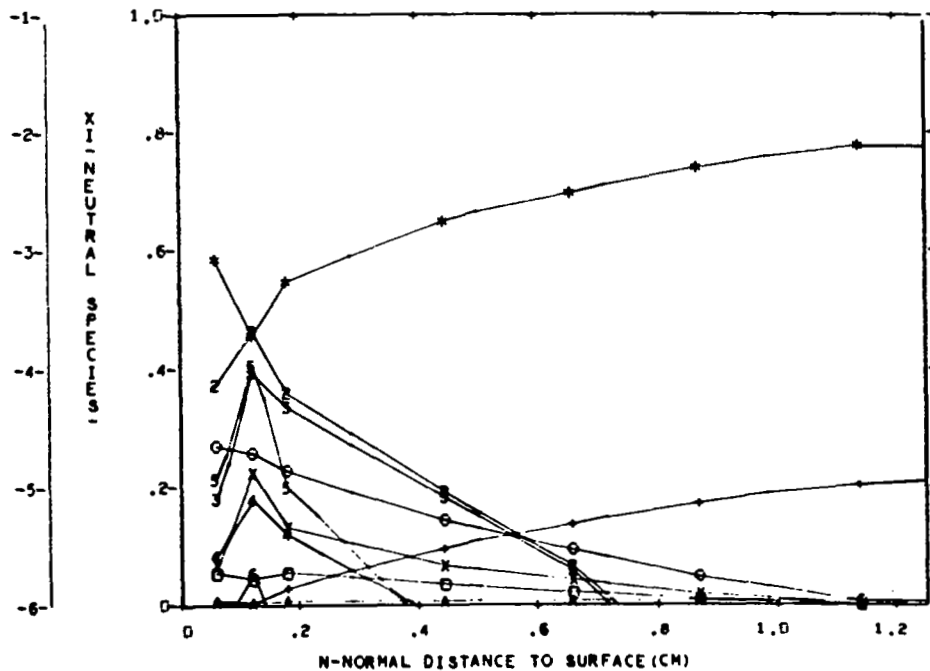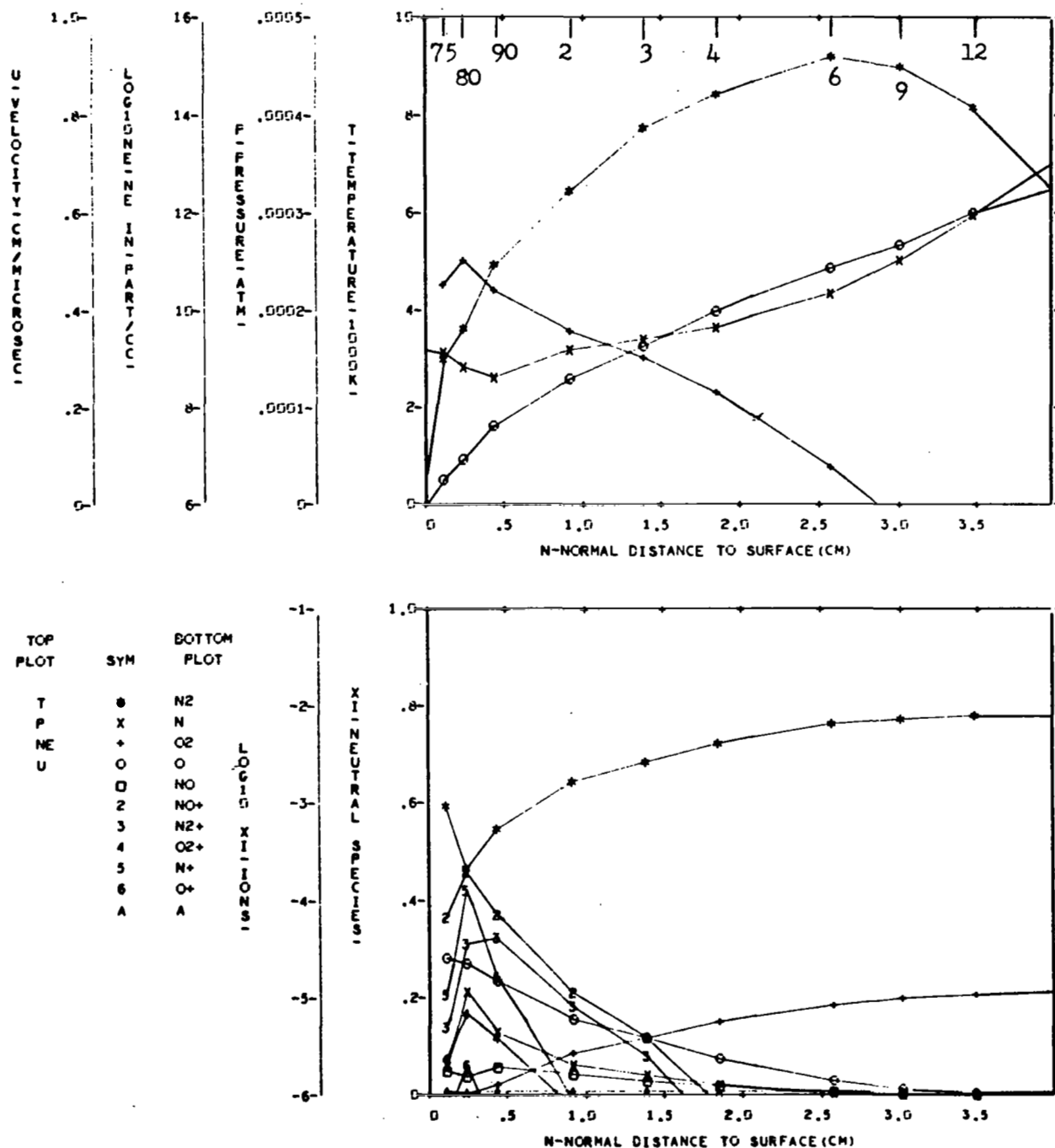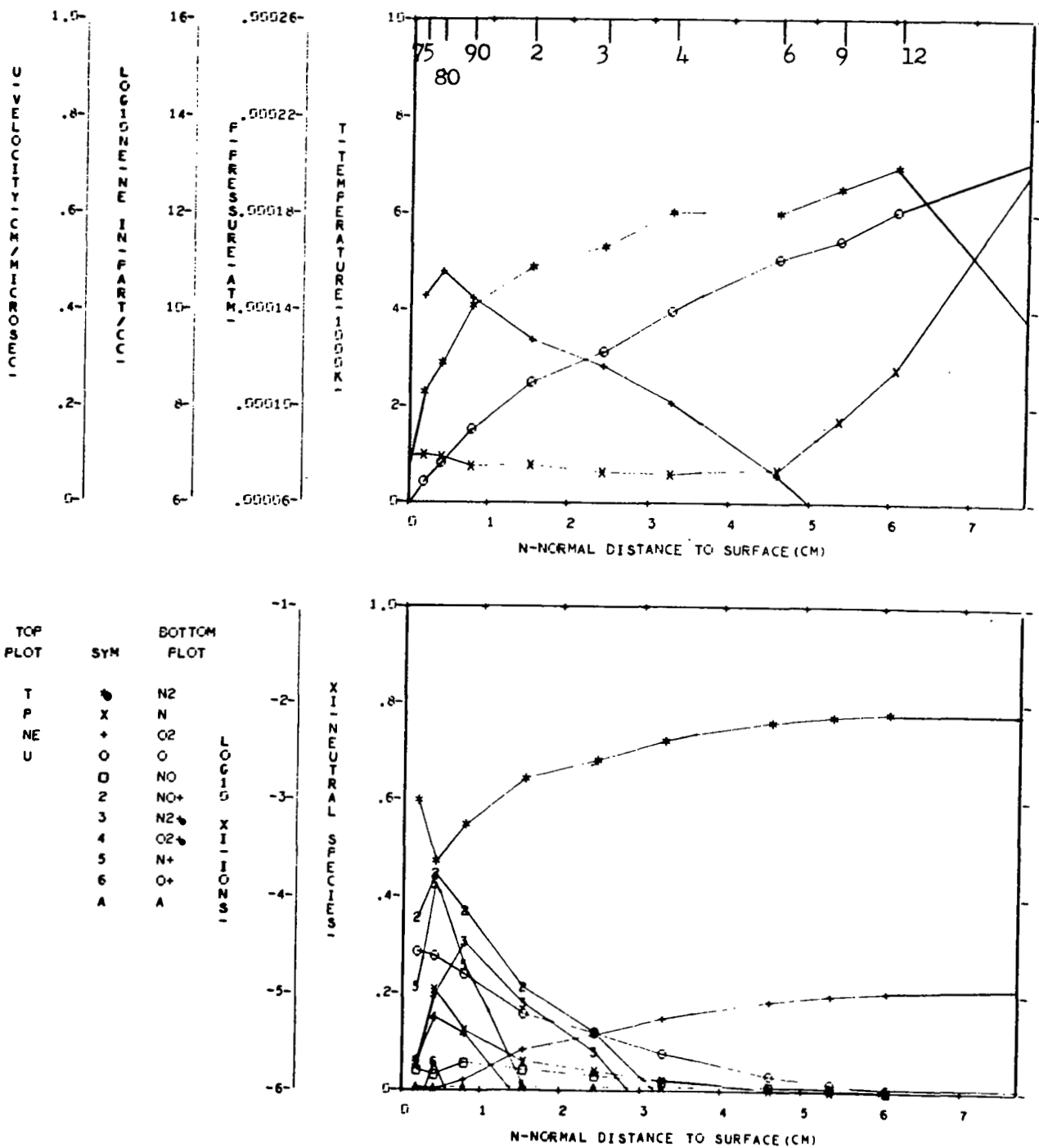FIGURE 43   EQUILIBRIUM FLOW FIELD PROPERTIES - CASE 8, NORMAL 1
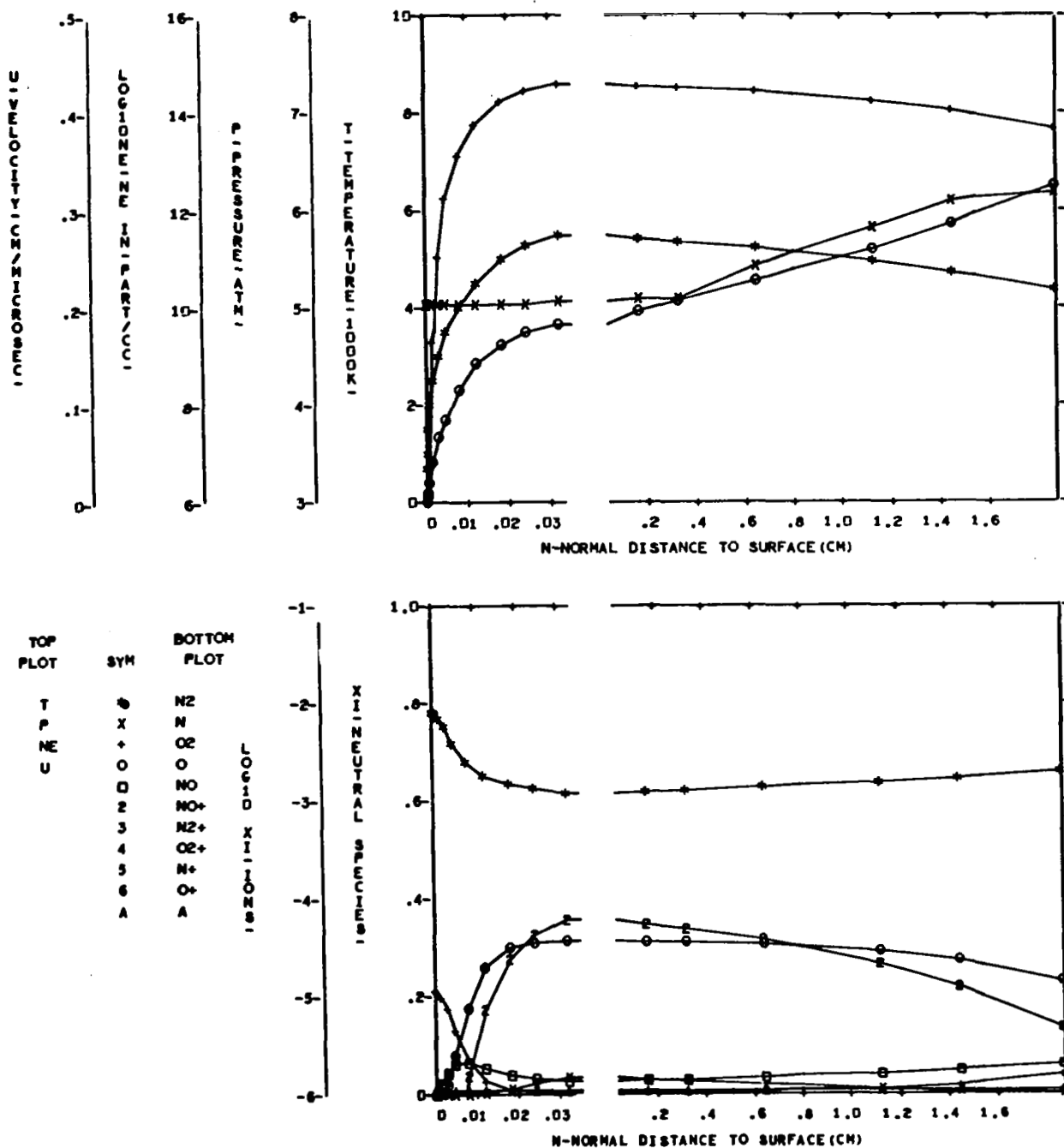
FIGURE 44 EQUILIBRIUM FLOW FIELD PROPERTIES - CASE 8, NORMAL 4

79
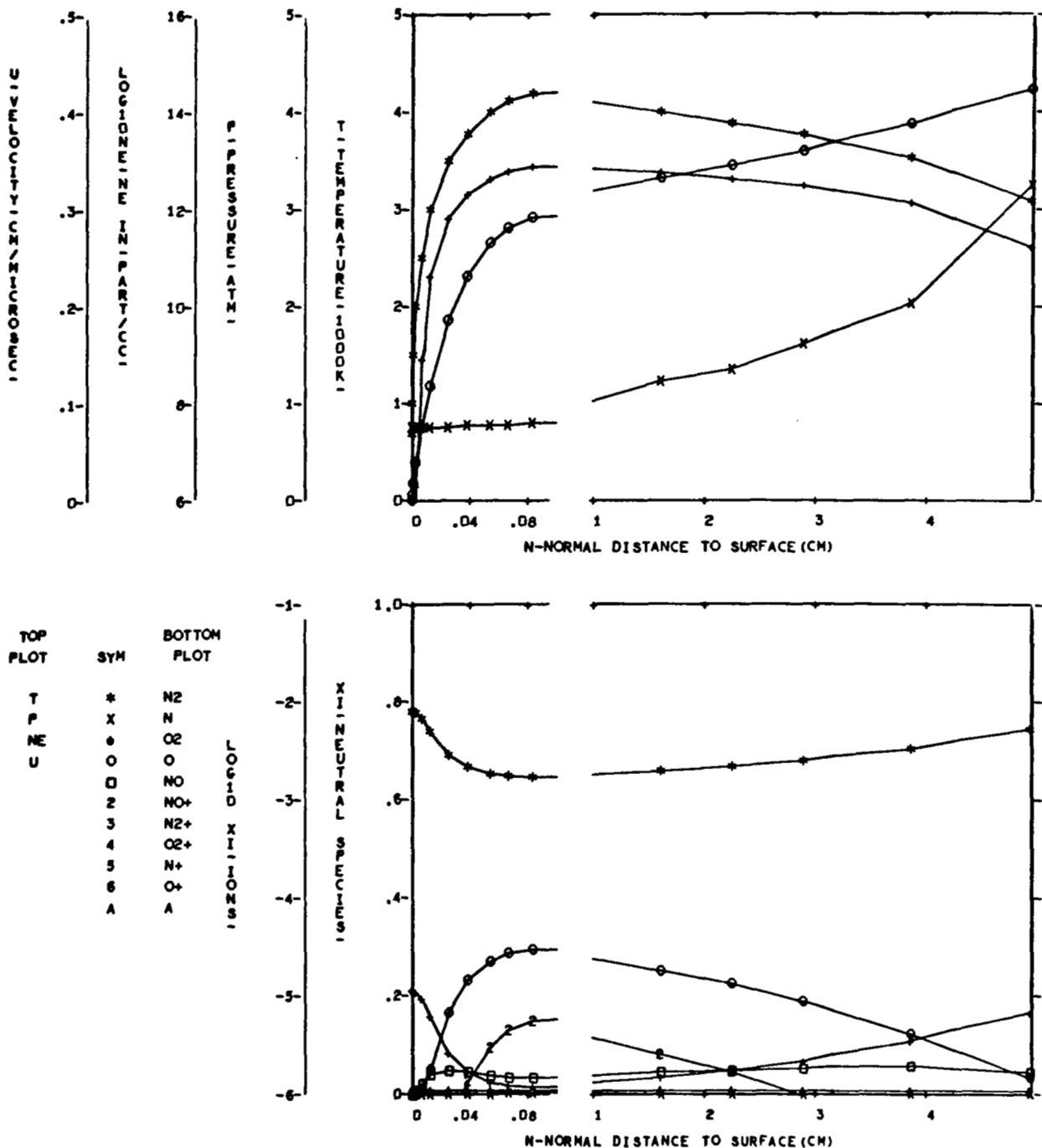
FIGURE 45 EQUILIBRIUM FLOW FIELD PROPERTIES - CASE 8, NORMAL 6

80
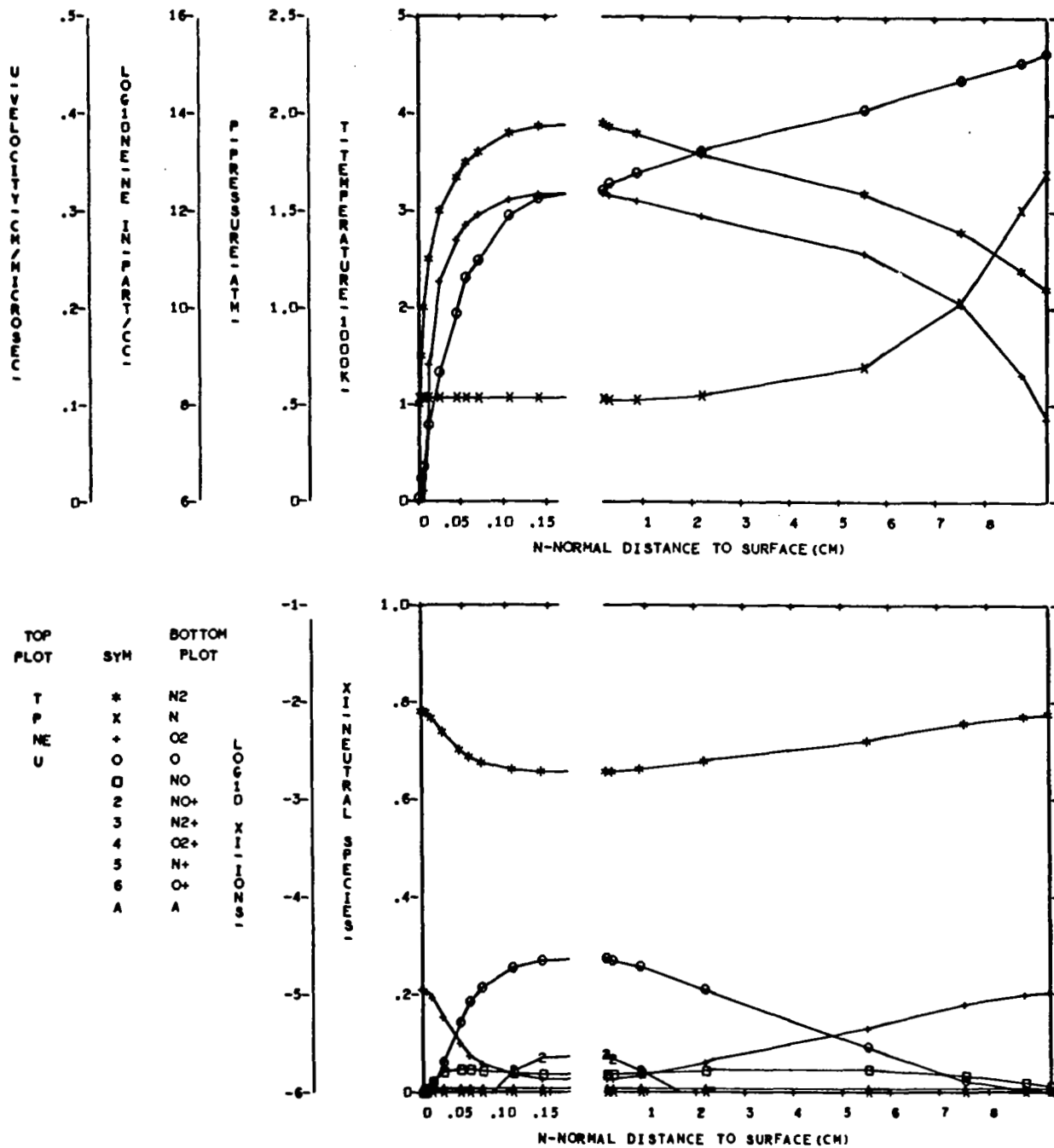
FIGURE 46 EQUILIBRIUM FLOW FIELD PROPERTIES - CASE 8, NORMAL 7

U - VELOCITY - CM/MICROSEC.

LOG10 NE - NE IN - PART/CC.

P - PRESSURE - ATM -

T - TEMPERATURE - 1000 K -

.10
.08
.06
.04
.02
0

16
14
12
10
8
6

1.1
1.0
.9
.8
.7
.6

25
20
15
10
5
0

N_e

P

u

T

0 .02 .04 .06 .08   .1   .2   .3   .4   .5   .6   .7   .8

N-NORMAL DISTANCE TO SURFACE (CM)

LOG10 XI - IONS -

XI - NEUTRAL SPECIES -

-1
-2
-3
-4
-5
-6

1.0
.8
.6
.4
.2
0

N^+ NO^+ N

O^+

O N_2^+

N_2

O_2
NO

A

0 .02 .04 .06 .08   .1   .2   .3   .4   .5   .6   .7   .8

N-NORMAL DISTANCE TO SURFACE (CM)
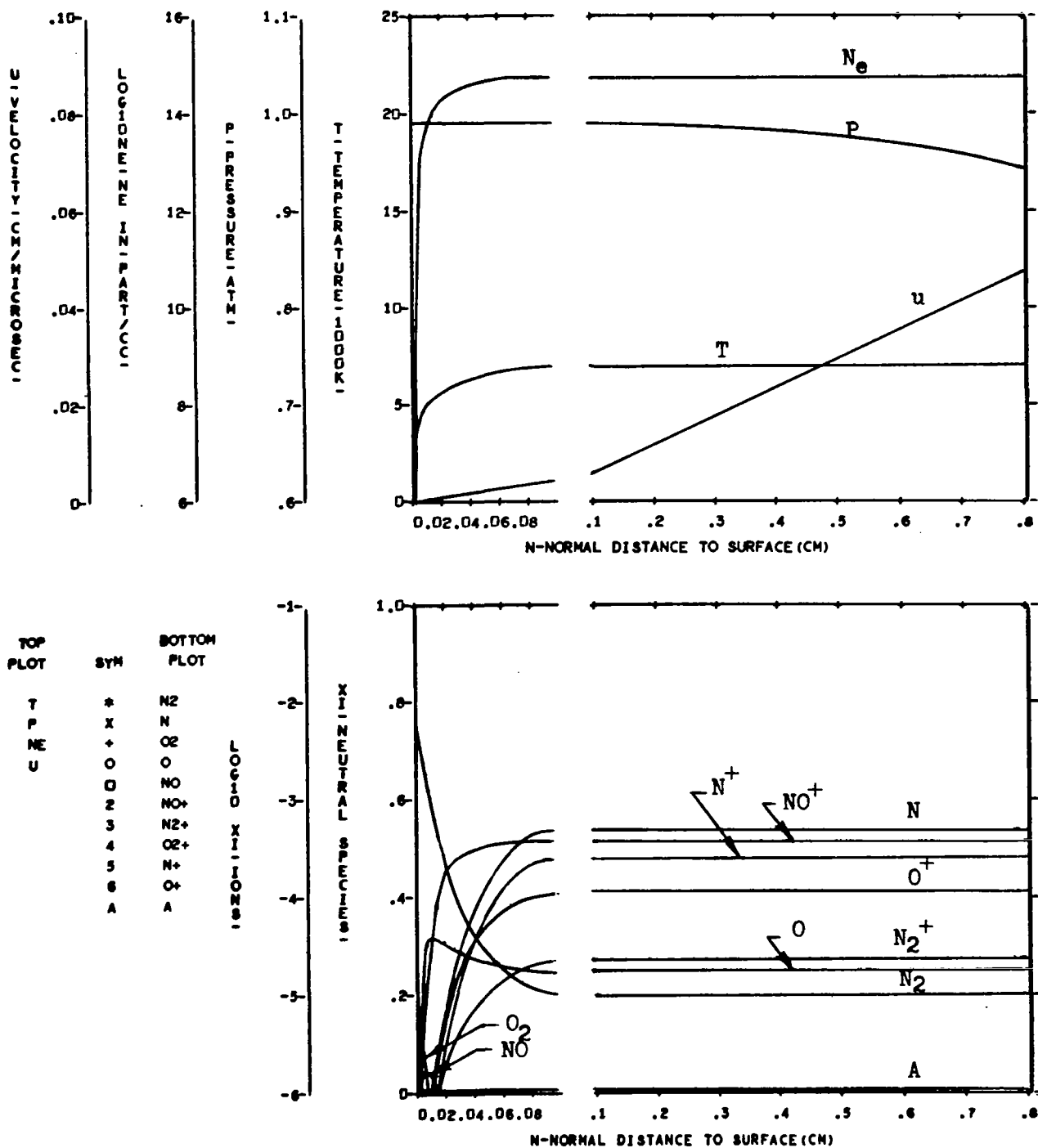
FIGURE 47 EQUILIBRIUM FLOW FIELD PROPERTIES - CASE 9, NORMAL 1
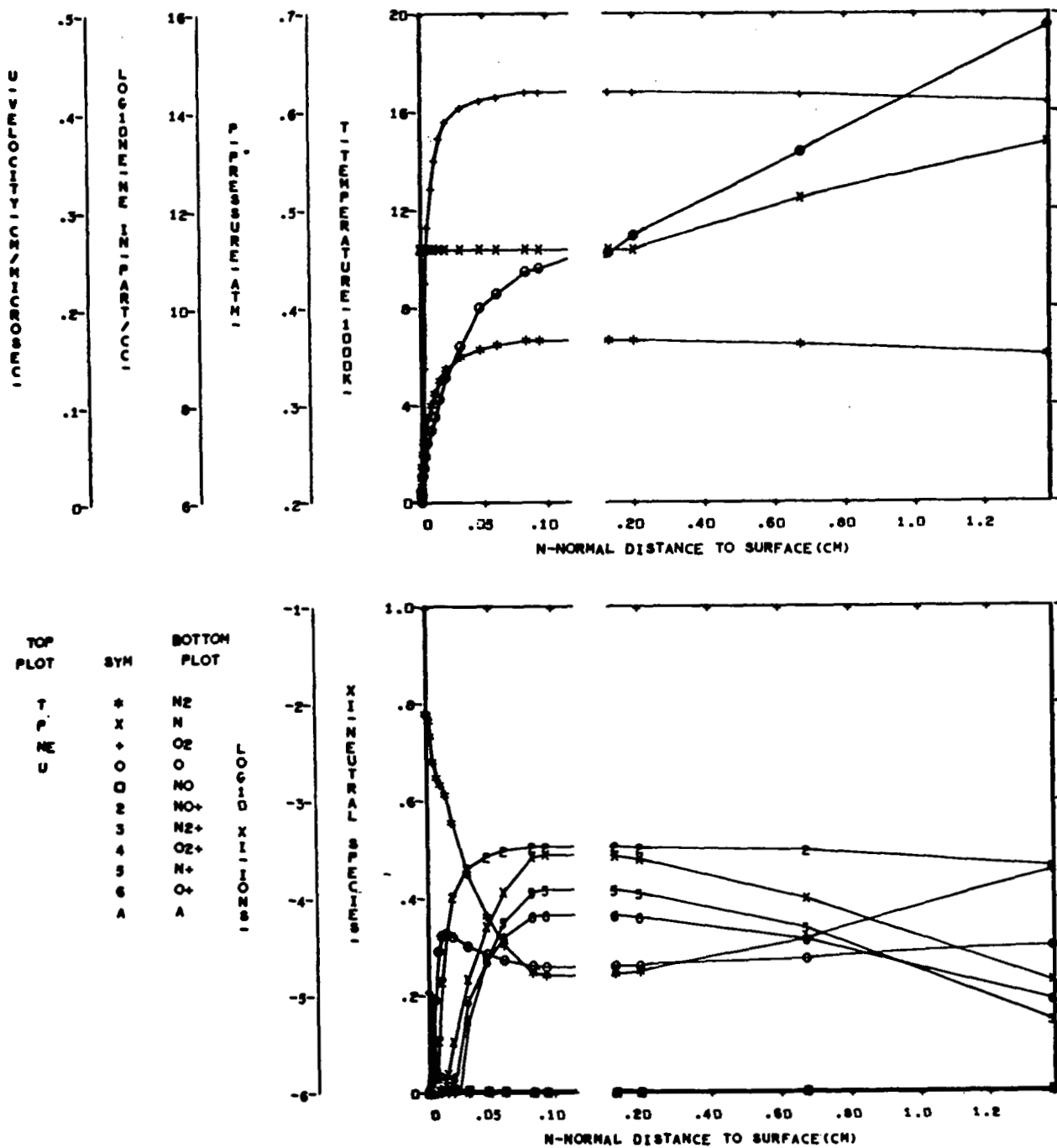
FIGURE 48   EQUILIBRIUM FLOW FIELD PROPERTIES - CASE 9, NORMAL 4
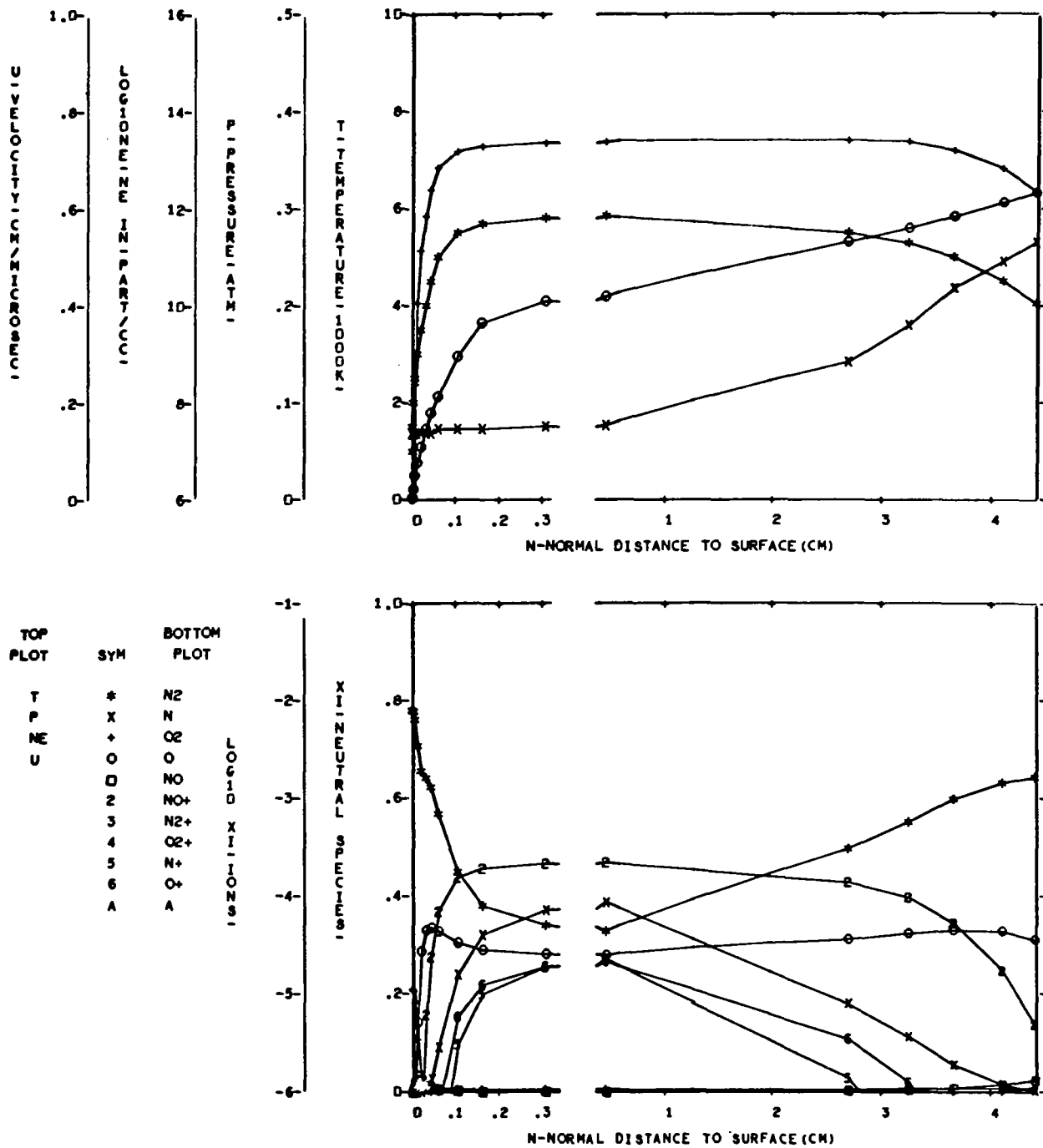
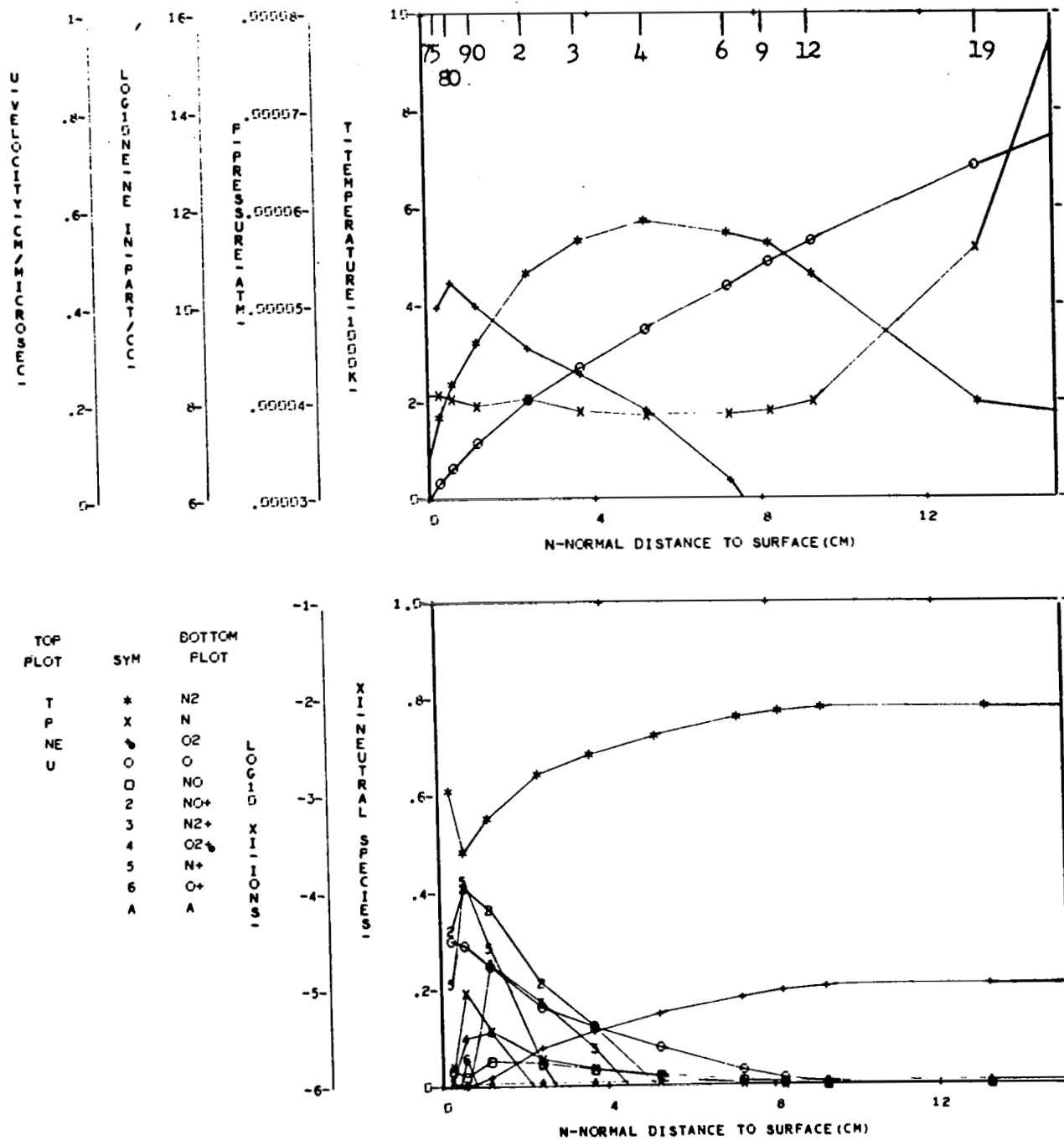FIGURE 49 EQUILIBRIUM FLOW FIELD PROPERTIES - CASE 9, NORMAL 6
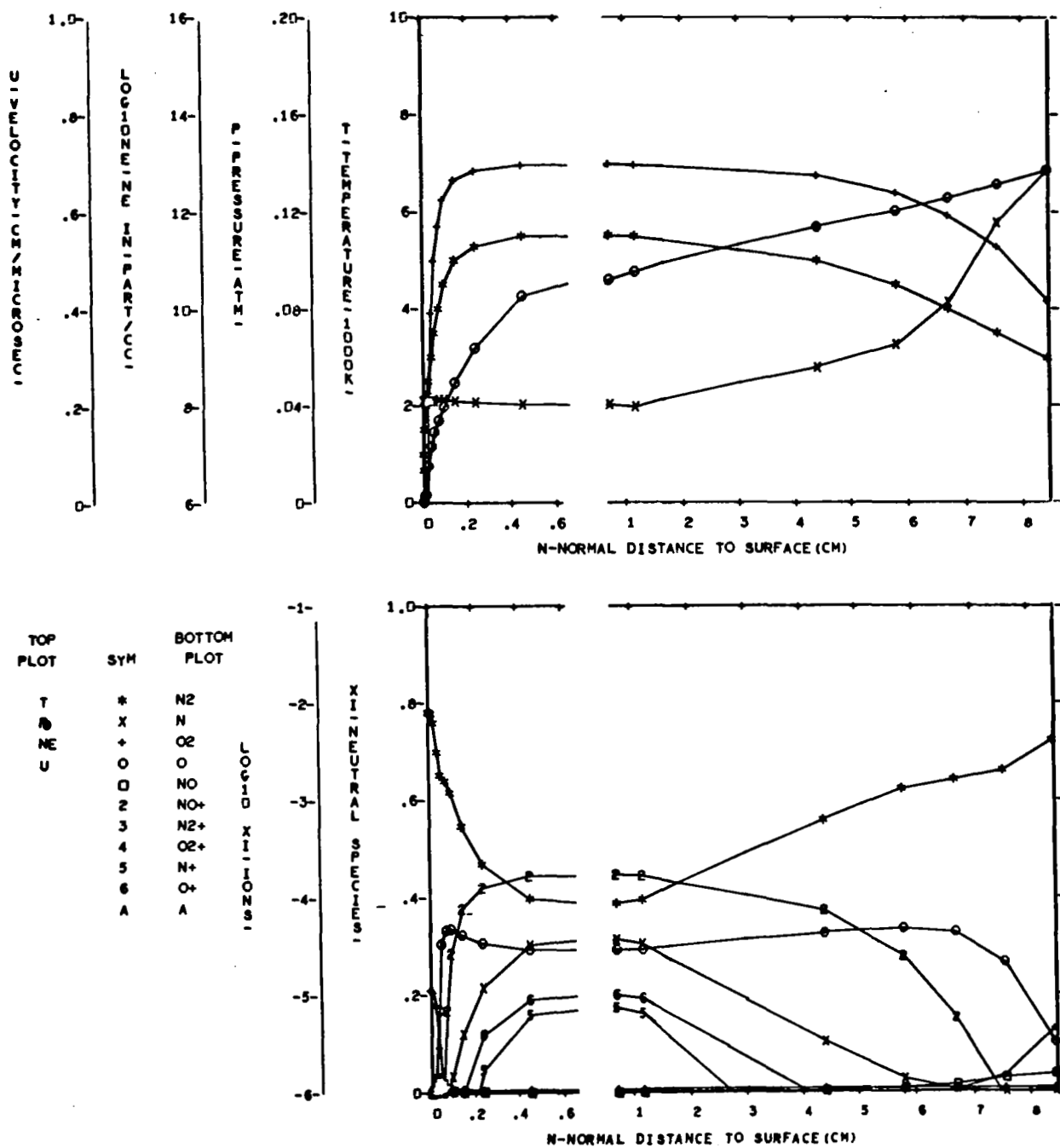
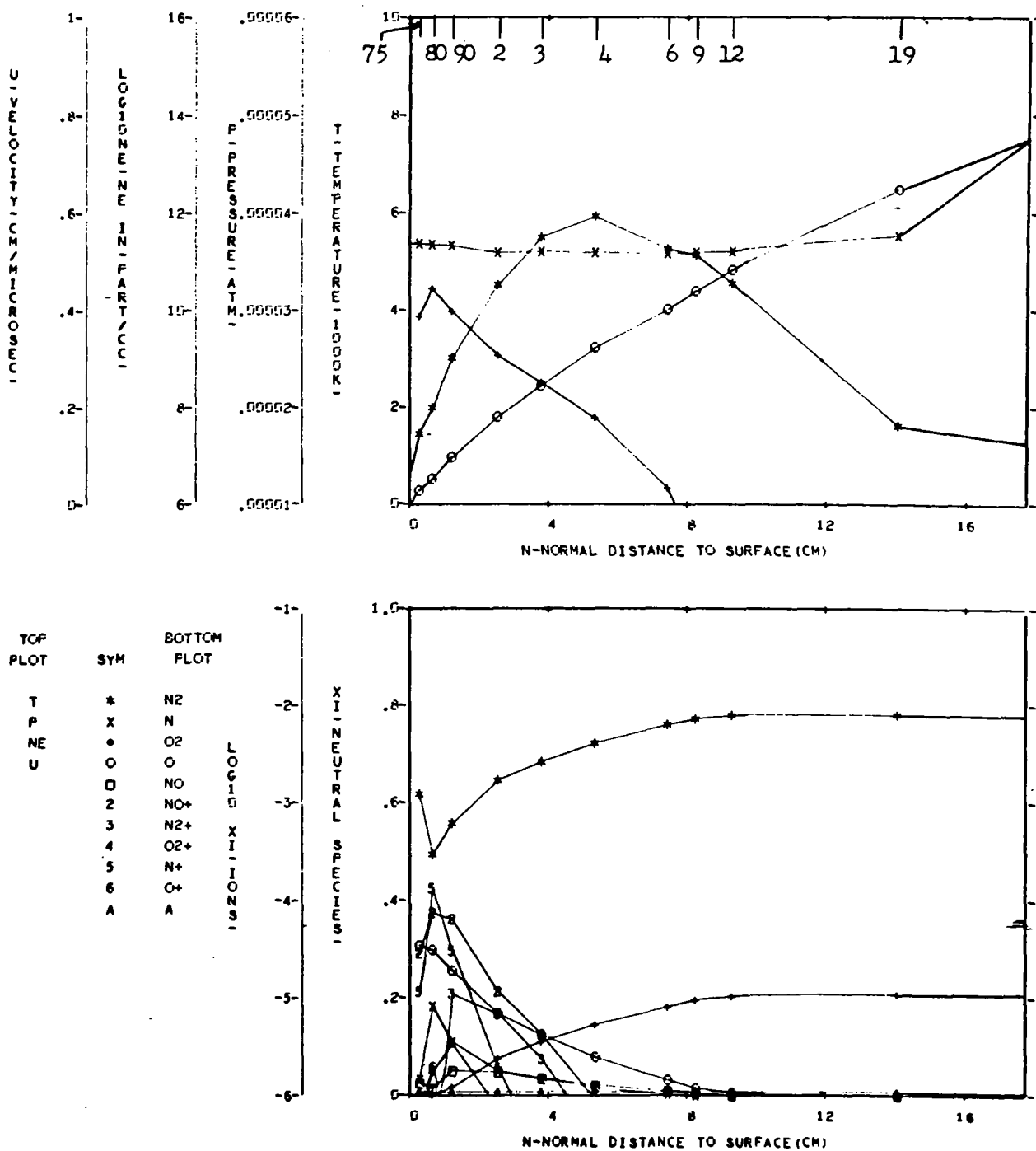FIGURE 50 EQUILIBRIUM FLOW FIELD PROPERTIES - CASE 9, NORMAL 7
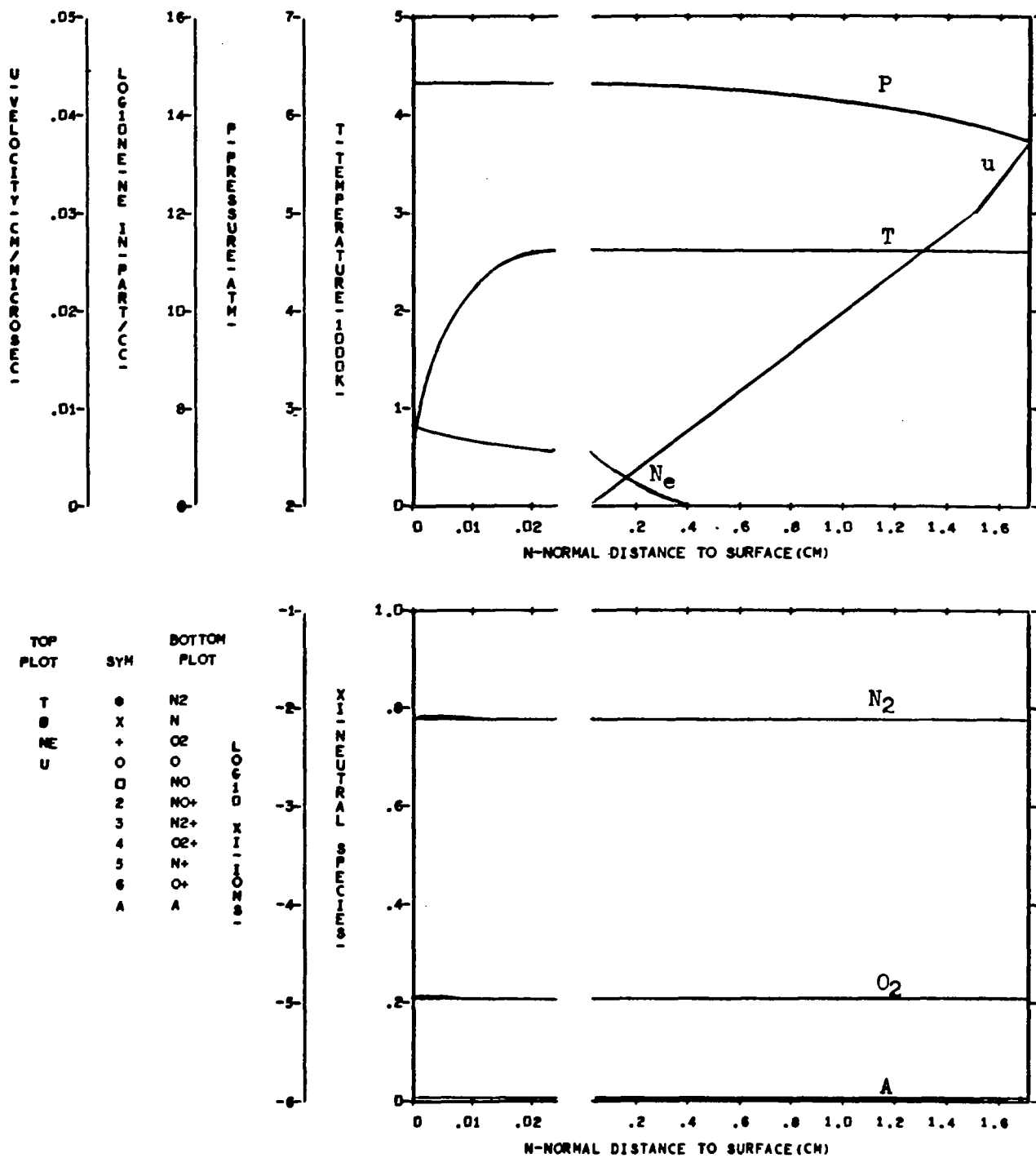
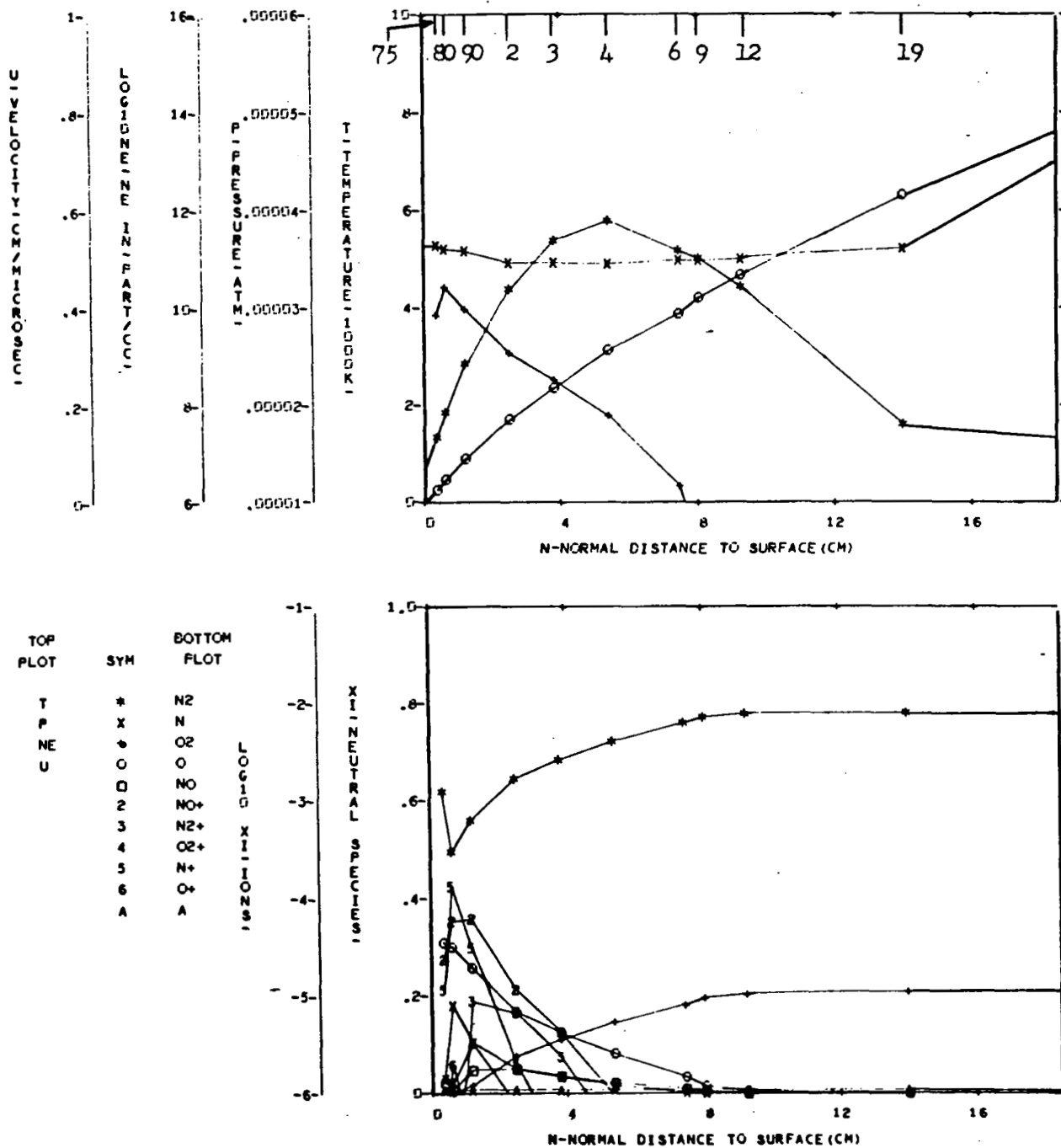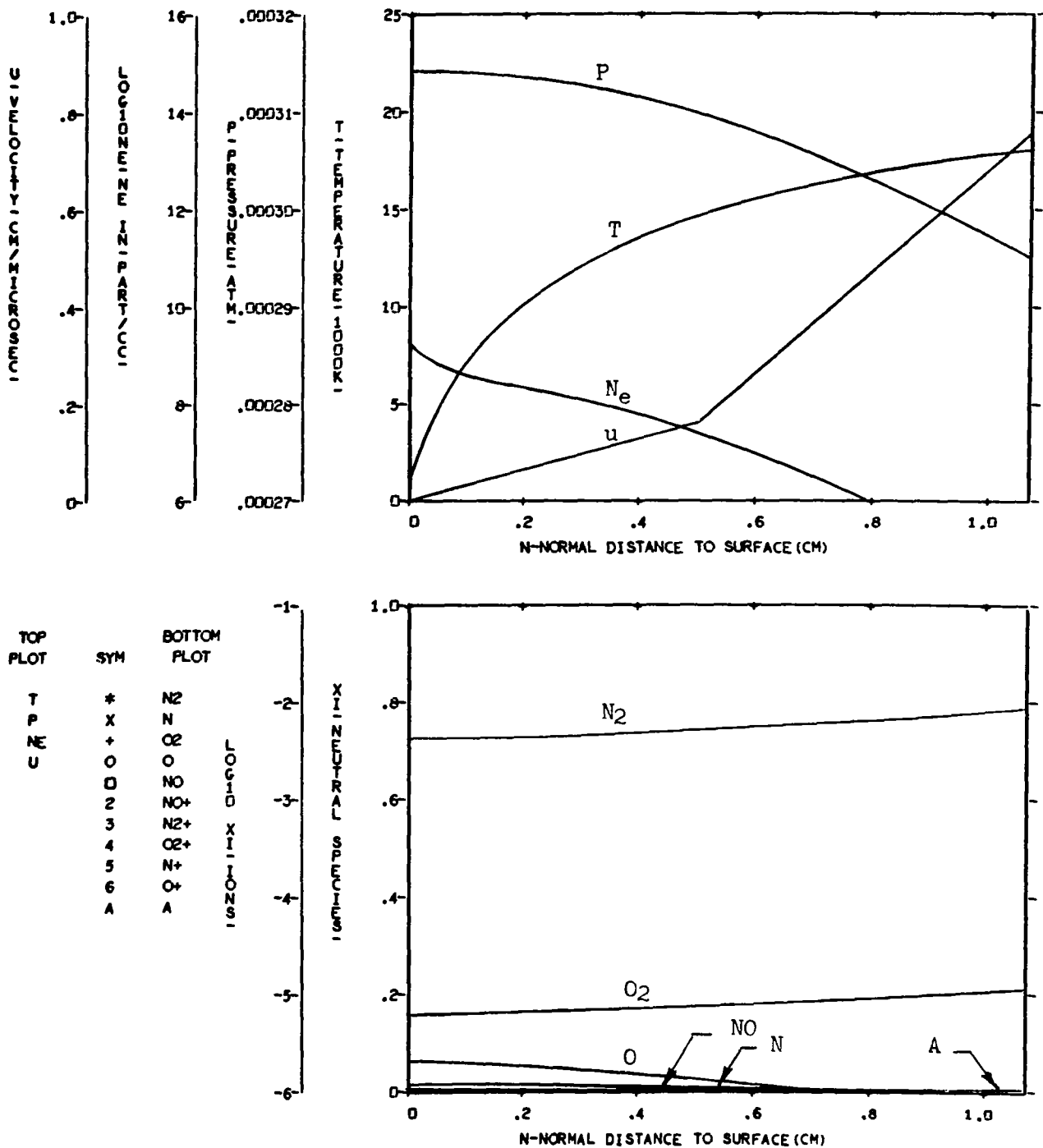FIGURE 51   NONEQUILIBRIUM FLOW FIELD PROPERTIES - CASE 1, NORMAL 1
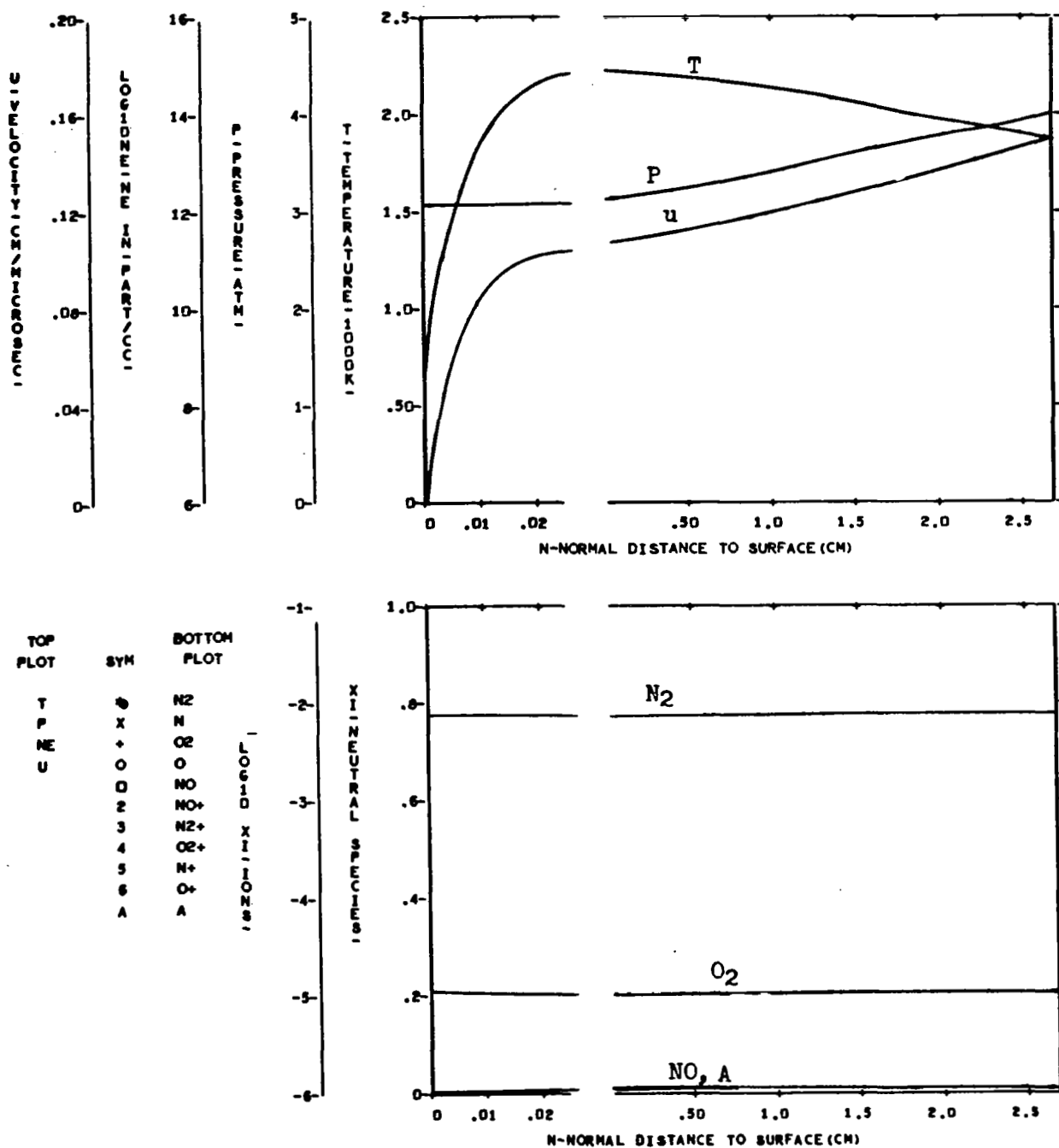
FIGURE 52. NONEQUILIBRIUM FLOW FIELD PROPERTIES - CASE 1, NORMAL 4
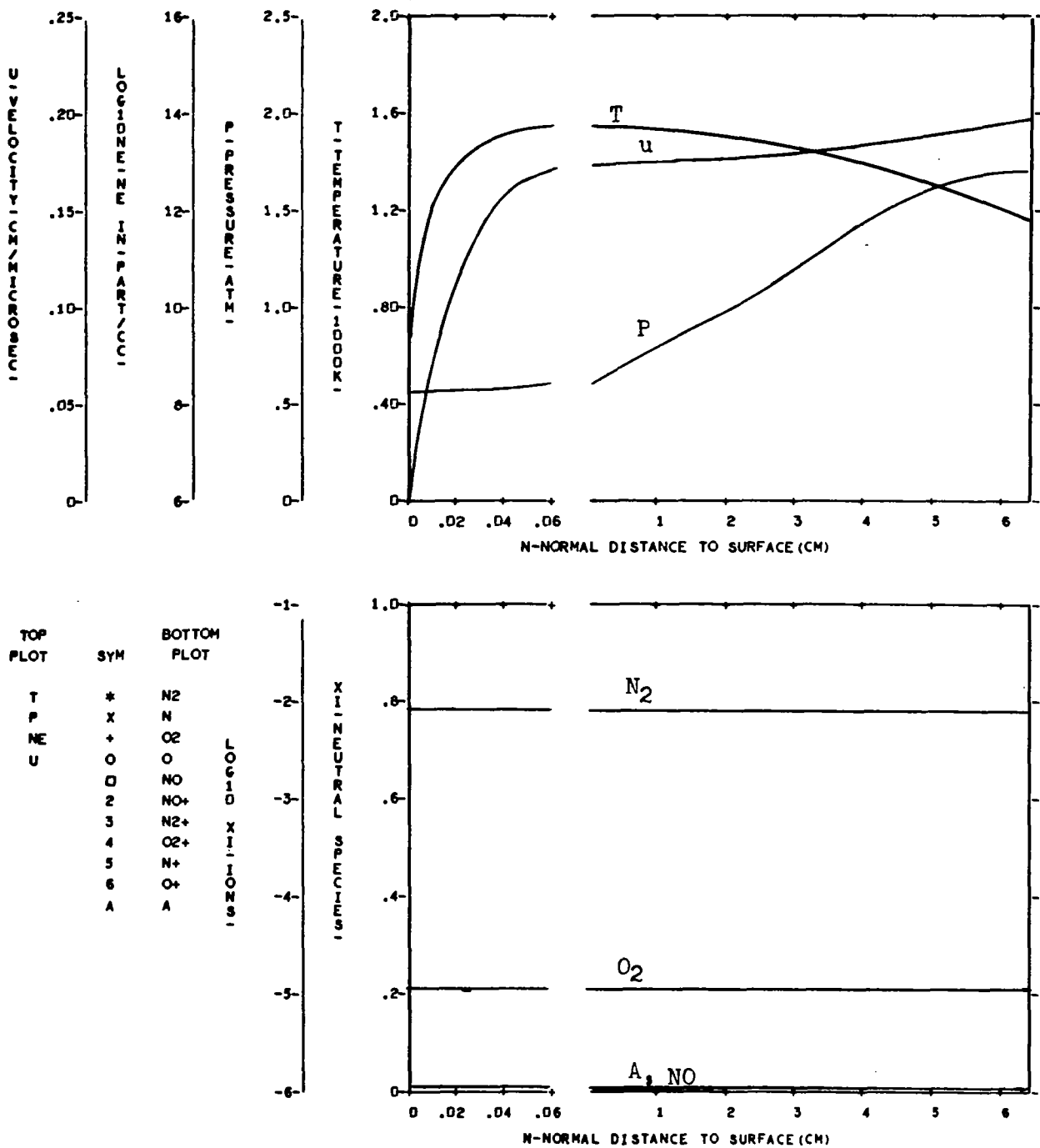
FIGURE 53 NONEQUILIBRIUM FLOW FIELD PROPERTIES - CASE 1, NORMAL 6
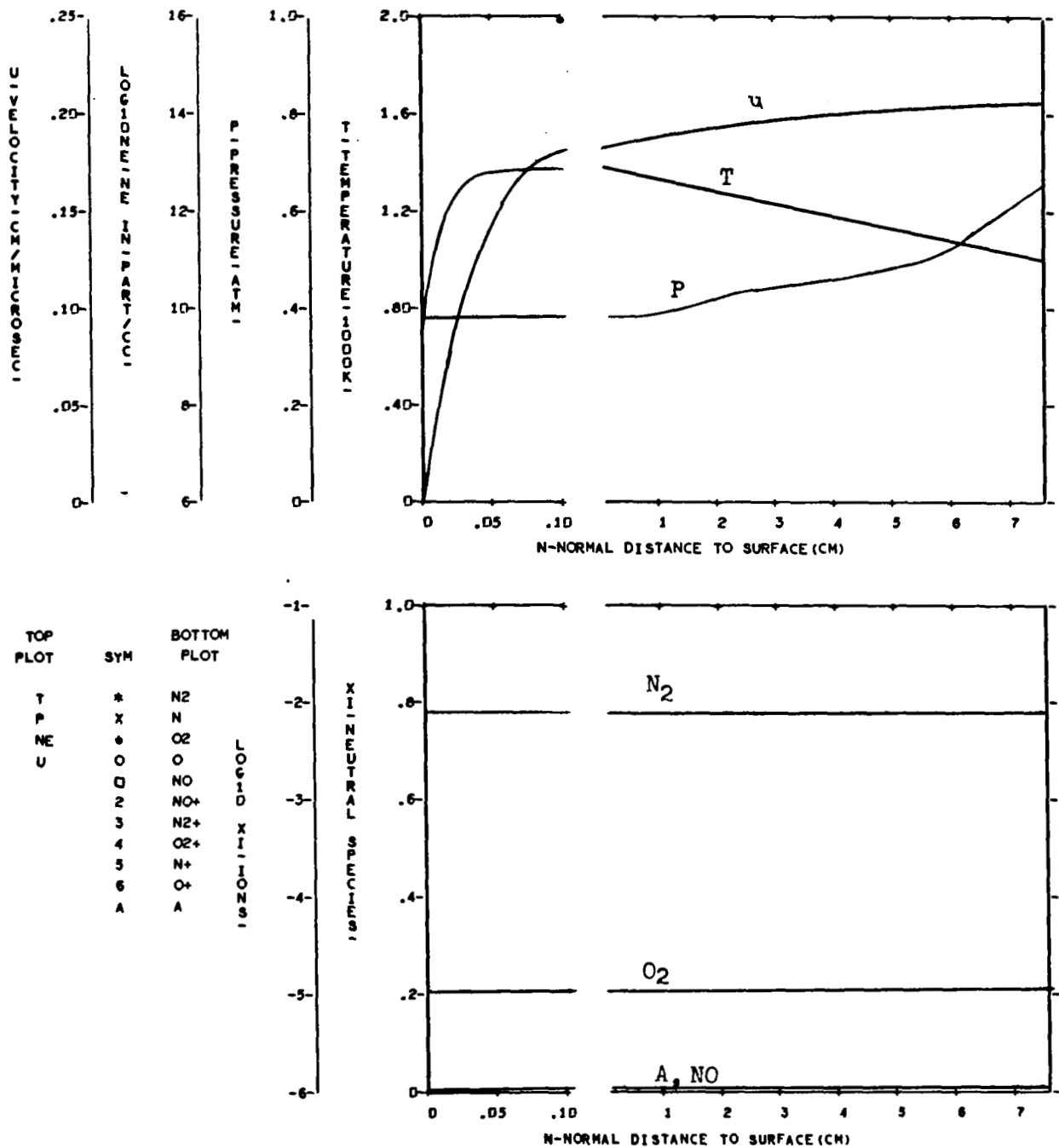
FIGURE 54. NONEQUILIBRIUM FLOW FIELD PROPERTIES - CASE 1, NORMAL 7
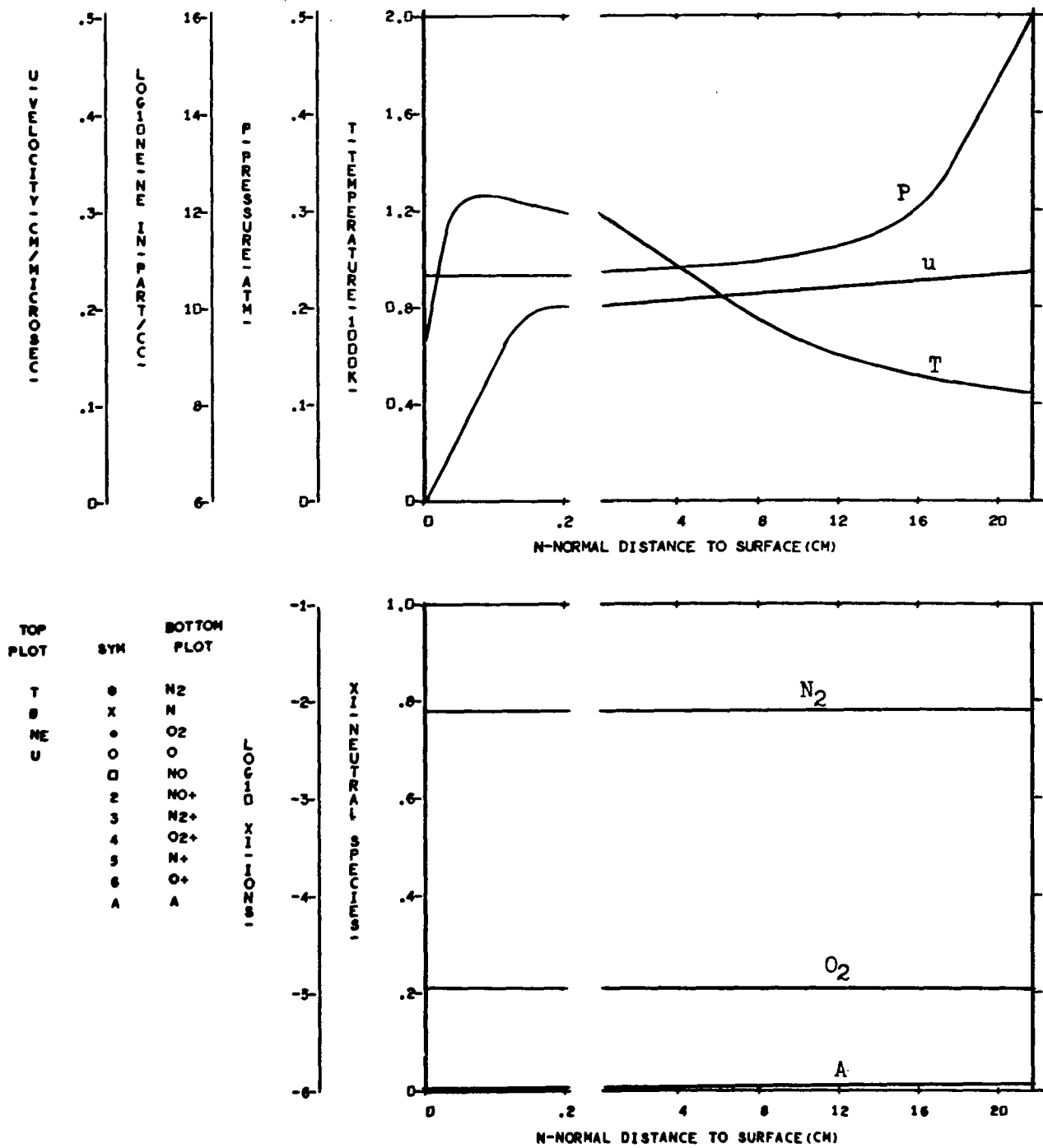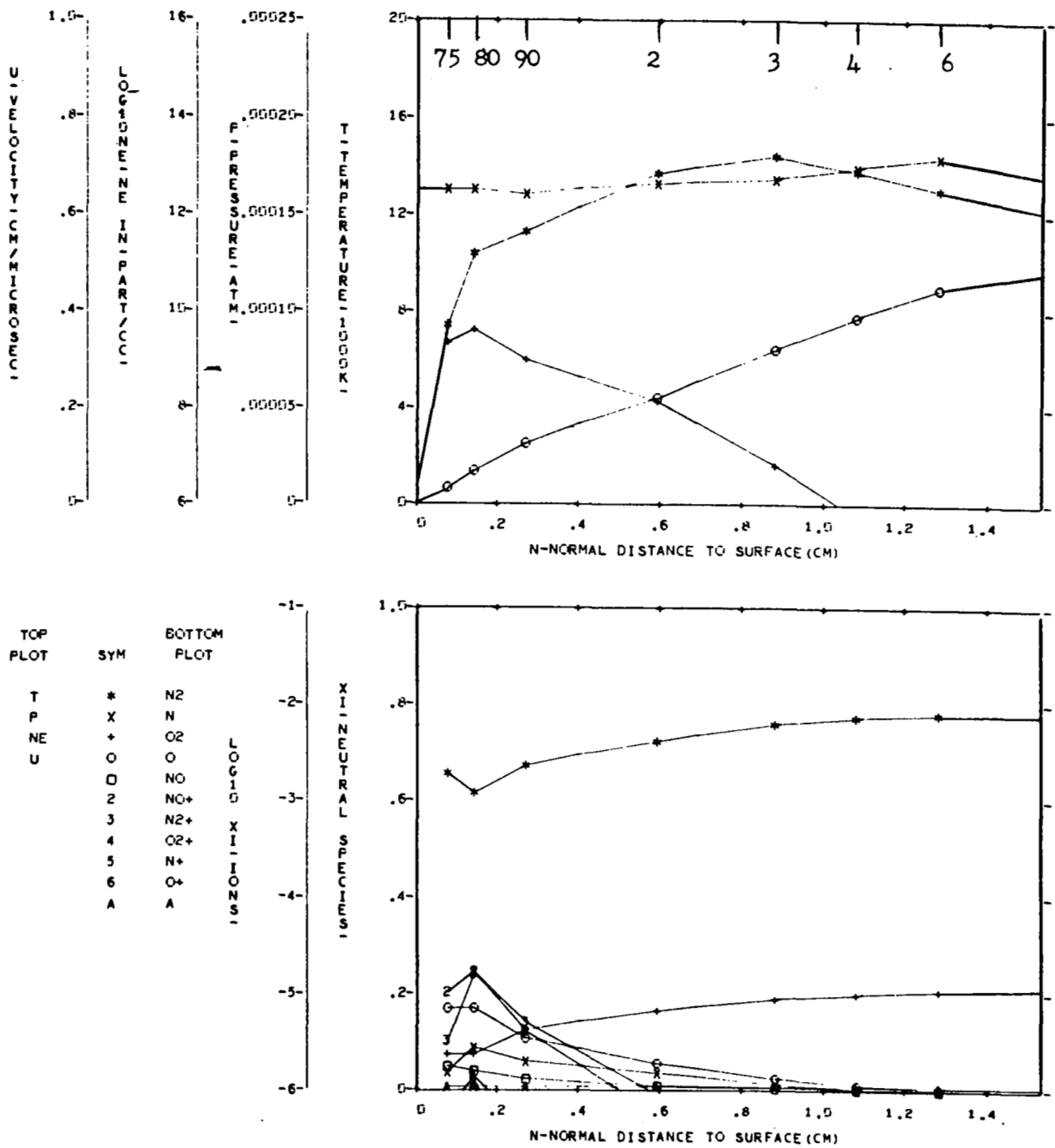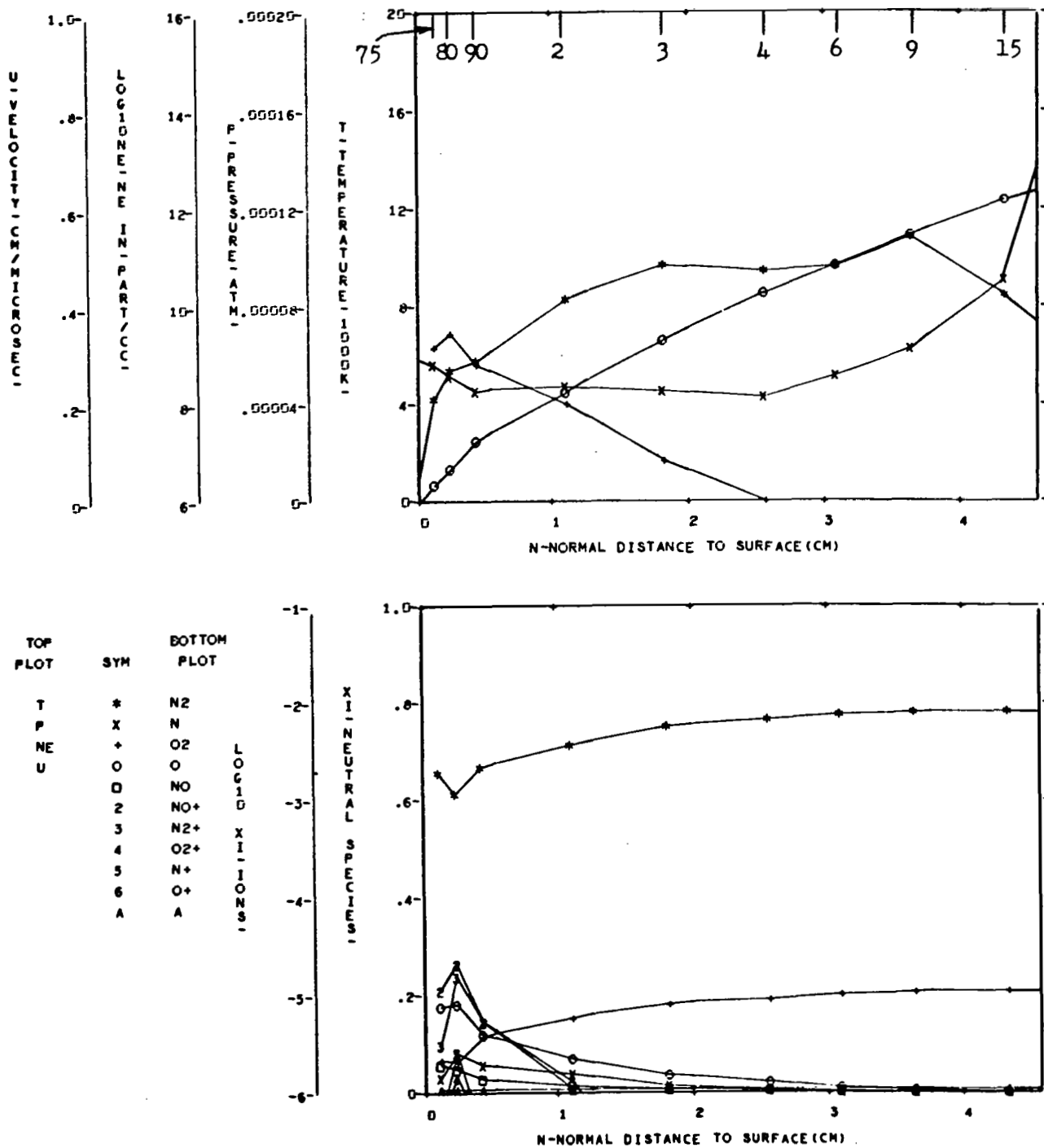
FIGURE 55 NONEQUILIBRIUM FLOW FIELD PROPERTIES - CASE 1, NORMAL 9
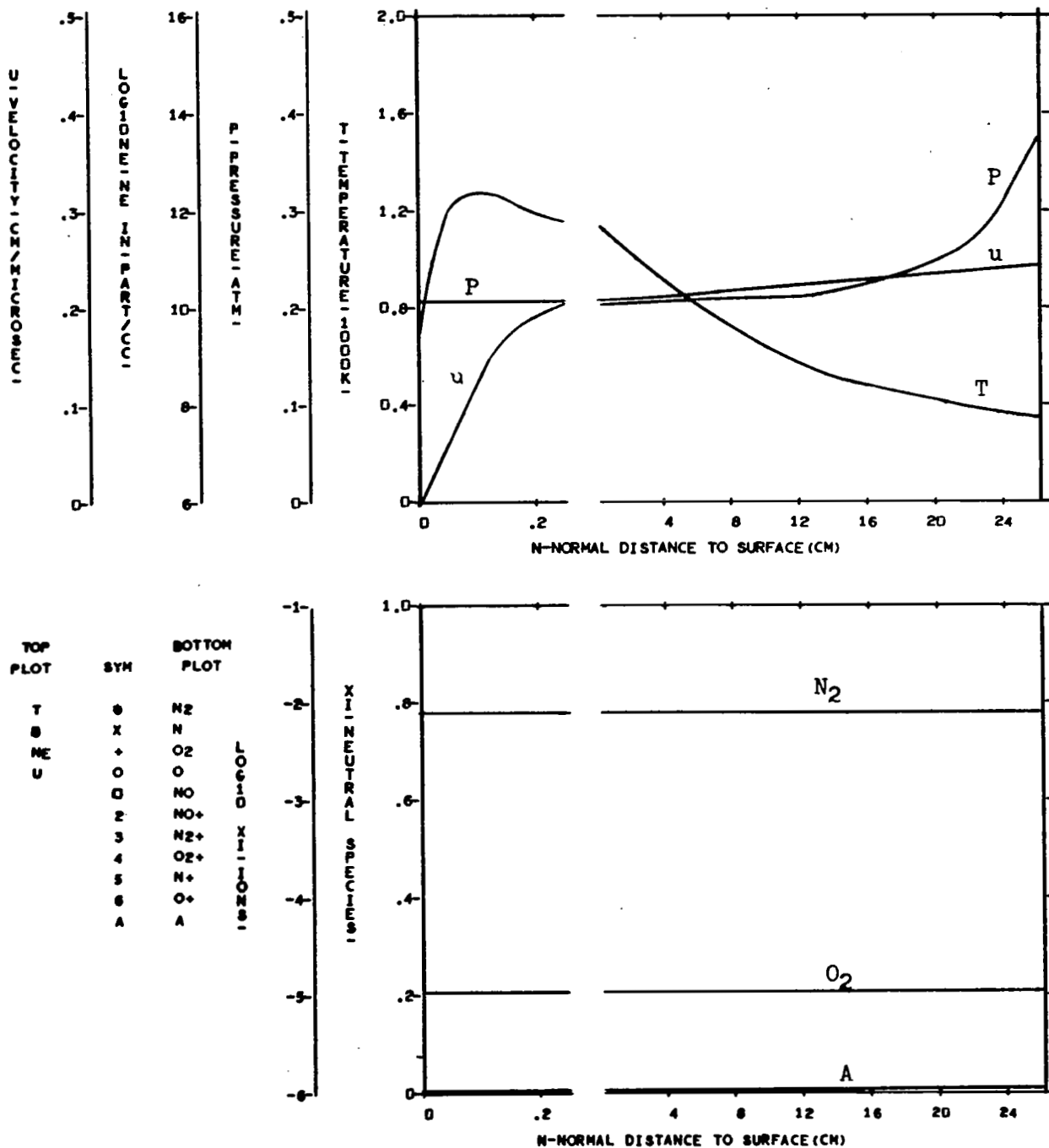
FIGURE 56 NONEQUILIBRIUM FLOW FIELD PROPERTIES - CASE 1, NORMAL 11

91
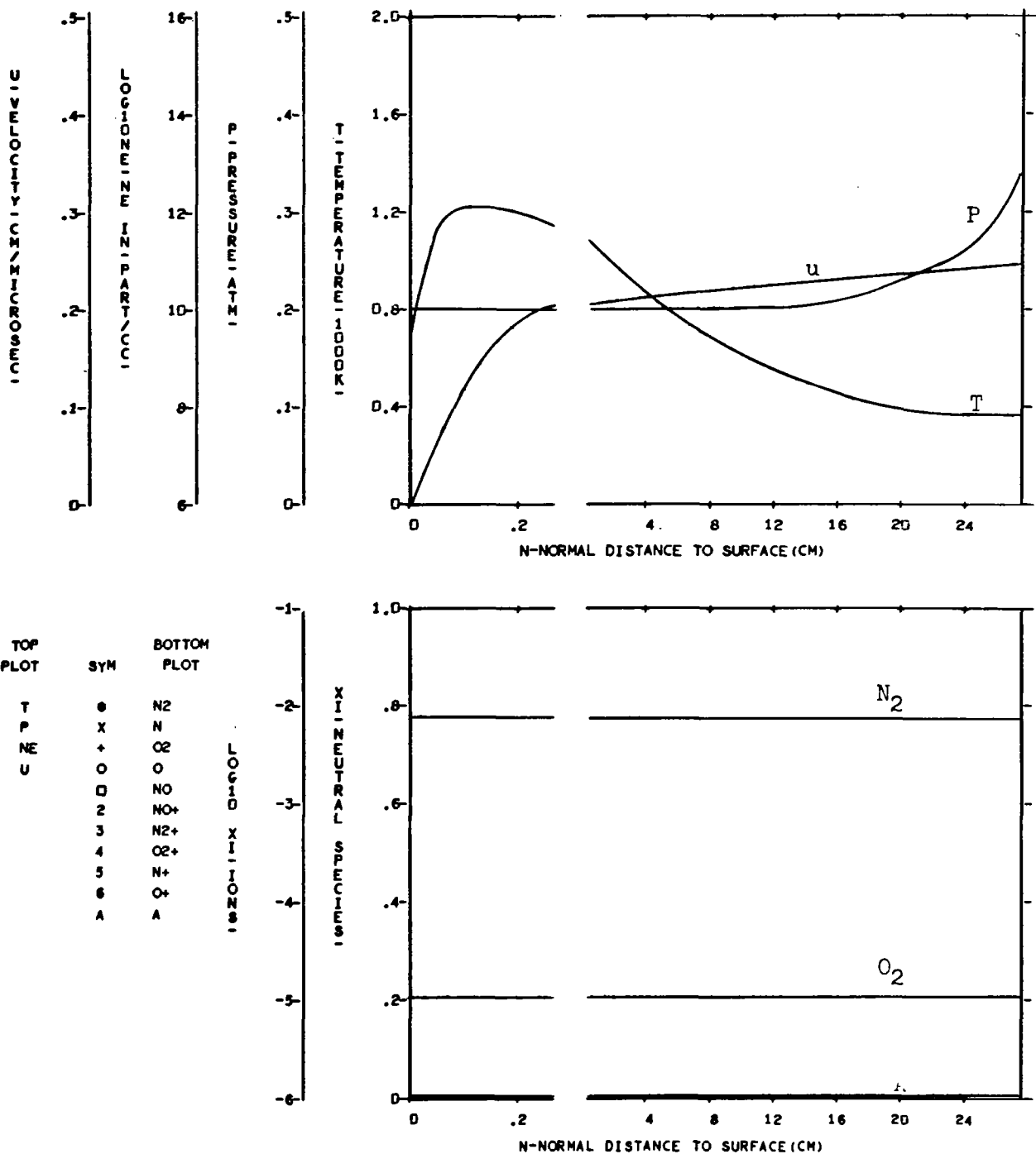
FIGURE 57 NONEQUILIBRIUM FLOW FIELD PROPERTIES - CASE 1, NORMAL 12
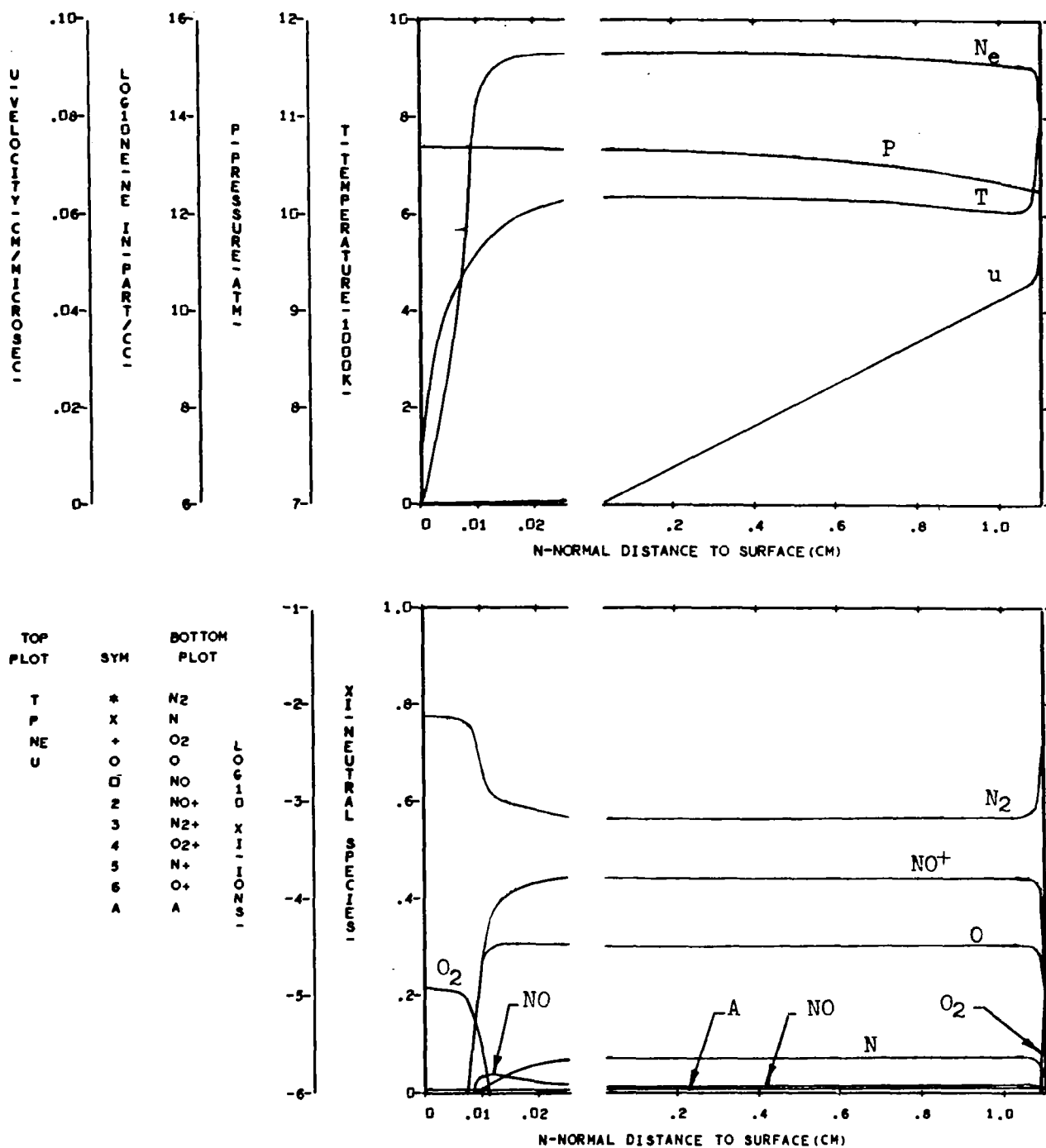
FIGURE 58 NONEQUILIBRIUM FLOW FIELD PROPERTIES - CASE 2, NORMAL 1

93
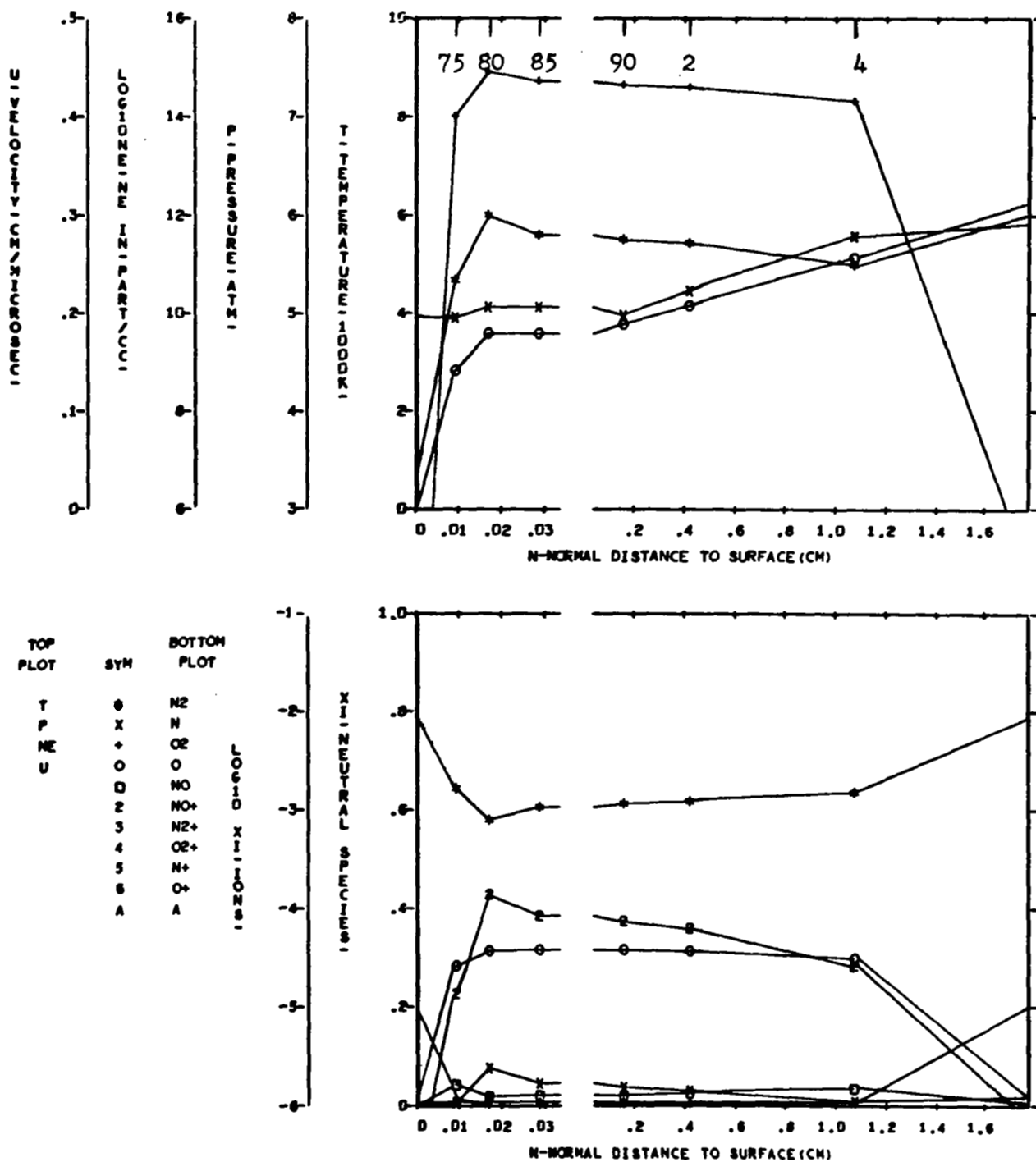
FIGURE 59 NONEQUILIBRIUM FLOW FIELD PROPERTIES - CASE 2, NORMAL 4
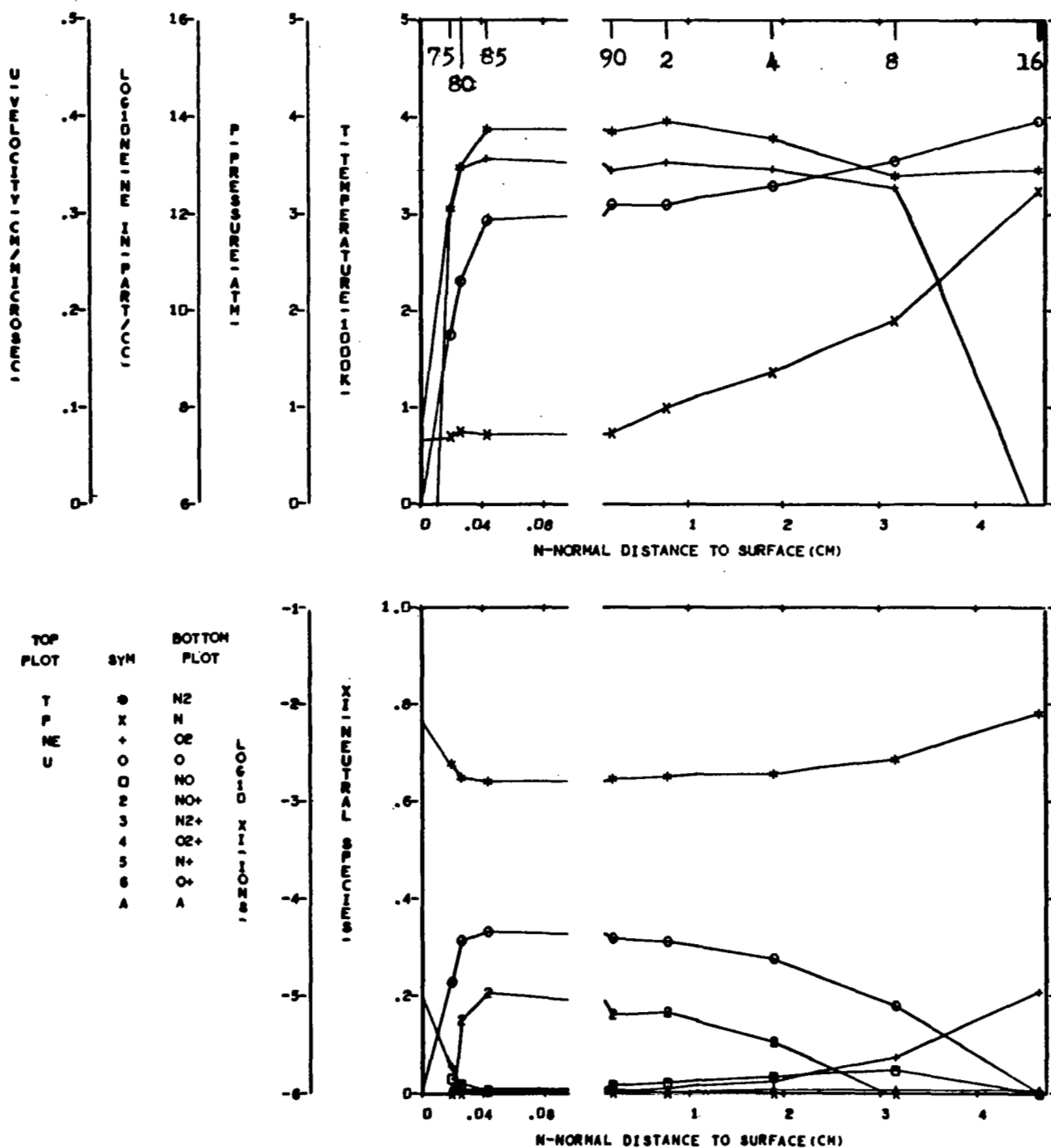
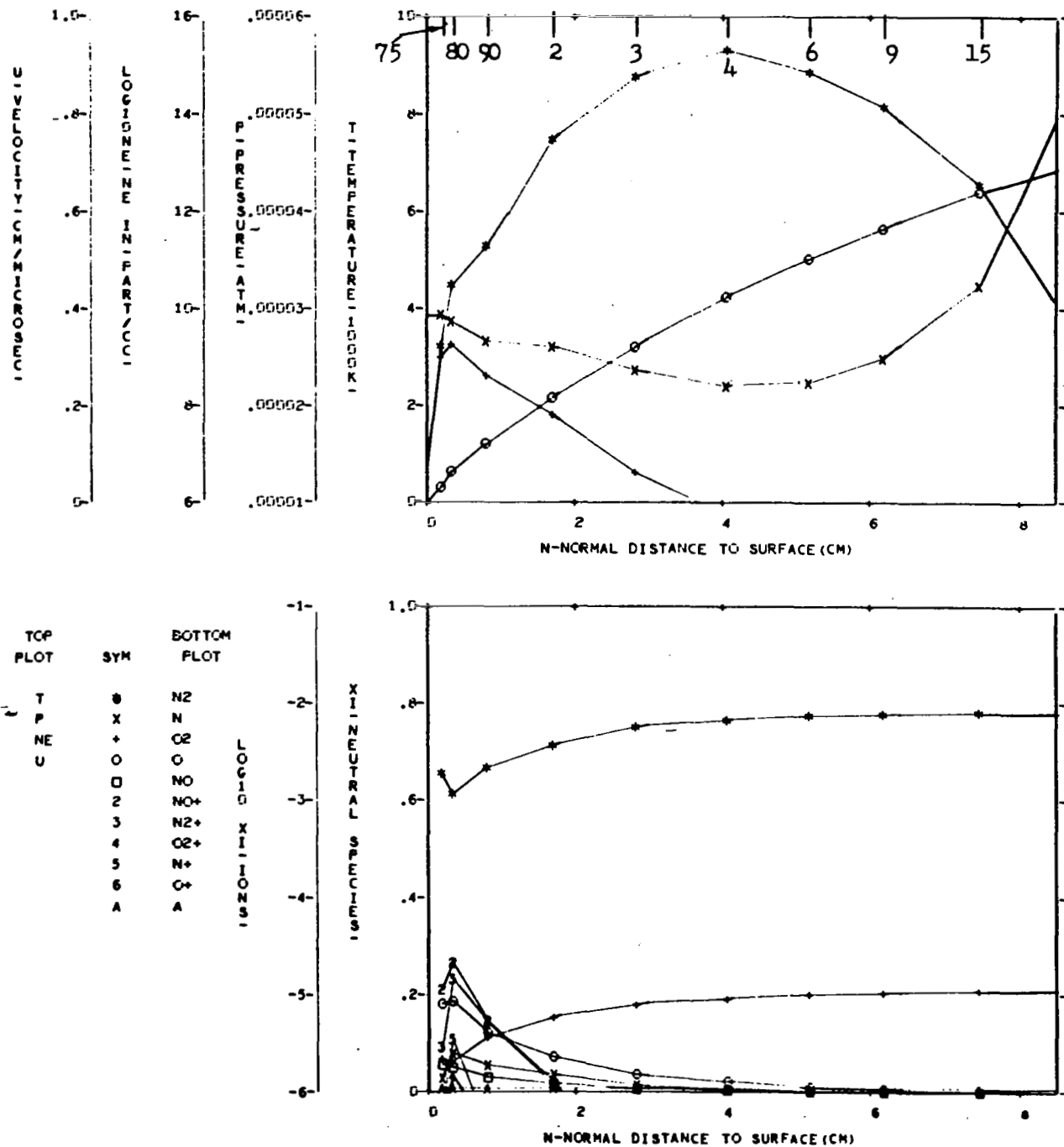FIGURE 60 NONEQUILIBRIUM FLOW FIELD PROPERTIES - CASE 2, NORMAL 6
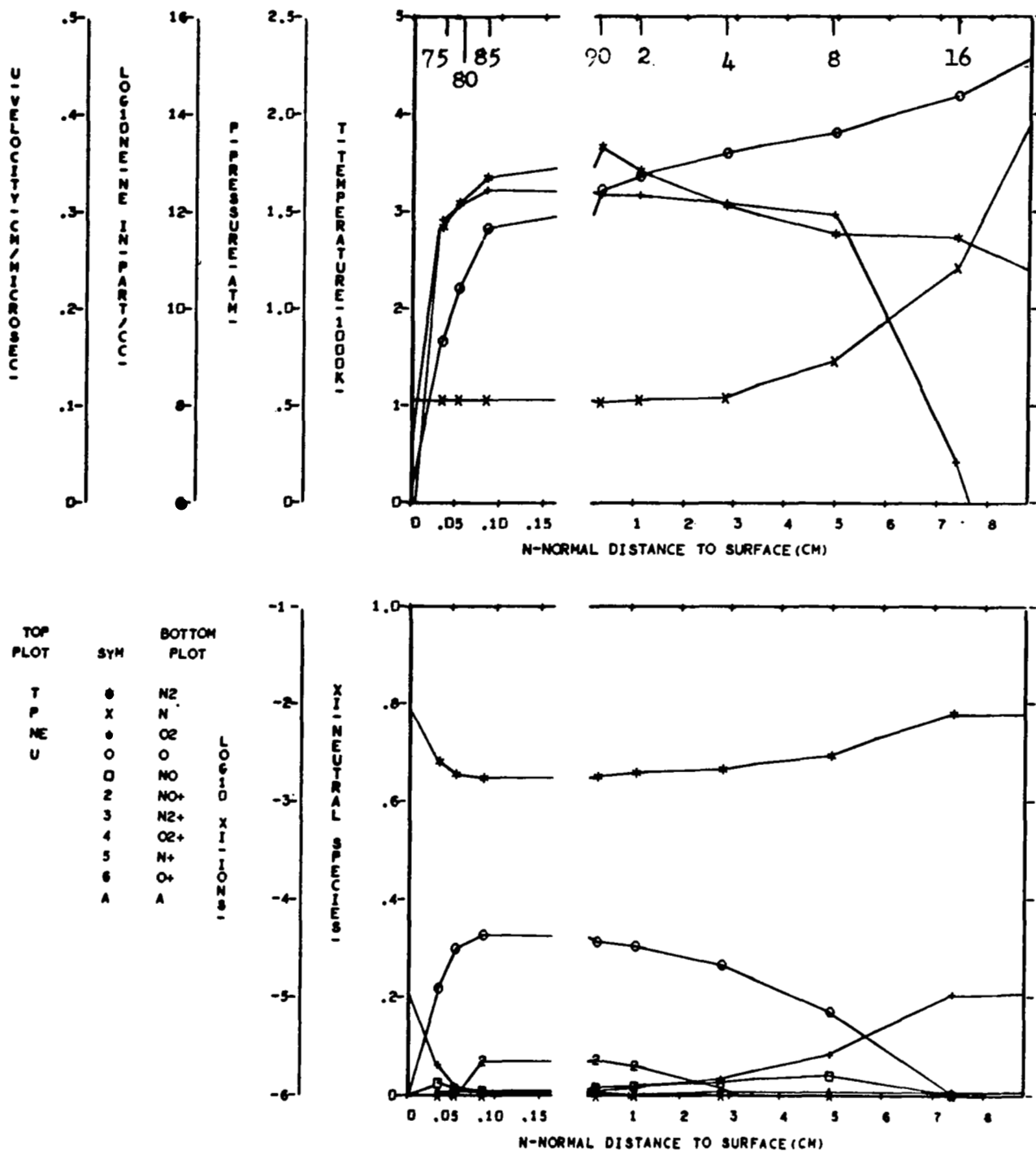
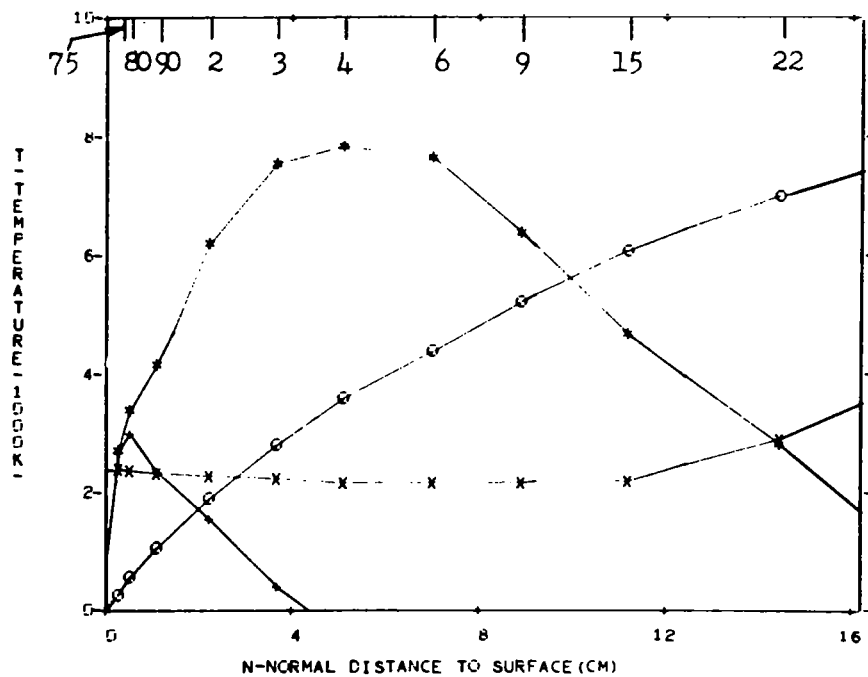FIGURE 61 NONEQUILIBRIUM FLOW FIELD PROPERTIES - CASE 2, NORMAL 7
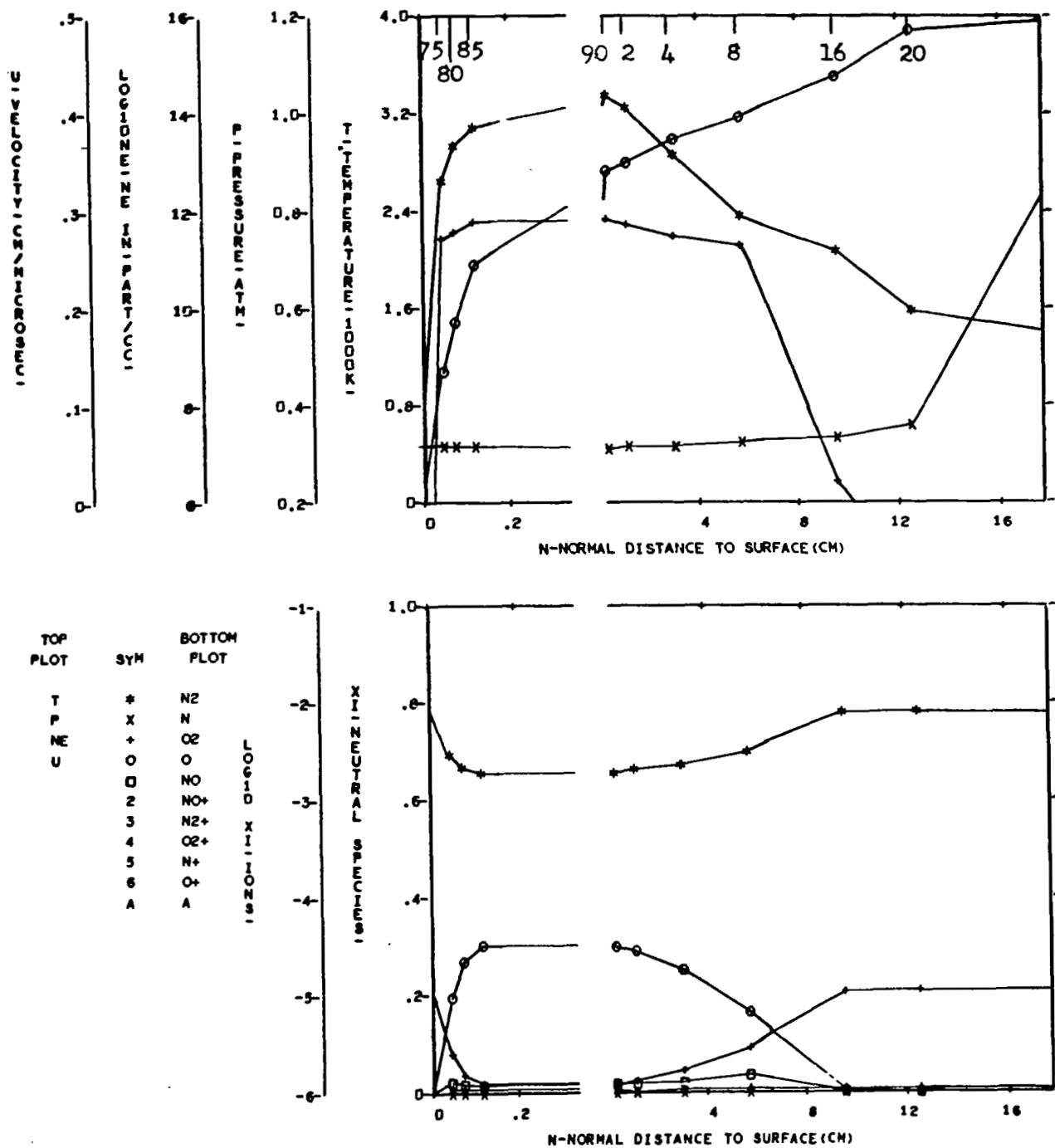
FIGURE 62 NONEQUILIBRIUM FLOW FIELD PROPERTIES - CASE 2, NORMAL 9

97
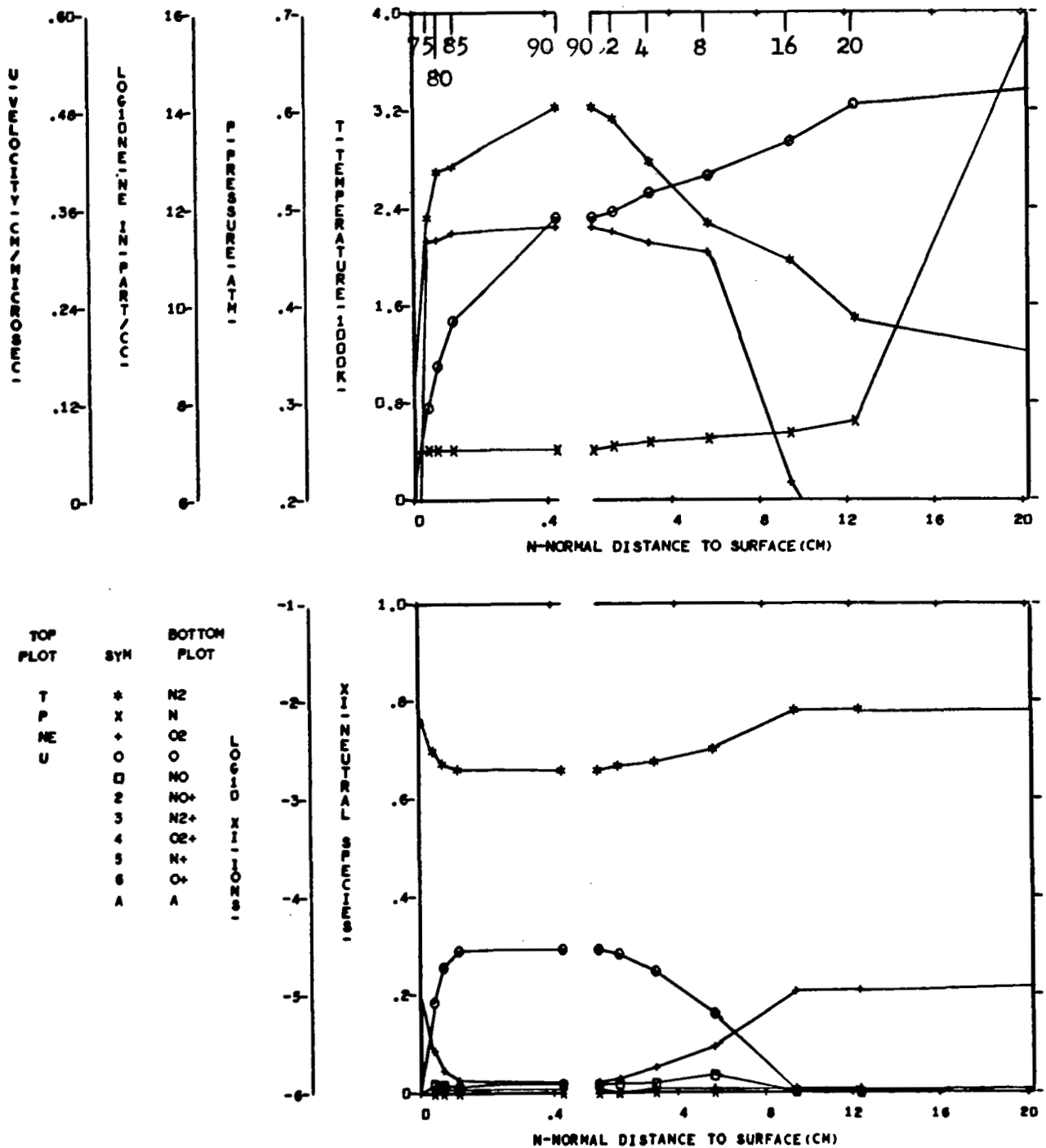
FIGURE 63 NONEQUILIBRIUM FLOW FIELD PROPERTIES - CASE 2, NORMAL 11
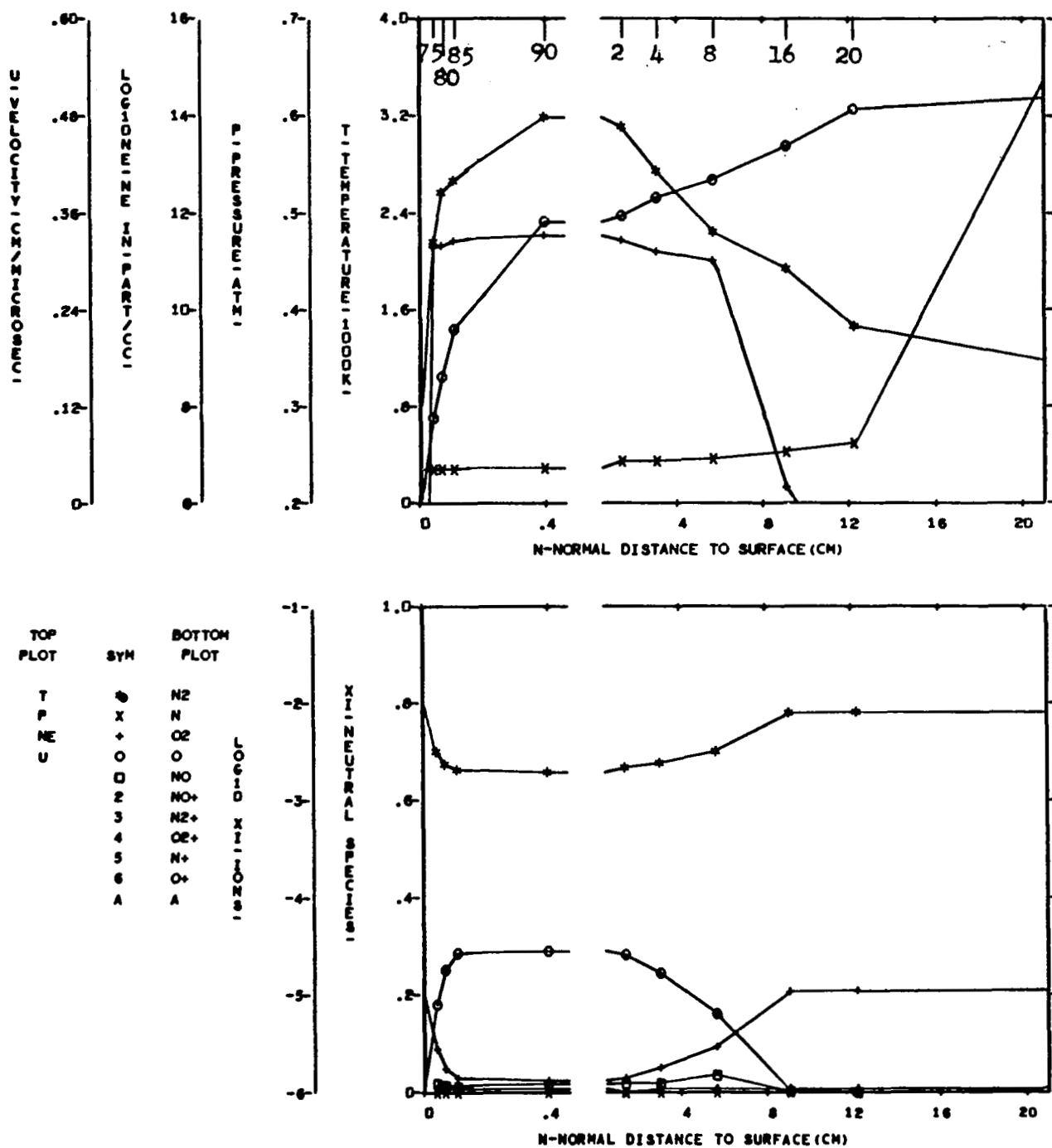
FIGURE 64. NONEQUILIBRIUM FLOW FIELD PROPERTIES - CASE 2, NORMAL 12
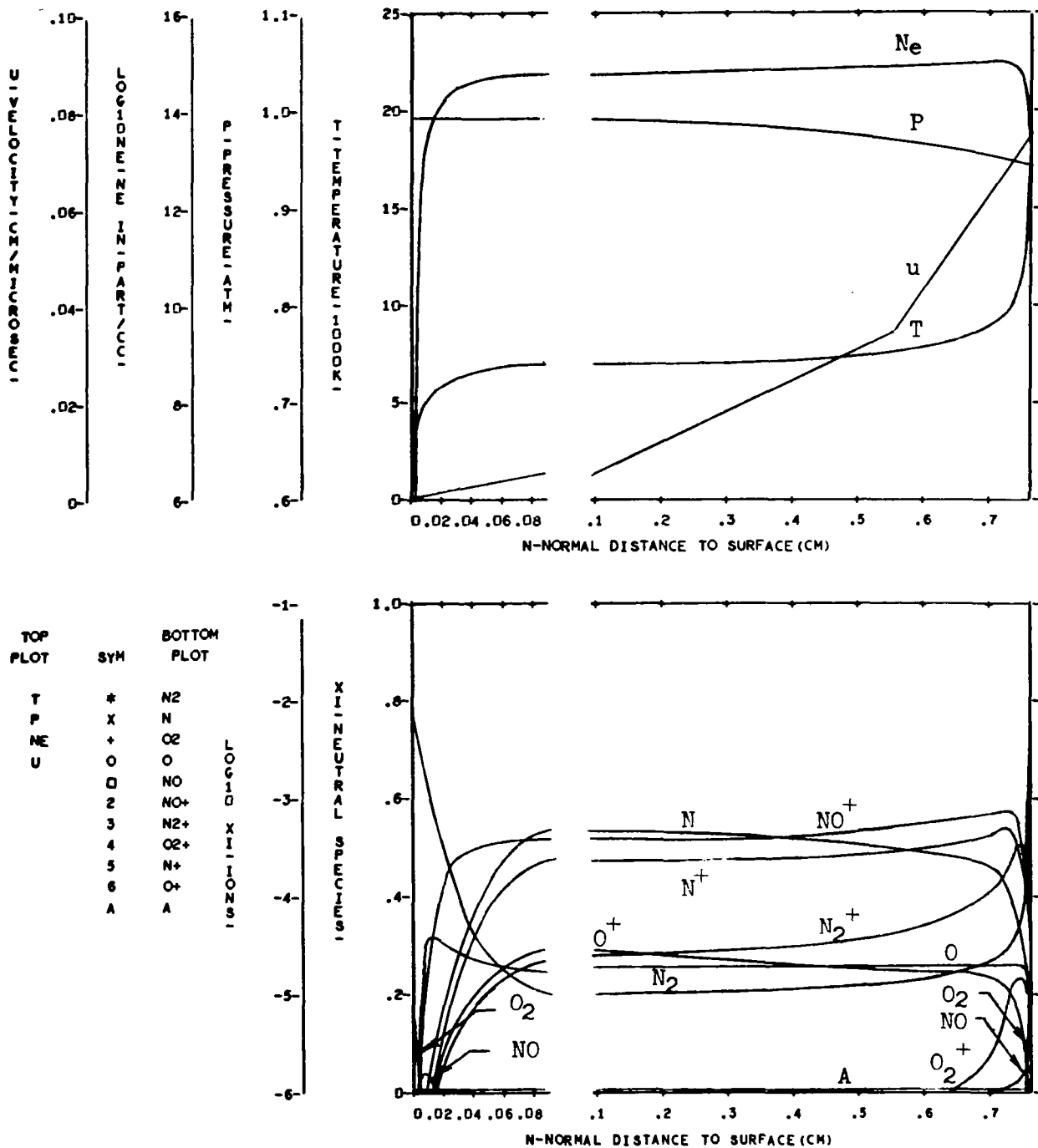
FIGURE 65 NONEQUILIBRIUM FLOW FIELD PROPERTIES - CASE 3, NORMAL 1
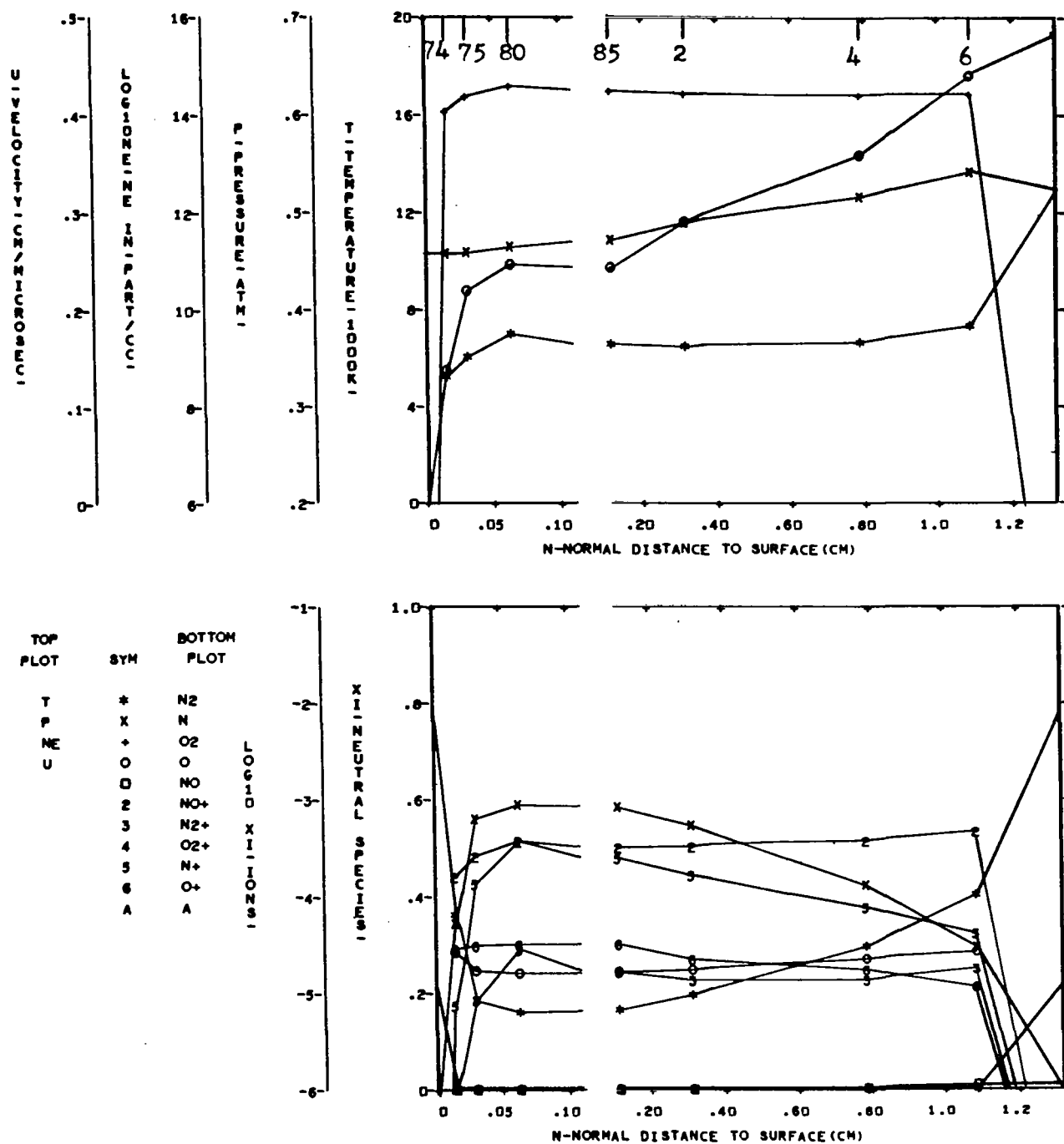
FIGURE 66 NONEQUILIBRIUM FLOW FIELD PROPERTIES - CASE 3, NORMAL 4
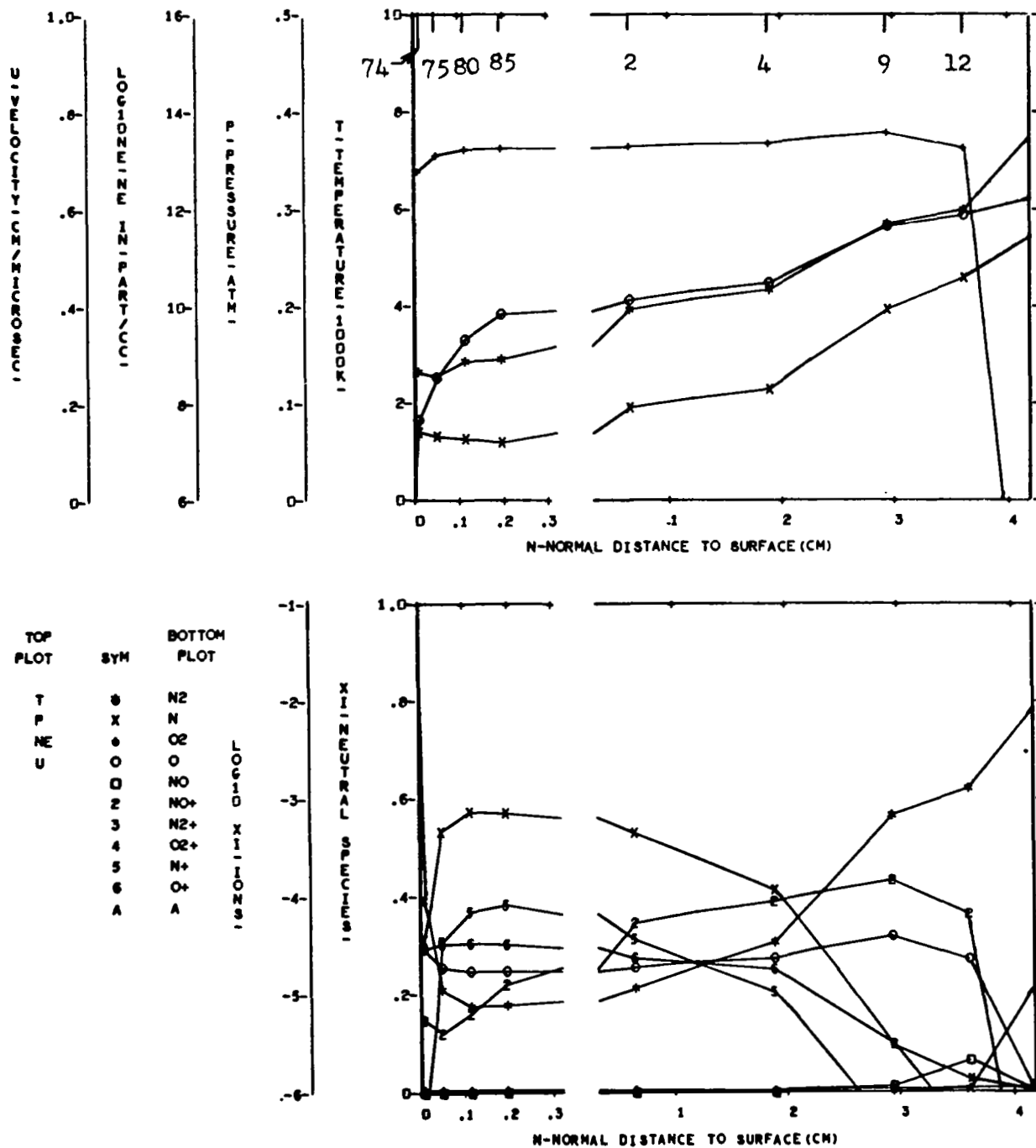
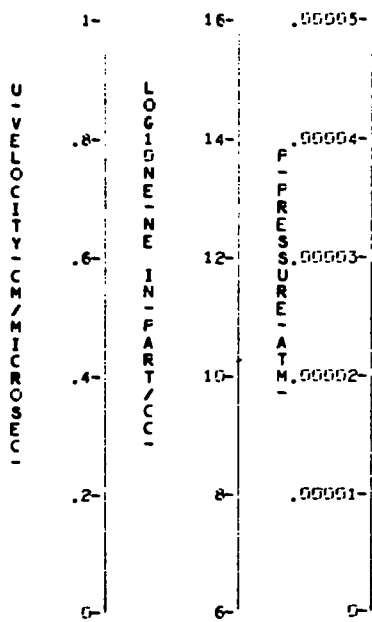FIGURE 67 NONEQUILIBRIUM FLOW FIELD PROPERTIES - CASE 3, NORMAL 6

102
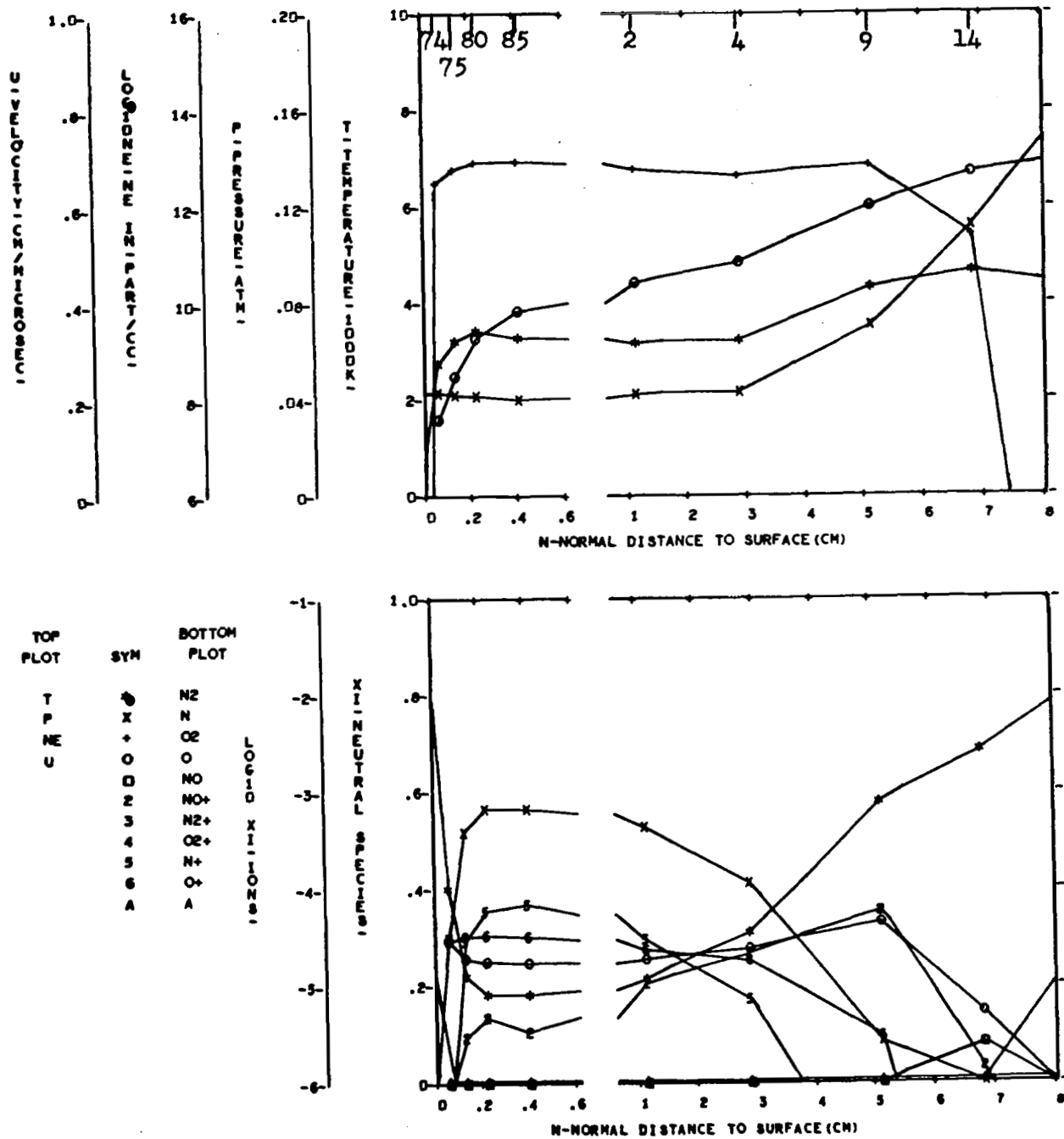
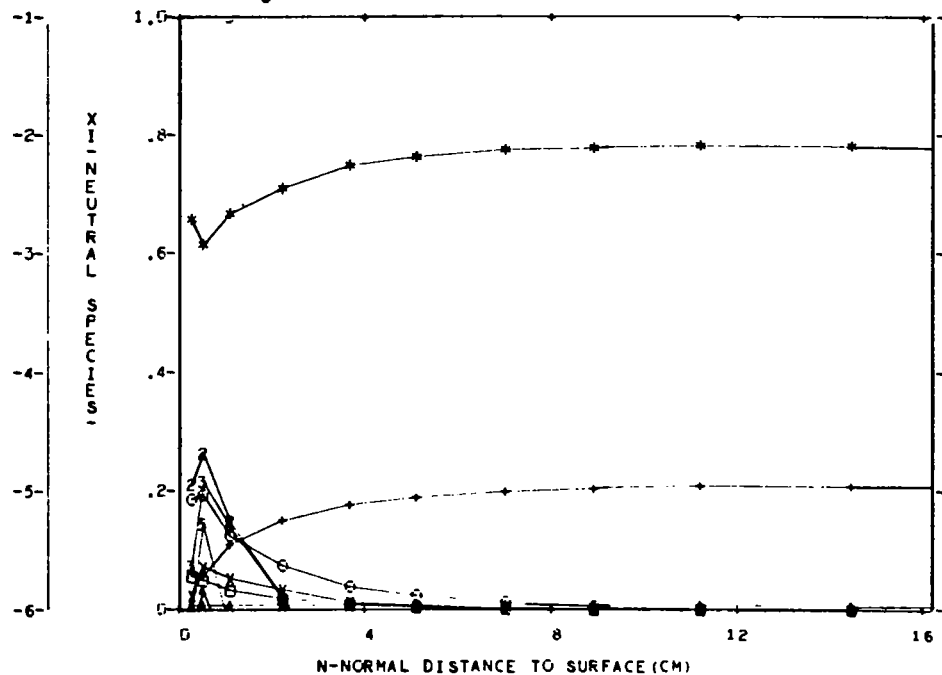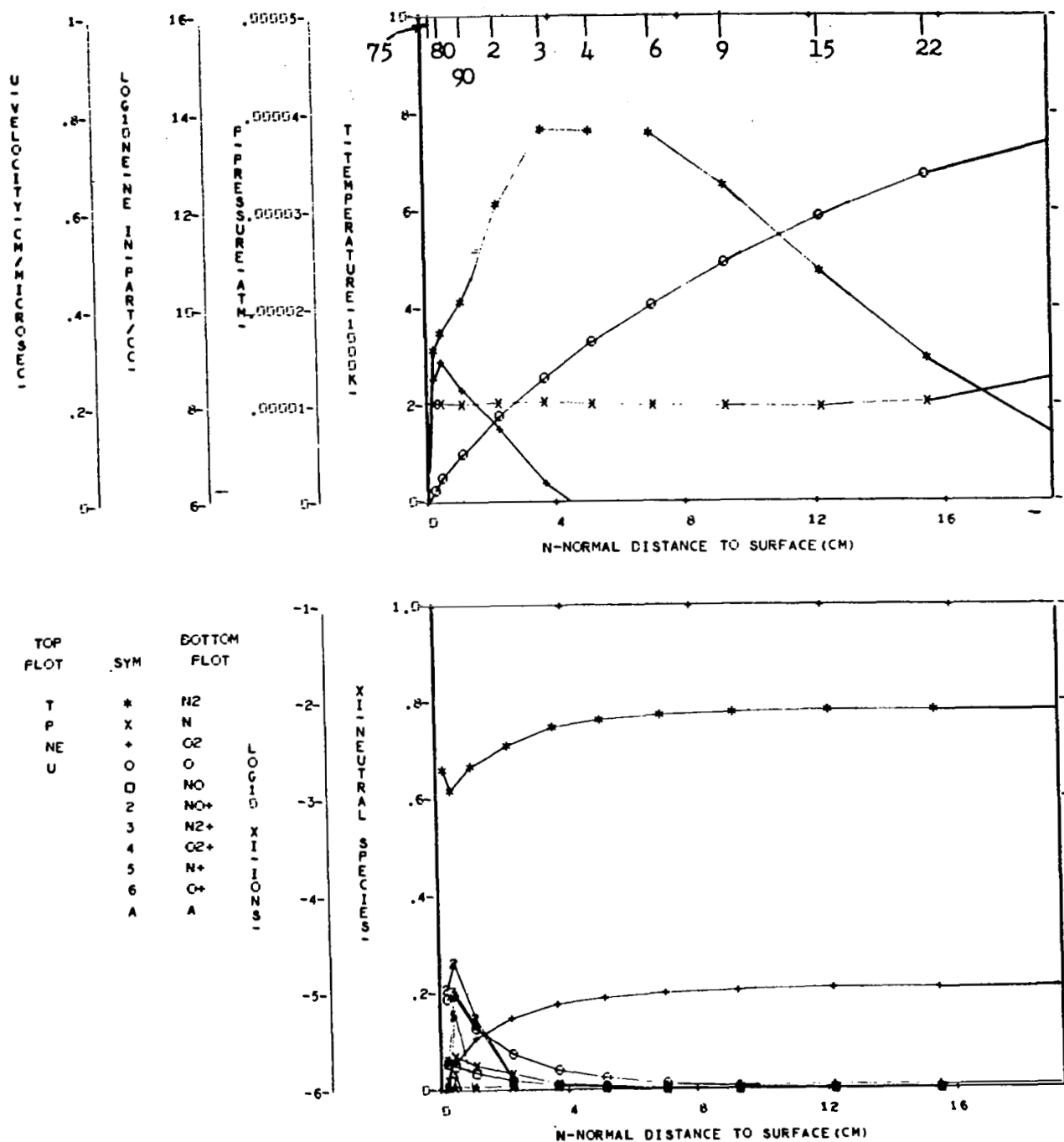FIGURE 68 NONEQUILIBRIUM FLOW FIELD PROPERTIES - CASE 3, NORMAL 7

103
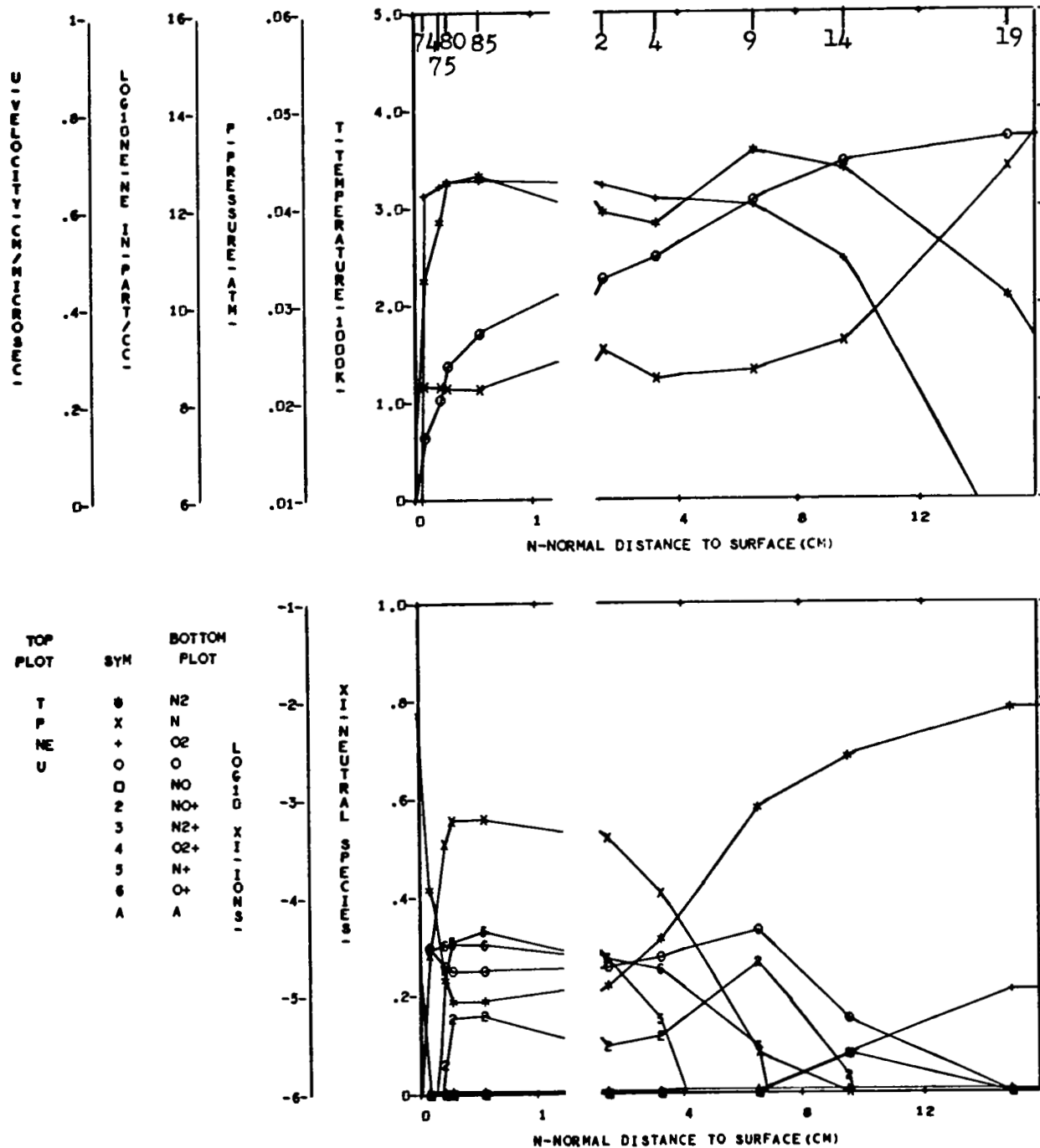
FIGURE 69 NONEQUILIBRIUM FLOW FIELD PROPERTIES - CASE 3, NORMAL 9
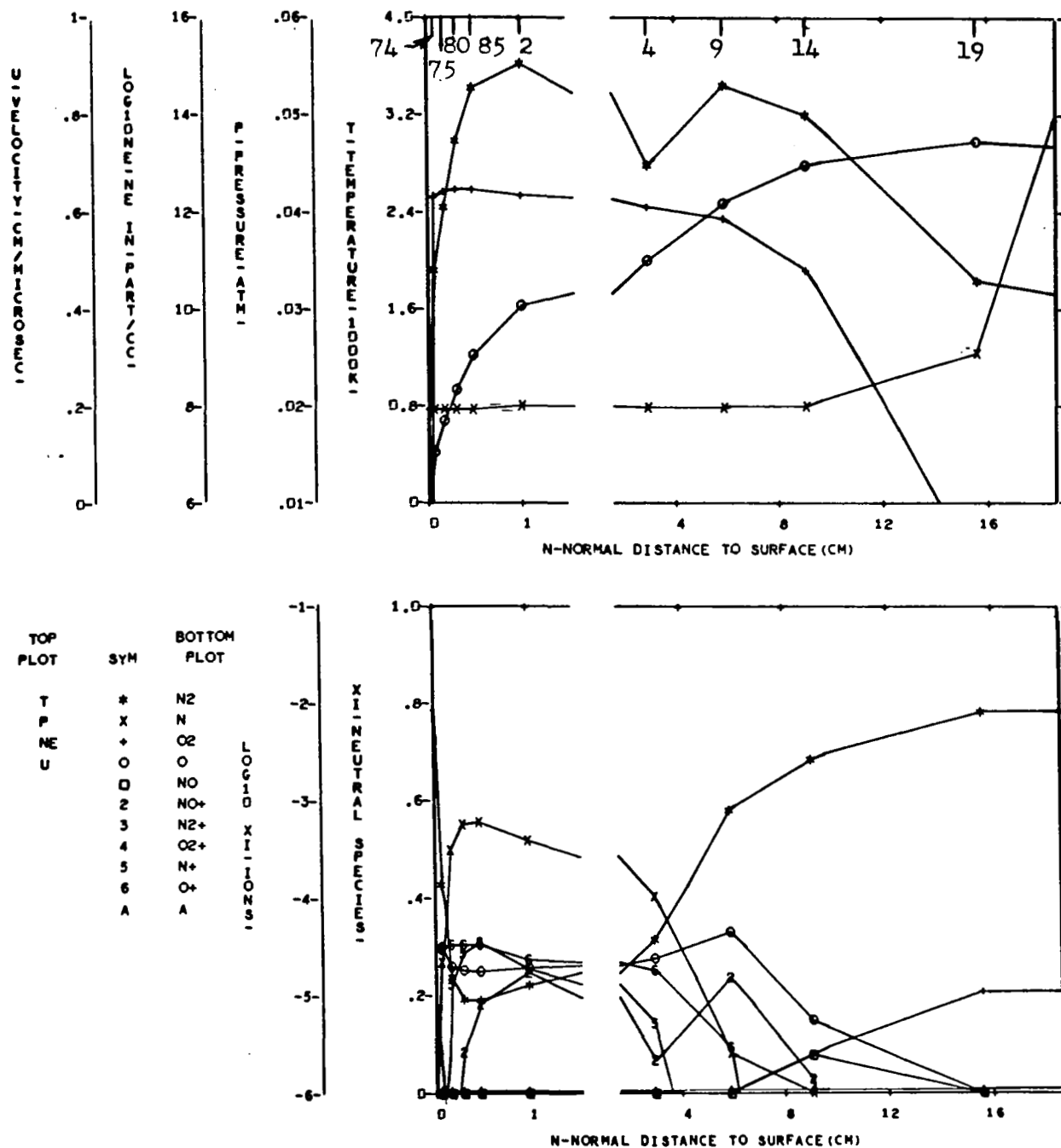
FIGURE 70 NONEQUILIBRIUM FLOW FIELD PROPERTIES - CASE 3, NORMAL 11

105
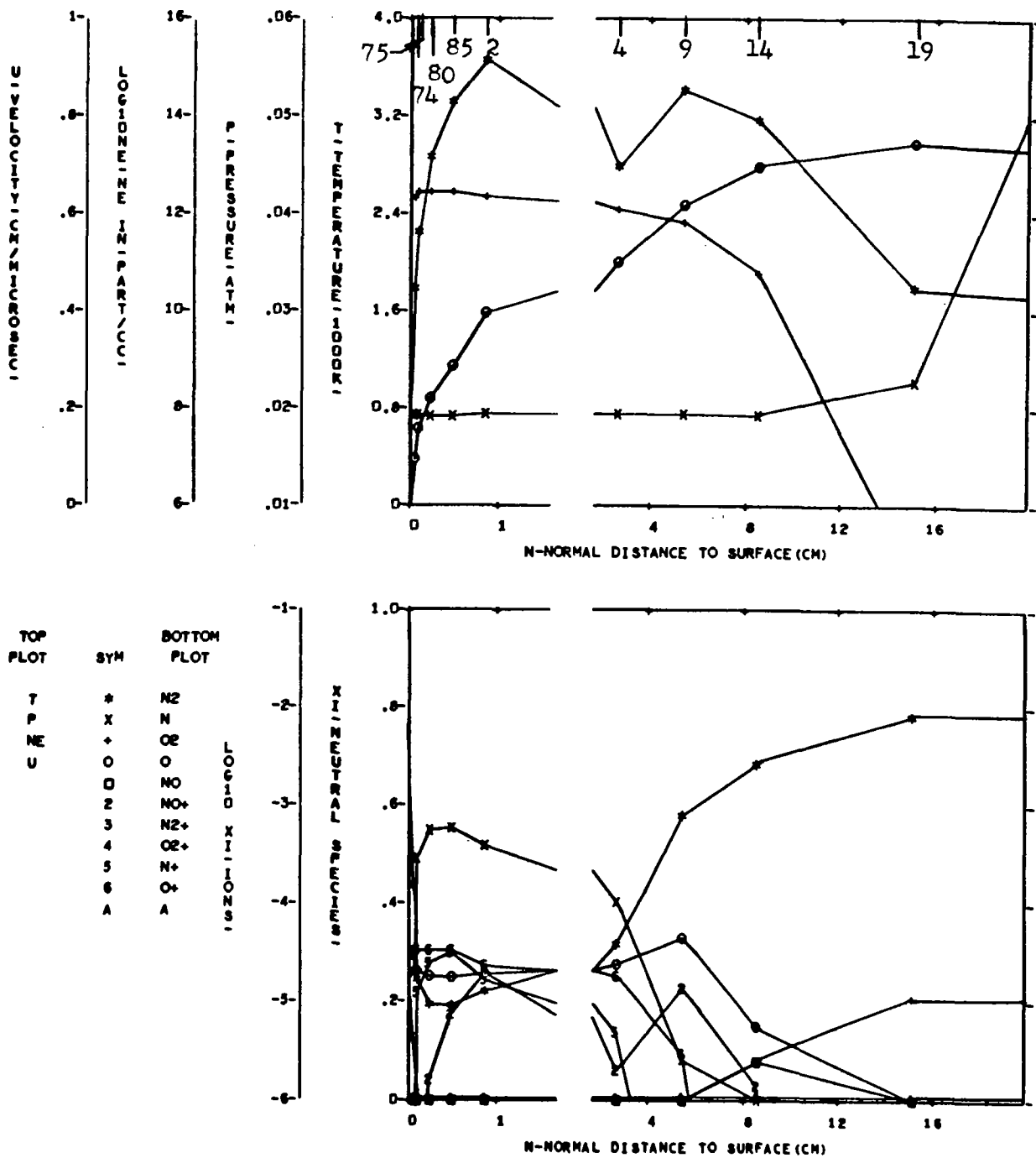
FIGURE 71 NONEQUILIBRIUM FLOW FIELD PROPERTIES - CASE 3, NORMAL 12

106

FIGURE 72   NONEQUILIBRIUM FLOW FIELD PROPERTIES - CASE 4, NORMAL 1
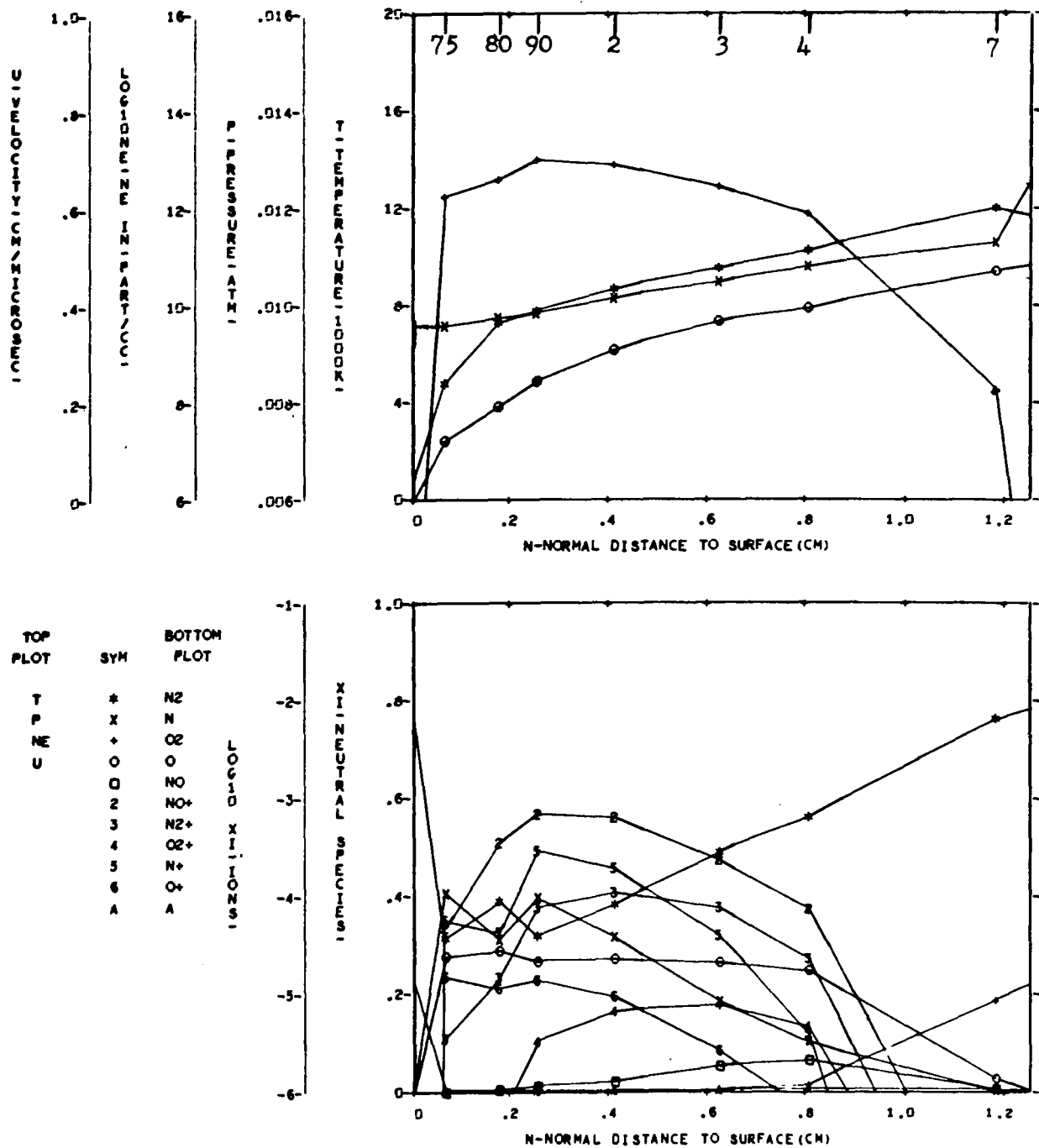
FIGURE 73   NONEQUILIBRIUM FLOW FIELD PROPERTIES - CASE 4, NORMAL 4
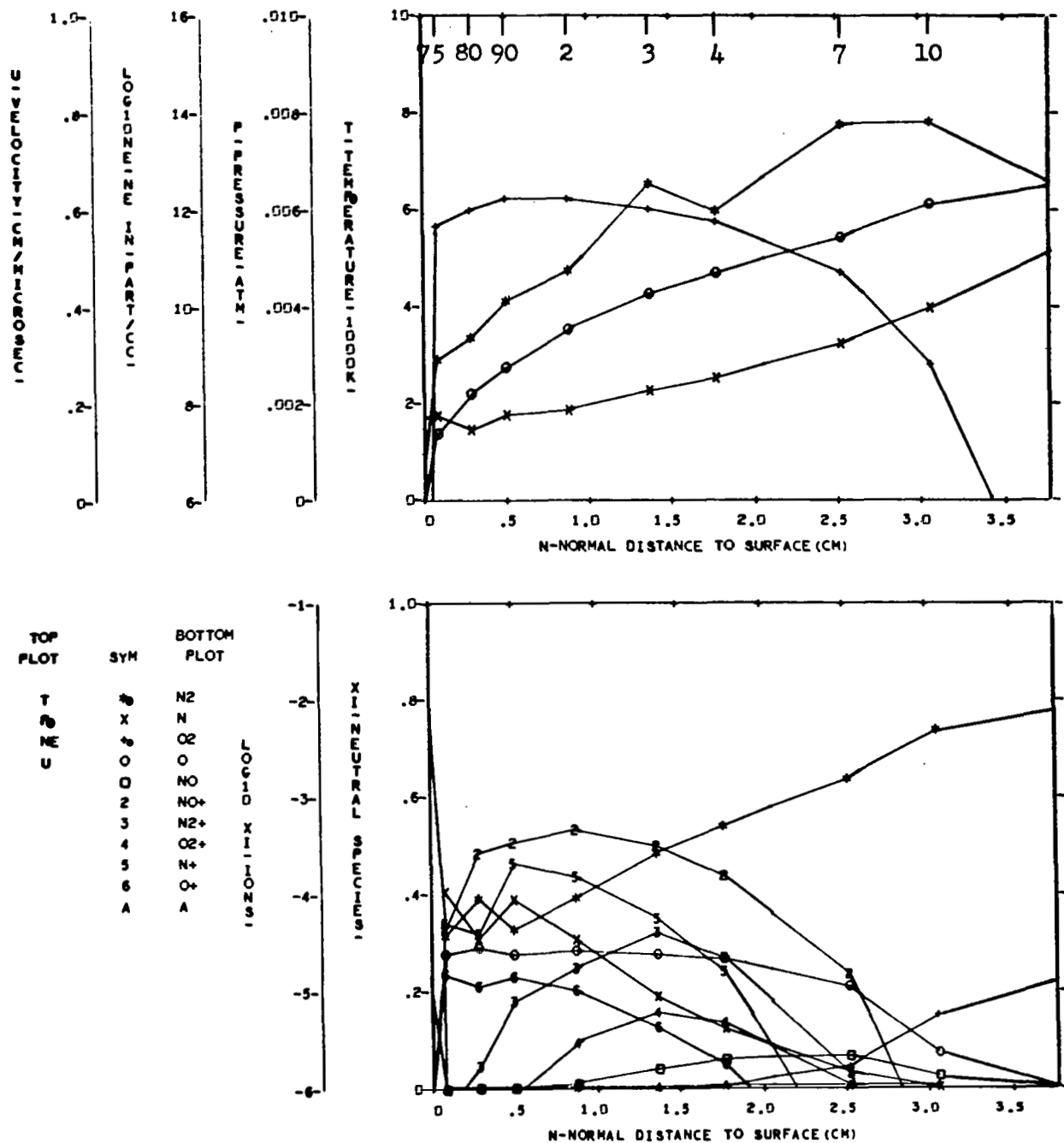
FIGURE 74 NONEQUILIBRIUM FLOW FIELD PROPERTIES - CASE 4, NORMAL 6
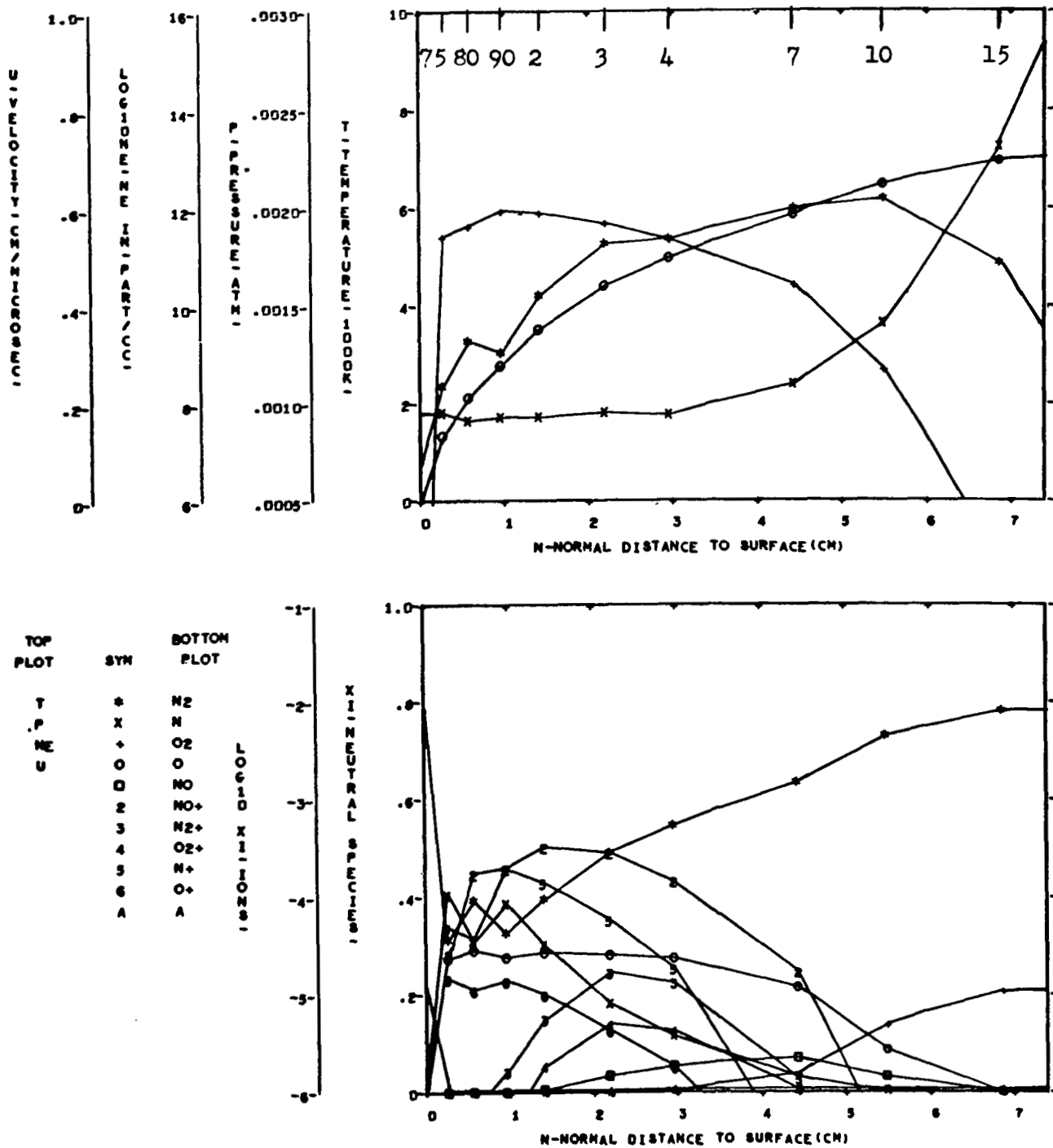
FIGURE 75 NONEQUILIBRIUM FLOW FIELD PROPERTIES - CASE 4, NORMAL 7
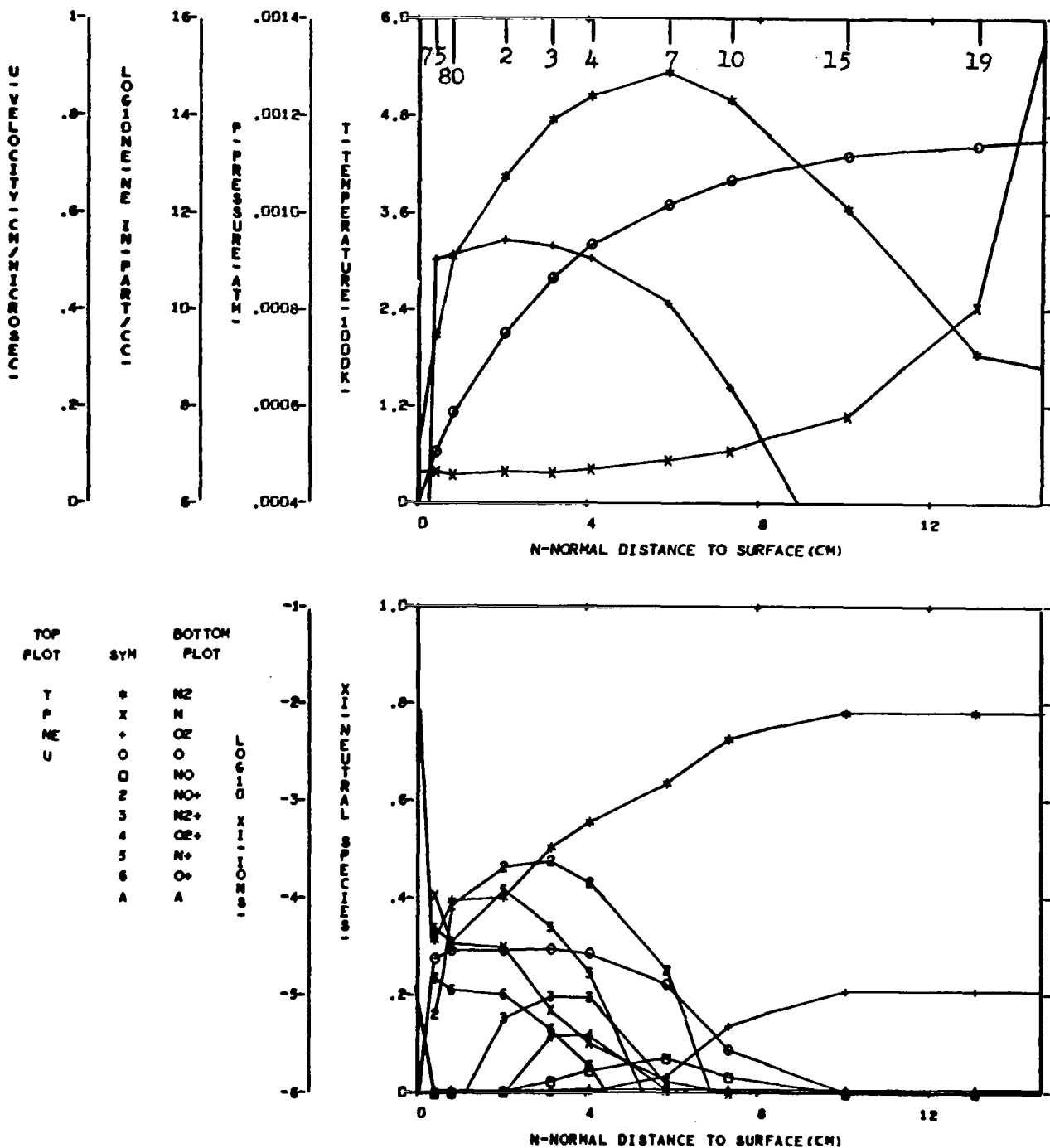
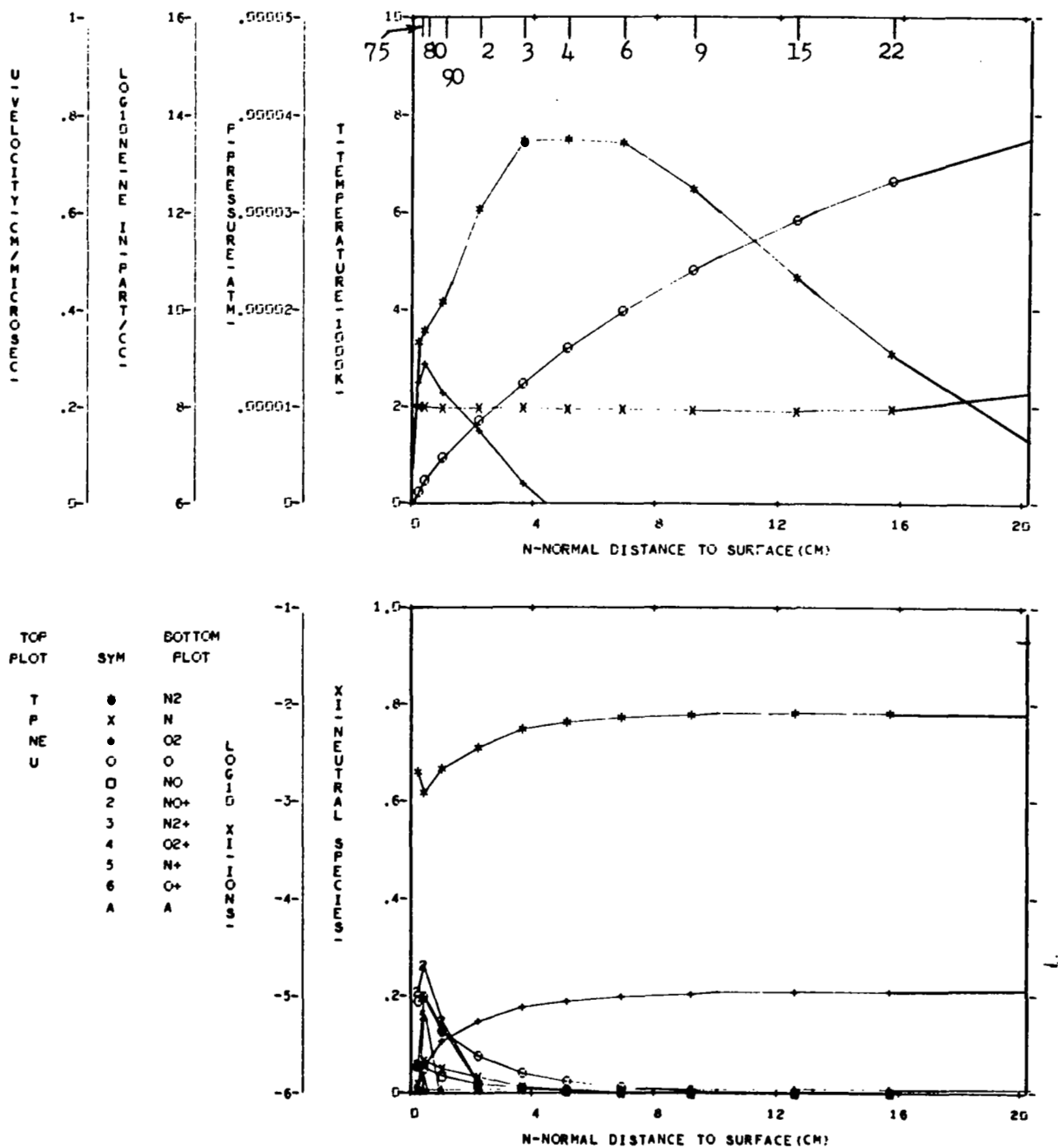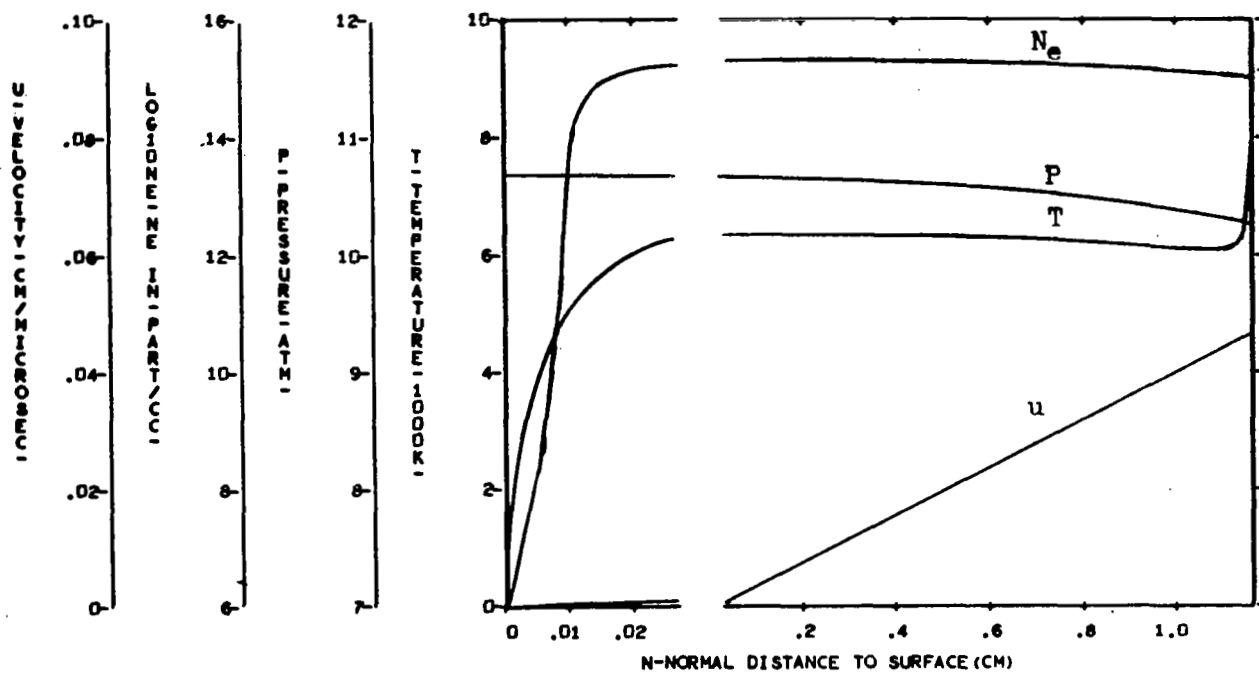FIGURE 76   NONEQUILIBRIUM FLOW FIELD PROPERTIES - CASE 4, NORMAL 9

111
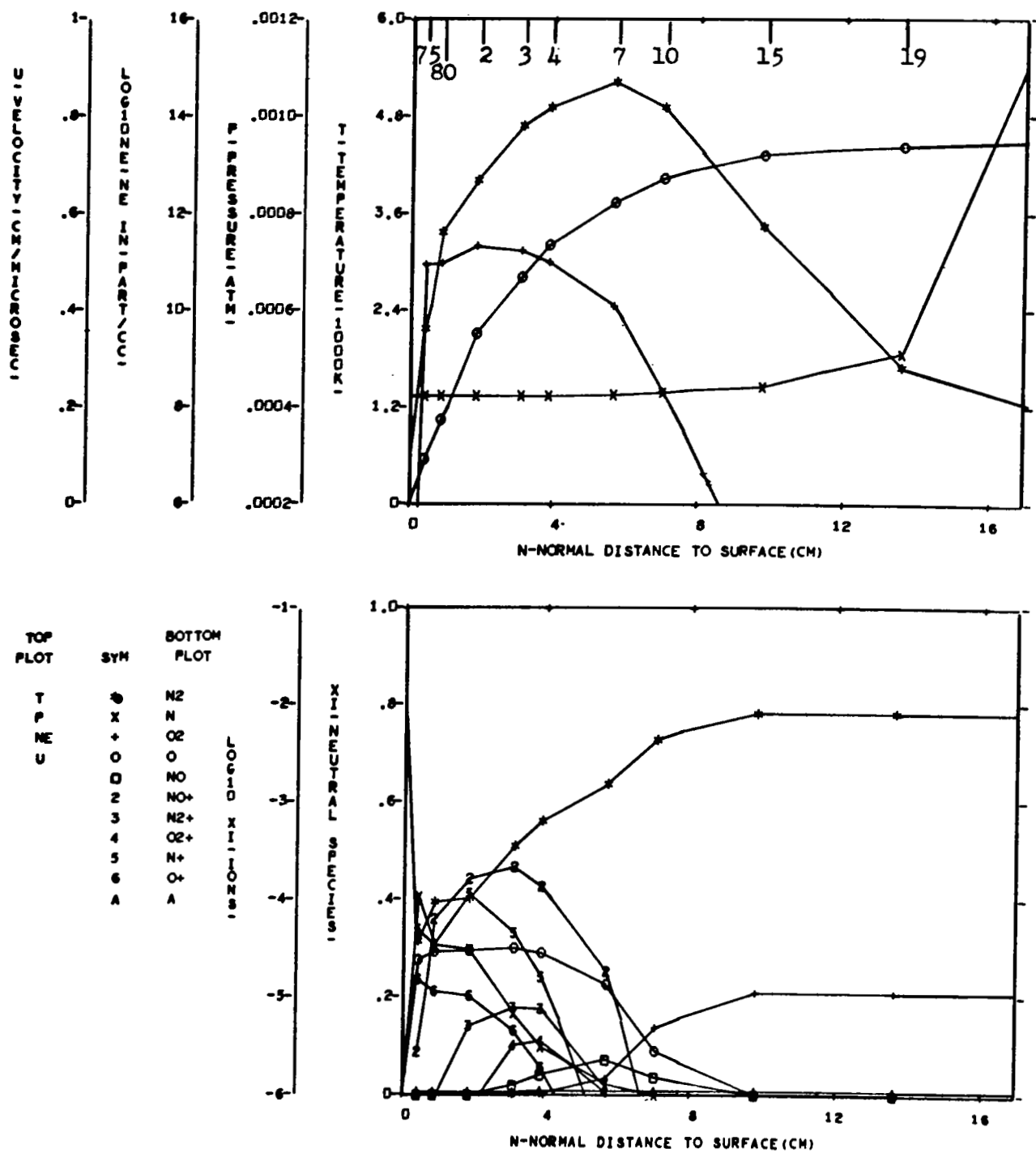
FIGURE 77 NONEQUILIBRIUM FLOW FIELD PROPERTIES - CASE 4, NORMAL 11

112
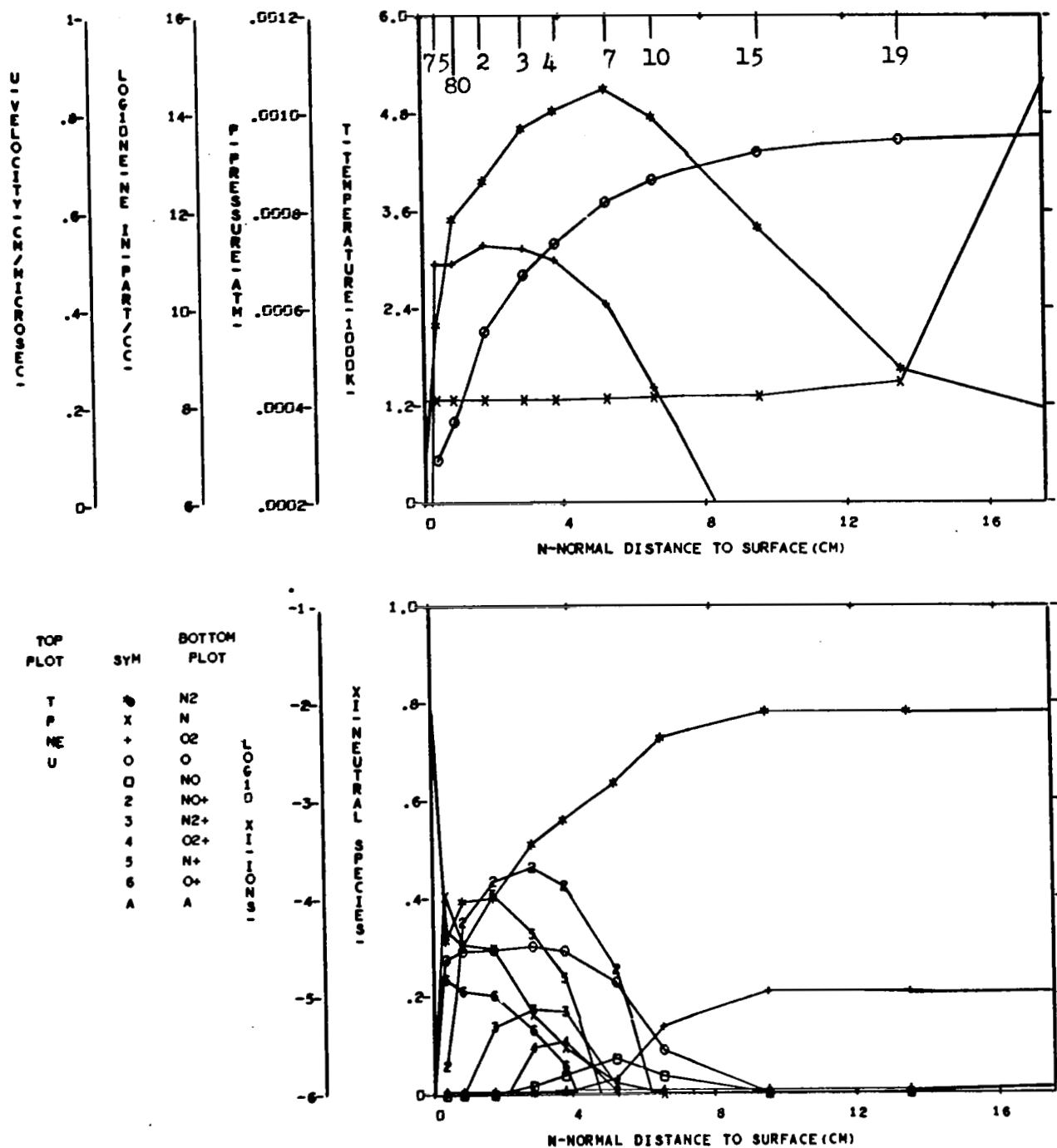
FIGURE 78 NONEQUILIBRIUM FLOW FIELD PROPERTIES - CASE 4, NORMAL 12

113
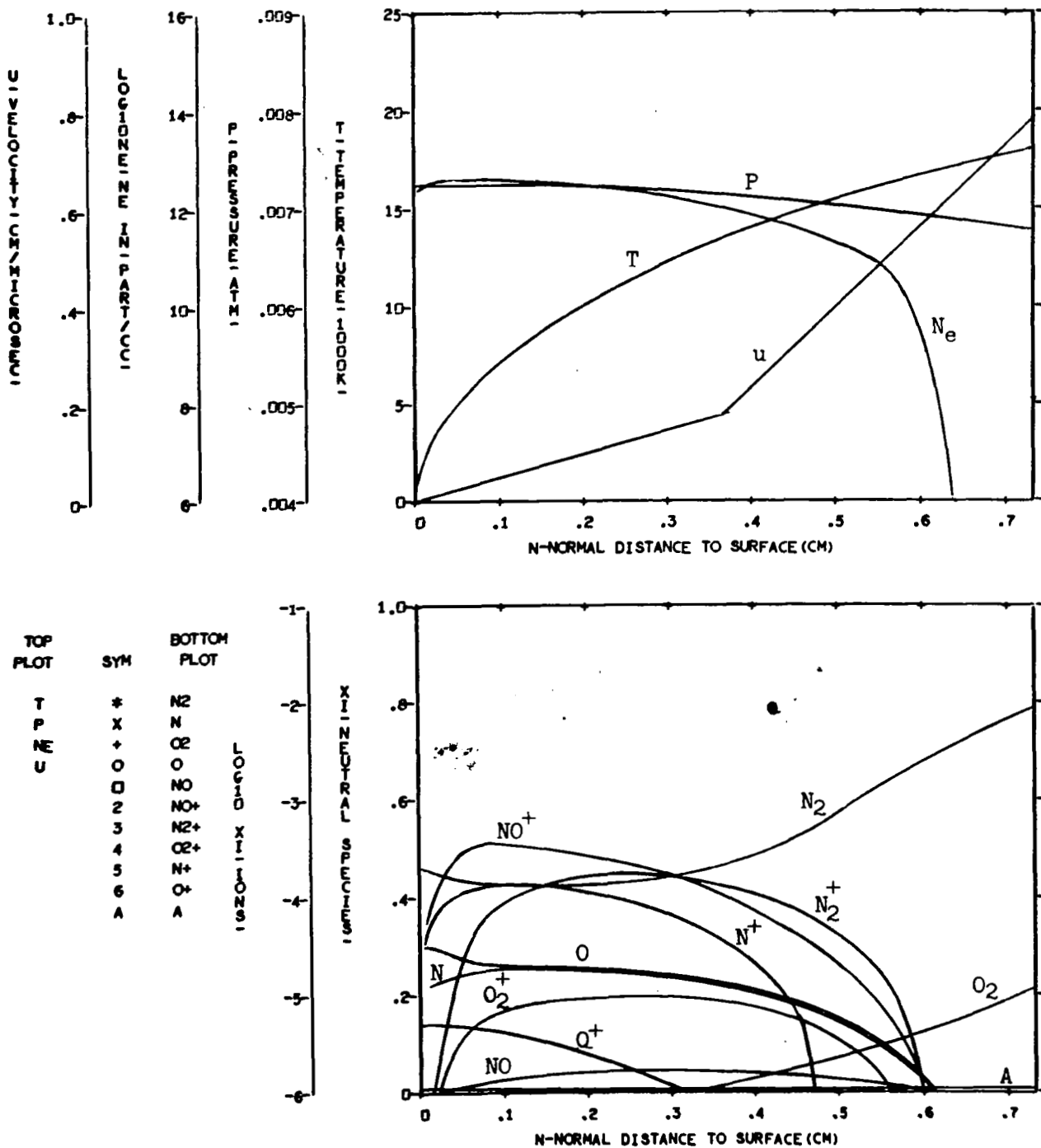
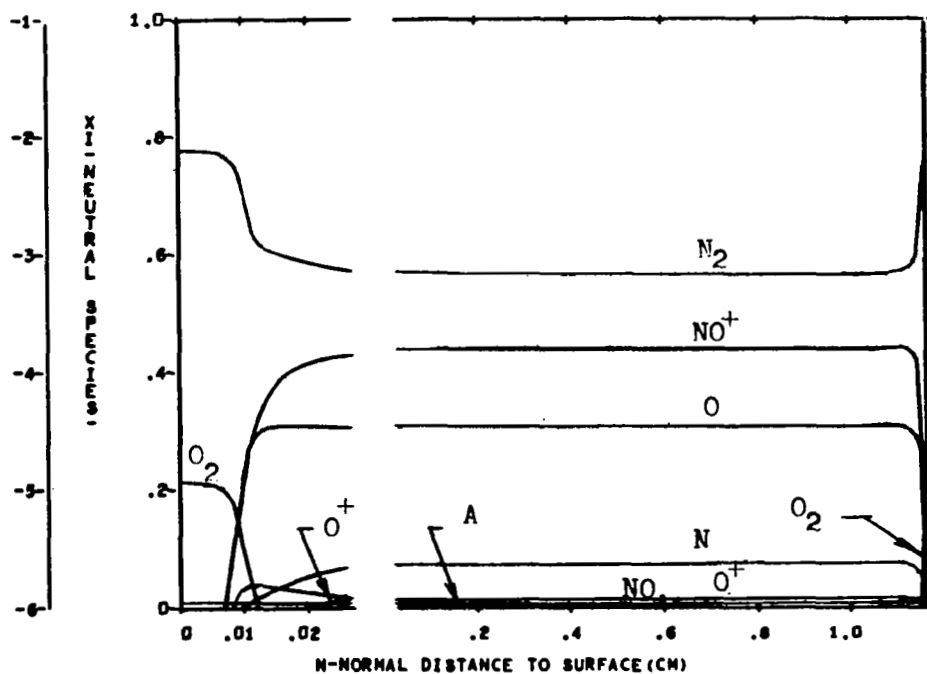FIGURE 79 NONEQUILIBRIUM FLOW FIELD PROPERTIES - CASE 5, NORMAL 1
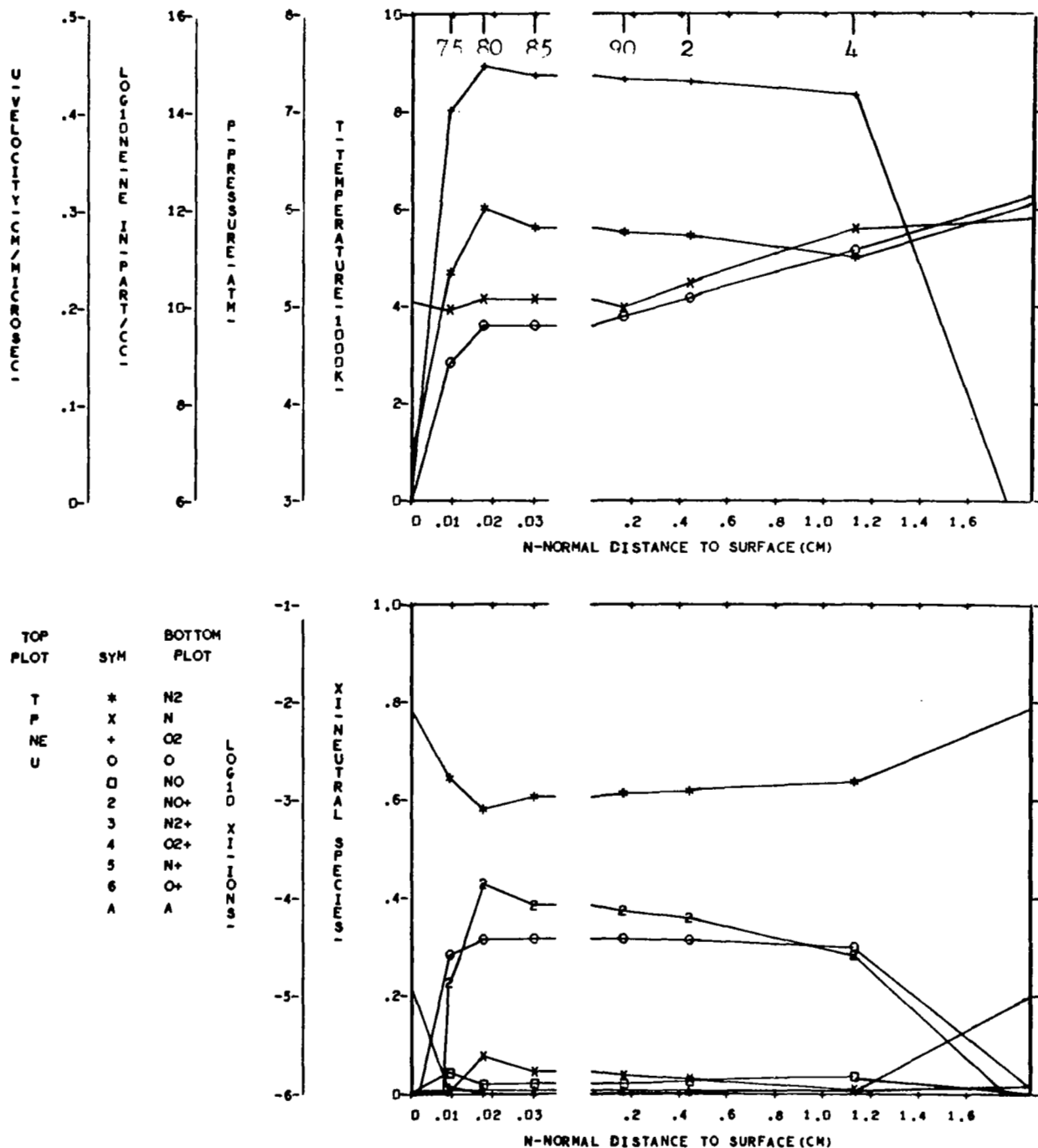
114
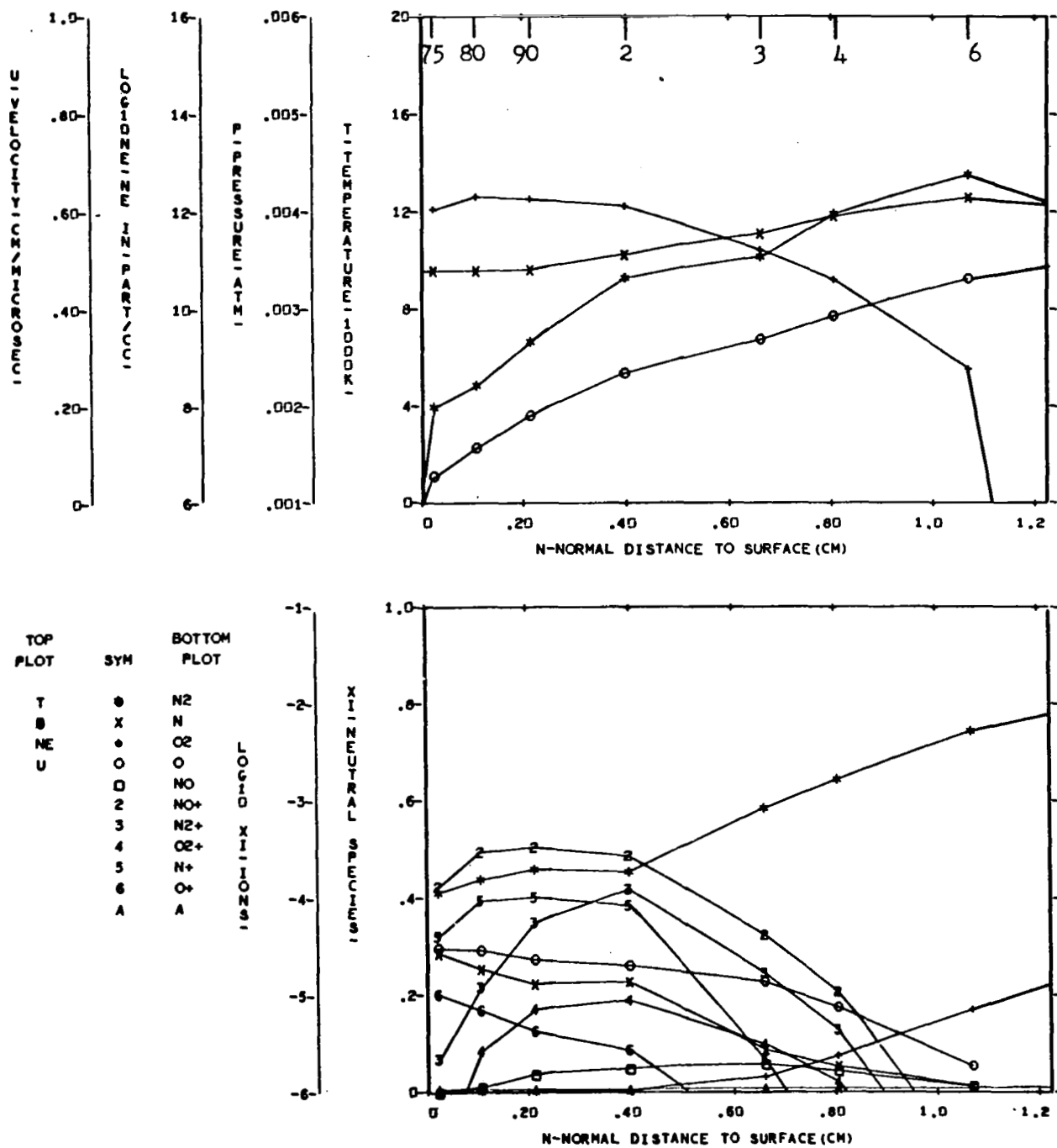
FIGURE 80 NONEQUILIBRIUM FLOW FIELD PROPERTIES - CASE 5, NORMAL 4
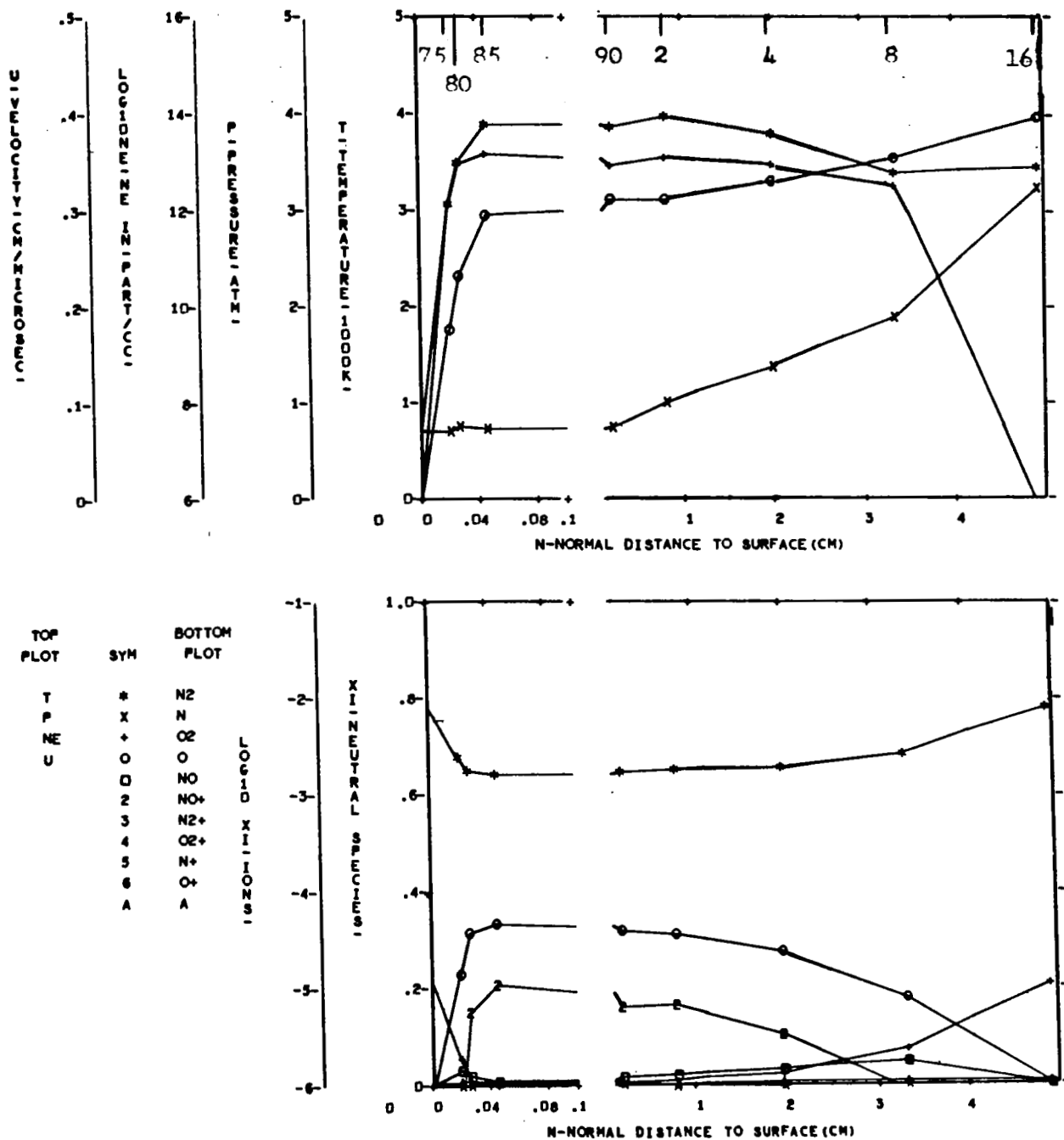
115
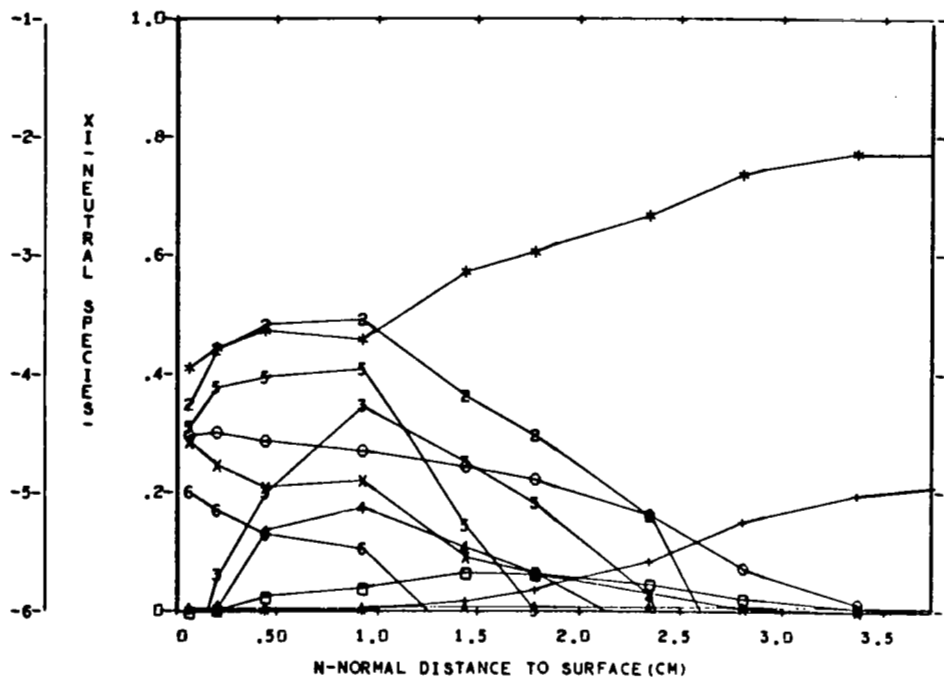
FIGURE 81 NONEQUILIBRIUM FLOW FIELD PROPERTIES - CASE 5, NORMAL 6
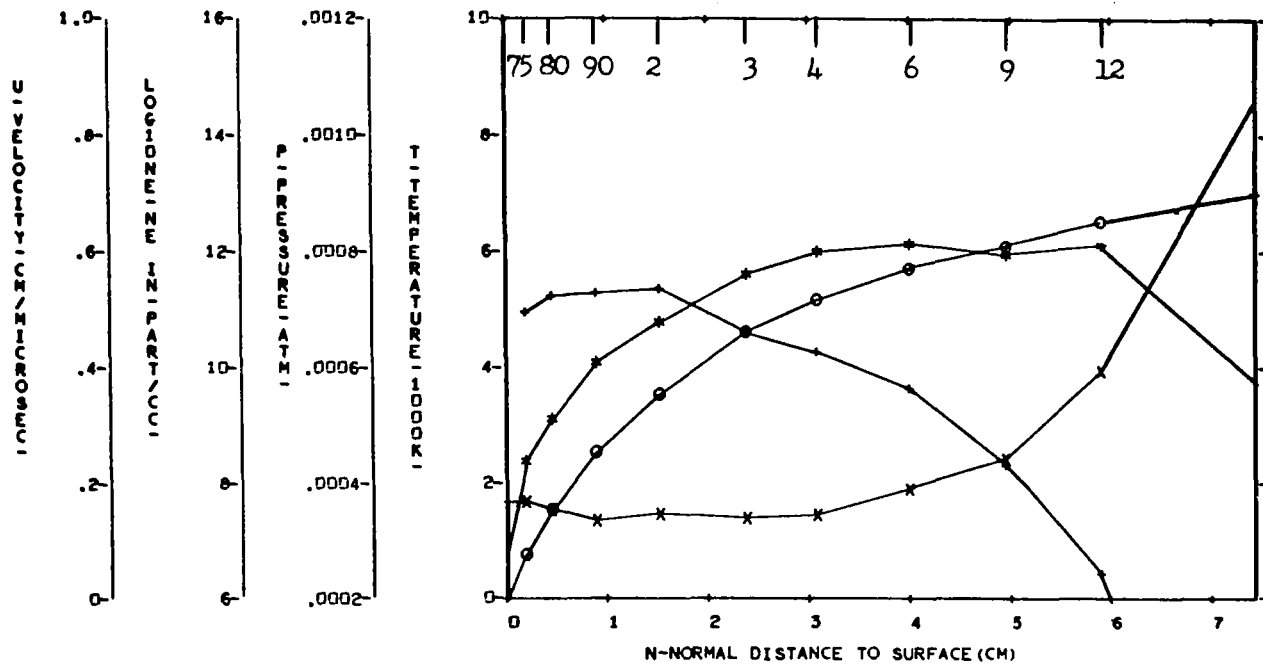
FIGURE 82 NONEQUILIBRIUM FLOW FIELD PROPERTIES - CASE 5, NORMAL 7

117

FIGURE 83 NONEQUILIBRIUM FLOW FIELD PROPERTIES - CASE 5, NORMAL 9

118

FIGURE 84 NONEQUILIBRIUM FLOW FIELD PROPERTIES - CASE 5, NORMAL 11

FIGURE 85 NONEQUILIBRIUM FLOW FIELD PROPERTIES - CASE 5, NORMAL 12

120

FIGURE 86 NONEQUILIBRIUM FLOW FIELD PROPERTIES - CASE 6, NORMAL 1

FIGURE 87   NONEQUILIBRIUM FLOW FIELD PROPERTIES - CASE 6, NORMAL 4

122

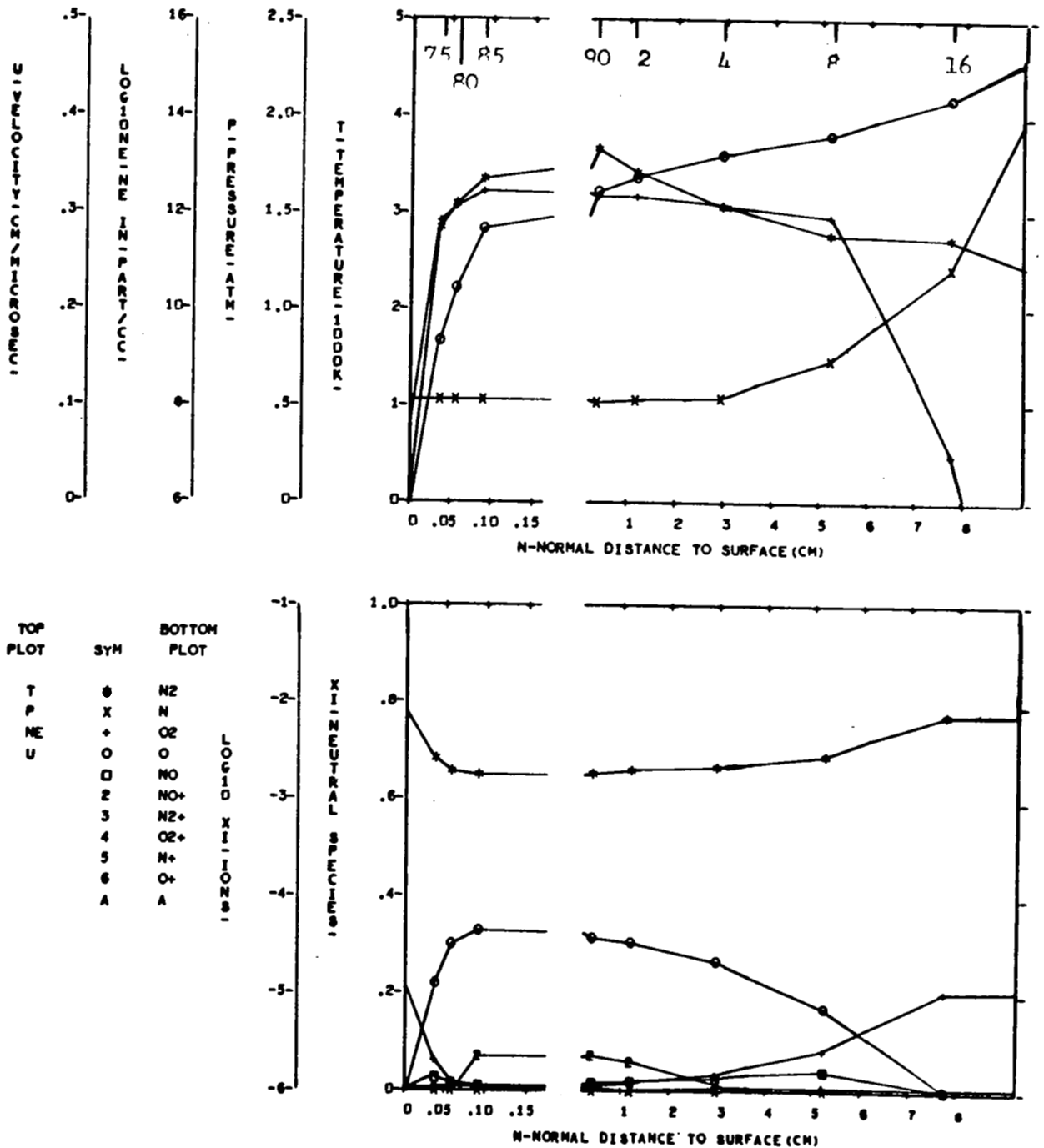FIGURE 88 NONEQUILIBRIUM FLOW FIELD PROPERTIES - CASE 6, NORMAL 6

123

FIGURE 89 NONEQUILIBRIUM FLOW FIELD PROPERTIES - CASE 6, NORMAL 7

FIGURE 90 NONEQUILIBRIUM FLOW FIELD PROPERTIES - CASE 6, NORMAL 9

125

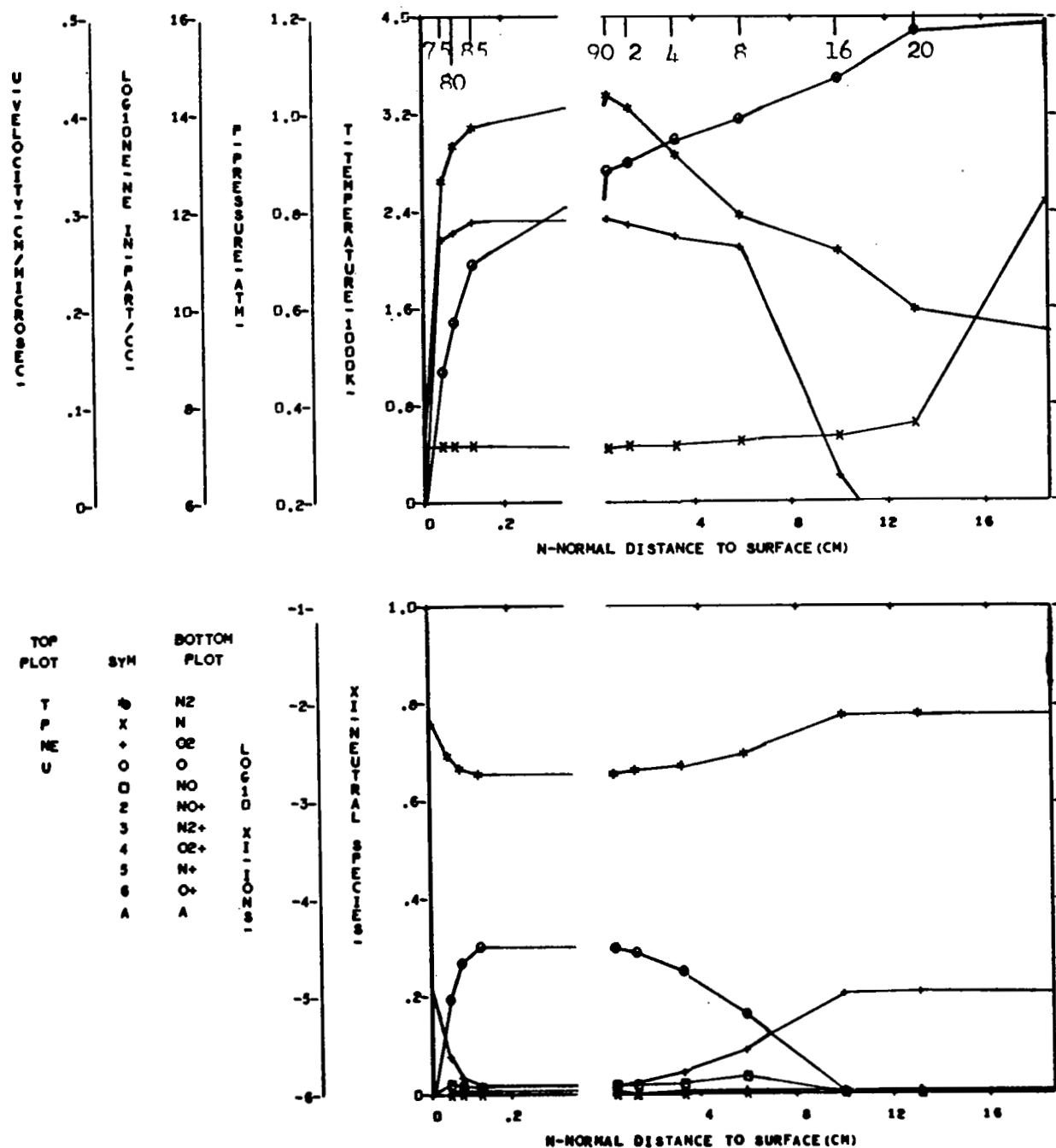FIGURE 91 NONEQUILIBRIUM FLOW FIELD PROPERTIES - CASE 6, NORMAL 11

126

FIGURE 92   NONEQUILIBRIUM FLOW FIELD PROPERTIES - CASE 6, NORMAL 12

FIGURE 93   NONEQUILIBRIUM FLOW FIELD PROPERTIES - CASE 7, NORMAL 1

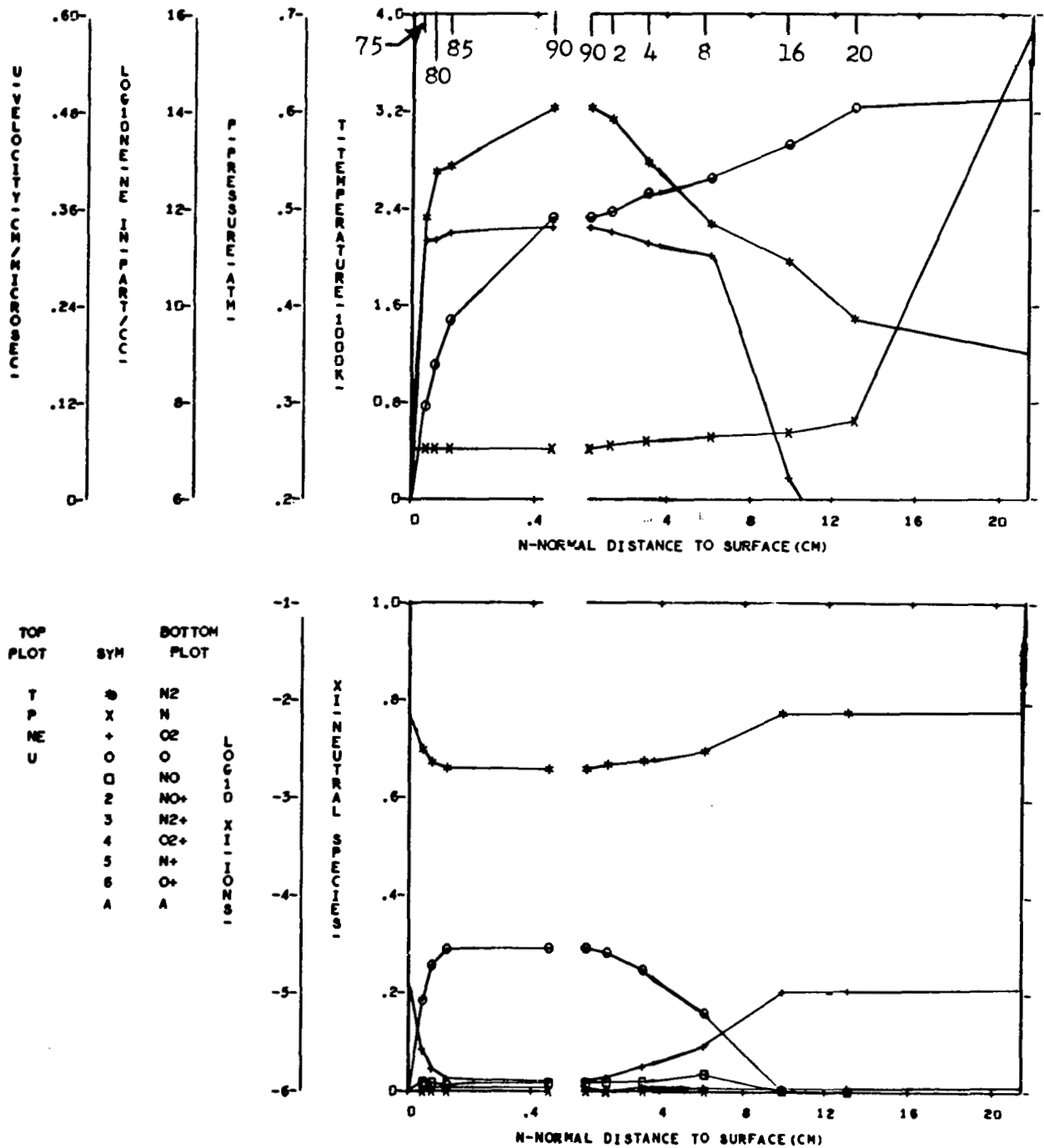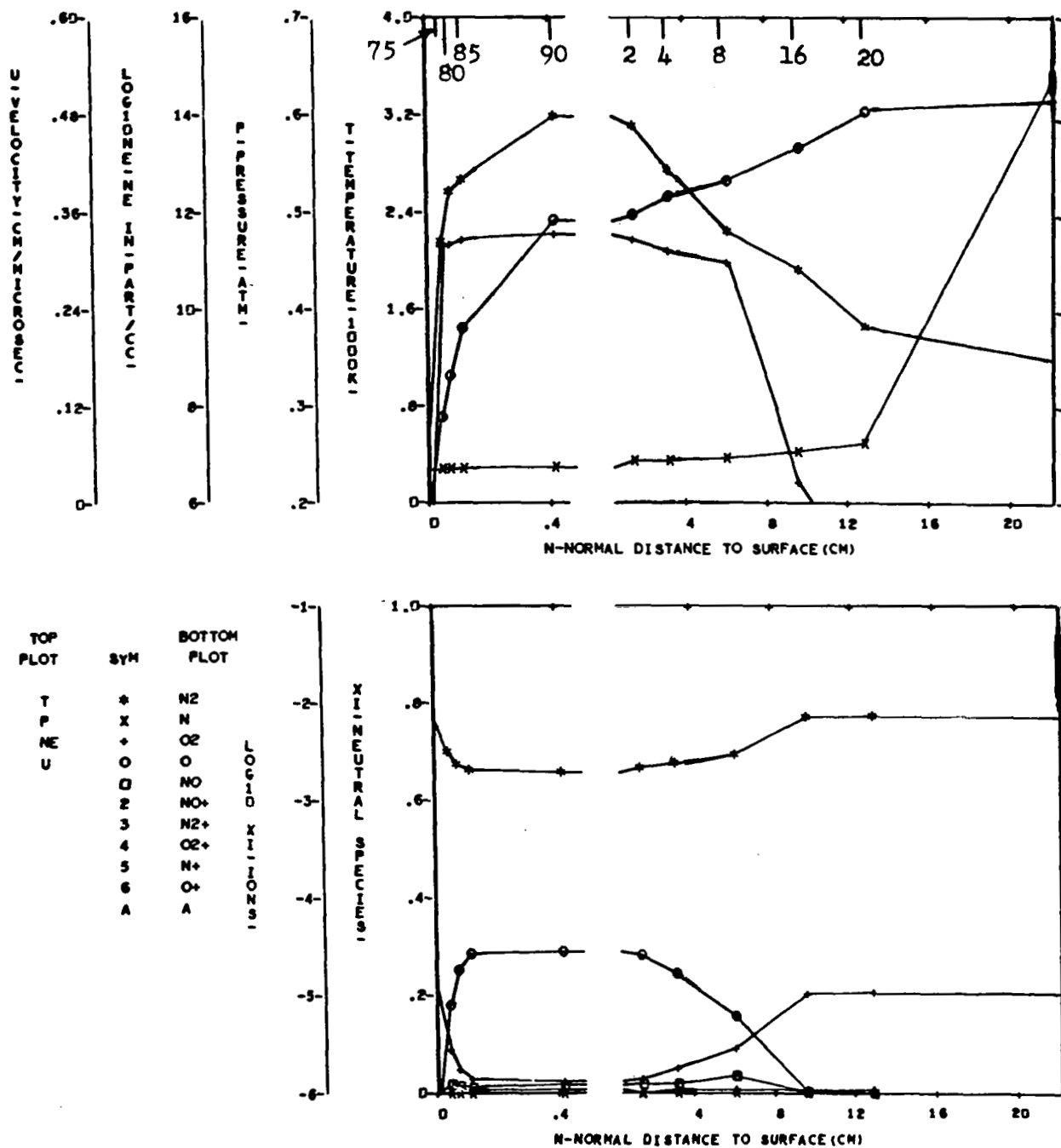FIGURE 94   NONEQUILIBRIUM FLOW FIELD PROPERTIES - CASE 7, NORMAL 4

129

FIGURE 95 NONEQUILIBRIUM FLOW FIELD PROPERTIES - CASE 7, NORMAL 6

130

FIGURE 96 NONEQUILIBRIUM FLOW FIELD PROPERTIES - CASE 7, NORMAL 7

131

FIGURE 97   NONEQUILIBRIUM FLOW FIELD PROPERTIES - CASE 7, NORMAL 9

FIGURE 98   NONEQUILIBRIUM FLOW FIELD PROPERTIES - CASE 7, NORMAL 11

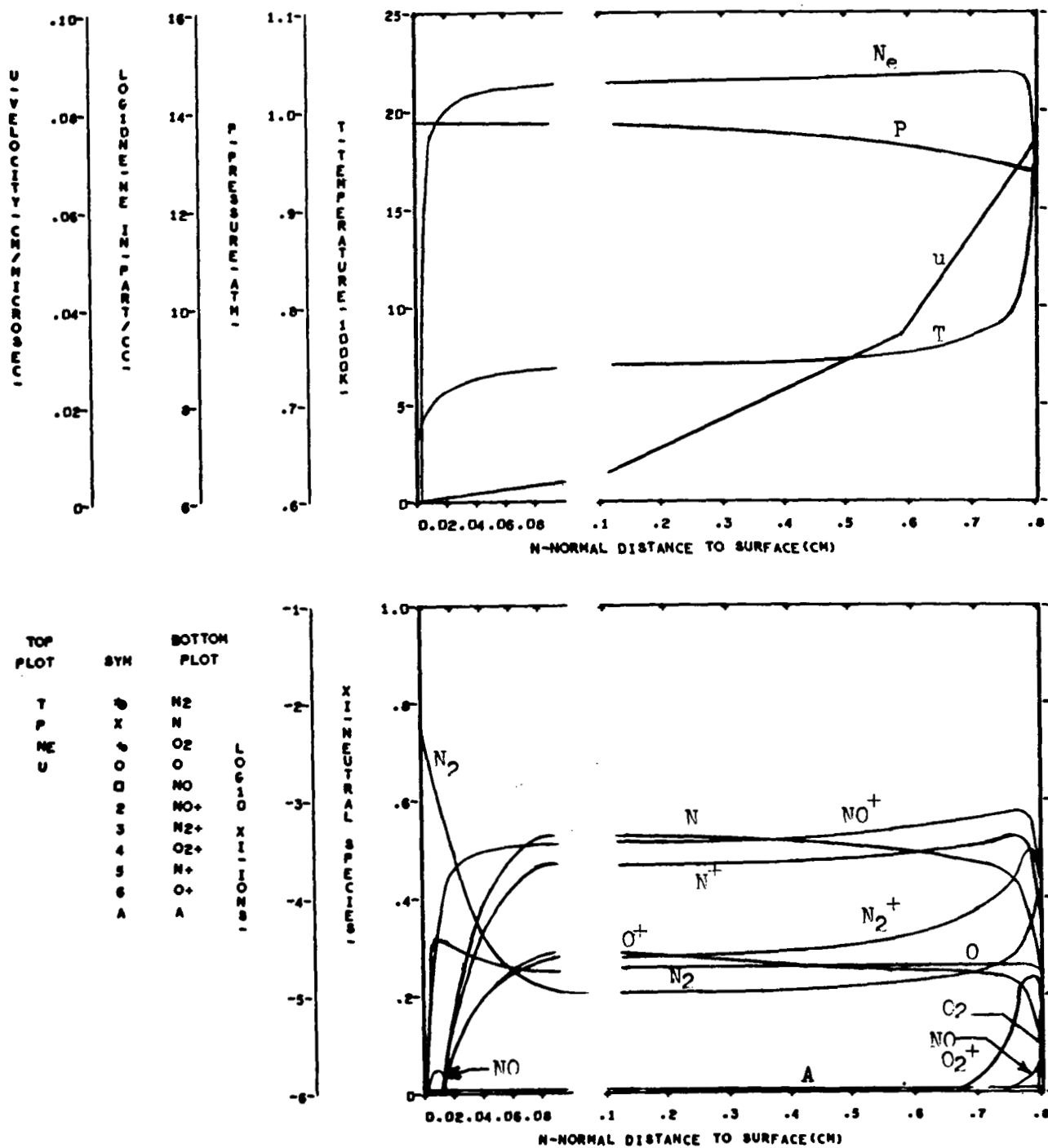FIGURE 99 NONEQUILIBRIUM FLOW FIELD PROPERTIES - CASE 7, NORMAL 12

134

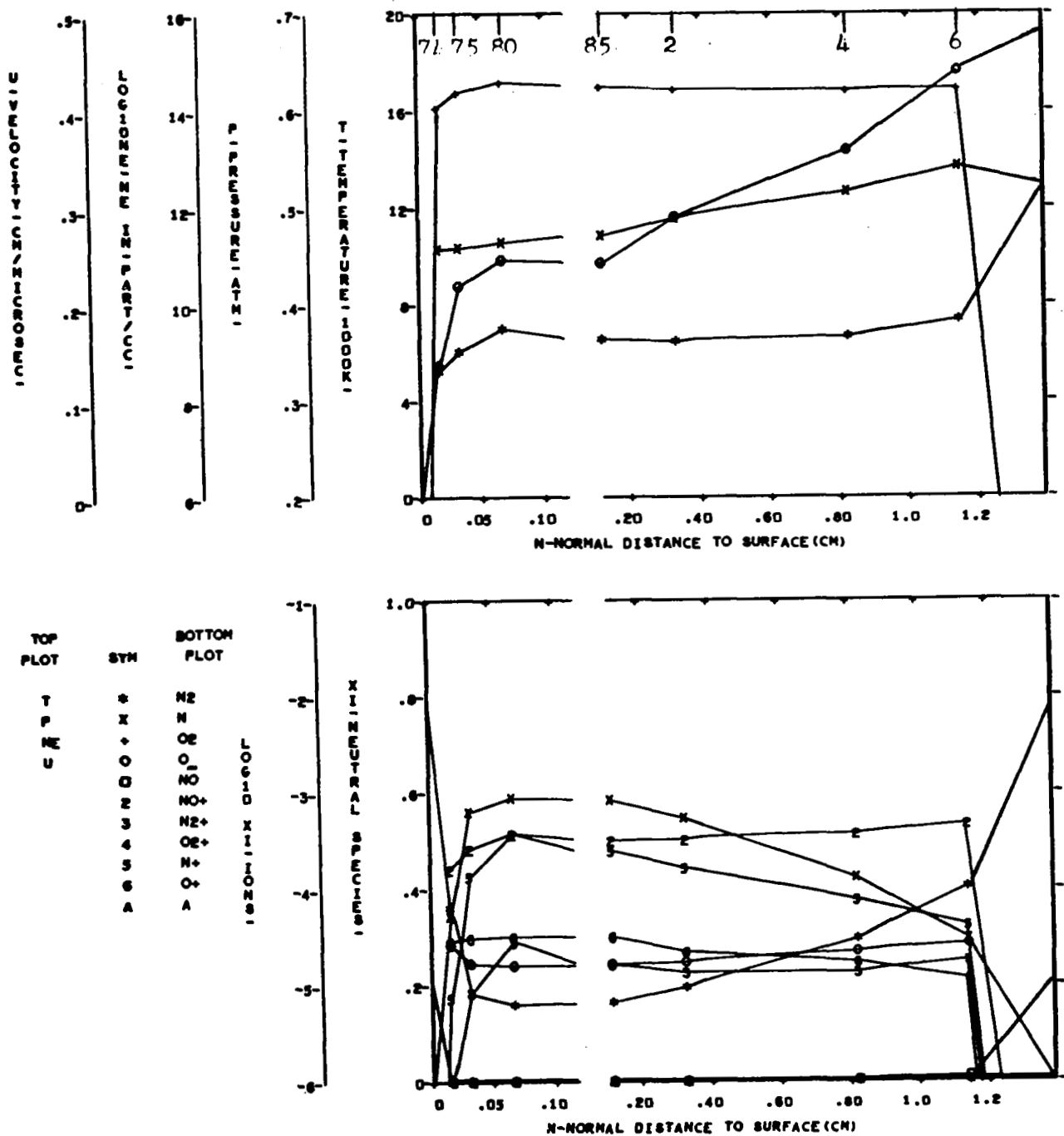FIGURE 100 NONEQUILIBRIUM FLOW FIELD PROPERTIES - CASE 8, NORMAL 1
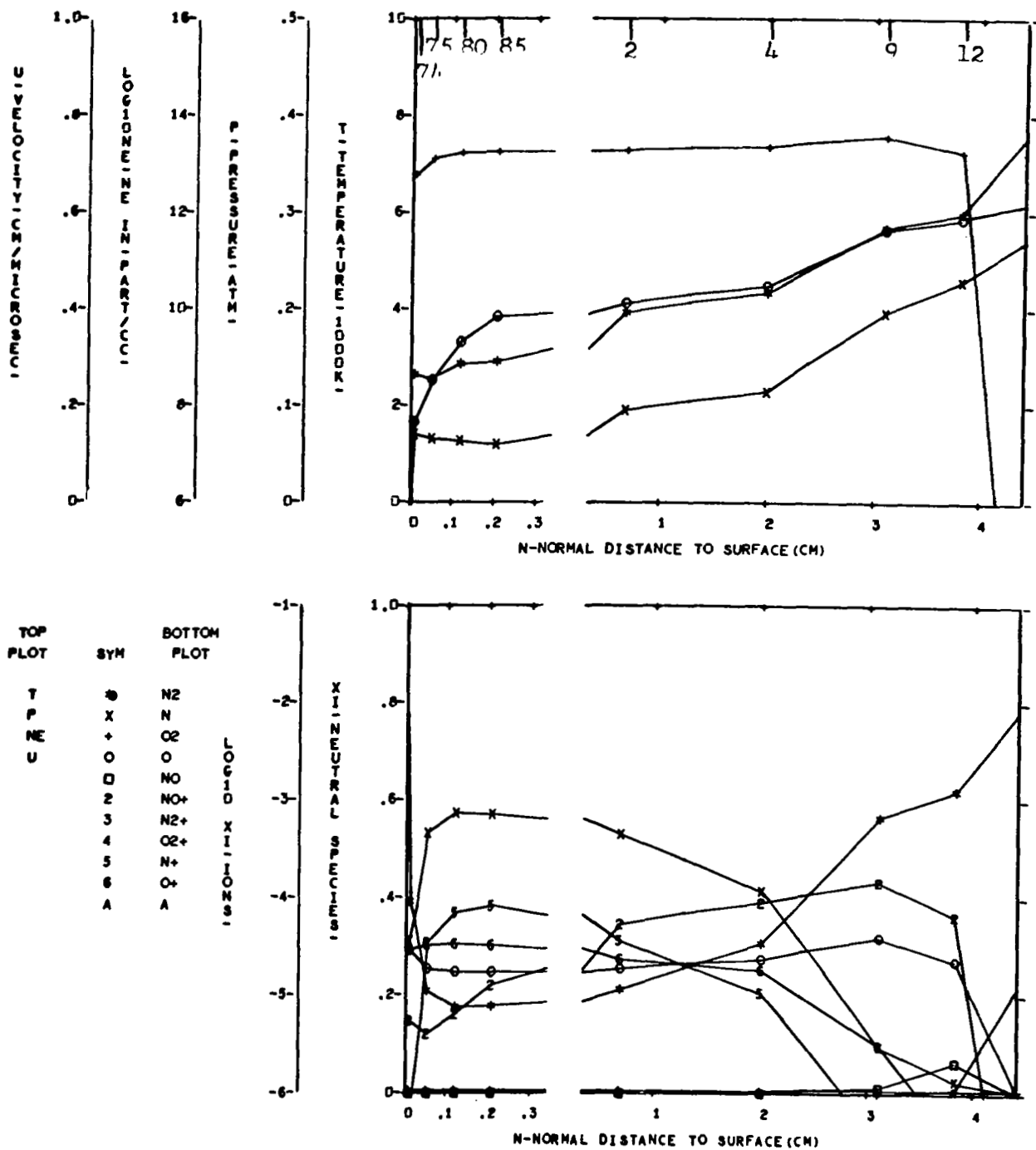
135

FIGURE 101 NONEQUILIBRIUM FLOW FIELD PROPERTIES - CASE 8, NORMAL 4

136

FIGURE 102 NONEQUILIBRIUM FLOW FIELD PROPERTIES - CASE 8, NORMAL 6
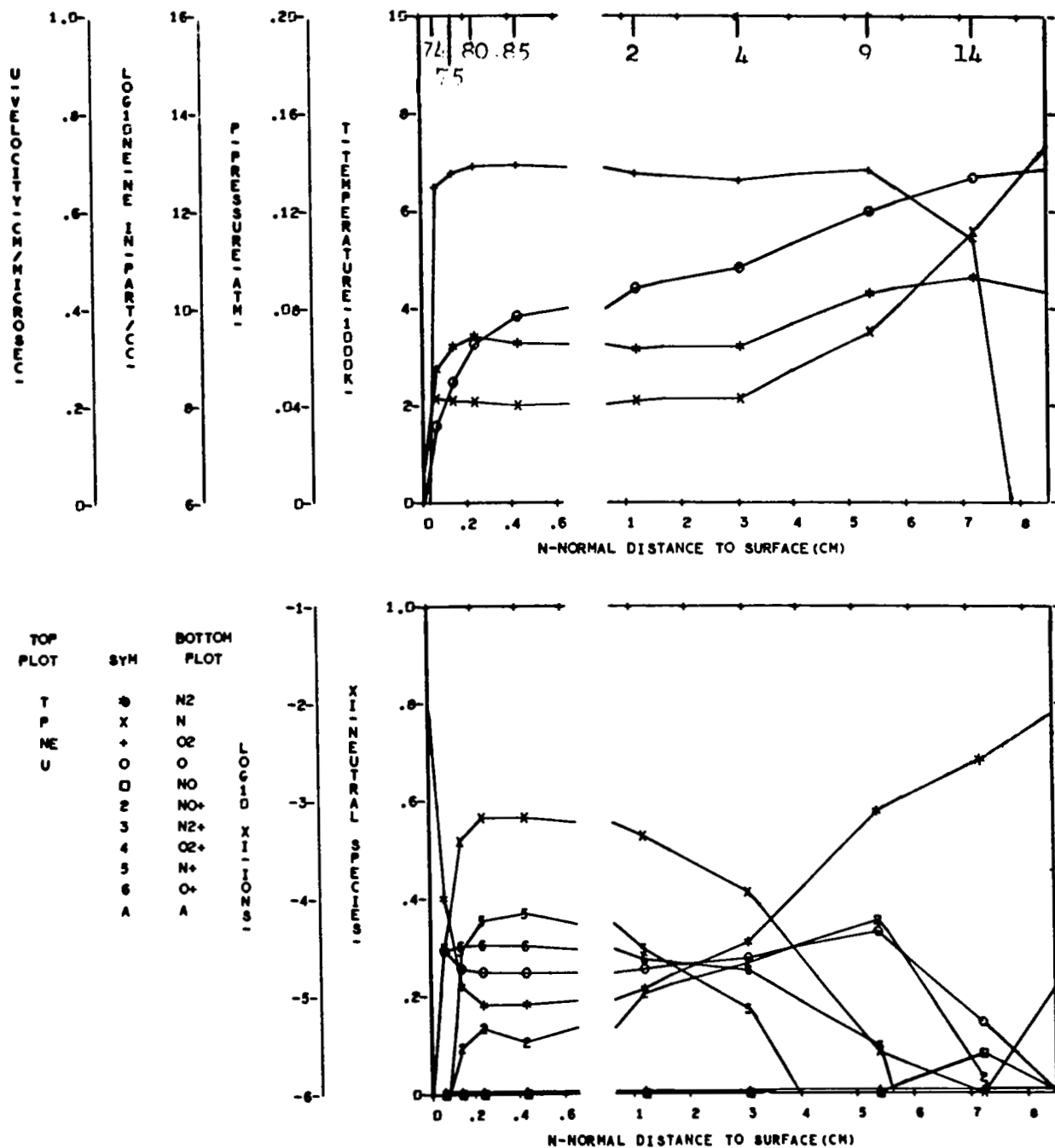
137

FIGURE 103 NONEQUILIBRIUM FLOW FIELD PROPERTIES - CASE 8, NORMAL 7

138

FIGURE 104. NONEQUILIBRIUM FLOW FIELD PROPERTIES - CASE 8, NORMAL 9

139

FIGURE 105 NONEQUILIBRIUM FLOW FIELD PROPERTIES - CASE 8, NORMAL 11

FIGURE 106 NONEQUILIBRIUM FLOW FIELD PROPERTIES - CASE 8, NORMAL 12

141

FIGURE 107 NONEQUILIBRIUM FLOW FIELD PROPERTIES - CASE 9, NORMAL 1

142

FIGURE 108 NONEQUILIBRIUM FLOW FIELD PROPERTIES - CASE 9, NORMAL 4

143

FIGURE 109 NONEQUILIBRIUM FLOW FIELD PROPERTIES - CASE 9, NORMAL 6

144

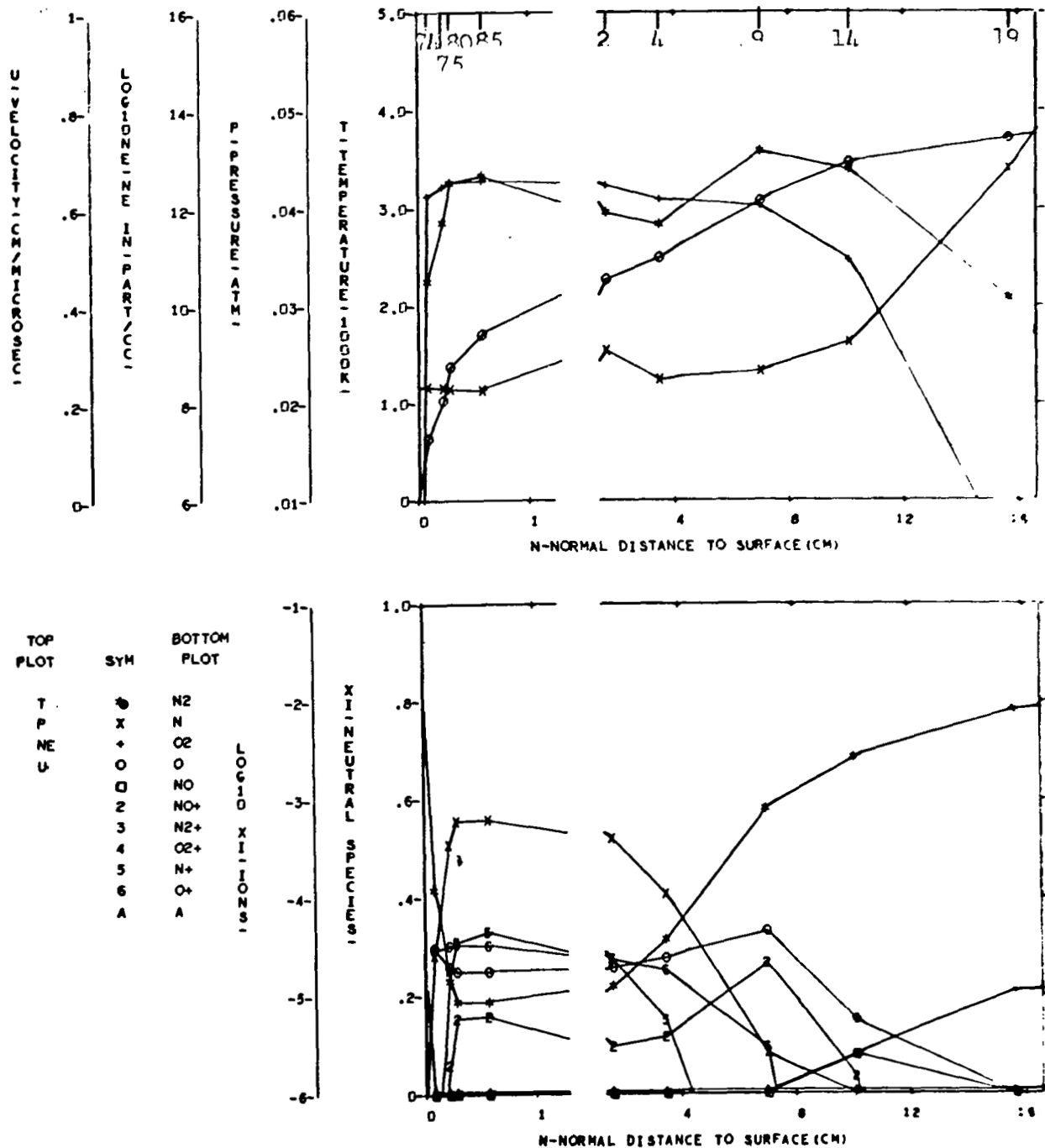FIGURE 110 NONEQUILIBRIUM FLOW FIELD PROPERTIES - CASE 9, NORMAL 7

145

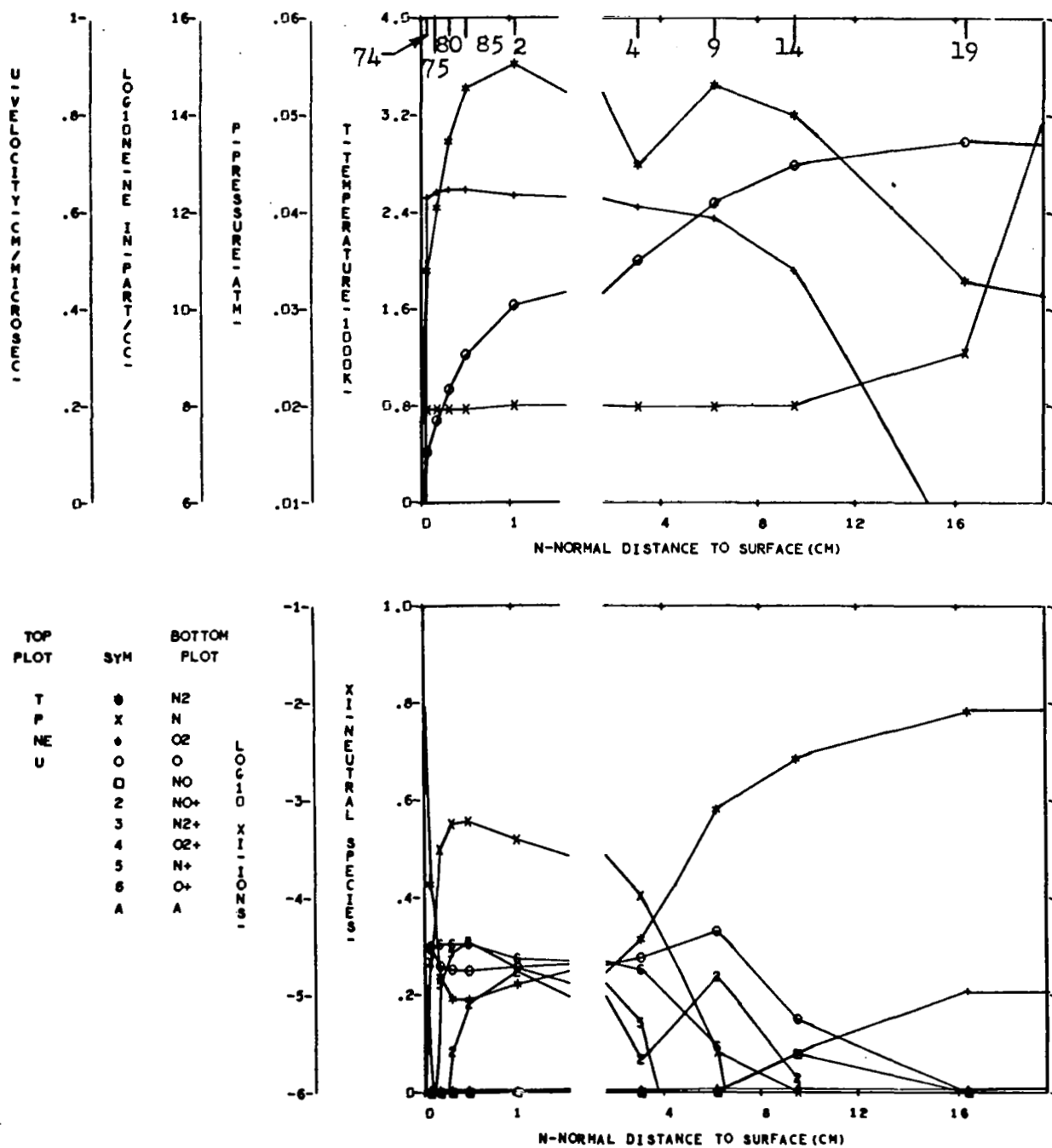FIGURE 111 NONEQUILIBRIUM FLOW FIELD PROPERTIES - CASE 9, NORMAL 9

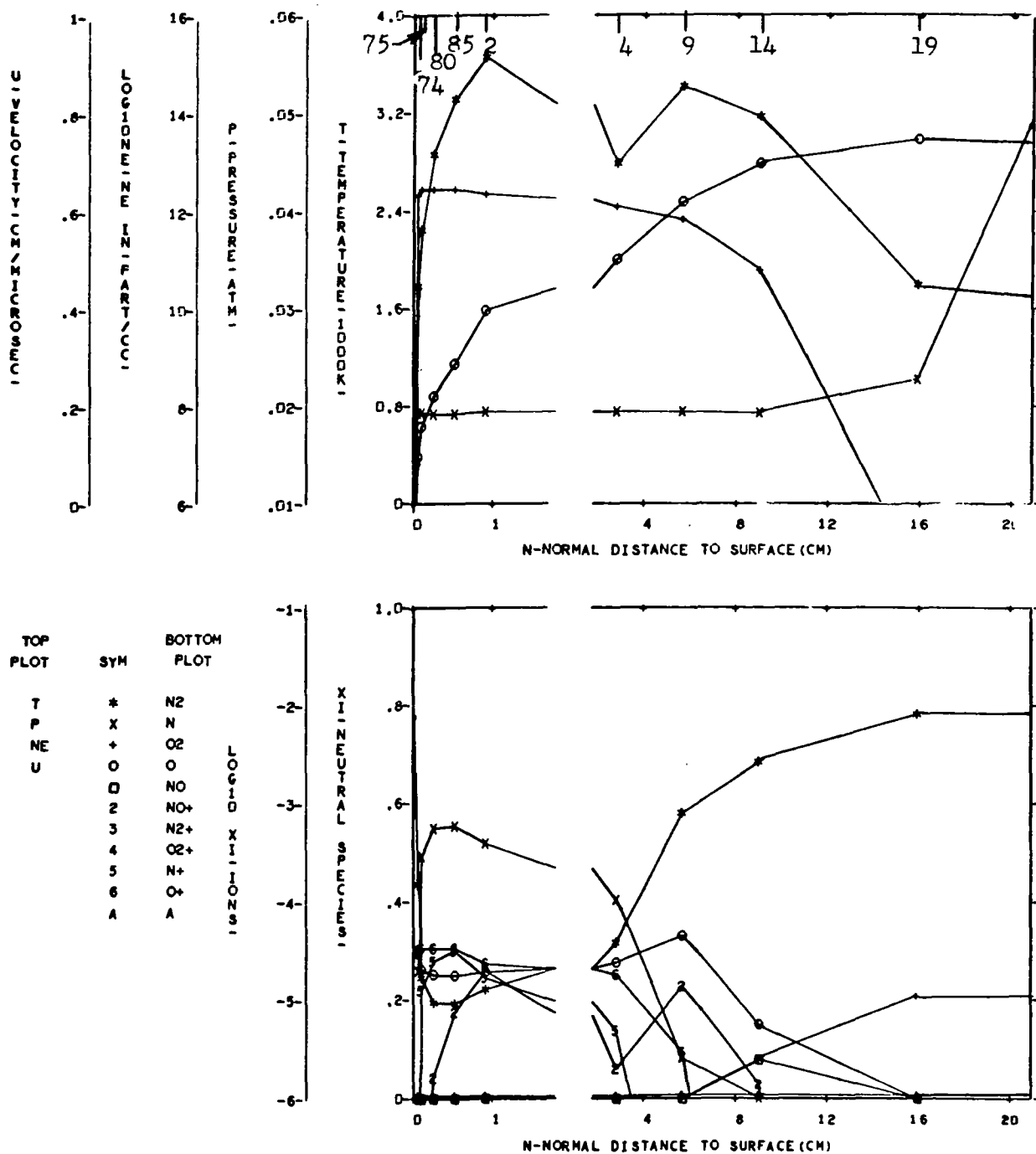FIGURE 112 NONEQUILIBRIUM FLOW FIELD PROPERTIES - CASE 9, NORMAL 11

147

FIGURE 113 NONEQUILIBRIUM FLOW FIELD PROPERTIES - CASE 9, NORMAL 12